ELECTROMAGNETIC EFFECT OF EDGES

A thesis presented for the degree of

Doctor of Philosophy

in Electrical Engineering,

in the University of Canterbury,

Christchurch, New Zealand

by

G.L. James, B.E.(Hons)

1973

There was a young man called James,
who looked to antennas for fame.
With consideration of edges,
regarding horns and reflectors,
he managed to go nearly insane.

ABSTRACT

The electromagnetic effect of edges on the radiation pattern of horn and reflector type antennas is investigated. An attempt is made to control the radiation pattern by changing the edge geometry. Both theoretical and experimental results are given.

Edge diffraction methods are discussed in detail and form the basis of the theoretical analysis. Comparisons are made with other methods where applicable.

The particular antennas considered are pyramidal horns, sectoral horns, and circularly symmetric paraboloidal reflectors illuminated by a source at the focus. Radiation from the horns is investigated only in those principal planes reducible to a two-dimensional problem. Scattering from the reflectors is considered as a three-dimensional problem.

ACKNOWLEDGEMENTS

I am happy to acknowledge the many people who, in some way, have contributed to the preparation of this thesis. These have included my supervisor, Dr V. Kerdemelidis for initially suggesting such an interesting and useful field of research, and for his unstinting assistance throughout this project; Mr A.N. Vernon for his remarkable skill and practical expertise in constructing the various antennas and associated equipment used for the radiation pattern measurements; staff and fellow students at the University of Canterbury, past and present, particularly Drs R.H.T. Bates, F.L. Ng and C.T. Wong, for numerous discussions, useful and otherwise; Mrs Sewell for her expert typing of a difficult manuscript; the University Grants Committee who enabled me to undertake this work by providing financial assistance; and finally my wife, Frances, for her encouragement and for her ability in handling our mutual responsibilities so well that I have been oblivious to the fact that many of them exist.

TABLE OF CONTENTS

CHAPTER ONE: INTRODUCTION

Yet, by your gracious patience,
I will a round unvarnish'd tale deliver

William Shakespeare (1564-1616)

The radiation pattern of an antenna is an important characteristic of its electric performance together with power gain, polarization, input impedance, bandwidth and noise temperature. In this thesis we consider the electromagnetic effect of edges on the radiation pattern of horn and reflector type antennas. In particular, we seek ways of reducing radiation in predetermined directions of space. This will be of use for receiving antennas in locations where the ambient noise is not distributed isotropically, and for transmitting antennas interfering with the operation of other antenna systems.

Radiation pattern design is, ideally, a problem of antenna synthesis where an antenna is developed to realize a given radiation pattern. Such a procedure is usually a formidable problem so that the earlier synthesis techniques were developed only for the relatively simple antenna configurations of equispaced linear arrays and line source distributions. From this work it was found that arrays could be designed - in theory at least - to have as great a directivity as desired by increasing the number of elements for the same overall length. The ability to obtain an arbitrarily large directivity in a required direction would avoid the necessity of seeking the reduction of radiation in directions of unwanted sources.

The theoretical possibility of such supergain antennas, i.e., a large gain possessed by a small antenna, was discovered initially by Oseen (1922). It was apparently forgotten for 21 years until Schelkunoff (1943) demonstrated it in his paper on linear arrays. Yaru (1951) attempted to show that such arrays are impractical. He considered a nine element broadside array producing a power gain of 8.5. The elemental spacing was $\frac{\lambda}{32}$. Using the method of Riblet (1947) to determine the current ratios it was found that extremely large phase-reversed currents, which must be adjusted to their correct value with an accuracy better than 1 part in 10^{11}, flowed in adjacent elements. The efficiency of the array was less than 10^{-14} percent. Bloch *et al.* (1953) pointed out, however, that these current distributions do not lead to maximum directivity, and to dismiss supergain arrays as impractical because some extremely inefficient current distributions have been found (e.g. Yaru (1951)) is unjustified. They showed that the current distribution required for maximum directivity of arrays with a finite number of identical elements, and any specified geometrical configuration, could be found analytically. An example is given of a supergain end-fire array consisting of four elements equispaced along a line 0.6λ long. Recently this approach was used for aperiodic linear arrays [Bacon and Medhurst (1969)]. Unfortunately these arrays, and other supergain antennas constructed to date, exhibit, in part, some of the serious limitations of supergain.

With supergain apparently unrealizable, our initial problem of reducing radiation in predetermined directions remains. Specific null placing techniques, such as given by Schelkunoff (1943), Strait (1967), Drane and McIlvenna (1970)

have been developed for equispaced linear arrays. For antenna systems deviating from equispaced linear arrays and line sources, synthesis procedures often involve considerable mathematical difficulties, and conclusive results have yet to be obtained for many of these systems.

With the difficulties associated with synthesis methods for antennas other than the linear antennas mentioned above, it is not surprising that most solutions to antenna problems have been attempted by the more direct analysis procedure. For antenna analysis, it is only necessary to know, or estimate, the current distribution on the antenna from which the radiation pattern is readily calculated. We then examine this pattern to see if it has any of the characteristics we require. Modifications to the radiation pattern can be achieved by altering the shape and size of the antenna. By calculated guesswork in the choice of these modifications, we may come closer to our required pattern.

Since only a small number of electromagnetic problems have exact solutions, it is usually necessary to approximate the current distribution on the antenna. For high-frequency scattering from perfectly conducting bodies the current distribution may be approximated by the methods of geometrical and physical optics. These methods break down, however, when the scattering body has points or curves of small radii of curvature (such as edges, corners, vertices) or when the contribution from the geometrical shadow region becomes important. To account for these effects two theories have been developed. One, by Keller (1962), extends geometrical optics by introducing diffracted rays to describe diffraction phenomena; another, by Ufimtsev (1962), extends physical optics

by an additional surface current term to correct for a non-planar surface. Both methods are developed from the known exact solution of simple shapes. By comparing the exact and approximate solutions (from geometrical or physical optics), some general laws can be deduced to yield corrections to the approximate methods. Since many bodies are made up from these simple shapes, we can find their scattering properties by applying these laws and sum the contributions from the individual shapes. Keller's theory is the simpler of the two and has been applied to numerous problems. In some cases, however, it gives infinities for the value of the field, and requires special consideration to extend it for three-dimensional problems. These difficulties do not exist with Ufimtsev's theory.

In this thesis we are concerned with bodies having sharp edges. Chapter 2 discusses edge diffraction in some detail. Keller's theory, with some important extensions, is given as it applies to edge diffraction. The equivalent edge current concept for three-dimensional problems is extended to include the more general case of cylindrical-wave oblique incidence to an edge. With the concepts discussed in chapter 2, we consider in chapter 3 those principal planes of rectangular electromagnetic horns which can be reduced to a two-dimensional problem. The edge diffraction approach is compared with the classical aperture field method, and in the case of the sectoral horns, with an exact solution. With this knowledge of the radiation mechanism from the antenna, we attempt to control its radiation pattern by changing the aperture edge geometry.

In chapter 4 we consider scattering from a paraboloidal reflector as a three-dimensional problem and use the equivalent edge current concept for the edge diffraction approach. This is compared with physical optics and Ufimtsev's theory as applied to the reflector. The Chapter is concluded by considering the effect on the reflector radiation pattern with changes in the edge geometry. Conclusions are drawn in chapter 5 on the work in the preceding chapters.

Two papers have been published on some of the topics presented in this thesis (James and Kerdemelidis, 1972; James and Kerdemelidis, 1973) and two further papers are in preparation.

CHAPTER TWO: EDGE DIFFRACTION THEORY

I have a paper afloat, with an electromagnetic theory of light, which 'till I am convinced to the contrary, I hold to be great guns.

James Clerk Maxwell (1865)

A useful approximation for estimating high-frequency scattering from a body can be obtained from expressions deduced from an exact canonical solution appropriate to the local geometry of the body. The Geometrical Theory of Diffraction (GTD) (Keller, 1962) is a well known method which uses this approach. It extends geometrical optics to allow the diffracted field to be given by ray tracing methods using the concept of diffracted rays from surface discontinuities on the body. The behaviour of these diffracted rays is determined by diffraction coefficients deduced from the canonical problem containing the same type of surface discontinuity. The existence of an exact canonical solution is not essential to provide diffraction coefficients if an adequate description of the field in the vicinity of the discontinuity can be obtained. Such an approach was taken by Senior (1972) to obtain diffraction coefficients for a discontinuity of curvature.

We are interested in the effect of antenna edges on the radiation patterns of horn and reflector type antennas. The appropriate canonical problem for edges is the infinite wedge illuminated by an electromagnetic wave. Solutions to this problem are discussed in 2.2. This is followed in 2.3 by a study of the GTD and some important extensions applicable to edge diffraction. We will use the simple ray tracing methods

of the GTD in Ch. 3 to analyse radiation in those principal planes of horn antennas which can be considered as two-dimensional problems. For edge-scattering in three-dimensions the GTD is not readily useful. A suitable approach, while still maintaining the advantage of using expressions deduced from exact solutions, is the equivalent edge current method discussed in 2.4. Previously, this approach was limited to normally incident uniform plane-waves. We extend the equivalent edge current method to the more general problem of non-uniform plane- and cylindrical-waves at oblique incidence.

Before we begin the discussion on edge diffraction theory, we will give solutions to Maxwell's equations which are required in later work.

2.1 SOLUTIONS TO MAXWELL'S EQUATIONS

2.11 Electromagnetic Potentials

Maxwell's equations for time-harmonic fields in unbounded space, with the time dependence $e^{j\omega t}$ suppressed, are

$$-\nabla_{\wedge} \underline{E} = j\omega\mu\underline{H} + \underline{M},$$
$$\nabla_{\wedge} \underline{H} = j\omega\varepsilon\underline{E} + \underline{J}, \tag{2.1}$$

where $\underline{H}$ is the magnetic field intensity, $\underline{E}$ is the electric field intensity, $\underline{M}$ is the magnetic source current, $\underline{J}$ is the electric source current, μ and ε are the (scalar) permeability and permittivity of space, and ω is the angular frequency. Solutions to (2.1) can be expressed in terms of a magnetic vector potential $\underline{A}$, and an electric vector potential $\underline{F}$, to give $\underline{E}$ and $\underline{H}$ explicitly as

$$\underline{E} = -\nabla \wedge \underline{F} - j\omega\mu\underline{A} + \frac{1}{j\omega\varepsilon}\nabla(\nabla.\underline{A}),$$

$$\underline{H} = \nabla \wedge \underline{A} - j\omega\varepsilon\underline{F} + \frac{1}{j\omega\mu}\nabla(\nabla.\underline{F}), \tag{2.2}$$

where

$$\nabla^2\underline{A} + K^2\underline{A} = -J,$$

$$\nabla^2\underline{F} + K^2\underline{F} = -\underline{M}. \tag{2.3}$$

Solving for the potentials in (2.3) yields

$$\begin{matrix}\underline{A}(\underline{r}) \\ \underline{F}(\underline{r})\end{matrix} = \iiint \begin{matrix}\underline{J}(\underline{r}) \\ \underline{M}(\underline{r})\end{matrix} G(\underline{r},\underline{r}')dV' \tag{2.4}$$

where the prime denotes the source coordinates as illustrated in Fig. 2.1; V' is the region, bounded by S' and containing the sources; and $G(\underline{r},\underline{r}')$ is the Green's function.

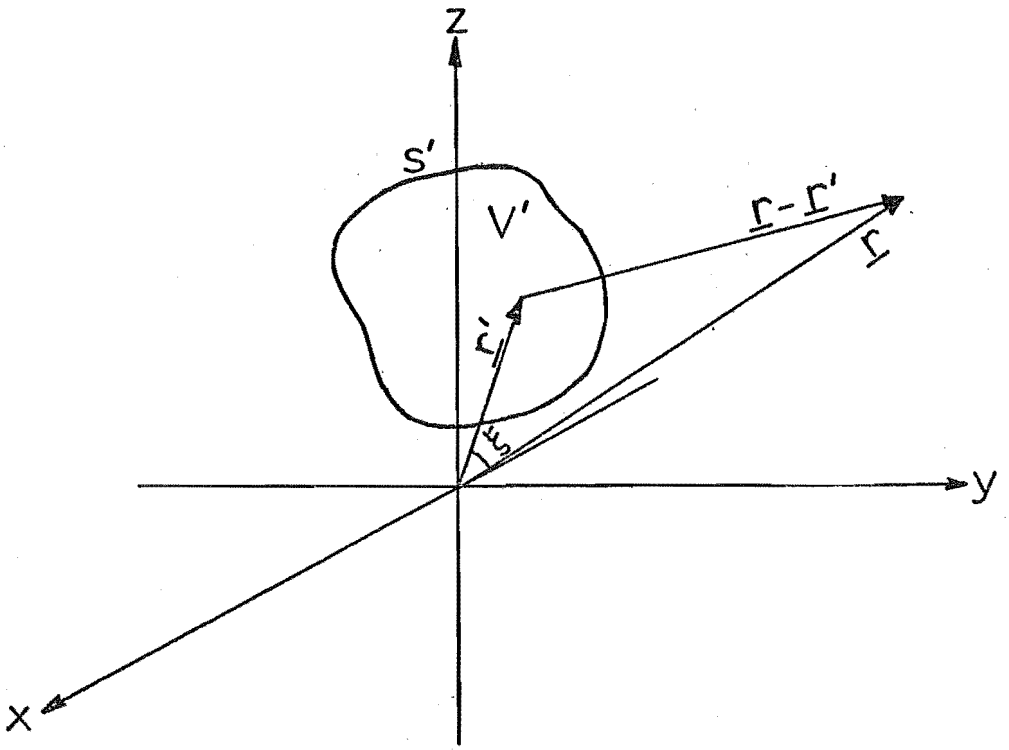

Fig. 2.1 Geometry for field integrals

If the potentials in (2.3) are linearly polarized, we can write them as $\underline{A} = \hat{c}\Psi_a$, $\underline{F} = \hat{c}\Psi_f$, where $\hat{c}$ is the unit vector in the direction of polarization. In source-free regions (2,3) then reduces to the Helmholtz equation

$$\nabla^2\Psi + k^2\Psi = 0. \tag{2.5}$$

2.12 The Radiation Field

To evaluate the radiation field from sources of finite extent, the integral solution for the potentials of (2.4) and the corresponding fields in (2.2) can be considerably simplified.

2.121 Three-dimensional source distributions

The Green's function, $G(\underline{r},\underline{r}')$, is given in three dimensions by

$$G(\underline{r},\underline{r}') = \frac{e^{-jk|\underline{r}-\underline{r}'|}}{4\pi|\underline{r}-\underline{r}'|} . \tag{2.6}$$

In the radiation zone we have $|\underline{r}| >> |\underline{r}'_{max}|$, and

$$|\underline{r}-\underline{r}'| \sim r - r'\text{Cos } \xi, \tag{2.7}$$

where ξ is defined in Fig. 2.1. Combining (2.4), (2.6) and (2.7) gives

$$\begin{matrix}\underline{A}(\underline{r}) \\ \underline{F}(\underline{r})\end{matrix} = \frac{e^{-jkr}}{4\pi r} \iiint \begin{matrix}\underline{J}(\underline{r}') \\ \underline{M}(\underline{r}')\end{matrix} e^{jkr'\text{Cos } \xi}\, dV', \tag{2.8}$$

where, for the three coordinate systems commonly used, as shown in Fig. 2.2, we have

$$r'\text{Cos } \xi = (x'\text{Cos } \phi + y'\text{Sin } \phi)\text{Sin } \theta + z'\text{Cos } \theta \tag{2.9}$$

for rectangular coordinates;

$$r'\text{Cos}\,\xi = \rho'\text{Sin}\,\theta\,\text{Cos}(\phi-\phi') + z'\text{Cos}\,\theta \qquad (2.10)$$

for cylindrical coordinates;

$$r'\text{Cos}\,\xi = r'[\text{Cos}\,\theta\,\text{Cos}\,\theta' + \text{Sin}\,\theta\,\text{Sin}\,\theta'\text{Cos}(\phi-\phi')] \qquad (2.11)$$

for spherical coordinates.

If we expand (2.2) for the radiation zone using (2.8) in spherical coordinates (r,ϕ,θ), we get

$$\begin{aligned} E_\theta &= -j\omega\mu A_\theta - jkF_\phi, \\ E_\phi &= -j\omega\mu A_\phi + jkF_\theta, \\ H_\phi &= \sqrt{\frac{\varepsilon}{\mu}}\,E_\theta, \\ H_\theta &= -\sqrt{\frac{\varepsilon}{\mu}}\,E_\phi. \end{aligned} \qquad (2.12)$$

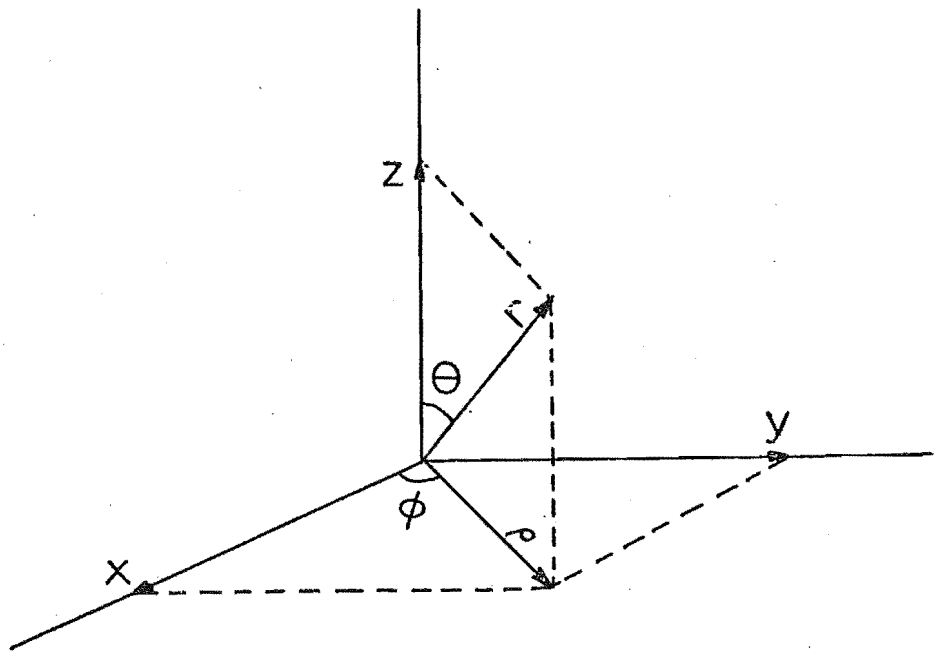

Fig. 2.2 Coordinate geometry

For the source-free region external to V' in Fig. 2.1, the electromagnetic field can be expressed in terms of equivalent source distributions, $\underline{J}_{s'}$, $\underline{M}_{s'}$ over s', replacing the

sources in V'. From (2.2) and (2.8) we obtain for the radiation field using these equivalent surface currents

$$\underline{E}(\underline{r}) = -j\omega\mu \frac{e^{-jkr}}{4\pi r} \iint [\sqrt{\frac{\epsilon}{\mu}}\, \underline{M}_{s'} \wedge \hat{r} + \underline{J}_{s'} - (\underline{J}_{s'} \cdot \hat{r})\hat{r}] e^{jkr'\mathrm{Cos}\,\xi}\, dS';$$

$$\underline{H}(\underline{r}) = j\omega\epsilon \frac{e^{-jkr}}{4\pi r} \iint [\sqrt{\frac{\mu}{\epsilon}}\, \underline{J}_{s'} \wedge \hat{r} - \underline{M}_{s'} + (\underline{M}_{s'} \cdot \hat{r})\hat{r}] e^{jkr'\mathrm{Cos}\,\xi}\, dS'. \tag{2.13}$$

2.122 Two-dimensional source distributions

For a two-dimensional distribution of currents, independent of z, the Green's function is given by (Harrington, 1961a)

$$G(\underline{\rho},\underline{\rho}') = \frac{1}{4j} H_0^{(2)}(k|\underline{\rho}-\underline{\rho}'|), \tag{2.14}$$

where $H_0^{(2)}$ is the zero order Hankel function of the second kind. In the radiation zone we have, as before, the condition $|\underline{\rho}| >> |\underline{\rho}'_{max}|$, and

$$|\underline{\rho}-\underline{\rho}'| \sim \rho - \rho'\mathrm{Cos}(\phi-\phi'). \tag{2.15}$$

We also have

$$H_0^{(2)}(k|\underline{\rho}-\underline{\rho}'|) \sim \sqrt{\frac{2j}{\pi k\rho}}\, e^{-jk\rho}\, e^{jk\rho'\mathrm{Cos}(\phi-\phi')}. \tag{2.16}$$

The vector potentials of (2.4) for the radiation field from a two-dimensional current distribution become

$$\begin{matrix}\underline{A}(\underline{\rho}) \\ \underline{F}(\underline{\rho})\end{matrix} = \frac{e^{-jk\rho}}{\sqrt{8j\pi k\rho}} \iint \begin{matrix}\underline{J}(\underline{\rho}') \\ \underline{M}(\underline{\rho}')\end{matrix} e^{jk\rho'\mathrm{Cos}(\phi-\phi')}\, dA', \tag{2.17}$$

where the integration is performed over the area A' occupied by the cross-section of the sources.

For the source-free region external to A', we can reduce (2.13) for equivalent two-dimensional source distributions to give

$$\underline{E}(\underline{\rho}) = -j\omega\mu \frac{e^{-jk\rho}}{\sqrt{8j\pi k\rho}} \int [\sqrt{\frac{\varepsilon}{\mu}}\, \underline{M}_{\ell'} \wedge \hat{\rho} + \underline{J}_{\ell'} - (\underline{J}_{\ell'} \cdot \hat{\rho})\hat{\rho}]e^{jk\rho'\cos(\phi-\phi')} d\ell',$$

$$\underline{H}(\underline{\rho}) = j\omega\varepsilon \frac{e^{-jk\rho}}{\sqrt{8j\pi k\rho}} \int [\sqrt{\frac{\mu}{\varepsilon}}\, \underline{J}_{\ell'} \wedge \hat{\rho} - \underline{M}_{\ell'} + (M_{\ell'} \cdot \hat{\rho})\hat{\rho}]e^{jk\rho'\cos(\phi-\phi')} d\ell', \tag{2.18}$$

where the integration is taken around the closed loop, ℓ', containing the cross-section of the sources. These sources are replaced by equivalent sources, $\underline{J}_{\ell'}$, $\underline{M}_{\ell'}$ on ℓ'.

If the potentials are linearly polarized in the z-direction we can write them as $\underline{A} = \hat{z}\Psi_a$, $\underline{F} = \hat{z}\Psi_f$. Then, in the radiation zone, we get, expanding (2.2) in the cylindrical coordinates (ρ,ϕ,z),

$$\begin{aligned} E_z &= -j\omega\mu\Psi_a, \\ E_\phi &= -jk\Psi_f, \\ H_\phi &= -\sqrt{\frac{\varepsilon}{\mu}}\, E_z, \\ H_z &= \sqrt{\frac{\varepsilon}{\mu}}\, E_\phi. \end{aligned} \tag{2.19}$$

2.2 SCATTERING BY A WEDGE

2.21 Incident field from a line-source

Consider a perfectly conducting wedge, in free space, with its edge situated on the z-axis as in Fig. 2.3.

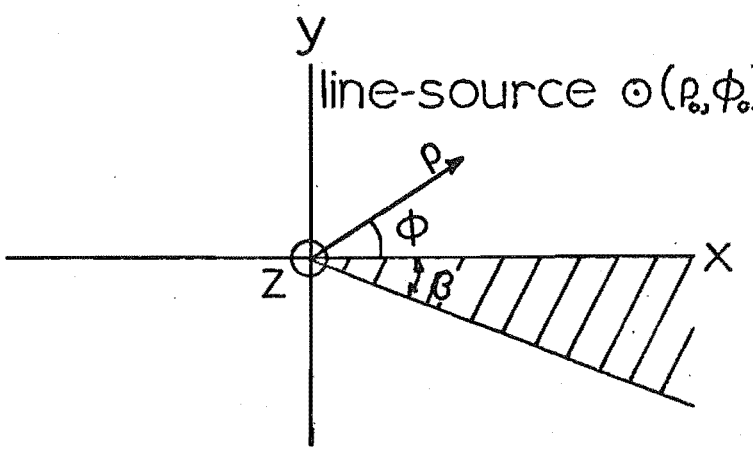

Fig. 2.3 Line-source near perfectly conducting wedge

The wedge is of infinite extent in both the positive and negative z-directions, with the faces of the wedge occupying the semi-infinite planes $\phi = 0,-\beta$. A line-source at (ρ_0,ϕ_0) provides the primary field, given by (Harrington, 1961b)

$$\begin{matrix} A_z(\underline{\rho}) \\ F_z(\underline{\rho}) \end{matrix} = \begin{matrix} I^e(\underline{\rho}_0) \\ I^m(\underline{\rho}_0) \end{matrix} \Psi_0, \tag{2.20}$$

where

$$\Psi_0 = \frac{1}{4j} H_0^{(2)}(k|\underline{\rho}-\underline{\rho}_0|), \tag{2.21}$$

$H_0^{(2)}$ is the zero order Hankel function of the second kind, and $I^e(\underline{\rho}_0)$ ($I^m(\underline{\rho}_0)$) is the magnitude of the electric (magnetic) line-source.

We seek solutions to (2.3) for the problem illustrated in Fig. 2.3. Since the incident field has only a z-component, the total field will also have only a z-component, because this will be sufficient to satisfy the boundary conditions on the wedge. Normalising the magnitude of the line-source to unity, (2.3) becomes

$$\nabla^2\Psi_{\substack{a \\ f}} + k^2\Psi_{\substack{a \\ f}} = -\frac{1}{\rho_0}\delta(\rho-\rho_0)\delta(\phi-\phi_0), \tag{2.22}$$

where $\delta(x)$ is the Dirac delta function, Ψ_a (Ψ_f) is the solution for a unit electric (magnetic) line-source at (ρ_0,ϕ_0) for the boundary condition $\Psi_a = 0$ ($\frac{\partial}{\partial\hat{n}}\Psi_f = 0$) on the wedge faces. Here $\hat{n}$ is the normal to these faces.

Separation of variables was the first method used to solve the problem (Macdonald, 1902; Macdonald, 1915), giving both an infinite set of eigenfunctions and an integral representation.

Solutions by transform methods have later been obtained (Kontorowich and Lebedev, 1939; Jones, 1964a) which are mathematically more tractable.

For the eigenfunction solution we have

$$\Psi_{\substack{a\\f}}(\rho,\phi) = \begin{cases} \frac{1}{j4N} \sum_{\nu} \varepsilon_\nu J_\nu(k\rho) H_\nu^{(2)}(k\rho_0)[\text{Cos } \nu(\phi-\phi_0) \mp \text{Cos } \nu(\phi+\phi_0)] & \rho<\rho_0 \\ \frac{1}{j4N} \sum_{\nu} \varepsilon_\nu J_\nu(k\rho_0) H_\nu^{(2)}(k\rho)[\text{Cos } \nu(\phi-\phi_0) \mp \text{Cos } \nu(\phi+\phi_0)] & \rho>\rho_0 \end{cases} \tag{2.23}$$

where

$$N = \frac{2\pi-\beta}{\pi},$$

$$\nu = \frac{M}{N}, \quad M = 0,1,2,\ldots,$$

$$\varepsilon_\nu = \begin{cases} 1 & \text{for } \nu = 0 \\ 2 & \text{for } \nu > 0, \end{cases}$$

J_ν is the ν^{th}-order Bessel function of the first kind, $H_\nu^{(2)}$ is the ν^{th}-order Hankel function of the second kind, and the upper (lower) sign applies for electric (magnetic) polarization.

Yet another form of solution is the linear sum of four terms (Jones, 1964a) giving incident, reflected and two diffraction terms (with the signs applying as above) as

$$\Psi_{\substack{a\\f}}(\rho,\phi) = [V_d(\rho,\phi-\phi_0) + V_{ir}(\rho,\phi-\phi_0)] \mp [V_d(\rho,\phi+\phi_0) + V_{ir}(\rho,\phi+\phi_0)], \tag{2.24}$$

where

$$V_{ir}(\rho,\Phi) = \begin{cases} \frac{1}{j4} H_0^{(2)}(k[\rho^2 + \rho_0^2 - 2\rho\rho_0 \text{Cos}(\Phi+2\pi NP)]^{\frac{1}{2}}); \\ \qquad |\Phi+2\pi NP| < \pi \text{ for } P = 0,\pm1,\pm2,\ldots \\ 0 \quad \text{otherwise}, \end{cases} \tag{2.25}$$

$$V_d(\rho,\Phi) = \frac{1}{j8\pi}\int_{-\infty}^{\infty} \frac{\sin(jw+\frac{\pi}{N})}{\mathrm{Cos}(jw+\frac{\pi}{N}) - \mathrm{Cos}(\frac{\Phi}{N})} \cdot$$

$$H_0^{(2)}(k[\rho^2+\rho_0^2+2\rho\rho_0\mathrm{Cosh}(Nw)]^{\frac{1}{2}})dw, \qquad (2.26)$$

and

$$\Phi = \phi \pm \phi_0.$$

For plane-wave illumination, the line-source is situated at a large distance from the edge so that $\rho_0 >> \rho$. In this case (2.23), (2.25) and (2.26) can be simplified by taking the asymptotic expansion of the Hankel function of the second kind i.e.

$$H_\nu^{(2)}(x) \sim \sqrt{\frac{2j}{\pi x}}\, j^\nu e^{-jx} \quad \text{for } x >> \nu \ , \qquad (2.27)$$

and applying to (2.23) to give

$$\Psi_{\substack{a\\f}}(\rho,\phi) \sim \frac{1}{N}\sum_\nu \varepsilon_\nu j^\nu J_\nu(k\rho)[\mathrm{Cos}\ \nu(\phi-\phi_0) \mp \mathrm{Cos}\ \nu(\phi+\phi_0)], \qquad (2.28)$$

where the expression has been multiplied by the normalizing factor

$$e^{jk\rho_0}\sqrt{8j\pi k\rho_0}. \qquad (2.29)$$

Similarly, simplifying (2.25) and (2.26), and using the binomial expansion for the Hankel function arguments, we get

$$V_{ir}(\rho,\Phi) \sim \begin{cases} \exp[jk\rho\mathrm{Cos}(\Phi+2\pi NP)]; & |\Phi+2\pi NP| < \pi \quad P = 0,\pm1,\pm2,\ldots, \\ 0 \quad \text{otherwise} \end{cases} \qquad (2.30)$$

$$V_d(\rho,\Phi) \sim \frac{1}{2\pi}\int_{-\infty}^{\infty} \frac{\mathrm{Sin}(jw+\frac{\pi}{N})}{\mathrm{Cos}(jw+\frac{\pi}{N}) - \mathrm{Cos}(\frac{\Phi}{N})} \exp[-jk\rho\mathrm{Cosh}(Nw)]dw, \qquad (2,31)$$

where the normalizing factor (2.29) applies. We have the geometrical optics field for the incident and reflected wave

from the wedge, given by (2.30), and a diffraction term, given by (2.31), due to the edge of the wedge.

Sommerfeld's solution to the wedge problem (Sommerfeld, 1954) is expressed as in (2.24), with $V_{ir}(\rho,\Phi)$ given by (2.30), and the diffraction term by

$$V_d(\rho,\Phi) = \frac{1}{2\pi N}\int_c \frac{e^{j k\rho \mathrm{Cos} w}}{1 - e^{\frac{-j(w+\Phi)}{N}}}\, dw, \tag{2.32}$$

where c is the appropriate path in the complex plane. For the special case of the half-plane when $N = 2$, Sommerfeld expressed the diffracted field in terms of a Fresnel integral, to obtain

$$V_d(\rho,\Phi) = -\sqrt{\frac{j}{\pi}}\, e^{j k\rho \mathrm{Cos}\Phi}\, \frac{|\mathrm{Cos}\,\frac{\Phi}{2}|}{\mathrm{Cos}\,\frac{\Phi}{2}}\, F(s), \tag{2.33}$$

where

$$F(s) = \int_s^\infty e^{-jt^2}\, dt, \quad \text{and} \tag{2.34}$$

$$s = \sqrt{k\rho(1 + \mathrm{Cos}\,\Phi)} \tag{2.35}$$

Note that the positive square root of s is taken.

By a contour integration of (2.32), Pauli (1938) obtained an infinite series solution of the form

$$V_d(\rho,\Phi) = \frac{2}{N}\sqrt{\frac{j}{\pi}}\, \frac{\mathrm{Sin}\,\frac{\pi}{N}\,|\mathrm{Cos}\,\frac{\Phi}{2}|}{[\mathrm{Cos}\,\frac{\pi}{N} - \mathrm{Cos}\,\frac{\Phi}{N}]}\, e^{j k\rho \mathrm{Cos}\Phi}\, F(s) + [\text{higher order terms}]. \tag{2.36}$$

The higher order terms can be neglected for large s, and are identically zero for the half-plane when $N = 2$. Equation (2.36) then reduces to (2.33). For large s the Fresnel integral in (2.36) can be replaced by its asymptotic value, viz.,

$$F(s) \sim \frac{e^{-js^2}}{2js} \sum_{m=0}^{\infty} j^m (\tfrac{1}{2})_m (s^2)^{-m}, \qquad (2.37)$$

where

$$(\tfrac{1}{2})_0 = 1; \quad (\tfrac{1}{2})_m = \tfrac{1}{2}(\tfrac{1}{2}+1) \ \ldots \ (\tfrac{1}{2}+m-1).$$

Substituting (2.37) into (2.36) we get

$$V_d(\rho,\Phi) \sim \frac{\operatorname{Sin}\frac{\pi}{N}}{N\sqrt{2j\pi k\rho}\,[\operatorname{Cos}\frac{\pi}{N} - \operatorname{Cos}\frac{\Phi}{N}]}\, e^{-jk\rho} \sum_{m=0}^{\infty} j^m (\tfrac{1}{2})_m (2k\rho\operatorname{Cos}^2\tfrac{\Phi}{2})^{-m} \qquad (2.38)$$

In the far-field, when ρ is very large, only the first term of the series in (2.38) is significant. The diffracted field then appears as a directional cylindrical-wave radiating from the edge. It is this property which allows the diffracted field to be treated by ray tracing techniques which forms the basis of the GTD to be discussed in section 2.3.

2.22 Non-normal incident plane-wave diffraction

In 2.21 the special case of the line-source situated at a large distance from the edge gave solutions for a plane-wave at normal incidence to the wedge. The quasi-two-dimensional problem of non-normal (oblique) incidence can be deduced from these results. Let $\Psi(\rho,\Phi,k)$ be the scalar potential solution to the Helmholtz equation (2.5) for the plane-wave, $\Psi_0(\rho,\Phi,k)$, normally incident upon the wedge, where

$$\Psi_0(\rho,\Phi,k) = \exp[jk\rho\operatorname{Cos}\Phi]. \qquad (2.39)$$

A plane-wave at oblique incidence of angle Θ_0 to the edge, i.e. to the z-axis, may be written as (from (2.10))

$$T_0(\rho,\Phi,\Theta_0,k) = \exp[\jmath k(\rho \operatorname{Sin}\Theta_0 \operatorname{Cos}\Phi - z\operatorname{Cos}\Theta_0]$$

$$= \Psi_0(\rho,\Phi,k \operatorname{Sin}\Theta_0) \exp[-\jmath kz \operatorname{Cos}\Theta_0]. \qquad (2.40)$$

The scalar potential solution, T, for oblique incidence is therefore given by

$$T = \Psi(\rho,\Phi,k \operatorname{Sin}\Theta_0) \exp[-\jmath kz \operatorname{Cos}\Theta_0]. \qquad (2.41)$$

In particular, the diffraction term of (2.36) for oblique incidence becomes

$$V_d(\rho,\Phi,z) = \frac{2}{N}\sqrt{\frac{\jmath}{\pi}} \frac{\operatorname{Sin}\frac{\pi}{N}\,\left|\operatorname{Cos}\frac{\Phi}{2}\right|}{[\operatorname{Cos}\frac{\pi}{N} - \operatorname{Cos}\frac{\Phi}{N}]} e^{\jmath k(\rho \operatorname{Sin}\Theta_0 \operatorname{Cos}\Phi - z\operatorname{Cos}\Theta_0)} \cdot$$

$$F(c) + [\text{higher order terms}], \qquad (2.42)$$

where

$$c = s\sqrt{\operatorname{Sin}\Theta_0}. \qquad (2.43)$$

For c large, (2.42) reduces to

$$V_d(\rho,\Phi,z)$$

$$\sim \frac{\operatorname{Sin}\frac{\pi}{N}\, e^{-\jmath k(\rho \operatorname{Sin}\Theta_0 + z\operatorname{Cos}\Theta_0)}}{N\sqrt{2\jmath\pi k\rho \operatorname{Sin}\Theta_0}\,[\operatorname{Cos}\frac{\pi}{N} - \operatorname{Cos}\frac{\Phi}{N}]} \sum_{m=0}^{\infty} \jmath^m (\tfrac{1}{2})_m (2k\rho \operatorname{Sin}\Theta_0 \operatorname{Cos}^2\tfrac{\Phi}{2})^{-m} \qquad (2.44)$$

2.23 Electromagnetic scattering

Consider an electromagnetic plane-wave incident on the wedge, the electric intensity given by

$$\underline{E}_0 = (a_x\hat{u}_x + a_y\hat{u}_y + a_z\hat{u}_z) \exp[\jmath k(\operatorname{Sin}\Theta_0(x\operatorname{Cos}\phi_0 + y\operatorname{Sin}\phi_0)$$

$$- z\operatorname{Cos}\Theta_0)], \qquad (2.45)$$

where $\operatorname{Sin}\Theta_0(a_x\operatorname{Cos}\phi_0 + a_y\operatorname{Sin}\phi_0) - a_z\operatorname{Cos}\Theta_0 = 0, \qquad (2.46)$

and $\hat{u}_x$, $\hat{u}_y$, $\hat{u}_z$ are the unit vectors in the cartesian coordinate

system. The resultant scattered field can be written in terms of the scalar potentials $T_{\substack{a\\f}}$ given from (2.41). Expressions for the total field are due to Jones (1953), and are given by

$$\begin{aligned}
\underline{E} &= \frac{a_z}{k \operatorname{Sin}^2\theta_0} (k\hat{u}_z - j\operatorname{Cos}\theta_0\nabla)T_a \\
&\quad + \frac{j}{k \operatorname{Sin}\theta_0} (a_x \operatorname{Sin}\phi_0 - a_y \operatorname{Cos}\phi_0)\hat{u}_z \wedge \nabla T_f, \\
\underline{H} &= \frac{a_z}{j\omega\mu \operatorname{Sin}^2\theta_0} \hat{u}_z \wedge \nabla T_a \\
&\quad + \left[\frac{a_x \operatorname{Sin}\phi_0 - a_y \operatorname{Cos}\phi_0}{\omega\mu \operatorname{Sin}\theta_0}\right] (k\hat{u}_z - j\operatorname{Cos}\theta_0\nabla)T_f.
\end{aligned} \tag{2.47}$$

For the electric diffracted far-field, $\underline{E}^d$, expressed in the cylindrical coordinates (ρ,ϕ,z), (2.47) reduces to

$$\begin{aligned}
E_\rho^d &= -a_z \operatorname{Cot}\theta_0 T_a^d, \\
E_\phi^d &= (a_x \operatorname{Sin}\phi_0 - a_y \operatorname{Cos}\phi_0) T_f^d, \\
E_z^d &= a_z T_a^d,
\end{aligned} \tag{2.48}$$

where T_a^d, T_f^d are the diffracted terms of the potentials obtained from the first term of (2.44) together with (2.24) to give

$$T_{\substack{a\\f}}^d \sim U_{\substack{a\\f}} \sqrt{\frac{\operatorname{Sin}\theta_0}{\rho}}\, e^{-jk(\rho \operatorname{Sin}\theta_0 + z \operatorname{Cos}\theta_0)}, \tag{2.49}$$

and $U_{\substack{a\\f}}$ is defined as

$$U_{\substack{a\\f}} = \frac{\operatorname{Sin}\frac{\pi}{N}}{N\sqrt{2j\pi k}\operatorname{Sin}\theta_0} \left[\frac{1}{\operatorname{Cos}\frac{\pi}{N} - \operatorname{Cos}\frac{\phi-\phi_0}{N}} \mp \frac{1}{\operatorname{Cos}\frac{\pi}{N} - \operatorname{Cos}\frac{\phi+\phi_0}{N}}\right] \tag{2.50}$$

If we consider the diffracted far-field at the point

$\rho = r \text{ Sin } \Theta_0$, $z = r \text{ Cos } \Theta_0$, then by substituting (2.50) into (2.49) and expressing $\underline{E}^d$ $\underline{H}^d$ in spherical coordinates, we get

$$
\begin{aligned}
E_r^d &= H_r^d = 0, \\
E_\phi^d &= (a_x \text{Sin } \phi_0 - a_y \text{ Cos } \phi_0)\ U_f \frac{e^{-jkr}}{\sqrt{r}}, \\
E_\theta^d &= -a_z \text{Cosec } \Theta_0\ U_a \frac{e^{-jkr}}{\sqrt{r}}, \\
H_\theta^d &= -\sqrt{\frac{\epsilon}{\mu}}\ E_\phi^d, \\
H_\phi^d &= \sqrt{\frac{\epsilon}{\mu}}\ E_\theta^d.
\end{aligned}
\tag{2.51}
$$

Thus, the diffracted far-field behaves as a plane-wave travelling along the r-vector from a source at the origin. With the variation in ϕ between 0-2π, the diffracted field appears to be travelling along a cone of semi-angle Θ_0, whose apex is on the edge.

2.24 The diffracted far-field for shadow boundaries and grazing incidence

We consider now three special cases in wedge scattering theory: (1) the field along shadow boundaries; (2) grazing incidence to the edge; and (3) grazing incidence to the wedge.

The diffracted far-field given by (2.48) was derived from (2.47) using (2. 44) with the assumption that c is large. There are, however, two conditions when $c = 0$ for the far-field assumption of $\rho \to \infty$, viz., (1) along the shadow boundaries when $\Phi = \pi$; (2) grazing incidence to the edge when $\Theta_0 = 0$. It is necessary to determine the behaviour of the diffracted far-field for these two conditions. In general, $T_{a,f}^d$ contains two diffraction terms as given in (2.24). We shall consider, initially, only one term for $c = 0$.

The diffraction term, $V_d(\rho,\Phi,z)$, is given by (2.42) for small values of c, from which we obtain the gradient (for the first term of (2.42)) for $\rho \to \infty$ at $c = 0$, as

$$\nabla V_d(\rho,\Phi,z)\Big|_{c=0} = jkV_d(\rho,\Phi,z)[\hat{u}_\rho \text{ Sin } \Theta_0 \text{Cos } \Phi - \hat{u}_\phi \text{ Sin } \Theta_0 \text{Sin } \Phi - \hat{u}_z \text{Cos } \Theta_0]. \tag{2.52}$$

We now consider the two possible far-field solutions to (2.47) when $c = 0$.

2.241 The field along shadow boundaries

Substituting (2.52) into (2.47) for $\Phi = \pi$, and using the relationship in (2.46), we get for the incident shadow boundary when $\phi = \pi + \phi_0$ the electric diffracted far-field as

$$\underline{E}^d = \mp \tfrac{1}{2}(a_x\hat{u}_x + a_y\hat{u}_y + a_z\hat{u}_z)\, e^{-jk(\rho \text{ Sin } \Theta_0 + z \text{ Cos } \Theta_0)}, \tag{2.53}$$

where the upper (lower) sign applies for $\Phi = \pi^-$ ($\Phi = \pi^+$). Equation (2.53) shows that along the incident shadow boundary, the diffracted far-field reduces to half the value of the incident plane-wave. This is necessary to compensate for the step-function characteristic of the geometrical optics term across the shadow boundary. A similar result is obtained for the reflected plane-wave along the reflected shadow boundary when $\phi = \pi - \phi_0$.

2.242 Grazing incidence to the edge

From (2.46) we have $a_z = 0$ for $\Theta_0 = 0$. Therefore substituting (2.52) into (2.47) with $\Theta_0 = 0$, we get for the diffraction term when $\phi = \Phi + \phi_0$ the electric far-field as

$$\underline{E}^d = -\frac{1}{N \text{ Tan } \frac{\pi}{2N}}(a_x\hat{u}_x + a_y\hat{u}_y)\, e^{-jkz}, \tag{2.54}$$

which is directly related to the incident plane-wave. Similarly, for the other diffraction term when $\phi = \Phi - \phi_0$ we obtain an expression which is directly related to the reflected plane-wave.

2.243 Grazing incidence to the wedge

As the third special case we consider grazing incidence to the wedge when $\phi_0 = 0$. For $\phi_0 = 0$, the potential T vanishes for electric polarization, but for magnetic polarization we get

$$T_f(\rho,\phi,z) = 2[V_d(\rho,\phi,z) + V_{ir}(\rho,\phi,z)]. \tag{2.55}$$

This corresponds to an incident wave of amplitude double that when $\phi_0 \neq 0$. Therefore, for magnetic polarization at grazing incidence to the wedge we have

$$T_f(\rho,\phi,z) = V_d(\rho,\phi,z) + V_{ir}(\rho,\phi,z) \tag{2.56}$$

2.3 GEOMETRICAL THEORY OF DIFFRACTION (GTD)

From the mathematical development in 2.2 we are now in a position to discuss the GTD as it applies to wedge scattering. Since the GTD is an extension of geometrical optics to describe diffraction phenomena, we will first briefly review geometrical optics.

2.31 Geometrical optics

At high frequencies, when significant medium changes occur over distances large compared to the wavelength, it can be assumed that, locally, the wavefront behaves as a plane-wave with $\underline{E}$ and $\underline{H}$ given by

$$\underline{E} = \underline{e}\, e^{-jkv},$$
$$\underline{H} = \underline{h}\, e^{-jkv}, \tag{2.57}$$

where the phases of $\underline{e}$ and $\underline{h}$ are independent of position, and v is the function satisfying the eikonal equation

$$\nabla^2 v = Q^2, \tag{2.58}$$

where Q is the refractive index (Jones, 1964c). The eikonal defines the wavefronts, i.e. surfaces of constant phase. Geometrical optics concentrates on the wavefronts and their associated rays, which are the loci of the direction of energy flow in the field. For an isotropic medium, the rays are normal to the wavefront.

Geometrical optics was originally developed to give a limited theory of light on the basis of the following three principles:

(1) in homogeneous media the rays are straight lines

(2) rays from a source travel out independent of each other

(3) rays obey the laws of reflection and refraction.

All these laws follow from Fermat's principle (Jones, 1964c) which introduces the notion of 'optical path length'. The optical path length along a curve c joining two points P_1, P_2 is defined by the line integral $\int_c Q\,ds$, where Q is the refractive index of the element ds. Fermat's principle states: 'the rays between P_1 and P_2 are those curves along which the optical path length is stationary with respect to infinitesimal variations in path'.

Amplitude variation along the ray is obtained by applying the principle of conservation of energy to a tube of rays. Fig. 2.4 shows two small portions of parallel wavefronts a distance ρ apart in a homogeneous medium, with some of the rays normal to them. ρ_1, ρ_2 are the principal radii of curvature of the wavefront through A.

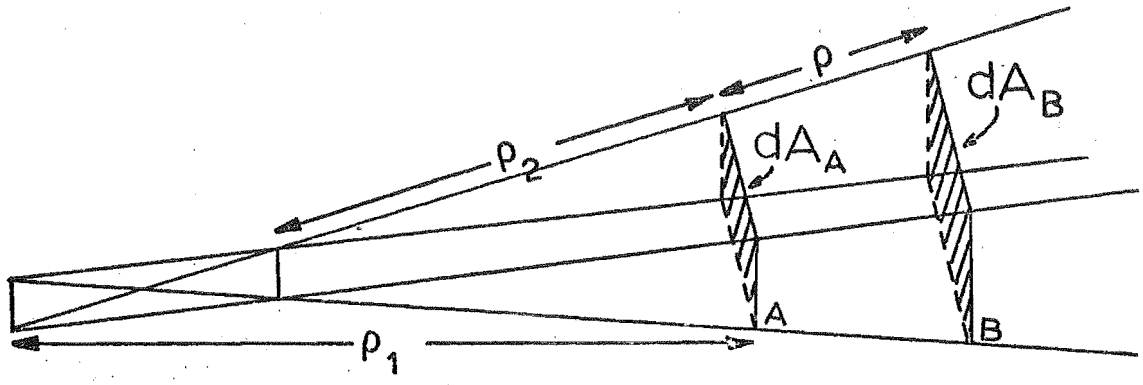

Fig. 2.4 A tube of rays

Referring the phase and amplitude to A, we get for the field, $\underline{E}_B$, at B in terms of the field, $\underline{E}_A$, at A

$$\underline{E}_B = \underline{E}_A \left[\frac{\rho_1\rho_2}{(\rho_1+\rho)(\rho_2+\rho)}\right]^{\frac{1}{2}} e^{-jk[v+\rho]}. \qquad (2.59)$$

A similar expression exists for $\underline{H}$. We see that for large ρ, the field decreases as ρ^{-1} as in a spherical-wave. If one radius is infinite, the decay is $\rho^{-\frac{1}{2}}$ for large ρ, as in a cylindrical-wave; and if both radii are infinite, the field is of constant amplitude, as for a plane-wave.

When $\rho = -\rho_1$ or $-\rho_2$, (2.59) becomes infinite and the geometrical optics representation is not valid at these points. Such points are called caustic points. The caustics are the loci of the two principal centres of curvature. To evaluate

the field of a caustic requires separate considerations, e.g. Kay and Keller (1954).

The derivation of geometrical optics from Maxwell's equations has been thoroughly investigated in a book by Kline and Kay (1965).

2.32 Geometrical theory of diffraction

The GTD is an extension of geometrical optics to describe diffraction phenomena by the introduction of additional rays, called 'diffracted rays' (Keller, 1962). Diffracted rays are produced when an incident ray strikes an edge, corner, or vertex of a boundary surface, or grazes such a surface. The behaviour of these rays is determined from an appropriate modification of Fermat's principle deduced from the canonical problem containing the same type of surface discontinuity, such as the wedge for edge diffraction. As we found in 2.2, the asymptotic expansion of the diffracted field for edge diffraction gives the field as propagating along a cone of rays. It is now assumed that diffraction is a purely local phenomenon, and that at each point of an arbitrarily curved edge a cone of diffracted rays is emitted. The axis of the cone is the tangent to the edge at the point of diffraction, and the half-angle being the angle between the incident ray and the above tangent to the edge. Thus, for edge diffraction, Fermat's principle becomes: 'An edge diffracted ray between P_1 and P_2 is a curve which has stationary optical length among all curves from P_1 to P_2 with one point on the edge'.

Neighbouring rays of the same cone intersect each other on the diffracting edge, so that the edge is a caustic of the diffracted rays. The amplitude of a fixed point not on the

edge is obtained from (2.59), which can be rewritten to give

$$|\underline{E}_A|\rho_2^{\frac{1}{2}} = |\underline{E}_B| \left[\frac{(\rho_1+\rho)(\rho_2+\rho)}{\rho_1}\right]^{\frac{1}{2}} \tag{2.60}$$

The right-hand side of (2.60) has a definite limit, say $|\underline{E}_0|$, as the point A in Fig. 2.4 tends to the edge. Using this in (2.59)

$$\underline{E}_B = \underline{E}_0 \left[\frac{\rho_1}{(\rho_1+\rho)\rho}\right]^{\frac{1}{2}} e^{-jk[v+\rho]}, \tag{2.61}$$

where ρ is measured from the edge, so that $\rho_2 = 0$ and ρ_1 is the distance from the edge to the other caustic.

We now assume that

$$\underline{E}_0 e^{-jkv} = \underline{\underline{D}}_e \underline{E} e^{-jkv_0}, \tag{2.62}$$

where $\underline{E}\, e^{-jkv_0}$ is the value of the incident field at the edge and $\underline{\underline{D}}_e$ is the diffraction coefficient tensor. Now (2.61) becomes

$$\underline{E}_B = \underline{\underline{D}}_e \underline{E} \left[\frac{\rho_1}{(\rho_1+\rho)\rho}\right]^{\frac{1}{2}} e^{-jk[v_0+\rho]} \tag{2.63}$$

The distance ρ_1 between the two caustics is found, from differential geometry, to be

$$\rho_1 = -\rho_c \operatorname{Sin}^2\beta_0 \left(\rho_c \frac{\partial\beta_0}{\partial e} \operatorname{Sin}\beta_0 + \operatorname{Cos}\delta\right)^{-1}, \tag{2.64}$$

where $\rho_c \gtrless 0$ denotes the radius of curvature of the edge, e is the distance along the edge, δ is the angle between the diffracted ray and the unit normal to the edge, and β_0 is the angle between the incident ray and the tangent to the edge.

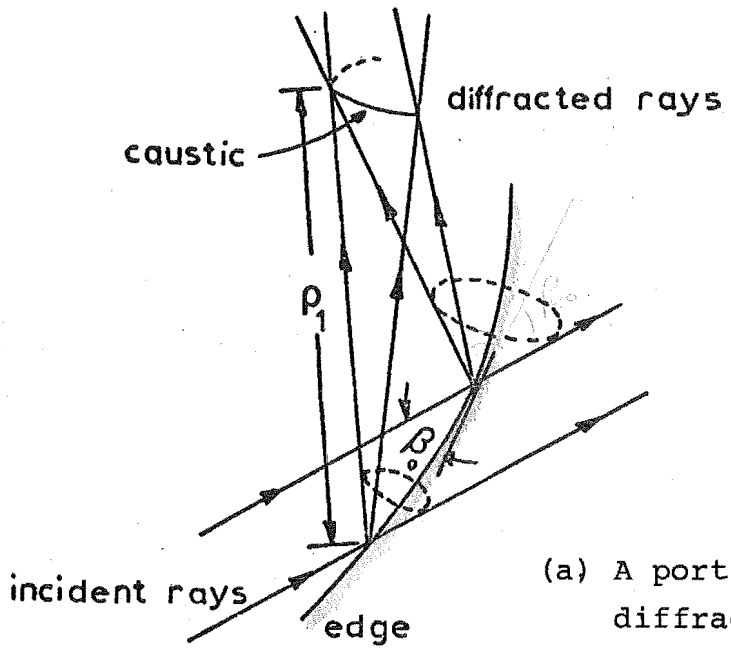

(a) A portion of the cone of diffracted rays from two points of diffraction.

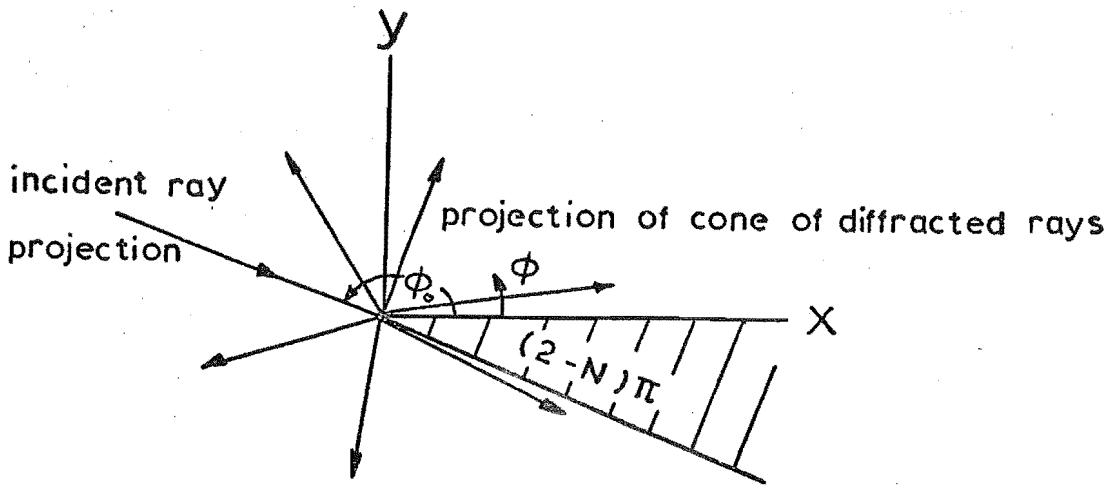

(b) Projection into an x-y plane at the point of diffraction.

Fig. 2.5 Diffraction from a curved edge.

The edge diffraction coefficient tensor, $\underline{\underline{D}}_e$, is determined by equating (2.51) for the wedge problem, with (2.63). Expressing the incident and diffracted field of (2.63) in spherical coordinates, we can readily show that

$$\underline{\underline{D}}_e = \begin{bmatrix} 0 & 0 & 0 \\ 0 & -U_f & 0 \\ -\text{Cot}\,\Theta_0 U_a & 0 & U_a \end{bmatrix}, \qquad (2.65)$$

where we have $\beta_0 = \Theta_0$ and U_a given by (2.50).

The field along a diffracted ray has now been completely determined.

A diffracted ray itself may cause diffraction, giving doubly diffracted rays, which may themselves create diffracted rays, and so on. These multiply diffracted rays behave in the same way as the first, or singly, diffracted rays. The total diffracted field at a point is the sum of all the diffracted rays through that point.

The edge diffraction coefficients U_a, U_f in (2.50) have been derived from the exact solution of the wedge assuming that the argument, c, of the Fresnel integral in the first term of (2.42) is large. When the argument of the Fresnel integral is less than unity, its asymptotic series expansion, (2.37), diverges and the diffraction coefficients of (2.50) are invalid. In particular, the value along the shadow boundaries in (2.50) is infinite. Also, for $N \neq 2$, the higher order terms of (2.42) become significant in the shadow boundary regions. These regions for plane-wave diffraction require special consideration, such as the boundary layer method of Buchal and Keller (1960), and uniform asymptotic

series solution of Ahluwalia *et al.* (1968). A mathematically more tractable solution is use of cylindrical-wave diffraction coefficients, where possible. We will now discuss these coefficients which are useful for many practical problems. Initially we restrict ourselves to two-dimensions. Application to three-dimensions will be discussed in 2.4.

2.33 Cylindrical-wave diffraction

For two-dimensional problems, where the incoming wave is at normal incidence to the edge and independent of the z-direction, (2.63) with (2.64), (2.65) reduce to

$$E_\phi^d = -a_\phi \, U_f \frac{e^{-jk\rho}}{\sqrt{\rho}} ,$$
$$E_z^d = a_z \, U_a \frac{e^{-jk\rho}}{\sqrt{\rho}} , \qquad (2.66)$$

where U_a is given by (2.50) with $\Theta_0 = \frac{\pi}{2}$, a_ϕ, a_z are the components of the incident electric field at the edge, and the phase reference is taken from the edge.

In two-dimensional radiation problems, the far-field for cylindrical-wave diffraction of a line-source near the edge is of considerable importance. This can be derived from (2.23), or (2.25) and (2.26) for the condition that $\rho >> \rho_0$. It is more instructive, however, to derive these far-field expressions from the plane-wave formulation, since this has been discussed in some detail.

The problem is illustrated in Fig. 2.6(a) with the line-source at (ρ_0, ϕ_0). Fig. 2.6(b) is the reciprocal problem which we solve first.

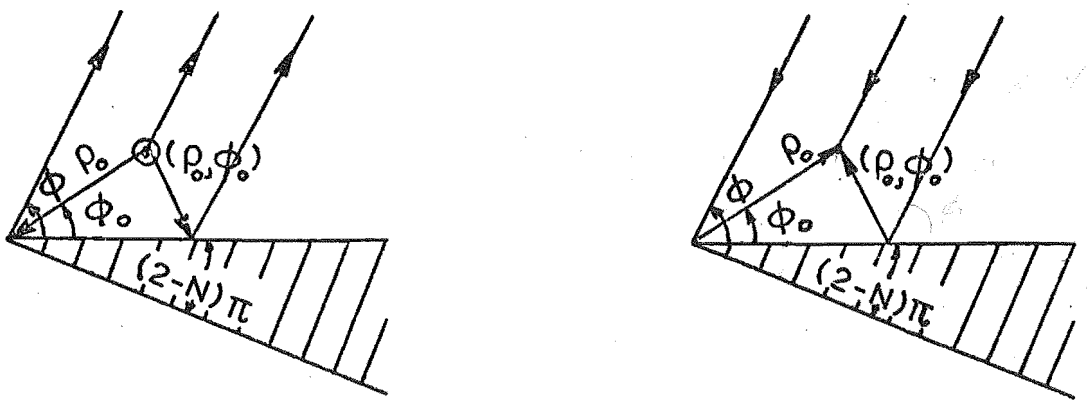

(a) line-source near wedge (b) reciprocal problem

Fig. 2.6

From (2.24) the scalar potential solution, Ψ_{a_f}, at a point (ρ_0,ϕ_0) for a plane-wave incident at an angle ϕ to the wedge is

$$\Psi_{a_f}(\rho_0,\phi_0) = [V_d(\rho_0,\phi_0-\phi) + V_{ir}(\rho_0,\phi_0-\phi)] \mp [V_d(\rho_0,\phi_0+\phi) + V_{ir}(\rho_0,\phi_0+\phi)]$$

$$= V(\rho_0,\phi_0-\phi) \mp V(\rho_0,\phi_0+\phi). \qquad (2.67)$$

By reciprocity with this problem, the far-field resulting from a z-directed line-source near the edge at (ρ_0,ϕ_0) (Fig. 2.6(a)) is given by

$$\Psi_{a_f}(\rho,\phi) = \frac{e^{-jk\rho}}{\sqrt{8j\pi k\rho}} [V(\rho_0,\phi-\phi_0) \mp V(\rho_0,\phi+\phi_0)], \qquad (2.68)$$

where the property $V(\rho,\Phi) = V(\rho,-\Phi)$ is used, and the term $\frac{e^{-jk\rho}}{\sqrt{8j\pi k\rho}}$, which we normalised out by (2.29) for plane-wave incidence, is introduced to account for the far-field radial distribution of the line-source. Thus, we can readily see that for the cylindrical-wave scattering of (2.68), we can use the expression for the diffracted field given by (2.66) if we

replace the plane-wave diffraction coefficient of (2.50) with

$$U_{\substack{a\\f}} = \frac{1}{\sqrt{8j\pi k}} \left[V_d(\rho_0, \phi-\phi_0) \mp V_d(\rho_0, \phi+\phi_0) \right], \tag{2.69}$$

and a_ϕ, a_z are the components of the electric field from the line-source in the direction of the edge.

For ρ small, the Fresnel integral formulation of (2.36) can be used for the diffraction terms in (2.69). The field is then continuous across the shadow boundaries. This is an important point. If we know the distance of the source from the edge, then we can obtain solutions which are finite everywhere. This is in contrast with the plane-wave edge diffraction coefficients of (2.50), which are invalid in the shadow boundary regions.

For $N \neq 2$, the higher order terms of the Pauli expansion in (2.36) can be significant for small values of ρ_0, because s, given by (2.35), will also be small. Since these higher order terms are not readily obtained, an alternative approach is to use the first few terms of the eigenfunction solution in (2.28) and subtract out the geometrical optics component (2.30), i.e.

$$V_d(\rho_0, \Phi) = \frac{1}{N} \sum_\nu \varepsilon_\nu j^\nu J_\nu(k\rho_0) \cos \nu\Phi - V_{ir}(\rho_0, \Phi). \tag{2.70}$$

Comparing (2.36) with (2.70) will give the error incurred by using the former expression for $N \neq 2$. This is shown graphically in Fig. 2.7 for various values of Φ. As we would expect, the error is largest in the shadow boundary region, where $\Phi = \pi$, and increases with decreasing values of ρ_0. In practical problems of interest, ρ_0 would rarely be smaller than 0.3λ. For such a minimum value of ρ_0, it can be seen from Fig. 2.7 that (2.36) is satisfactory for wedge angles up

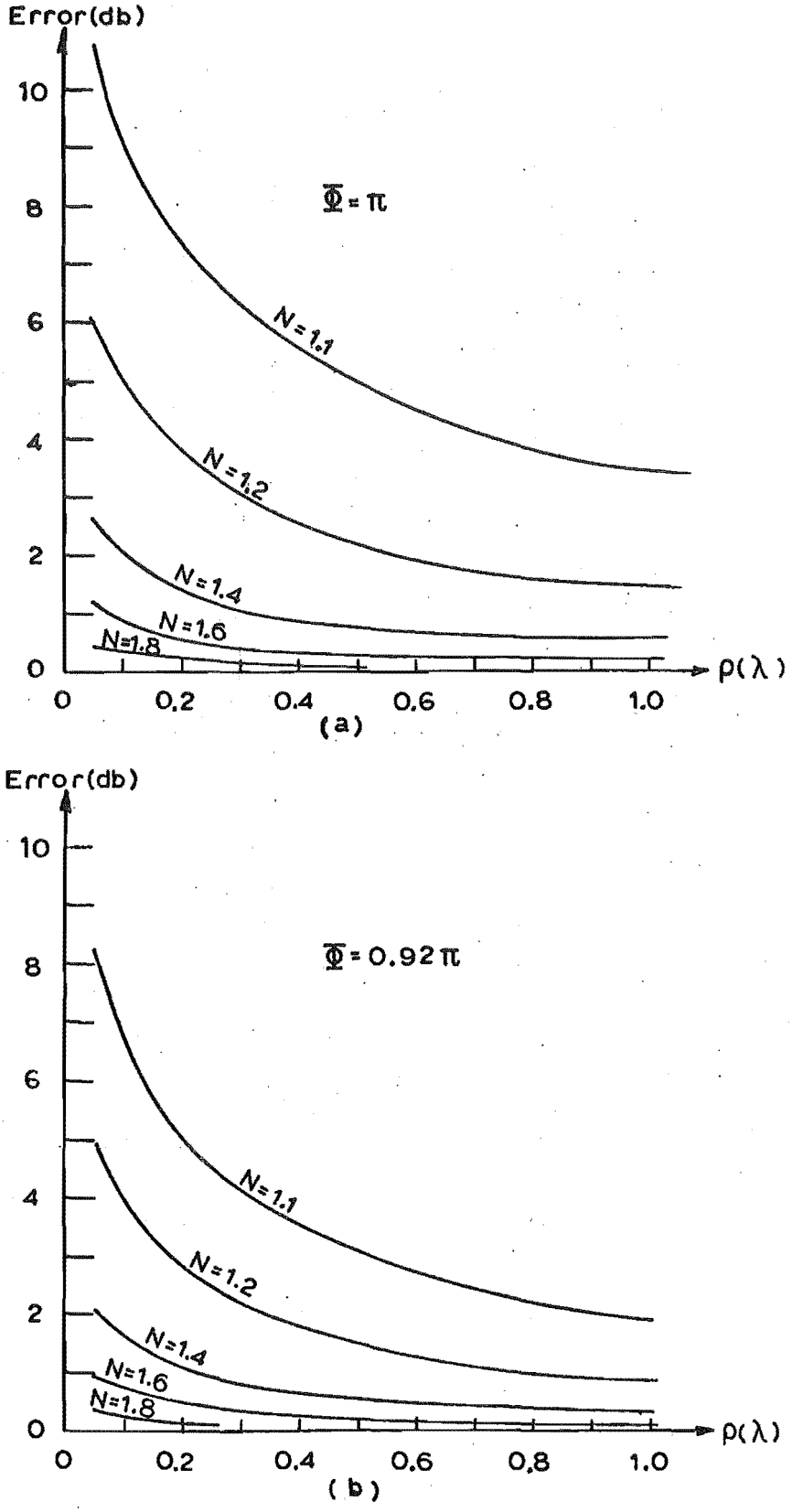

Fig. 2.7 Error between exact solution (2.70) and the first term of (2.36) for the cylindrical-wave diffraction term $V_d(\rho_0, \Phi)$.

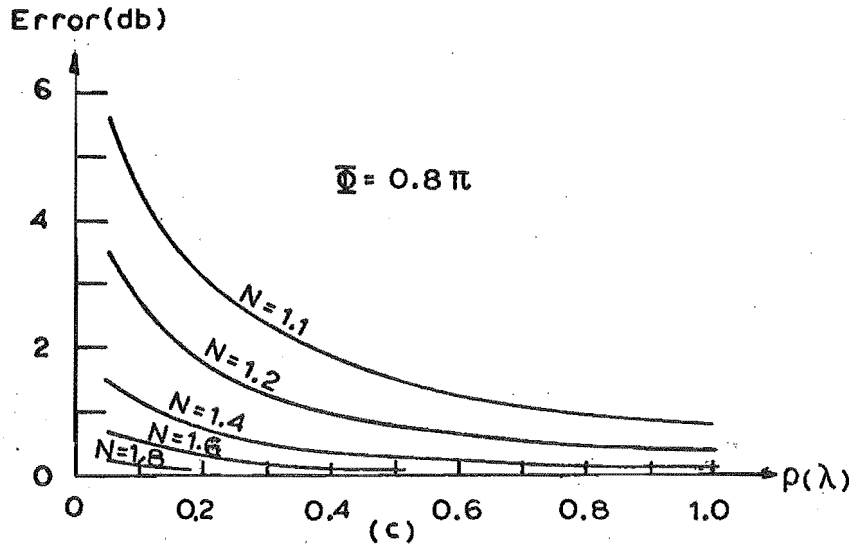
Error(db)
6
4
2
0
Φ = 0.8π
N=1.1
N=1.2
N=1.4
N=1.6
N=1.8
ρ(λ)
0
0.2
0.4
0.6
0.8
1.0

(c)

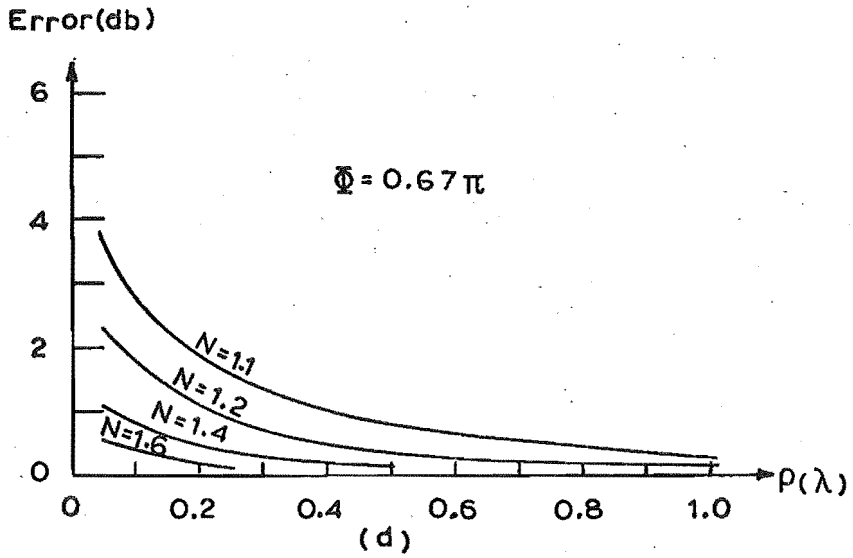
Error(db)
6
4
2
0
Φ = 0.67π
N=1.1
N=1.2
N=1.4
N=1.6
ρ(λ)
0
0.2
0.4
0.6
0.8
1.0

(d)

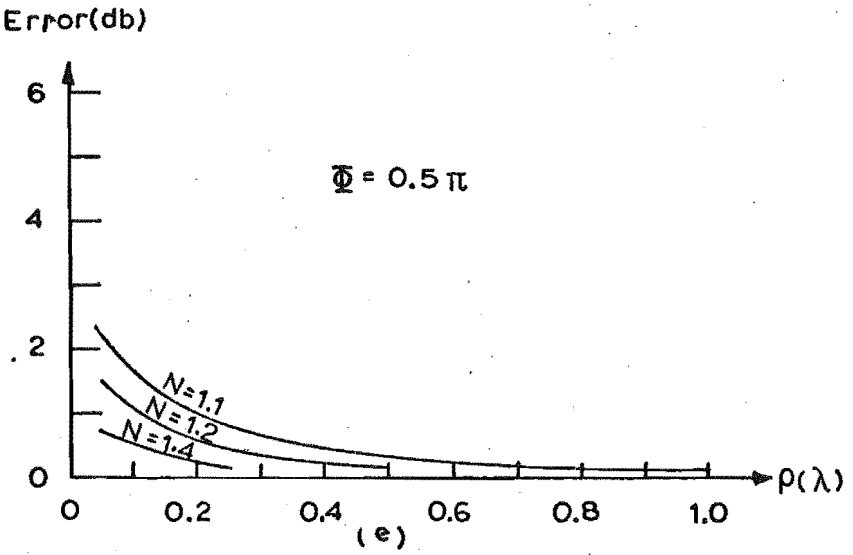
Error(db)
6
4
2
0
Φ = 0.5π
N=1.1
N=1.2
N=1.4
ρ(λ)
0
0.2
0.4
0.6
0.8
1.0

(e)

about 90^{o}. With larger wedge angles, (2.70) should be used, and is readily evaluated provided ρ_0 does not go much greater than a wavelength.

2.34 Slope-wave diffraction

In the analysis so far we have assumed that the incident field is uniform. If the incident field is non-uniform, then the above results do not predict the consequent modification to the diffracted field. This effect, for a half-plane, can be deduced from the work of Ahluwalia *et al.* (1968), and is given in Appendix A. The result can then be extended, heuristically, to the wedge.

The effect of non-uniform incidence is to create higher order terms in the asymptotic solution of the diffracted field. The first higher order term, given in Appendix A for the half-plane, is proportional to the derivative, with respect to the incident angle, of the incident field. It is called the slope-wave diffraction term for convenience.

From (A.21) in Appendix A, we can write, heuristically, the slope-wave correction field, E_ϕ^s, E_z^s to (2.66) for the wedge as

$$E_\phi^s = -\frac{g_\phi}{jk}\frac{\partial U_f}{\partial \phi_0}\frac{e^{-jk\rho}}{\sqrt{\rho}}\,,$$
$$E_z^s = -\frac{g_z}{jk}\frac{\partial U_a}{\partial \phi_0}\frac{e^{-jk\rho}}{\sqrt{\rho}}\,, \tag{2.71}$$

where for plane-wave diffraction,

$$g_\phi = \left.\frac{\partial a_\phi}{\partial \phi}\right|_{\phi=\phi_0}\,,$$
$$g_z = \left.\frac{\partial a_z}{\partial \phi}\right|_{\phi=\phi_0}\,. \tag{2.72}$$

For cylindrical-wave diffraction,

$$g_\phi = \frac{1}{\rho_0} \frac{\partial a_\phi}{\partial \phi}\bigg|_{\phi=\phi_0}, \qquad g_z = \frac{1}{\rho_0} \frac{\partial a_z}{\partial \phi}\bigg|_{\phi=\phi_0}, \tag{2.73}$$

where a_ϕ, a_z are the components of the electric field from the line-source in the direction of the edge.

Writing $\frac{\partial}{\partial \phi_0} U_{a_f}$ as $S^p_{a_f}$ for plane-wave diffraction, as $S^c_{a_f}$ for cylindrical-wave diffraction, then from (2.50) for normal incidence we get

$$S^p_{a_f} = \frac{\operatorname{Sin} \frac{\pi}{N}}{N^2 \sqrt{2j\pi k}} \left[\frac{\operatorname{Sin} \frac{\phi-\phi_0}{N}}{(\operatorname{Cos} \frac{\pi}{N} - \operatorname{Cos} \frac{\phi-\phi_0}{N})^2} \pm \frac{\operatorname{Sin} \frac{\phi+\phi_0}{N}}{(\operatorname{Cos} \frac{\pi}{N} - \operatorname{Cos} \frac{\phi+\phi_0}{N})^2} \right], \tag{2.74}$$

and from (2.69) we get

$$S^c_{a_f} = - \frac{1}{\sqrt{8j\pi k}} [V_d'(\rho_0, \phi-\phi_0) \pm V_d'(\rho_0, \phi+\phi_0)], \tag{2.75}$$

where

$$V_d'(\rho_0, \Phi) = \frac{\partial}{\partial \Phi} V_d(\rho_0, \Phi). \tag{2.76}$$

We can derive $V_d'(\rho_0, \Phi)$ from (2.36) to obtain

$$V_d'(\rho_0, \Phi) = \frac{2}{N} \sqrt{\frac{j}{\pi}} \operatorname{Sin} \frac{\pi}{N} \left\{ \frac{k\rho_0 \operatorname{Sin} \Phi \left|\operatorname{Cos} \frac{\Phi}{2}\right|}{\operatorname{Cos} \frac{\pi}{N} - \operatorname{Cos} \frac{\Phi}{N}} \left[\frac{e^{-jk\rho_0}}{2s} - j e^{jk\rho_0 \operatorname{Cos}\Phi} F(s) \right] \right.$$
$$\left. + e^{jk\rho_0 \operatorname{Cos}\Phi} F(s) \frac{\varepsilon_1 [\frac{1}{2} \operatorname{Sin} \frac{\Phi}{2} (\operatorname{Cos} \frac{\pi}{N} - \operatorname{Cos} \frac{\Phi}{N}) + \frac{1}{N} \operatorname{Sin} \frac{\Phi}{N} \operatorname{Cos} \frac{\Phi}{2}]}{(\operatorname{Cos} \frac{\pi}{N} - \operatorname{Cos} \frac{\Phi}{N})^2} \right\}, \tag{2.77}$$

where

$$\varepsilon_1 = \begin{cases} -1 & \text{for } 0 \leq \Phi < \pi \\ +1 & \text{for } \pi \leq \Phi < 2\pi \end{cases}$$

For s large we can use (2.74) to give $S_{\substack{a\\f}}^{c}$ as

$$S_{\substack{a\\f}}^{c} \sim S_{\substack{a\\f}}^{p} \frac{e^{-j k\rho_0}}{\sqrt{8j\pi k\rho_0}} \quad . \tag{2.78}$$

The exact solution for $N \neq 2$ may be obtained from (2.70) yielding

$$V_d'(\rho_0,\Phi) = -\frac{1}{N}\sum_{\nu} \varepsilon_\nu j^\nu \nu J_\nu(k\rho_0) \text{ Sin } \nu\Phi - V_{ir}'(\rho_0,\Phi), \tag{2.79}$$

where

$$V_{ir}'(\rho_0,\Phi) = -jk\rho_0 \text{ Sin } \Phi \, V_{ir}(\rho_0,\Phi). \tag{2.80}$$

Fig. 2.8 gives the error between (2.77) and the exact term of (2.79) when $N \neq 2$. The error is nearly double (in terms of decibels) that of the equivalent results given in Fig. 2.7 for uniform plane-wave incidence diffraction coefficients. As before, the evaluation of (2.79) is limited to a maximum value of ρ_0 of between one and two wavelengths. Larger values of ρ_0 require an excessive number of terms.

Although we have considered slope-wave diffraction for normal incidence, it is readily extended to oblique incidence by the method given in 2.22.

2.4 THE EQUIVALENT EDGE CURRENT METHOD

Most of the work that has appeared in the literature to date using the GTD has been restricted to two-dimensional problems. We have shown that use of cylindrical-wave diffraction coefficients (where possible) for such problems gives results which are finite everywhere as compared to

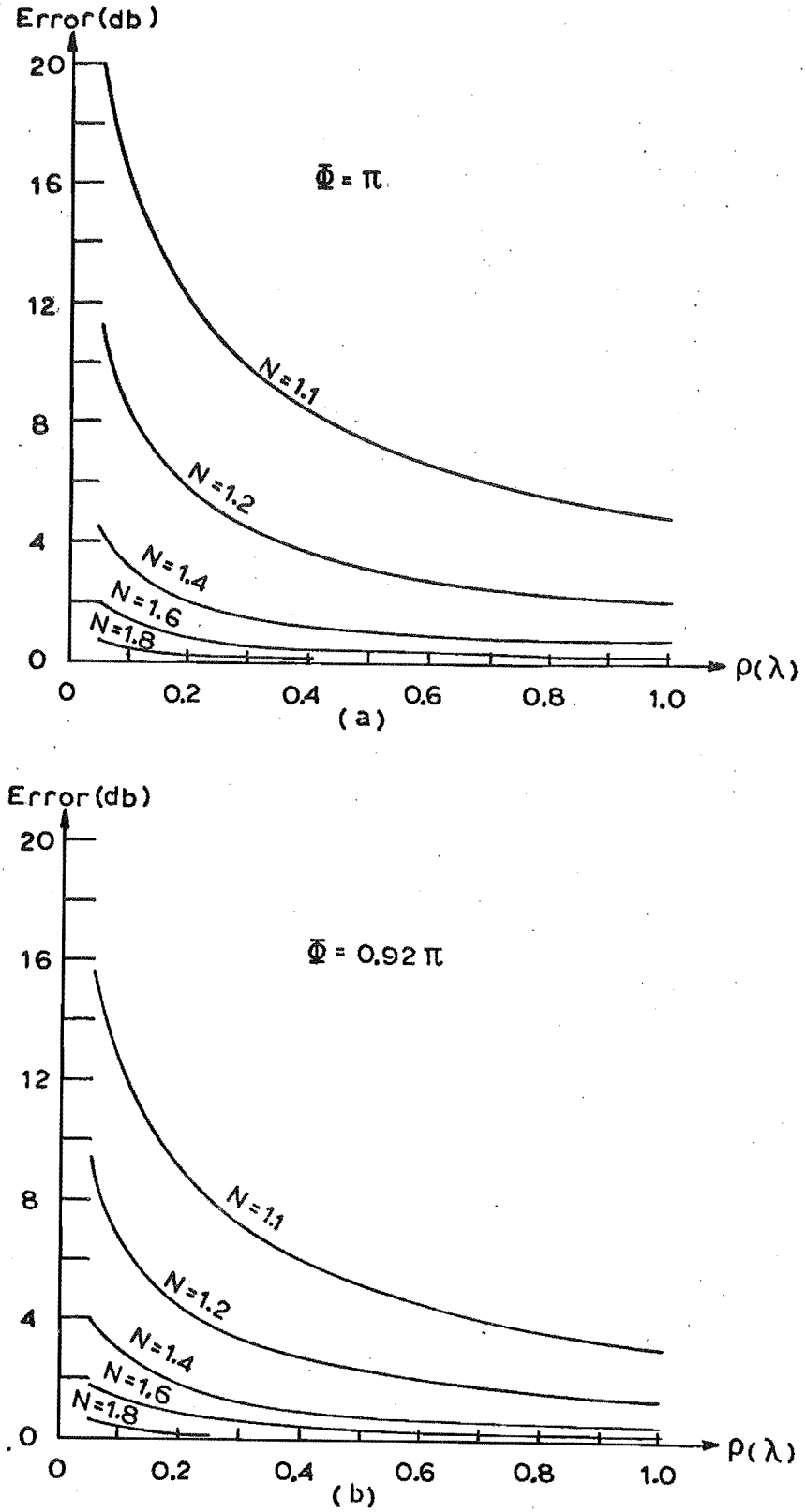

Fig. 2.8 Error between exact solution (2,79) and approximate solution (2.77) for $N \neq 2$ for cylindrical slope-wave diffraction.

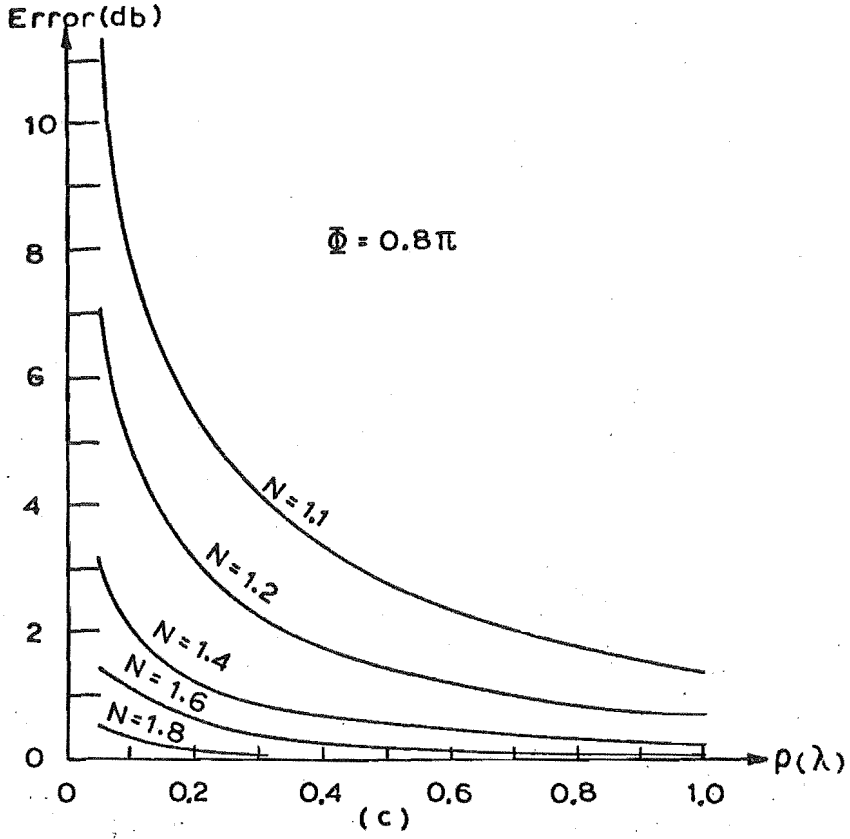
Error(db)
10
8
6
4
2
0
Φ = 0.8π
N=1.1
N=1.2
N=1.4
N=1.6
N=1.8
0
0.2
0.4
0.6
0.8
1.0
ρ(λ)
(c)

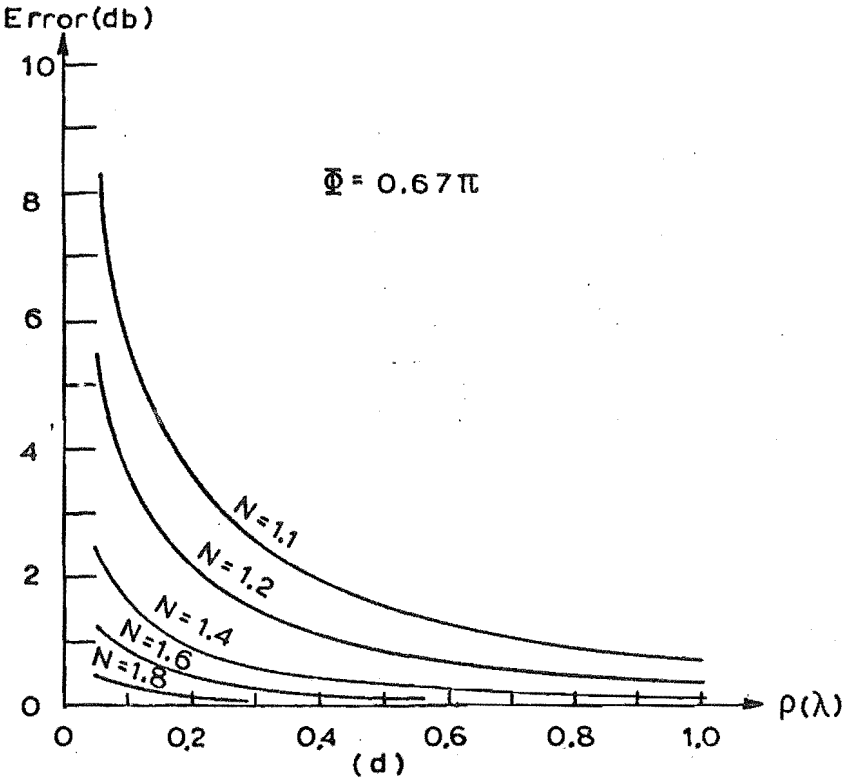
Error(db)
10
8
6
4
2
0
Φ = 0.67π
N=1.1
N=1.2
N=1.4
N=1.6
N=1.8
0
0.2
0.4
0.6
0.8
1.0
ρ(λ)
(d)

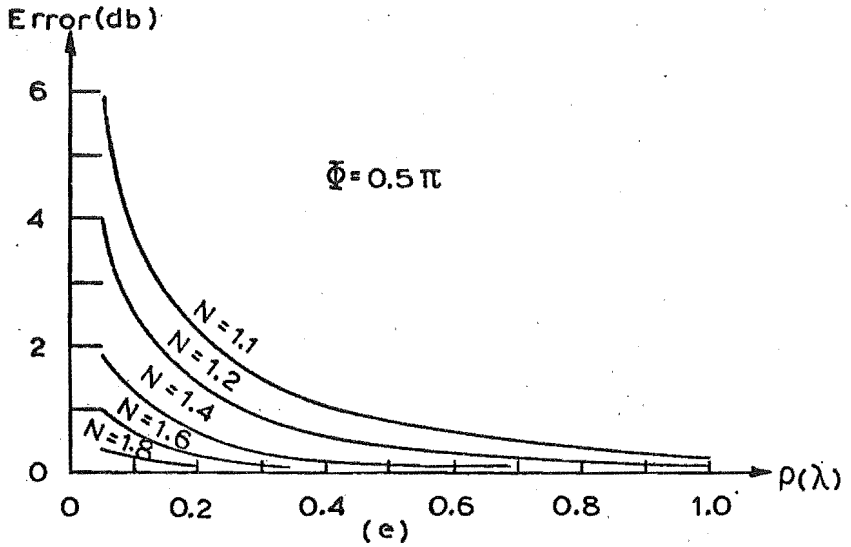
Error(db)
6
4
2
0
Φ=0.5π
N=1.1
N=1.2
N=1.4
N=1.6
N=1.8
0
0.2
0.4
0.6
0.8
1.0
ρ(λ)
(e)

plane-wave diffraction coefficients which give infinities along the shadow boundaries. In chapter three we shall use the ray tracing methods of the GTD to analyse the radiation patterns of horn antennas reducible to two-dimensions.

When the edge is of finite curvature and/or length, we have two additional problems: (1) use of ray tracing methods for diffraction from curved edges results in the formation of caustics of the diffracted rays. At and near a caustic, the evaluation of the field requires special consideration since ray tracing methods are invalid. Buchal and Keller (1960) used boundary layer methods about a caustic (and also the shadow boundaries) to evaluate the field in this region. A particular case is the field in an axial caustic (Keller, 1957) where an exact solution of a suitable canonical problem is used on and near the axis.

(2) The second problem is the choice of a suitable factor to account for the three-dimensional effect of the finite curvature and/or length of the edge. An example is given by Ryan and Rudduck (1968) for radiation from rectangular waveguides. To account for the finite length of the waveguide walls, they deduce a factor from the radiation pattern of a line-source of finite length.

A method which neatly overcomes these two problems is to use equivalent edge currents derived from the infinite wedge problem. These equivalent currents are then used in the potential integral solution of (2.4) to obtain the diffracted field. This equivalent current concept was used with notable success by Millar (1955, 1956a, 1956b) to solve for the axial and aperture fields in the case of an aperture in a plane screen. Recently, it has been used in other edge diffraction

problems (Ryan and Peters, 1969). All these applications were cases of uniform plane-waves at normal incidence. In what follows, we derive equivalent currents for non-uniform plane- and cylindrical-waves at oblique incidence.

We begin with the far-field from an infinitely long z-directed filament of electric current I_e (magnetic current I_m) given by (Harrington, 1961b)

$$E_z = -j\omega\mu I_e \sqrt{\frac{1}{8j\pi k\rho}}\, e^{-jk\rho},$$
$$E_\phi = -jkI_m \sqrt{\frac{1}{8j\pi k\rho}}\, e^{-jk\rho}. \tag{2.81}$$

For a scalar plane-wave at normal incidence to a wedge polarized in the z-direction, the radiation fields are directly proportional to the scalar potentials as given by (2.19). Therefore, the electric diffracted far-field $E_z^d (E_\phi^d)$ for electric (magnetic) polarization is given by

$$E_z^d = -j\omega\mu\Psi_a^d,$$
$$E_\phi^d = -jk\Psi_f^d. \tag{2.82}$$

By equating (2.82) with (2.81) using the far-field plane-wave diffraction coefficient, given by the first term of (2.38), in Ψ_{a}^{d}, we can readily show that the equivalent currents, I_{e}^{p}, for plane-wave diffraction are given by

$$I_{e}^{p} = \frac{2}{N} \operatorname{Sin}\frac{\pi}{N} \left[\frac{1}{\operatorname{Cos}\frac{\pi}{N} - \operatorname{Cos}\frac{\phi-\phi_0}{N}} \mp \frac{1}{\operatorname{Cos}\frac{\pi}{N} - \operatorname{Cos}\frac{\phi+\phi_0}{N}} \right]. \tag{2.83}$$

Equation (2.83) is the form of the equivalent currents used by previous researchers. As for plane-wave diffraction coefficients, it is invalid in the shadow boundary regions.

For cylindrical-wave diffraction we use the potential as given by (2.68) in (2.82) to obtain the equivalent currents, $I^c_{e\,m}$, for a line-source distance ρ_0 from the edge, giving

$$I^c_{e\,m} = [V_d(\rho_0, \phi-\phi_0) \mp V_d(\rho_0, \phi+\phi_0)]. \tag{2.84}$$

For large ρ_0

$$I^c_{e\,m} \sim I^p_{e\,m} \frac{e^{-jk\rho_0}}{\sqrt{8j\pi k\rho_0}} . \tag{2.85}$$

The direction of the currents derived in (2.83), (2.84) is along the edge, i.e., the z-axis.

It is now assumed that in an element of a curved and/or finite length edge, equivalent currents are given by (2.83) or (2.84) for a correspondingly oriented infinite wedge. These currents are then used in the potential integral solution of (2.4) to give the diffracted field. To be more general, however, we require equivalent currents that account for oblique incidence. In 2.23 we showed that, for electromagnetic scattering, the diffracted far-field behaves as a plane-wave travelling along the r-direction given by

$$\hat{u}_r = \hat{u}_\rho \text{ Sin } \Theta_0 + \hat{u}_z \text{ Cos } \Theta_0, \tag{2.86}$$

where Θ_0 is the angle of incidence to the edge. From the solution for oblique incidence in 2.22, we can write the equivalent currents for a cylindrical-wave at oblique incidence to the edge, with radius of curvature r_0, from (2.42) with the transforms $\rho = r \text{ Sin } \Theta_0$, $z = r \text{ Cos } \Theta_0$, giving

$$I^c_{e\,m} = [Y_d(r_0, \phi-\phi_0) \mp Y_d(r_0, \phi+\phi_0)], \tag{2.87}$$

where

$$Y_d(r_0,\Phi) = \frac{2}{N}\sqrt{\frac{j}{\pi}}\ \frac{\operatorname{Sin}\frac{\pi}{N}\left|\operatorname{Cos}\frac{\Phi}{2}\right|}{\operatorname{Cos}\frac{\pi}{N}-\operatorname{Cos}\frac{\Phi}{N}}\ e^{jkr_0(\operatorname{Sin}^2\theta_0\operatorname{Cos}\Phi-\operatorname{Cos}^2\theta_0)}\ F(p), \tag{2.88}$$

and

$$p = \operatorname{Sin}\theta_0\ \sqrt{kr_0(1+\operatorname{Cos}\Phi)}.$$

For large r_0

$$I^c_{e_m} \sim I^p_{e_m}\ \frac{e^{-jkr_0}}{\sqrt{8j\pi kr_0}}\ ,$$

where

$$I^p_{e_m} = \frac{2}{N}\operatorname{Sin}\frac{\pi}{N}\operatorname{Cosec}\theta_0\left[\frac{1}{\operatorname{Cos}\frac{\pi}{N}-\operatorname{Cos}\frac{\phi-\phi_0}{N}} \mp \frac{1}{\operatorname{Cos}\frac{\pi}{N}-\operatorname{Cos}\frac{\phi+\phi_0}{N}}\right]. \tag{2.89}$$

Equation (2.89) gives the equivalent currents for scalar plane-wave illumination at oblique incidence. The currents are no longer oriented along the edge for oblique incidence, but are in the direction given by

$$\hat{u}_\ell = -\hat{u}_\rho\operatorname{Cos}\theta_0 + \hat{u}_z\operatorname{Sin}\theta_0. \tag{2.90}$$

This direction, and hence the direction of the equivalent currents, changes with ϕ.

For electromagnetic plane-wave incidence, as given by (2.51), the equivalent electric (magnetic) source current $\underline{J}$ ($\underline{M}$) are readily derived to give

$$\begin{aligned}\underline{J} &= -\hat{u}_\ell\ \frac{a_z}{j\omega\mu}\operatorname{Cosec}\theta_0\ I^p_e\ ,\\ \underline{M} &= \hat{u}_\ell\ \frac{a_\phi}{jk}\ I^p_m\ ,\end{aligned} \tag{2.91}$$

where $I^p_{e_m}$ is given by (2.89). If the source of the electromagnetic wave is at known distance from the edge, then we can

use the cylindrical-wave equivalent currents of (2.87) in (2.91) to provide valid and finite solutions in the shadow boundary regions. We take this approach in chapter four when we analyse the radiation pattern of reflector antennas.

In 2.34 we discussed slope-wave diffraction for a non-uniform incident field. By analogy with the above derivation, we can obtain slope-wave correction equivalent currents. Defining the slope-wave equivalent currents, I_{se}, I_{sm}, as

$$I^{se}_{sm} = -\frac{1}{jk}\frac{\partial}{\partial\phi_0} I^{e}_{m} , \tag{2.92}$$

then from (2.87), (2.88) we get

$$I^{c}_{se\,sm} = [Y_{sd}(r_0,\phi-\phi_0) \pm Y_{sd}(r_0,\phi+\phi_0)], \tag{2.93}$$

where

$$Y_{sd}(r_0,\Phi) = \frac{2\,\mathrm{Sin}\frac{\pi}{N}}{Nk\sqrt{j\pi}}\left[\frac{kr_0\mathrm{Sin}^2\theta_0\mathrm{Sin}\Phi\left|\mathrm{Cos}\frac{\Phi}{2}\right|}{\mathrm{Cos}\frac{\pi}{N}-\mathrm{Cos}\frac{\Phi}{N}}\cdot\right.$$

$$\left[\frac{e^{-jkr_0}}{2p} - je^{jkr_0(\mathrm{Sin}^2\theta_0\mathrm{Cos}\Phi-\mathrm{Cos}^2\theta_0)}F(p)\right]$$

$$\left.+\, e^{jkr_0(\mathrm{Sin}^2\theta_0\mathrm{Cos}\Phi-\mathrm{Cos}^2\theta_0)}F(p)\;\frac{\varepsilon_1[\frac{1}{2}\mathrm{Sin}\frac{\Phi}{2}(\mathrm{Cos}\frac{\pi}{N}-\mathrm{Cos}\frac{\Phi}{N})+\frac{1}{N}\mathrm{Sin}\frac{\Phi}{N}\mathrm{Cos}\frac{\Phi}{2}]}{(\mathrm{Cos}\frac{\pi}{N}-\mathrm{Cos}\frac{\Phi}{N})^2}\right] \tag{2.94}$$

and from (2.89) we get

$$I^{c}_{se\,sm} \sim I^{p}_{se\,sm}\frac{e^{-jkr_0}}{\sqrt{8j\pi kr_0}} ,$$

where

$$I^{p}_{se\,sm} = -\frac{2\,\mathrm{Sin}\frac{\pi}{N}}{jkN^2}\mathrm{Cosec}\,\theta_0\left[\frac{\mathrm{Sin}\frac{\phi-\phi_0}{N}}{(\mathrm{Cos}\frac{\pi}{N}-\mathrm{Cos}\frac{\phi-\phi_0}{N})^2} \pm \frac{\mathrm{Sin}\frac{\phi+\phi_0}{N}}{(\mathrm{Cos}\frac{\pi}{N}-\mathrm{Cos}\frac{\phi+\phi_0}{N})^2}\right] \tag{2.95}$$

Finally, we can write the equivalent source currents to include the slope-wave term for electromagnetic wave incidence as

$$\begin{aligned} \underline{J} &= -\hat{u}_\iota \frac{1}{j\omega\mu} \operatorname{Cosec} \theta_0 \ (a_z I_e + g_z I_{se}), \\ \underline{M} &= \hat{u}_\iota \frac{1}{jk} \ (a_\phi I_m + g_\phi I_{sm}), \end{aligned} \tag{2.96}$$

where g_z, g_ϕ are given by (2.72) or (2.73). The choice between plane-wave and cylindrical-wave equivalent currents depends on the problem to be solved. The cylindrical-wave terms are considerably more complicated than the plane-wave terms, but they give results that are valid in the shadow boundary regions.

CHAPTER THREE:

RADIATION FROM RECTANGULAR ELECTROMAGNETIC HORNS

What I tell you three times is true.

Lewis Carroll (1832-1898)

The earliest technique used for the theoretical evaluation of radiation from electromagnetic horns was the aperture field method (Barrow and Chu, 1939). It is well known that this method will give valid results only in the region near the forward axis. A more accurate representation of the radiation fields from horns has been found in the application of the edge diffraction methods discussed in chapter 2. Kinber (1962a) used this approach, in conjunction with the Brillouin ray technique for the fields inside the horn, to obtain the radiation from sectoral horns in the principal plane containing the flare. Later the E-plane of a pyramidal horn was considered by Russo *et al.* (1965) and Yu *et al.* (1966), and the H-plane by Yu and Rudduck (1969). The conical horn has also been analysed by edge diffraction methods (Hamid, 1968).

The radiation patterns of the two principal planes for rectangular horns can be determined (except for an unimportant constant) from two-dimensional source distributions for the aperture field method. Using edge diffraction methods, only the unflared planes of sectoral horns and the E-plane of a pyramidal horn can be reduced to a two-dimensional problem for the entire radiation pattern. In what follows we restrict our analysis to these planes where we can use and evaluate the ray tracing methods of the GTD. This will provide us with an

evaluation of edge diffraction methods when we consider three-dimensional problems in chapter four.

Before attempting radiation pattern control in the above-mentioned planes, we investigate the characteristics of the radiation from the unperturbed horn. In 3.1 and 3.2 we consider sectoral horns where the unflared principal planes can be modelled by the two-dimensional parallel-plate waveguide problem. Radiation from parallel-plate waveguides has been solved by several methods: aperture field and exact Wiener-Hopf solution, Collin and Zucker (1969); GTD approach, Ryan and Rudduck (1968), Rudduck and Wu (1969), Lee (1969); and a surface integration technique combined with the GTD, Wu *et al.* (1969). We will consider this problem in some detail as it allows us to compare the approximate methods of the GTD and the aperture field method with the exact solution. In addition, there are two points we wish to comment on regarding the GTD approach. They are: (1) it has not been shown mathematically in the literature that the field is finite along the shadow boundaries for both the *TEM* and TE_{10} mode in the guide; (2) there exists an anomaly in the use of the slope-wave term.

In 3.3 we briefly consider radiation from a pyramidal horn, and in 3.4 attempt radiation pattern control with the knowledge obtained from the previous three sections.

3.1 H-PLANE SECTORAL HORN

To evaluate the radiation from an H-plane sectoral horn when excited by a rectangular waveguide supporting the dominant TE_{10} mode (Fig. 3.1), we consider first the solution to the boundary value problem for the horn extending to infinity in the s-direction in Fig. 3.1.

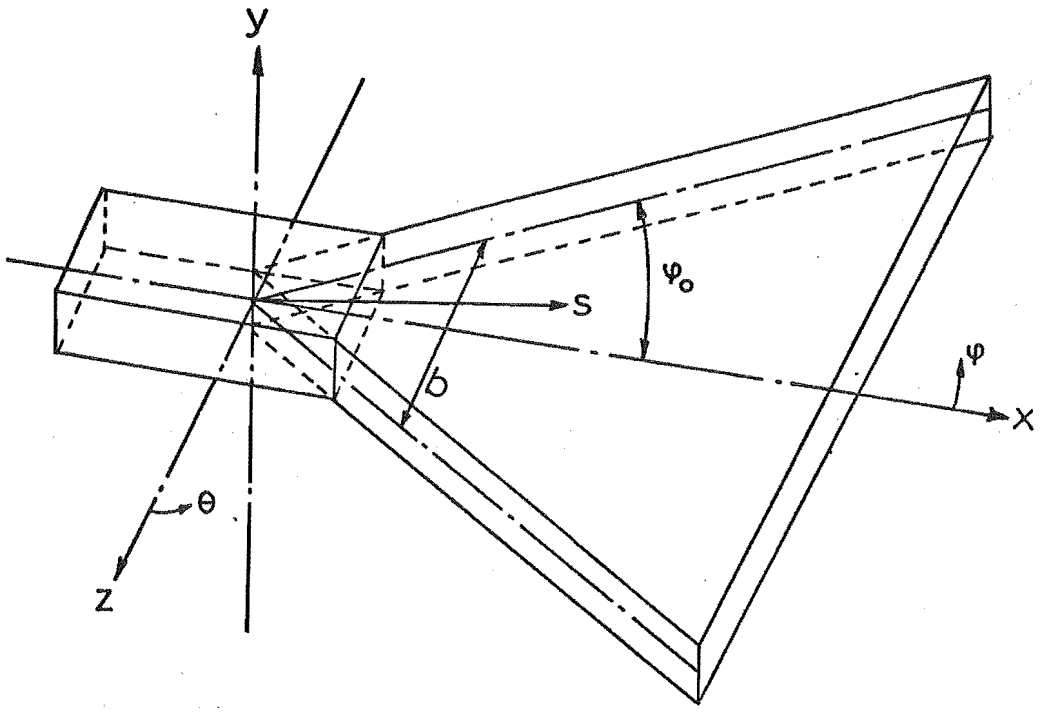

Fig. 3.1 H-plane sectoral horn

The modes excited in the sectoral horn by this arrangement are the TE_{mo} modes. From Barrow and Chu (1939), the fields for these modes are given, in the (s,φ,y) cylindrical coordinates in Fig. 3.1, by

$$E_y = A \cos m\nu\,\varphi\; H^{(2)}_{m\nu}(ks),$$

$$H_s = \frac{m\nu\, A \sin m\nu\,\varphi}{j\omega\mu s}\; H^{(2)}_{m\nu}(ks), \tag{3.1}$$

$$H_\varphi = -jA\sqrt{\frac{\varepsilon}{\mu}}\cos m\nu\,\varphi\; H^{(2)\prime}_{m\nu}(ks),$$

where $\nu = \frac{\pi}{2\varphi_0}$, $H^{(2)}_{m\nu}$ is the Hankel function of the second kind of order $m\nu$, and $H^{(2)\prime}_{m\nu}(x) = \frac{\partial}{\partial x} H^{(2)}_{m\nu}(x)$.

For the conditions that $m\nu \ll ks$, we can simplify (3.1) by taking the asymptotic expansion of the Hankel function, given by (2.27), to give for the fields in the horn

$$E_y \sim A \cos m\nu\varphi \sqrt{\frac{2j}{\pi ks}}\, j^{m\nu}\, e^{-jks},$$

$$H_s \sim \frac{m\nu A \sin m\nu\varphi}{j\omega\mu s} \sqrt{\frac{2j}{\pi ks}}\, e^{-jks}, \qquad (3.2)$$

$$H_\varphi \sim - A \sqrt{\frac{\varepsilon}{\mu}} \cos m\nu\varphi \sqrt{\frac{2j}{\pi ks}}\, j^{m\nu}\, e^{-jks},$$

from which we get $\frac{E_y}{H_\varphi} \sim - \sqrt{\frac{\mu}{\varepsilon}}$ for each mode, i.e., plane-wave propagation. For the modes to propagate in the horn the condition $b > \frac{m\lambda}{2}$ must be satisfied, where b is the spacing between the E-plane walls. The dimensions of the rectangular waveguide feed are such that only the dominant TE_{10} mode can propagate in the guide. As the H-plane of the waveguide is flared into a sectoral horn, the higher order modes will be able to propagate as the conditon $b > \frac{m\lambda}{2}$ is satisfied. Considerable attentuation, however, will have occurred to the higher order modes in the region of the horn where they are below cut-off. For this reason, the field in the horn can be approximated as given by the dominant mode alone. When the horn is of finite length, S_L, we can evaluate radiation from the horn either from the field in the aperture (aperture field method), or from the effect of the incident field upon the aperture edges (edge diffraction method).

3.11 E-plane radiation pattern

Assuming the length of the horn satisfies the condition $S_L >> \frac{\nu}{k}$, the incident field at the aperture can be approximated by a plane-wave for the dominant mode. Only the E-plane edges are illuminated since the field is zero along the H-plane walls (assuming H_s is negligible). Except for the mid-point of the E-plane edges, the field is at oblique incidence to the edge. The diffraction mechanism from the

edges is illustrated in Fig. 3.2. For radiation into the E-plane, i.e. when $\theta = \frac{\pi}{2}$ in Fig. 3.1, we can see from Fig. 3.2 that the major contribution of the radiation field comes from the mid-point of the E-plane edges where the illuminating field is at normal incidence. At other points along the E-plane edges the field is at oblique incidence and diffracts the field away from the E-plane. Thus, for the E-plane radiation pattern, we can use the parallel-plate waveguide model of Fig. 3.3 supporting the *TEM* mode. The incident field is given from (3.2) for $\psi = 0$.

We can now use the ray tracing methods of the GTD discussed in 2.3 to estimate the radiation from the parallel-plate waveguide of Fig. 3.3. Other methods are the aperture field method, which we will begin with, and the exact Wiener-Hopf solution which will be used as a comparison with the approximate methods in 3.113.

3.111 Aperture field method

To evaluate the radiation field by the aperture field method, we begin with the expression for the radiation zone from two-dimensional source distributions given by (2.18), i.e.

$$\underline{E}(\underline{\rho}) = -j\omega\mu \frac{e^{-jk\rho}}{\sqrt{8j\pi k\rho}} \int \left[\sqrt{\frac{\varepsilon}{\mu}}\, \underline{M}_{\ell'} \wedge \hat{\rho} + \underline{J}_{\ell'} - (\underline{J}_{\ell'} \cdot \hat{\rho})\hat{\rho}\right] e^{jk\rho' \cos(\phi-\phi')} d\ell' . \tag{3.3}$$

We choose, as the region containing the sources, the surface across the aperture of the guide and along the outside walls of the plates. The region exterior to the waveguide is assumed to be source free. To evaluate the field in this source free region it is necessary to know, or assume, the equivalent sources on the chosen surface containing the actual

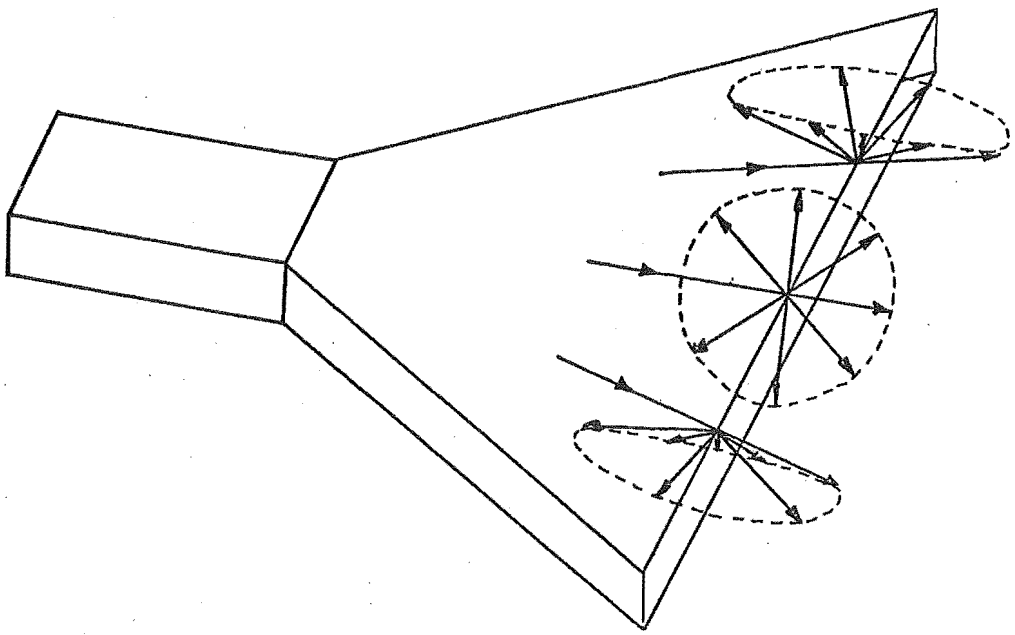

Fig. 3.2 Diffraction mechanism at the E-plane edges of an H-plane sectoral horn.

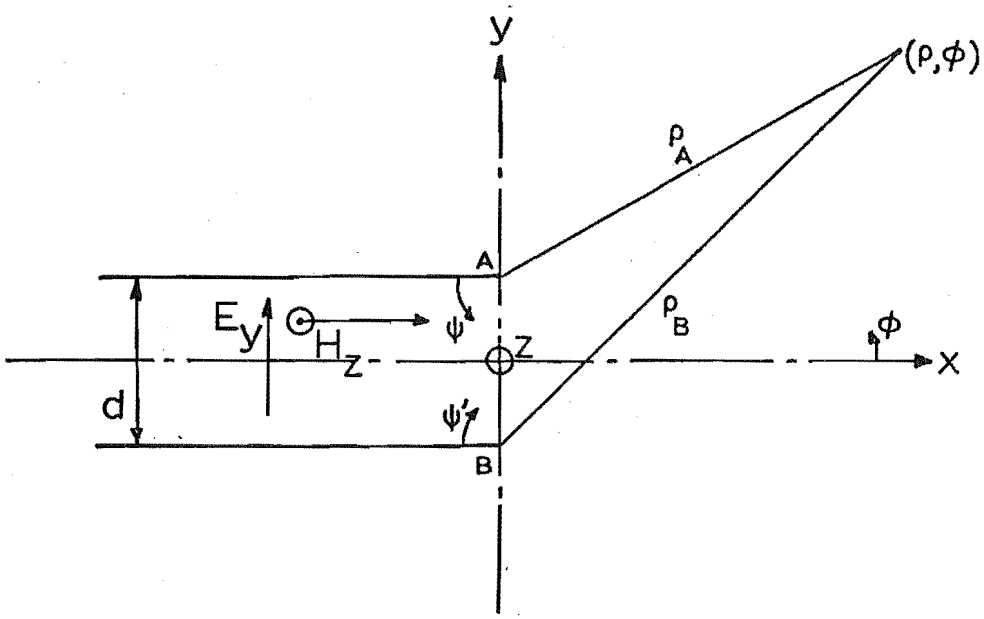

Fig. 3.3 *TEM* mode in parallel-plate waveguide.

sources. The aperture field method approximates the equivalent sources by assuming that they are zero on the outside walls of the waveguide and are given entirely by the fields in the aperture. The equivalent sources, $\underline{J}_{\ell'}$, $\underline{M}_{\ell'}$ are given by

$$\begin{aligned} \underline{J}_{\ell'} &= \hat{n} \wedge \underline{H}, \\ \underline{M}_{\ell'} &= \underline{E} \wedge \hat{n}, \end{aligned} \tag{3.4}$$

where $\hat{n}$ is the outward normal from the surface surrounding the actual sources. For the equivalent sources in the aperture of the problem illustrated in Fig. 3.3, we have

$$\begin{aligned} \underline{J}_{\ell'} &= -\hat{u}_y \sqrt{\frac{\epsilon}{\mu}}\, E_y, \\ \underline{M}_{\ell'} &= -\hat{u}_z\, E_y. \end{aligned} \tag{3.5}$$

Substituting (3.5) into (3.3) yields, for the radiation field,

$$E_\phi = K_1 \operatorname{Cos}^2\left(\frac{\phi}{2}\right) \frac{\operatorname{Sin} u}{u}, \tag{3.6}$$

where
$$u = \frac{kd}{2} \operatorname{Sin} \phi, \tag{3.7}$$

$$K_1 = \sqrt{\frac{jd^2}{\lambda \rho}}\, E_y\, e^{-jk\rho}. \tag{3.8}$$

3.112 Edge diffraction method

To solve the problem using edge diffraction methods, we use the GTD approach given in 2.3 by considering, initially, each plate as an isolated half-plane. Consider the lower half-plane with the edge at B in Fig. 3.3. The incident field at the edge is a plane-wave at grazing incidence. From (2.66) (2.56), (2.50), with $N = 2$, $\phi_0 = 0$, we get for the diffracted far-field

$$E^{d}_{\psi'} = - \frac{E_y}{\sqrt{8j\pi k\rho_B}} \operatorname{Sec}\left(\frac{\psi'}{2}\right) e^{-jk\rho_B} \tag{3.9}$$

Similarly, for the upper edge at A, we get

$$E^{d}_{\psi} = - \frac{E_y}{\sqrt{8j\pi k\rho_A}} \operatorname{Sec}\left(\frac{\psi}{2}\right) e^{-jk\rho_A}. \tag{3.10}$$

Relating ψ, ψ', and ρ_A, ρ_B, to the general coordinate system, (ρ, ϕ, z) in Fig. 3.3, then

$$\begin{aligned} \psi &= \pi + \phi, \\ \psi' &= \pi - \phi, \\ \rho_A &= \rho - \frac{d}{2} \operatorname{Sin} \phi, \\ \rho_B &= \rho + \frac{d}{2} \operatorname{Sin} \phi. \end{aligned} \tag{3.11}$$

Adding the effective sources at A, B given by (3.9), (3.10) at a point (ρ, ϕ) in the far-field using the relationships in (3.11), we obtain the radiation field, E_ϕ, for $|\phi| < \frac{\pi}{2}$ as

$$E_\phi = K_1 \operatorname{Cos}\left(\frac{\phi}{2}\right) \frac{\operatorname{Sin} u}{u}\Bigg|_{|\phi| < \frac{\pi}{2}}, \tag{3.12}$$

where u, K_1 have been defined by (3.7), (3.8). For $|\phi| \geq \frac{\pi}{2}$ one of the sources is shielded by the opposite waveguide wall and the radiation field is given from one source only, i.e.

$$E_\phi = \frac{E_y}{\sqrt{8j\pi k\rho}} \operatorname{Cosec}\left(\frac{|\phi|}{2}\right) e^{-jk\rho}\Bigg|_{|\phi| \geq \frac{\pi}{2}}. \tag{3.13}$$

Although the individual source terms of (3.9), (3.10) have an infinity on the shadow boundary when ψ or $\psi' = \pi$, the total solution is finite on this boundary as we can see from (3.12).

Comparing (3.12) with the equivalent solution, (3.6), using the aperture field method, shows that the two solutions are identical on the forward axis. The difference between the two terms is a multiplication factor of Cos $\frac{\phi}{2}$. Since the difference increases with the angle of radiation, it indicates that the neglected currents, in the aperture field approach, on the outside walls of the guide are contributing to the major part of the difference. These wall currents are implicit in the GTD formulation.

Coupling effects between the aperture edges, which are not possible to evaluate from aperture field theory, can be included using the GTD. From (3.9) and (3.10) we have an effective magnetic line-source along each edge to account for edge diffraction from the incident plane-wave. The line-source at B (see Fig. 3.3) creates cylindrical-wave diffraction at the opposite edge A. Similarly, cylindrical-wave diffraction occurs from A to B. These higher order diffraction effects create, in turn, their own cylindrical-wave diffraction with the opposite edge, and the phenomenon continues *ad infinitum*.

Consider the evaluation of the first order cylindrical-wave diffraction term, ${}^{A}E_{\phi}^{d}$, from B to A in Fig. 3.3. The intensity, R_B, of the line-source in the direction of the edge at A is obtained from (3.9), i.e.,

$$R_B \frac{e^{-jk\rho_B}}{\sqrt{8j\pi k\rho_B}} = E_{\psi'}^{d}\Big|_{\psi' = \frac{\pi}{2}}$$

$$\therefore \qquad R_B = -\sqrt{2}\, E_y. \tag{3.14}$$

For cylindrical-wave diffraction we use (2.66) in conjunction with (2.69). Thus we can write ${}^{A}E_{\phi}^{d}$ as

$$ {}^{A}E_{\phi}^{d} = R_B \left[V_d(d,\psi - \tfrac{\pi}{2}) + V_d(d,\psi + \tfrac{\pi}{2}) \right] \frac{e^{-j k \rho_A}}{\sqrt{8 j \pi k \rho_A}} \qquad (3.15) $$

The source at B, given by (3.9), is a non-uniform line-source. Therefore, in addition to (3.15) there will be a slope-wave term, ${}^{A}E_{\phi}^{S}$, obtained from (2.71), (2.73), (2.75) to give

$$ {}^{A}E_{\phi}^{S} = \frac{R_B'}{j k d} \left[V_d'(d,\psi - \tfrac{\pi}{2}) - V_d'(d,\psi + \tfrac{\pi}{2}) \right] \frac{e^{-j k \rho_A}}{\sqrt{8 j \pi k \rho_A}} \qquad (3.16) $$

where

$$ R_B' = \frac{\partial}{\partial \psi'} R_B \Big|_{\psi' = \frac{\pi}{2}} $$

$$ = \tfrac{1}{2} R_B . $$

Similarly for cylindrical-wave diffraction from A to B we have

$$ {}^{B}E_{\phi}^{d} = R_A \left[V_d(d,\psi' - \tfrac{\pi}{2}) + V_d(d,\psi' + \tfrac{\pi}{2}) \right] \frac{e^{-j k \rho_B}}{\sqrt{8 j \pi k \rho_B}} $$

$$ {}^{B}E_{\phi}^{S} = \frac{R_A'}{j k d} \left[V_d'(d,\psi' - \tfrac{\pi}{2}) - V_d'(d,\psi' + \tfrac{\pi}{2}) \right] \frac{e^{-j k \rho_B}}{\sqrt{8 j \pi k \rho_B}} \qquad (3.17) $$

where $R_A' = \tfrac{1}{2} R_A$, and $R_A = R_B$. These higher order terms at each edge can now be added at a point (ρ,ϕ) in the far-field using the relationships of (3.11). The resultant is added to (3.12) to give the total solution for $|\phi| < \frac{\pi}{2}$. As before for $|\phi| \geq \frac{\pi}{2}$, radiation is from only one edge. The total solution is then given by adding (3.15), (3.16) to (3.13).

Higher order terms created by the above cylindrical-wave diffraction can also be evaluated, but the labour involved is considerable. Lee (1969) has derived a system of rays from the exact solution which automatically takes care of the coupling between the plates. Although this gives the exact far-field solution for parallel-plate waveguides, it is not

instructive in assessing coupling effects between plates for more general problems.

3.113 Comparison of measured and theoretical solutions

The solution to the parallel-plate waveguide problem of Fig. 3.3 falls into the small class of electromagnetic problems for which an exact analytical solution exists. We will use this solution to give a comparison with the approximate methods.

The normalised radiation pattern from the exact solution is given by (Collin and Zucker, 1969)

$$|E_\phi| = e^{\frac{kd}{4}(\cos\phi - 1)} \left[\frac{\sin u}{u}\right]^{\frac{1}{2}}, \qquad (3.18)$$

provided $d < \lambda$, and u is given by (3.7).

In Fig. 3.4 are plotted the various solutions to the problem. It is seen that the GTD, without coupling terms, gives a considerable improvement over the aperture field method for large values of ϕ. A further improvement is obtained by taking the first coupled rays between the edges. With the addition of the slope-wave term, there is a further improvement in some regions and a deterioration in others.

We can see from Fig. 3.4 that the GTD gives a discontinuity at $\phi = \frac{\pi}{2}$ as one of the sources is shielded by the opposite guide wall. To effect a smooth transition, Rudduck and Wu (1969) took only the second diffracted ray from the nearest edge. With the addition of the slope-wave term from the nearest edge, they give results which are close to the exact solution. Although we cannot see any physical justification for dropping the coupling terms from one of the edges, it is interesting to note that this is similar to the

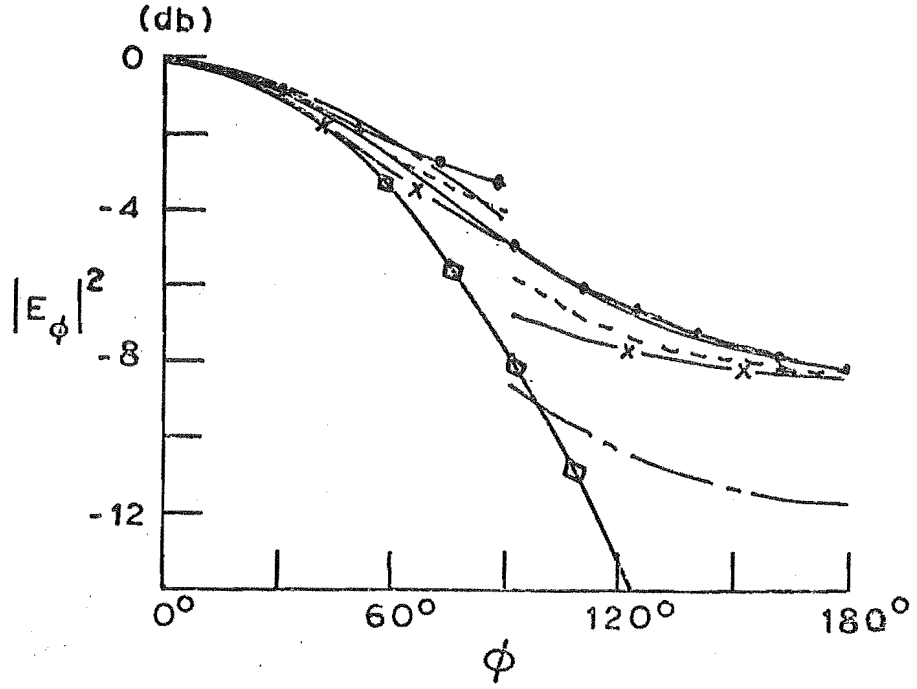

Fig. 3.4 Radiation from parallel-plate waveguide supporting the *TEM* mode. $d = 0.3\lambda$

Aperture field method

GTD without coupling terms

GTD with first order coupling term

Addition of slope-wave term

Subtraction of slope-wave term

Exact Wiener-Hopf solution

results of Lee (1969). The solution Lee derived from the exact Wiener-Hopf solution is given by edge sources from the first diffracted rays, plus an additional source at one edge only to automatically take care of the coupling between plates.

The slope-wave term result as given by Rudduck and Wu is as shown in Fig. 3.4 with the slope-wave term subtracted, and not added, in the total solution. This does not appear to correspond to their mathematical formulation. With the slope-wave term subtracted, there is an improvement in the back half-space and deterioration in the front half-space. This result would appear more reasonable since the field in the back half-space can only be due to the currents flowing on the outside wall of the nearest half-plane. We thus would expect the slope-wave term to give a more accurate result in this region in particular. This addition or subtraction of the slope-wave term is a point which has yet to be clarified. It is interesting to note that by changing the slope-wave term from addition to subtraction at $\phi = \frac{\pi}{2}$, the resultant curve follows closely that for the exact solution.

Measurements on H-plane sectoral horns were carried out to test the validity of the parallel-plate waveguide model for the E-plane radiation pattern. The procedure for measuring the radiation patterns is discussed in appendix C. A sectoral horn of dimensions $S_L = 8.56\lambda$ (at 9.5 GHz), $\psi_0 = 15^o$, was used for the experimental verification of the methods to be discussed in 3.4. We will call this the basic horn for convenience. It is seen from Fig. 3.5 that there is some discrepancy with the radiation pattern computed for the parallel-plate waveguide and the measured pattern of the basic horn. Differences would be expected in the far side-lobes

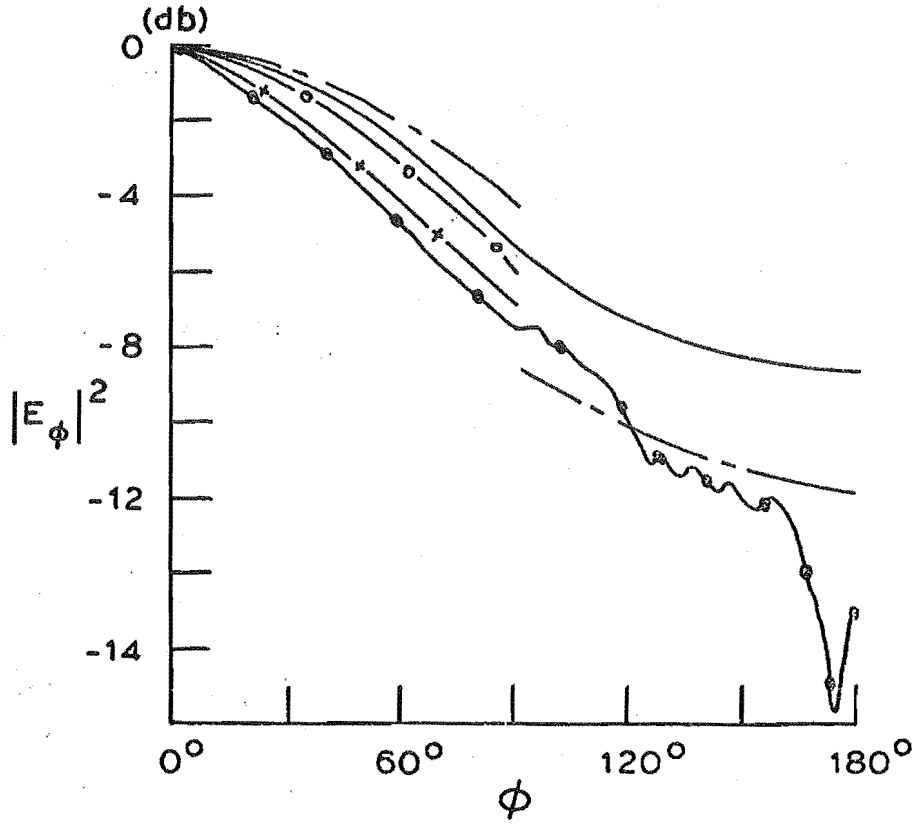

Fig. 3.5 E-plane radiation pattern of H-plane sectoral horn.
$d = 0.3\lambda$

●——●	$S_L = 9.46\lambda$, $\psi_0 = 15^\circ$	Measured
—+—+—	$S_L = 9.46\lambda$, $\psi_0 = 45^\circ$	
—o—o—	$S_L = 16.4\lambda$, $\psi_0 = 15^\circ$	
——·——	GTD without coupling	Theory from parallel-plate waveguide model.
————	Exact Wiener-Hopf solution	

since the horn is of finite length and scattering will occur at the back of the horn. This effect is compounded by the feeding arrangement to the horn. To determine the source of error in the forward direction we measured the radiation pattern of two other horns in this direction. One being a wide angle horn, and the other a longer horn than the basic horn but with the same flare angle. Both of these horns are not practical as their dimensions are far removed from an optimum design.

The wide angle horn, although meeting the criteria $m\upsilon << ks_L$ more accurately than the basic horn for the dominant mode, allows more readily the propagation of higher order modes as the condition $b > \frac{m\lambda}{2}$ is satisfied sooner. The longer horn, however, more accurately satisfies $m\upsilon << ks_L$ without any deterioration in the attenuation of the higher order modes. Fig. 3.5 shows that the longer horn comes the closest to the parallel-plate waveguide pattern. Note that the edge diffraction result without coupling terms gives a good representation of radiation from the basic horn in the back half-space.

3.12 Radiation in other planes

Radiation in other planes is readily determined from the aperture field method which will give valid results in regions near the forward axis. The expressions will be considerably complicated, however, by the phase error across the aperture in the H-plane. (This does not affect the E-plane expression because the two planes are orthogonal.)

The diffraction mechanism at the edges does not allow a two-dimensional model to be used for any other plane, other

than the E-plane, for analysis by edge diffraction methods. A solution can be obtained in terms of the equivalent edge currents discussed in 2.4. We need, however, to take a closer look at the assumptions made to obtain the E-plane pattern. It was assumed for the E-plane that H_s in (3.2) was of little significance at the aperture of the horn. This is true for the E-plane, but in the H-plane this term gives the major diffraction effect. We can see this from the diffraction mechanism in the H-plane illustrated in Fig. 3.6.

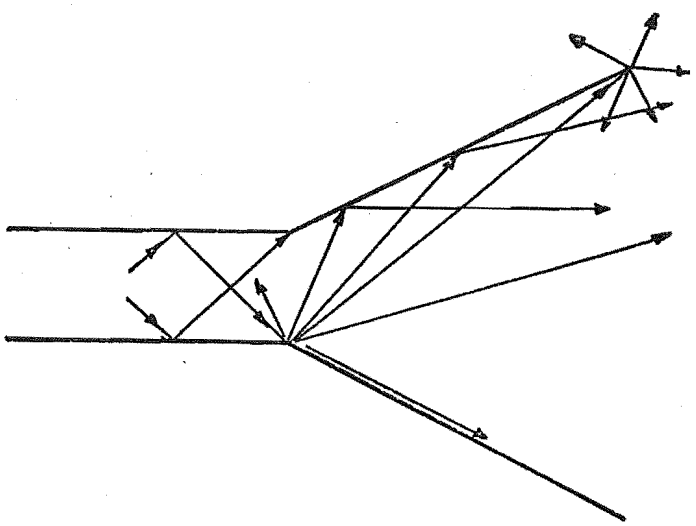

Fig. 3.6 Diffracted rays in H-plane of H-plane sectoral horn.

The TE_{10} mode in the guide is formed by the combination of two plane waves travelling along the guide as shown. These component waves diffract at the waveguide-horn junction to give diffracted rays, some of which are incident to the H-plane edges. This consequent diffraction will be small, since the incident ray is near grazing incidence to the horn wall with electric polarization, and will tend to zero as the horn length tends to infinity. For this condition we are left with only the plane-wave given by E_y and H_φ in (3.2). Kinber

(1962a) obtained the cylindrical-wave diffraction at the H-plane edges using the Brillouin ray technique for the fields inside the horn. Some of the rays from the sources on the H-plane edges reflect back into the horn to give higher order reflection and diffraction. Kinber accounted for these effects by the images in the horn walls from the edge equivalent sources. His failure to consider the diffraction along the E-plane edges, however, gave an inadequate result for the back-lobe. This was demonstrated by Yu and Rudduck (1969) for the H-plane of a pyramidal horn.

Slope-wave diffraction which occurs at the H-plane edges has not been considered, but it may be significant, especially for large horns.

3.2 E-PLANE SECTORAL HORN

As for the previous section, we begin with the solution to the boundary value problem for the E-plane sectoral horn illustrated in Fig. 3.7.

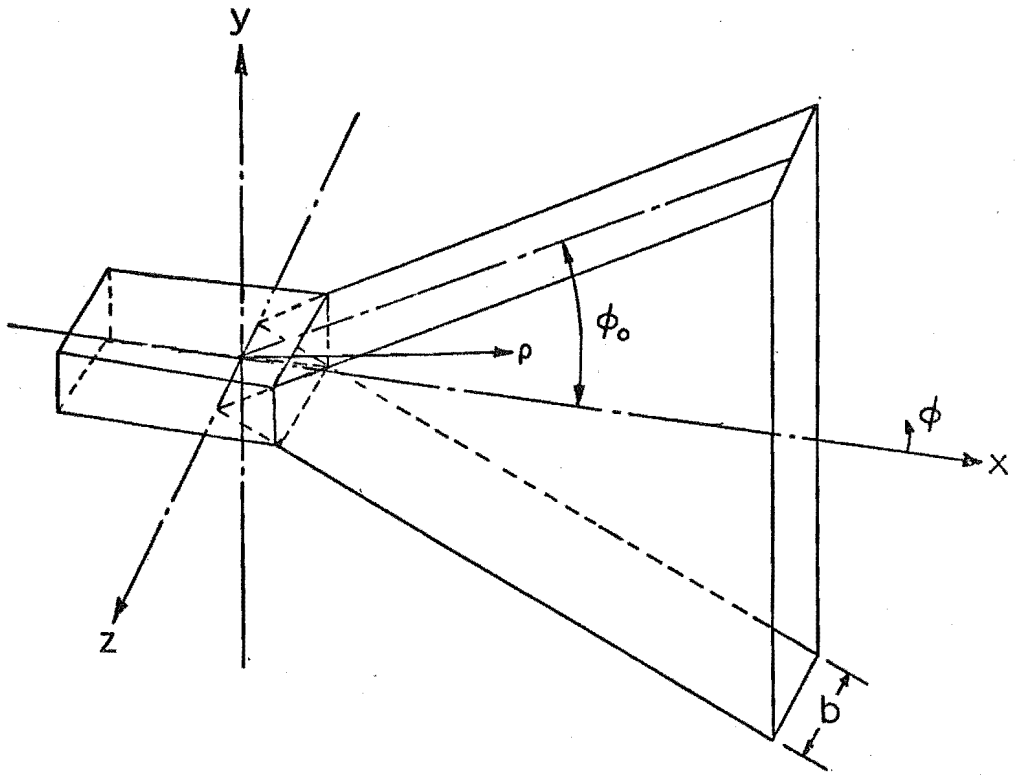

Fig. 3.7 E-plane sectoral horn

If the horn is excited by a rectangular waveguide supporting the TE_{mo} modes, then the field in the horn is given by (Barrow and Chu, 1939)

$$
\begin{aligned}
E_\phi &= A \cos\left(\frac{m\pi z}{b}\right) H_1^{(2)}(\gamma_m \rho), \\
H_z &= \frac{jA\gamma_m}{\omega\mu} \cos\left(\frac{m\pi z}{b}\right) H_0^{(2)}(\gamma_m \rho), \\
H_\rho &= \frac{jAm\pi}{\omega\mu b} \sin\left(\frac{m\pi z}{b}\right) H_1^{(2)}(\gamma_m \rho),
\end{aligned}
\tag{3.19}
$$

where $\gamma_m = \sqrt{k^2 - \left(\frac{m\pi}{b}\right)^2}$, and b is the dimension of the unflared wall. For $\gamma_m \rho >> 1$, the asymptotic expansion of (3.19) yields

$$
\begin{aligned}
E_\phi &\sim -A \cos\left(\frac{m\pi z}{b}\right) \sqrt{\frac{2}{j\pi\gamma_m\rho}}\, e^{-j\gamma_m\rho}, \\
H_z &\sim -\frac{A\gamma_m}{\omega\mu} \cos\left(\frac{m\pi z}{b}\right) \sqrt{\frac{2}{j\pi\gamma_m\rho}}\, e^{-j\gamma_m\rho}, \\
H_\rho &\sim \frac{Am\pi}{j\omega\mu b} \sin\left(\frac{m\pi z}{b}\right) \sqrt{\frac{2}{j\pi\gamma_m\rho}}\, e^{-j\gamma_m\rho}.
\end{aligned}
\tag{3.20}
$$

If only the TE_{10} mode exists in the waveguide, then we see from (3.19) that the higher order modes are in the cut-off condition for the entire length of the horn since the dimension b does not change from the waveguide dimension. This is in contrast to the H-plane sectoral horn where higher order modes can be supported when the E-plane wall separation is greater than the cut-off condition. Thus we would expect the higher order modes to be considerably more attenuated in the E-plane horn. Also, the asymptotic expansion of (3.19) given by (3.20) would be a more accurate representation of the field in the horn than the equivalent formulation of (3.2) for the H-plane horn. This is because the orders of the Hankel functions are lower in (3.19) compared with (3.1), and are not

dependent on the flare angle or any other horn dimension.

3.21 H-plane radiation pattern

For a finite horn of length ρ_L, the H-plane radiation pattern can be evaluated (by arguments similar to the E-plane of the H-plane sectoral horn) from the parallel-plate waveguide model of Fig. 3.8 supporting the TE_{10} mode.

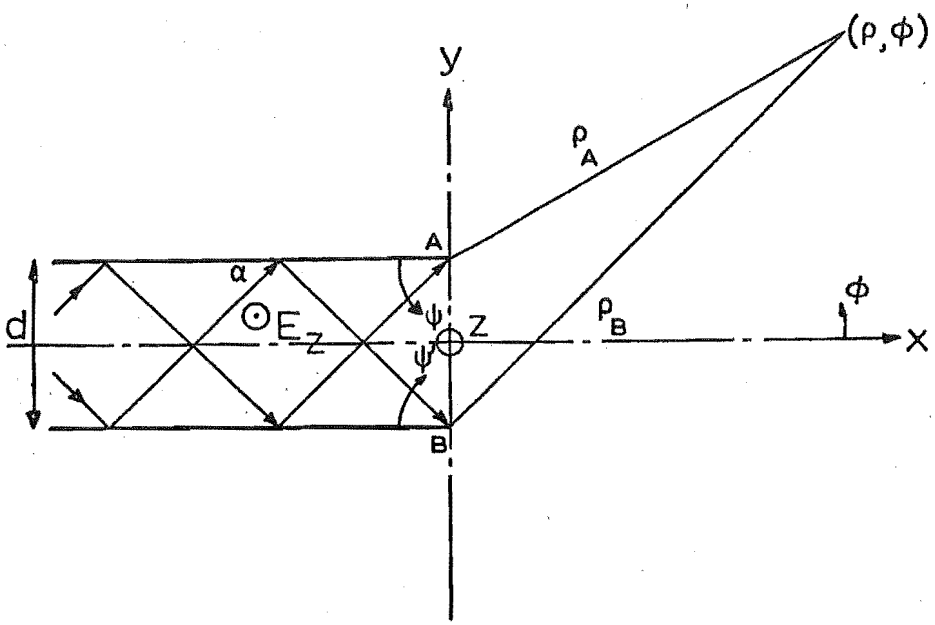

Fig. 3.8 Parallel-plate waveguide supporting the TE_{10} mode.

This mode can be considered as consisting of two plane waves propagating between the two plates with angle of incidence (and reflection), α, given by

$$\alpha = \text{Sin}^{-1} \left(\frac{\lambda}{2d}\right), \tag{3.21}$$

where d is the spacing between the plates. The electric field is parallel to the walls and proportional to Cos $\left(\frac{\pi y}{d}\right)$.

3.211 Aperture field method

Using the aperture field method, as outlined in 3.111, we obtain the radiation field from the equivalent sources in the aperture as

$$E_z = K_2 \operatorname{Cos}^2 \frac{\phi}{2} \frac{\operatorname{Cos} u}{(\frac{\pi}{2})^2 - u^2} \tag{3.22}$$

where $K_2 = \frac{\pi d E_0}{2} \sqrt{\frac{j}{\lambda\rho}}\, e^{-jk\rho}$, and $u = \frac{kd}{2} \operatorname{Sin} \phi$ as before.

When $u \to \frac{\pi}{2}$, it is necessary to take the limit of (3.22) giving

$$E_z\Big|_{u=\frac{\pi}{2}} = \frac{K_2}{\pi} \operatorname{Cos}^2 \frac{\phi}{2} . \tag{3.23}$$

3.212 Edge diffraction method

As before we consider, initially, each edge in isolation. From (2.66), (2.50) for electric polarization with $N = 2$, $\phi_0 = \alpha$, we get for the edge at B in Fig. 3.8

$$E_z^d = - \frac{E_0}{\sqrt{8j\pi k\rho_B}} \left[\operatorname{Sec} \frac{\psi'-\alpha}{2} - \operatorname{Sec} \frac{\psi'+\alpha}{2}\right] e^{-jk\rho_B} \tag{3.24}$$

Similarly for the edge at A we get

$$E_z^d = - \frac{E_0}{\sqrt{8j\pi k\rho_A}} \left[\operatorname{Sec} \frac{\psi-\alpha}{2} - \operatorname{Sec} \frac{\psi+\alpha}{2}\right] e^{-jk\rho_A} . \tag{3.25}$$

Adding these effective sources at a point (ρ,ϕ) in the far-field and using the relationships in (3.11) we get, after some trigonometrical manipulation, the radiation field for $|\phi| < \frac{\pi}{2}$ as

$$E_z = K_3 \left.\frac{\operatorname{Cos} u \operatorname{Cos} \frac{\phi}{2} \operatorname{Sin} \frac{\alpha}{2}}{\operatorname{Cos} \alpha - \operatorname{Cos} \phi}\right|_{|\phi| < \frac{\pi}{2}} , \tag{3.26}$$

where $K_3 = \frac{4E_0}{\sqrt{2j\pi k\rho}} e^{-jk\rho}$. For $|\phi| \geq \frac{\pi}{2}$, the field is given by (3.24) or (3.25).

On the shadow boundary when $\phi = \alpha$, it is necessary to take the limit of (3.26). We can write cos u, using (3.21), as

$$\text{Cos } u = \text{Cos } (\frac{kd}{2} \text{ Sin } \phi)$$

$$= \text{Sin } \left[\frac{\pi}{2} (1 - \frac{\text{Sin } \phi}{\text{Sin } \alpha})\right].$$

Substituting into (3.26) we get, as $\phi \to \alpha$

$$E_z \underset{\phi \to \alpha}{\to} \frac{\pi K_3 \text{Cos } \frac{\phi}{2} \text{ Sin } \frac{\alpha}{2}}{2 \text{ Sin } \alpha} \left[\frac{\text{Sin } \alpha - \text{Sin } \phi}{\text{Cos } \alpha - \text{Cos } \phi}\right]$$

$$= \frac{-\pi K_3 \text{Cos } \frac{\phi}{2} \text{ Sin } \frac{\alpha}{2}}{2 \text{ Sin } \alpha} \text{ Cot } \frac{\phi+\alpha}{2}.$$

Finally, when $\phi = \alpha$, we have

$$E_z\Big|_{\phi=\alpha} = - \frac{\pi K_3}{4} \text{ Cot } \alpha. \tag{3.27}$$

We have shown by (3.27) that, as for the *TEM* mode, the total solution is finite along the shadow boundaries, despite the infinities in the plane-wave diffraction terms.

Using the same terminology as in 3.112, the first order cylindrical-wave diffraction between the edges is given by

$$\begin{aligned} {}^{A}E_z^d &= R_B [V_d(d, \psi - \tfrac{\pi}{2}) - V_d(d, \psi + \tfrac{\pi}{2})] \frac{e^{-jk\rho_A}}{\sqrt{8j\pi k\rho_A}}, \\ {}^{B}E_z^d &= R_B [V_d(d, \psi' - \tfrac{\pi}{2}) - V_d(d, \psi' + \tfrac{\pi}{2})] \frac{e^{-jk\rho_B}}{\sqrt{8j\pi k\rho_B}} \end{aligned} \tag{3.28}$$

where $R_B \frac{e^{-jk\rho_B}}{\sqrt{8j\pi k\rho_B}} = E_z^d\Big|_{\psi' = \frac{\pi}{2}}$.

Similarly, we could write the expression for the slope-wave term. The significance of the slope-wave term decreases with increased separation of the plates. Rudduck and Wu (1969) demonstrated that for guide widths greater than $\frac{\lambda}{2}$, which is the condition for TE_{10} mode propagation in a guide, the evaluation of the first coupled rays without the slope-wave

term gave adequate results. For this reason, coupled with the dubious advantage of including the slope-wave term as shown in 3.112, we shall not evaluate it for the TE_{10} mode.

3.212 Comparison of measured and theoretical solutions

The normalised radiation pattern from the exact solution for the TE_{10} mode in the parallel-plate waveguide is given by (Collin and Zucker, 1969)

$$|E_z| = \frac{\pi}{2} e^{\frac{kd}{4}(\cos\phi - 1)} \cos\frac{\phi}{2} \left| \frac{\cos u}{(\frac{\pi}{2})^2 - u^2} \right|^{\frac{1}{2}} . \qquad (3.29)$$

In Fig. 3.9 are plotted the various solutions to the problem. It is seen that the trends are similar to the *TEM* mode case. The aperture field method gives poor agreement except for the region of the main axis. Edge diffraction methods give results which follow closely the exact solution. Fig. 3.10 shows that good agreement exists between the theoretical and experimental results except in the back-lobe region. This is to be expected because of the finite length of the horn and the feeding arrangement as we discussed in 3.113 for the H-plane horn. Comparing Fig. 3.10 with Fig. 3.5 for the H-plane horn, we see that better agreement is obtained for the E-plane horn. This confirms our discussion at the beginning of 3.2 where it was shown that the parallel-plate waveguide model would be a more accurate representation for the E-plane horn than for the H-plane horn. Also, the latter horn is more susceptible to higher order mode propagation.

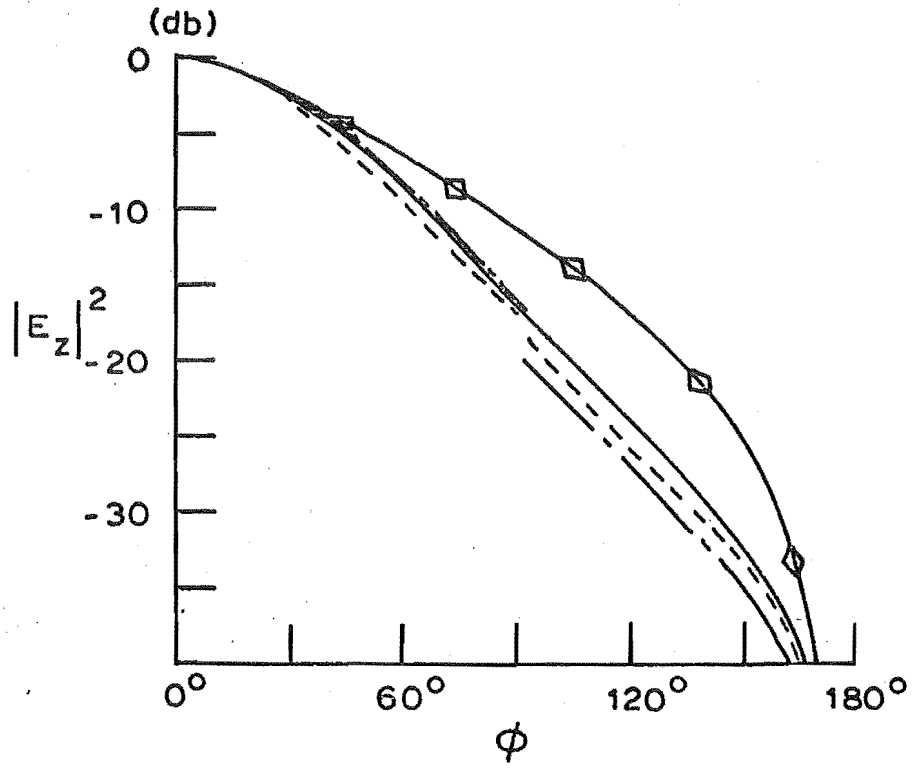

Fig. 3.9 Radiation from parallel-plate waveguide supporting the TE_{10} mode. $d = 0.8\lambda$

Aperture field theory

GTD without coupling terms

GTD with first order coupling term

Exact Wiener-Hopf solution.

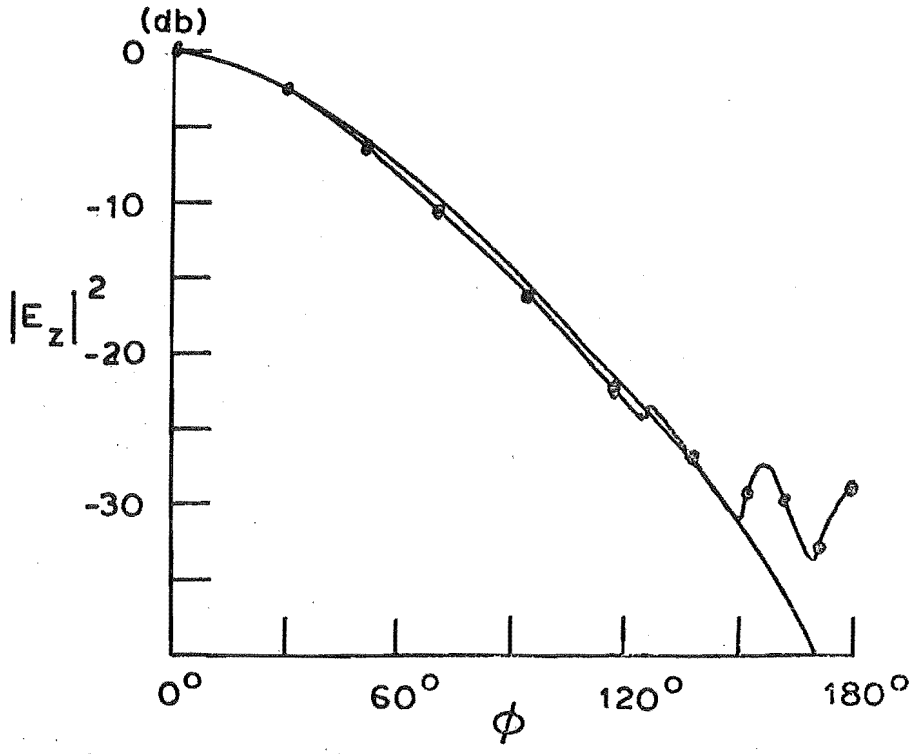

Fig. 3.10 H-plane radiation pattern of E-plane sectoral horn.
$d = 0.8\lambda$

$\rho_L = 8.85$
$\phi_0 = 16^\circ$
Measured

Exact Wiener-Hopf solution from parallel-plate waveguide model.

3.22 Radiation in other planes

Many of the comments that were made in 3.12 also apply here. The aperture field method readily allows an estimation of the radiation field with the complication of phase errors across the aperture. A solution using edge diffraction methods could be obtained using equivalent edge currents. It would not be necessary to account for slope-wave diffraction as all the edges are strongly illuminated. Kinber (1962a) obtained a partial solution by considering diffraction at the E-plane edges only. An analysis has yet to be made on sectoral

horns taking account of diffraction on all the aperture edges. The equivalent edge currents used in the next chapter for reflector antennas is a method that is readily applicable to horn type antennas.

3.3 PYRAMIDAL HORN

The pyramidal horn is illustrated in Fig. 3.11.

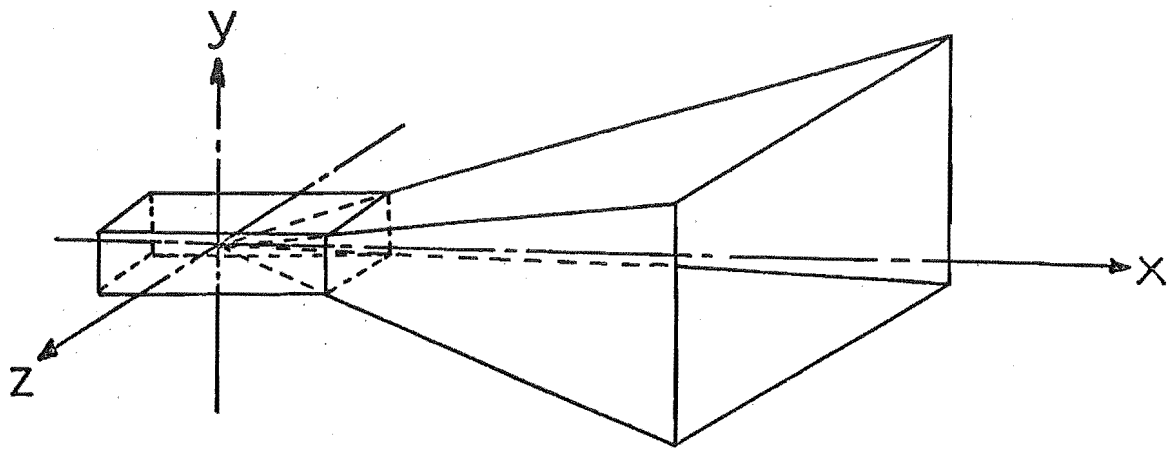

Fig. 3.11 Pyramidal horn.

Since the geometry of the horn does not fit into any separable coordinate system, it is not possible to solve explicitly for the modes. The usual practice is to design a pyramidal horn from the knowledge obtained in the study of E and H-plane sectoral horns. The aperture fields can be considered to be due to a point-source at the throat of the horn with the wavefront having a sinusoidal distribution in the H-plane.

3.31 E-plane radiation pattern

As for the H-plane sectoral horn, the major contribution of radiation into the E-plane comes from the mid-point of the E-plane edges. The pyramidal horn differs in that the field at the aperture for the E-plane is a cylindrical-wave and not a plane-wave as for the H-plane sectoral horn.

Fig. 3.12 shows the two-dimensional E-plane model used for edge diffraction analysis.

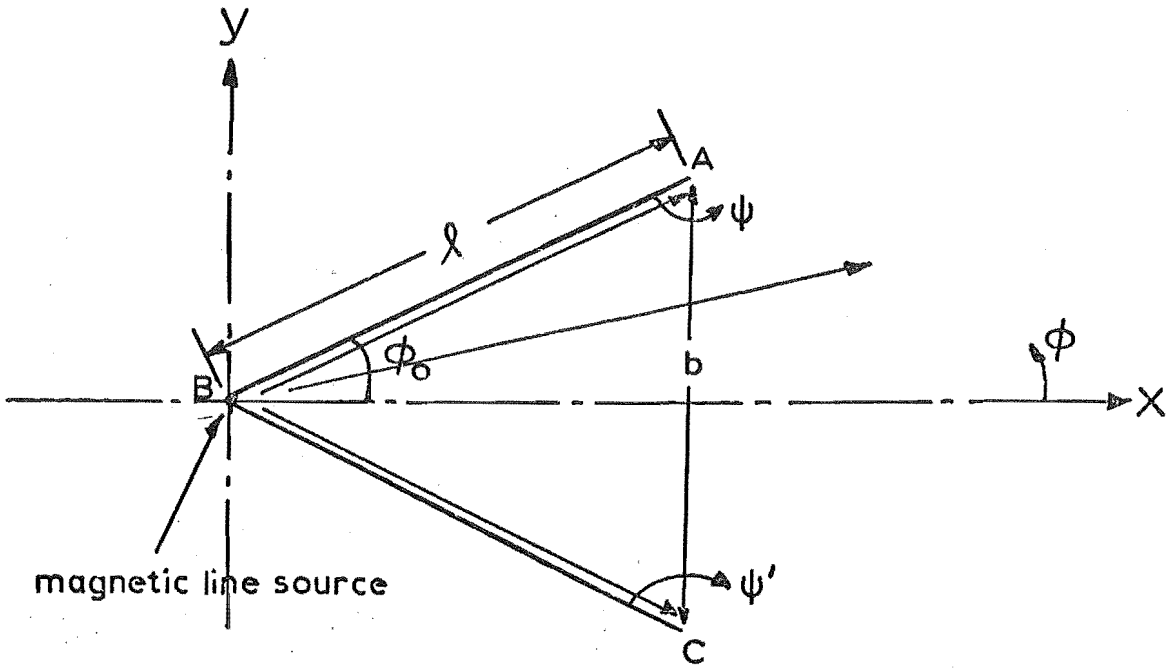

Fig. 3.12 E-plane model for pyramidal horn

Considering the horn walls as isolated half-planes illuminated by a unit strength magnetic line-source at grazing incidence, the far-field from the effective sources at A, B, C in Fig. 3.12, is readily derived from (2.66), (2.69) to give

$$E_\phi = -jk \frac{e^{-jk\rho}}{\sqrt{8j\pi k\rho}} [\varepsilon_2 + \varepsilon_3 V_d(\ell, \pi+\phi-\phi_0) e^{jk\ell \cos(\phi-\phi_0)} + \varepsilon_4 V_d(\ell, \pi-\phi-\phi_0) e^{jk\ell \cos(\phi+\phi_0)}] \qquad (3.30)$$

where

$$\varepsilon_2 = \begin{cases} 1 & \text{for } |\phi| < \phi_0 \\ 0 & \text{otherwise} \end{cases},$$

$$\varepsilon_3 = \begin{cases} 1 & \text{for } -\frac{\pi}{2} < \phi < \pi+\phi_0 \\ 0 & \text{otherwise} \end{cases},$$

$$\varepsilon_4 = \begin{cases} 1 & \text{for } -\pi-\phi_0 < \phi < \frac{\pi}{2} \\ 0 & \text{otherwise.} \end{cases}$$

The terms $\varepsilon_2, \varepsilon_3, \varepsilon_4$ account for the shielding of the sources by the horn walls. The resultant pattern is finite along the shadow boundaries provided that cylindrical-wave diffraction coefficients are used. Russo *et al.* (1965) were the first to use this approach for the pyramidal horn. A more comprehensive analysis was given by Yu *et al.* (1966) where the coupling between the walls was considered in some detail. Better agreement was obtained with experiment in the far sidelobe region at the expense of considerably greater mathematical computations. For development purposes, first order diffraction effects given by (3.30) are sufficiently accurate for typical horn antennas.

The far-field radiation pattern can be found, as before, by the aperture field method. The cylindrical-wave in the aperture, however, considerably complicates the resulting expressions since the aperture plane is not on a surface of constant phase. If the condition $\frac{b^2}{4\ell^2} << 1$ holds, then we may approximate the aperture field by a plane-wave distribution with a quadratic phase error (Collin and Zucker, 1969). Fig. 3.13 compares the aperture field theory using this approximation (results obtained from Wolff, 1966) with (3.30) using the GTD in the region near the forward axis for a range of horn sizes. The distance ℓ is fixed and b is varied. We note that there is good agreement between the two methods which tends to improve with decreasing values of b. Since the GTD approach makes no assumption regarding the phase error of the field in the aperture, it is to be preferred for large values of b. It also gives a simpler formulation

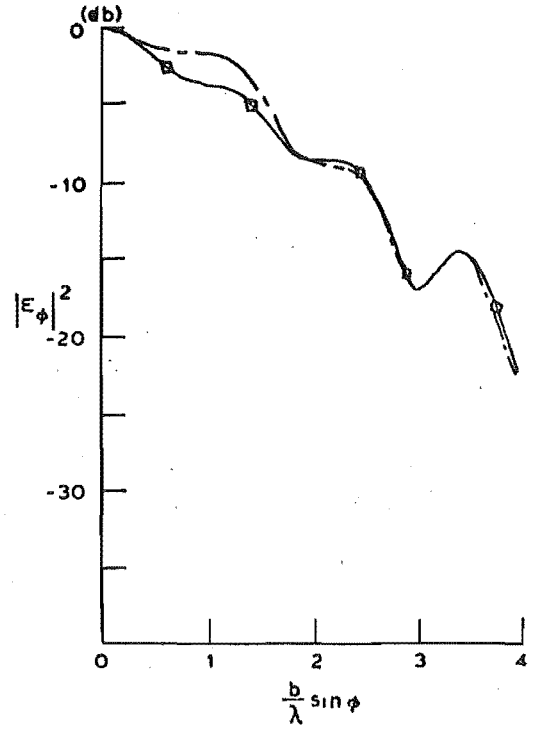

(a) $\frac{b^2}{4\ell\lambda} = 1$

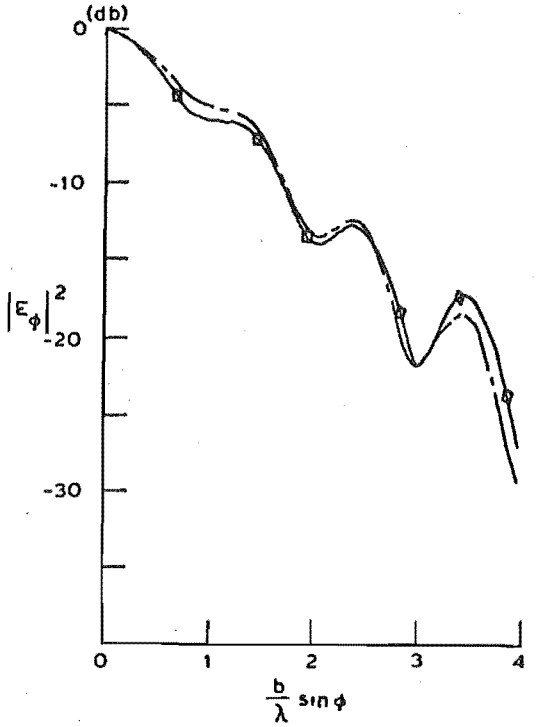

(b) $\frac{b^2}{4\ell\lambda} = \frac{3}{4}$

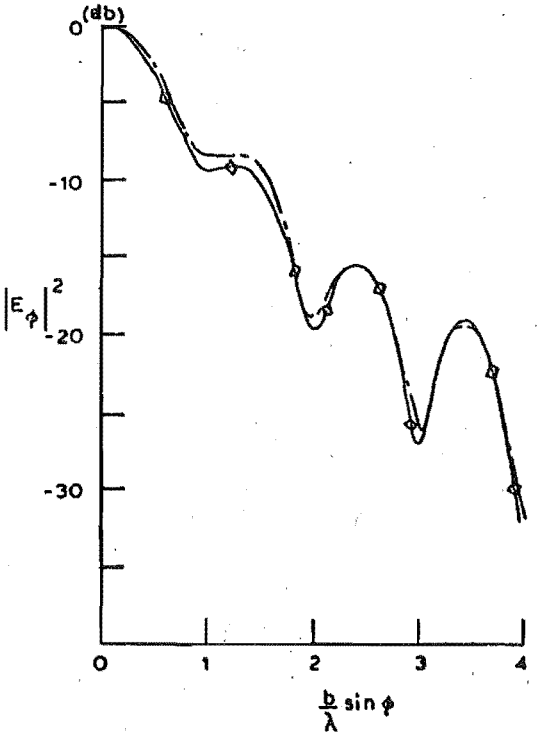

(c) $\frac{b^2}{4\ell\lambda} = \frac{1}{2}$

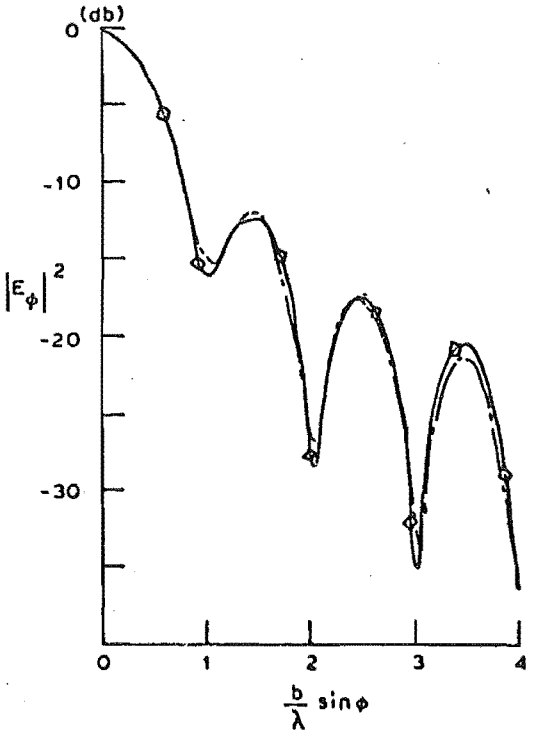

(d) $\frac{b^2}{4\ell\lambda} = \frac{1}{4}$

Fig. 3.13 Comparison between GTD and aperture field method for various horn sizes.

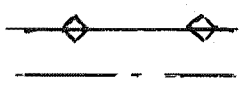

Aperture field

GTD

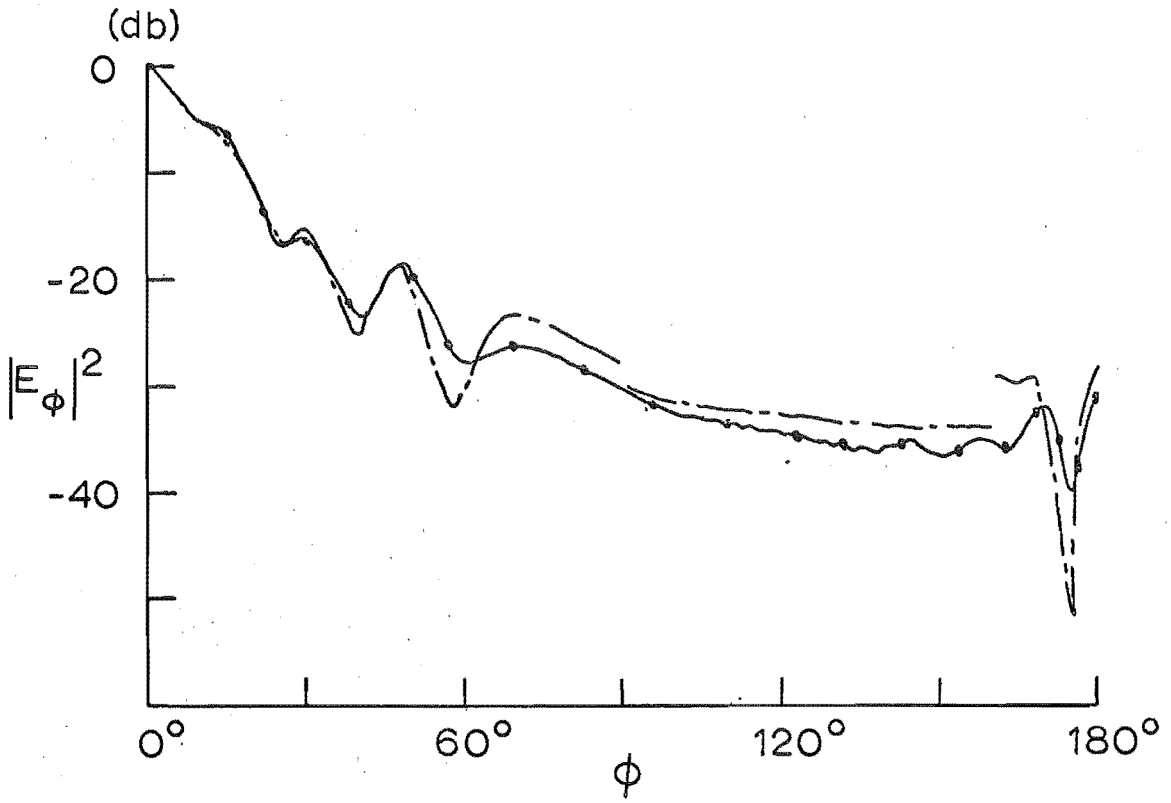

Fig. 3.14 E-plane of pyramidal horn

$\ell = 8.56\lambda$, $\phi_0 = 15^\circ$.

Measured

GTD

for the far-field.

Fig. 3.14 gives the measured E-plane radiation pattern for a typical pyramidal horn compared with the GTD formulation of (3.30). This simple mathematical expression can be seen to give a satisfactory result on which to develop theoretical methods of radiation pattern control.

3.32 Radiation in other planes

For radiation into other planes, care must be taken in accounting for the diffraction along the H-plane edges. The H-plane radiation pattern is deduced as discussed in 3.12 for the H-plane sectoral horn, where the radial component of the magnetic field must be considered. Yu and Rudduck (1969) have calculated the H-plane pattern of a pyramidal horn showing the contribution of rays from the E-plane edges, with and without the finite length effect of these edges.

For planes other than the principal planes, it will be necessary to account for the oblique incidence to the H-plane edges. In addition the slope-wave term may be of importance. There has not appeared to date a general analysis of radiation from a pyramidal horn using edge diffraction methods.

3.4 RADIATION PATTERN CONTROL

We now attempt to modify the radiation patterns considered in the previous sections by shaping the antenna edge at the critical points of radiation. A null placement method is given in 3.41 by a stepped edge antenna, and in 3.42 we discuss flanged aperture horns. We conclude this section by briefly considering other methods of radiation pattern control of electromagnetic horns.

3.41 Null placement by a stepped edge

3.411 A quasi-two-dimensional problem

Consider the quasi-two-dimensional problem where the edge of a half-plane has a step structure of height σ at the origin as illustrated in Fig. 3.15. Let an incoming plane-wave illuminate the edge at grazing incidence, with the magnetic component of the field parallel to the z-axis. When $\sigma = 0$, the problem reduces to the half-plane and the far-field solution is given by (3.10), i.e.,

$$E_\phi^d = E_y \operatorname{Cosec} \frac{\phi}{2} \frac{e^{-jk\rho}}{\sqrt{8j\pi k\rho}} \quad , \tag{3.31}$$

where $\psi = \pi+\phi$ has been substituted into (3.10).

For $\sigma > 0$ the field is normally incident to the edge along $-\infty \leq z < 0$ and we consider the diffracted field, ${}^{A}E_\phi^d$, in the x-y plane from this portion of the screen to be given by one half of (3.31) since this section of edge exists on only half of the z-axis, i.e.,

$${}^{A}E_\phi^d = \frac{E_y}{2} \operatorname{Cosec} \frac{\phi}{2} \frac{e^{-jk\rho}}{\sqrt{8j\pi k\rho}} \tag{3.32}$$

Similarly we have for the diffracted field, ${}^{B}E_\phi^d$, for the edge along $0 < z \leq \infty$ at $x = \sigma$

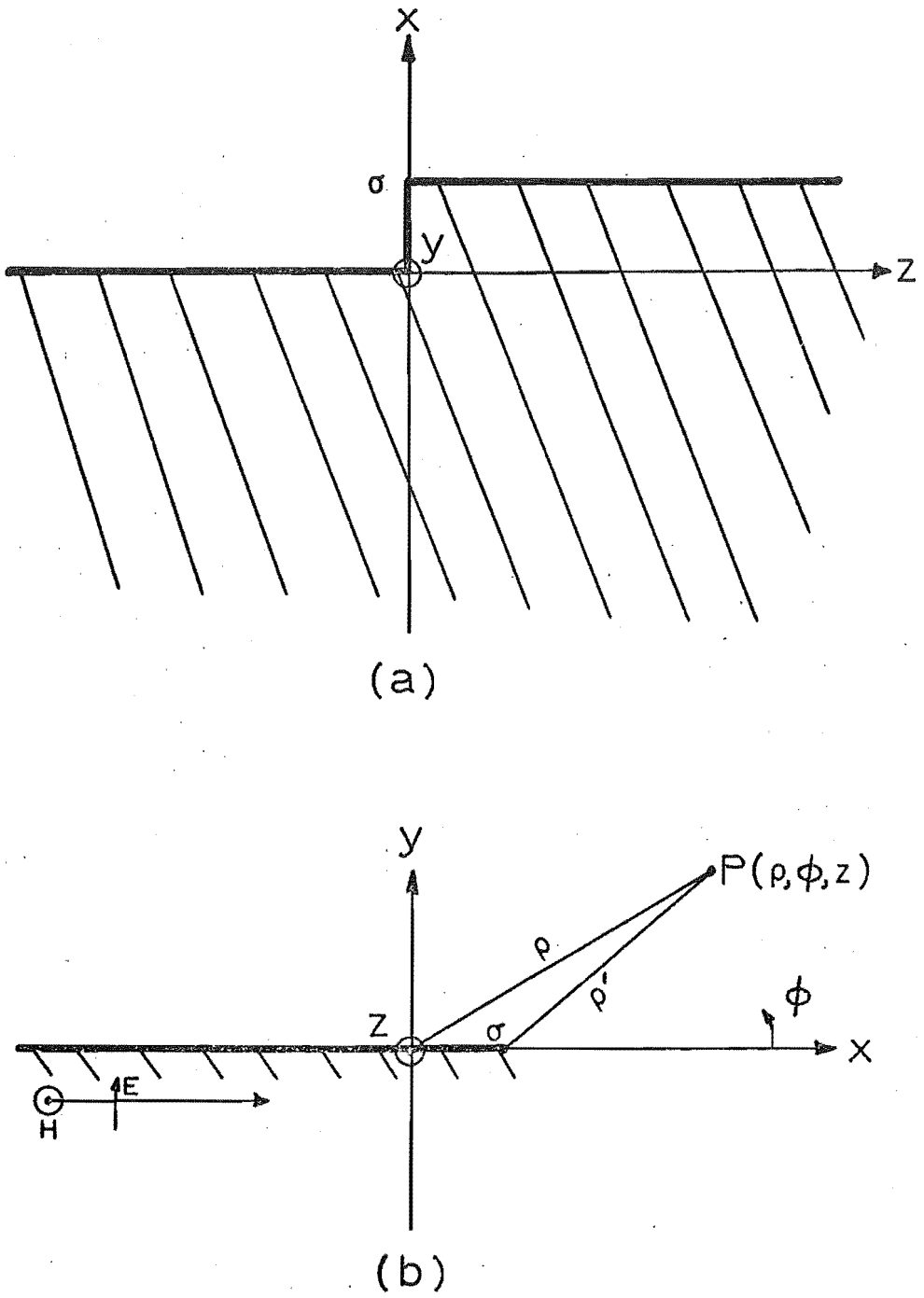

Fig. 3.15 Modified half-plane

$$B_{E_\phi}^{d} = \frac{E_y}{2} \operatorname{Cosec} \frac{\phi}{2} \frac{e^{-jk\rho'}}{\sqrt{8j\pi k\rho'}} \; e^{-jk\sigma}, \tag{3.33}$$

where we have referred the phase of the incident plane-wave to the origin. For the element of edge along the x-axis, the incident field is at grazing incidence to the edge. It was shown in 2.242 that for this condition the incident wave is not disturbed by the edge. Thus the total diffraction effect is given by the two line-sources given by (3.32) and (3.33). Adding these sources in the far-field in the x-y plane, and making the usual far-field assumptions, we obtain the resultant radiation pattern, E_ϕ^d, as

$$E_\phi^d(\rho,\phi) = \frac{E_y}{2} f(\phi) \left[1 + e^{-jk\sigma(1 - \operatorname{Cos} \phi)}\right] \frac{e^{-jk\rho}}{\sqrt{8j\pi k\rho}} \; , \tag{3.34}$$

where σ is expressed in terms of wavelengths and $f(\phi) = \operatorname{Cosec} \frac{\phi}{2}$. It can readily be shown that nulls will occur in (3.34) when

$$\phi = \operatorname{Cos}^{-1} \left[1 - \frac{n\lambda}{2\sigma}\right]; \quad n \text{ odd}. \tag{3.35}$$

Fig. 3.16 shows the placement of nulls with variation in σ, where it is seen that a multiplicity of nulls is possible with increasing values of σ. Also, as the angle decreases and σ increases, the method becomes less frequency sensitive.

If the wave is not at grazing incidence to the half-plane, then, by the same procedure, null placement in the x-y plane is found to be given by

$$\phi = \operatorname{Cos}^{-1} \left[\operatorname{Cos} \alpha - \frac{n\lambda}{2\sigma}\right]; \; n \text{ odd}, \tag{3.36}$$

where α is the angle of incidence to the half-plane.

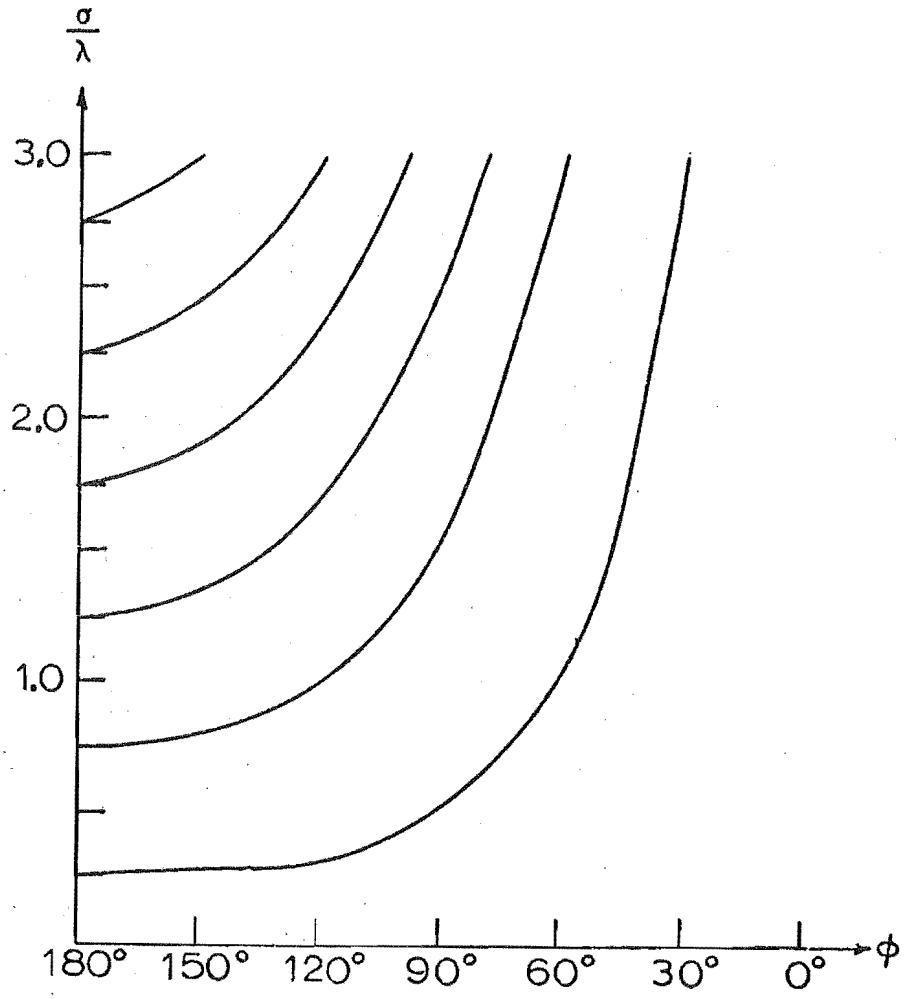

Fig. 3.16 Null-placement by modified half-plane

For the element of edge along the x-axis, the incoming field is no longer at grazing incidence to the edge. This section of the edge will then scatter the incoming wave, giving rise to radiation in other planes. The problem is now a three-dimensional one which can be attempted by the equivalent edge current method. In this chapter we restrict ourselves to the x-y plane and ray tracing methods.

An attempt has been made by Budin (1968) to evaluate the diffraction effect of stepped fences using the Kirchoff-Fresnel diffraction theory approach. (This approach is similar to the aperture field method.) He explains the diffraction effect from

the clothoid representation of the Fresnel integral. Our approach for the single stepped edge in Fig. 3.15 is, however, more direct, simple, and readily allows a physical interpretation

3.412 Application to H-plane sectoral horn

The method of null placement described in 3.411 is directly applicable in the E-plane of an H-plane sectoral horn by shaping the mid-point of the E-plane edges as in Fig. 3.15. This can be achieved either by cutting out the horn wall as in Fig. 3.17, or by placing metal plates on the outside walls perpendicular to the E-plane.

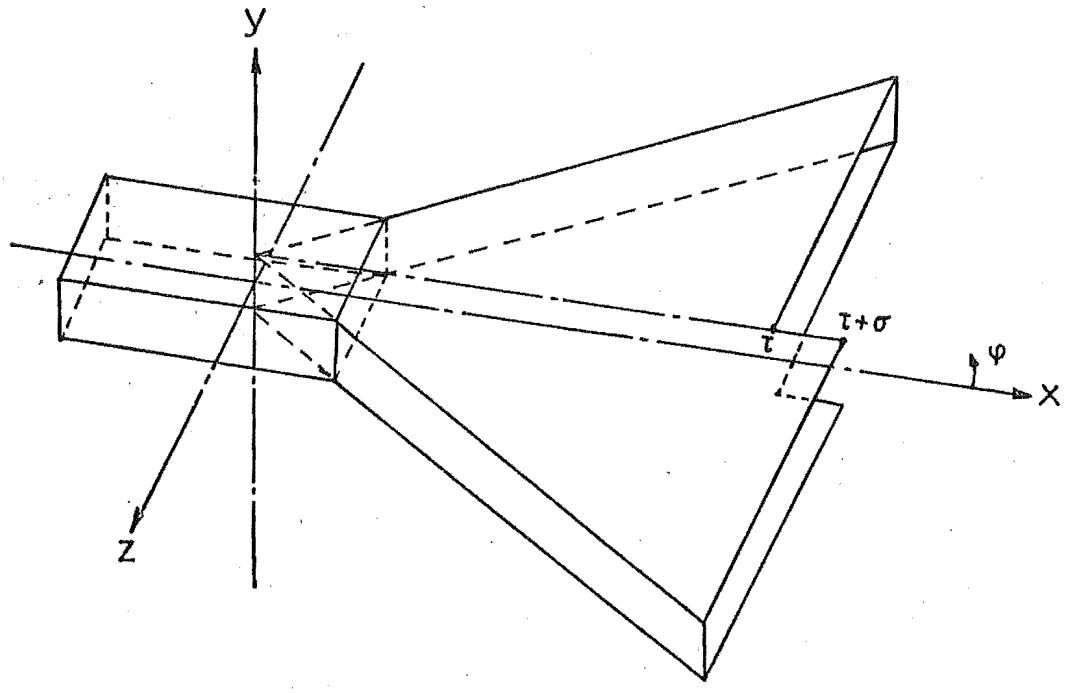

Fig. 3.17 Stepped E-plane edge H-plane sectoral horn

The latter method is more flexible as it allows for the value of σ to be altered by shifting the position of the plates.

From the parallel-plate waveguide model of Fig. 3.3 we can see that for $|\phi| \geq \frac{\pi}{2}$ the E-plane radiation pattern from the stepped edge horn is given directly by (3.34) for the edge diffraction method without coupling terms. For $|\phi| < \frac{\pi}{2}$ the only change in (3.34) is in $f(\phi)$ which, from (3.12), is

given by $\frac{j2kd}{u}$ Cos $\frac{\phi}{2}$ Sin u. Thus null placement in the E-plane of an H-plane sectoral horn is given directly from Fig. 3.16.

Since the higher order terms are not at grazing incidence to the edge they will not, in general, place nulls in the same positions given by the incident wave. The higher order terms, therefore, will give a component of field at nulls given by the incident wave. We could not expect any approximate theory to give a satisfactory estimate of the level of the null. In practice, we have found that a reduction of 15-20 db is readily obtained at the desired angle. Reduction of up to 30 db has been achieved but the level of the null is very sensitive to the positioning of the metal plates. A more important attribute of the theory is the accurate prediction of the position of the nulls. Fig. 3.18 gives two typical results. It is seen that the measured pattern gives the nulls in the positions as predicted in Fig. 3.16. Note that the null placement is independent of the horn length, provided the latter is not excessively small, i.e., less than a wavelength. In Fig. 3.18(a) we have plotted the GTD result with the first coupled rays between the plates. As we found in Fig. 3.5 for the same horn, GTD without coupling terms gave a better representation of the E-plane radiation pattern. The addition of the coupling terms appears to be incorrect for the basic horn, so we will not compute coupling terms for the remaining results where this horn is used for experimental verification. For horns following the parallel-plate pattern more closely, inclusion of the higher order terms will give better agreement with experiment.

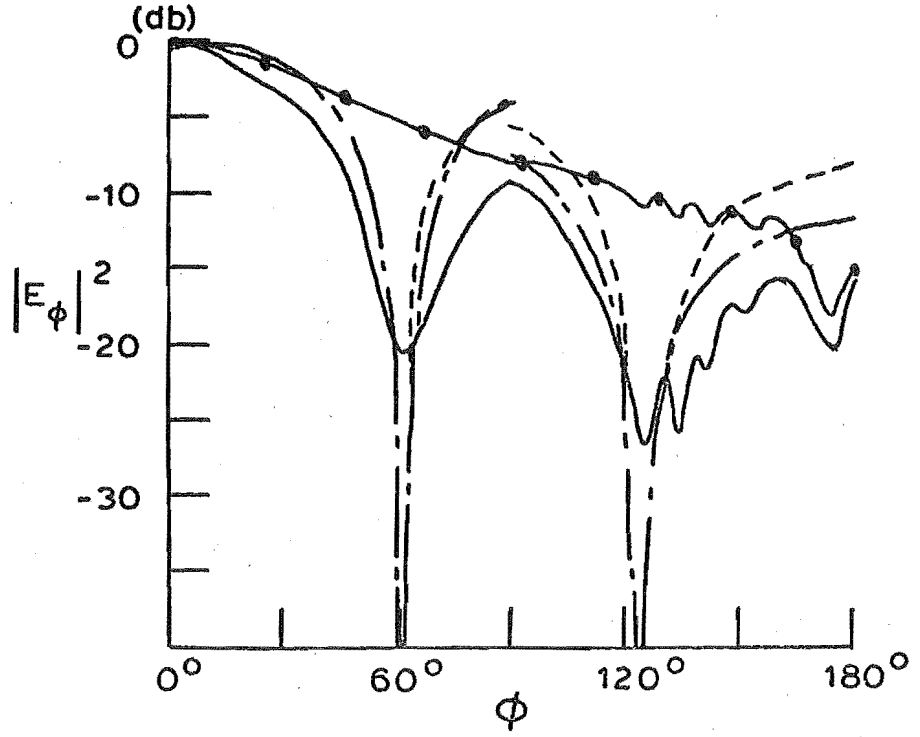

(a) $\sigma = 0.95\lambda$

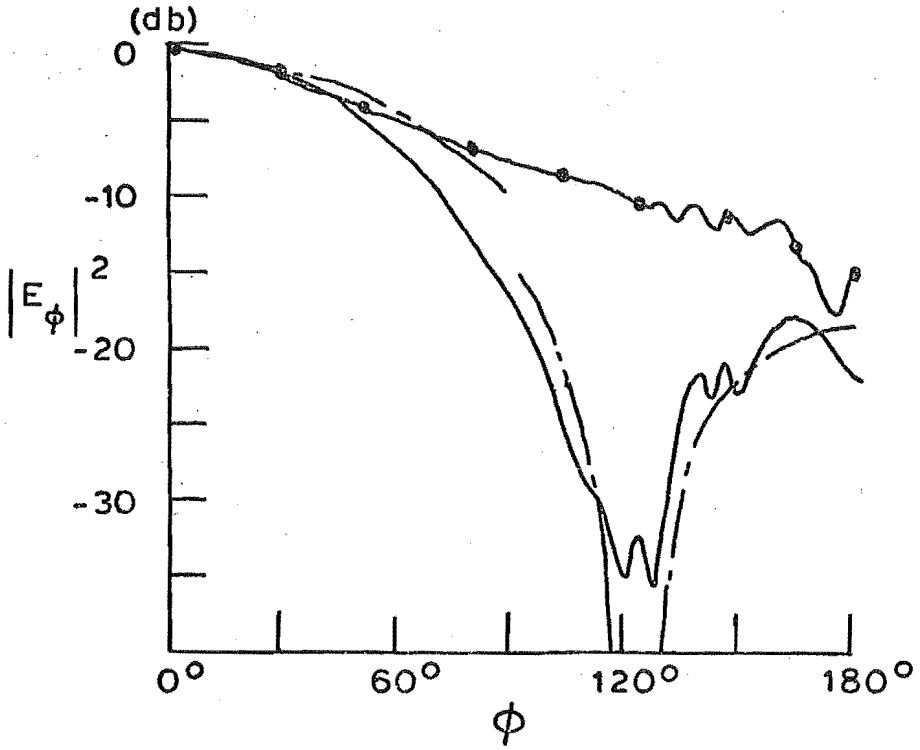

(b) $\sigma = 0.32\lambda$

Fig. 3.18 E-plane radiation pattern of H-plane sectoral horn
$d = 0.3\lambda$

—●—●— unperturbed pattern] Measured
——— with perturbation]

——·—— GTD without coupling term] with perturbation
- - - - - - - GTD with first coupling term]

Measurements in the H-plane indicated that shaping the E-plane edges had little effect in this plane. Fig. 3.19 gives the H-plane pattern for the above horn with and without a stepped edge.

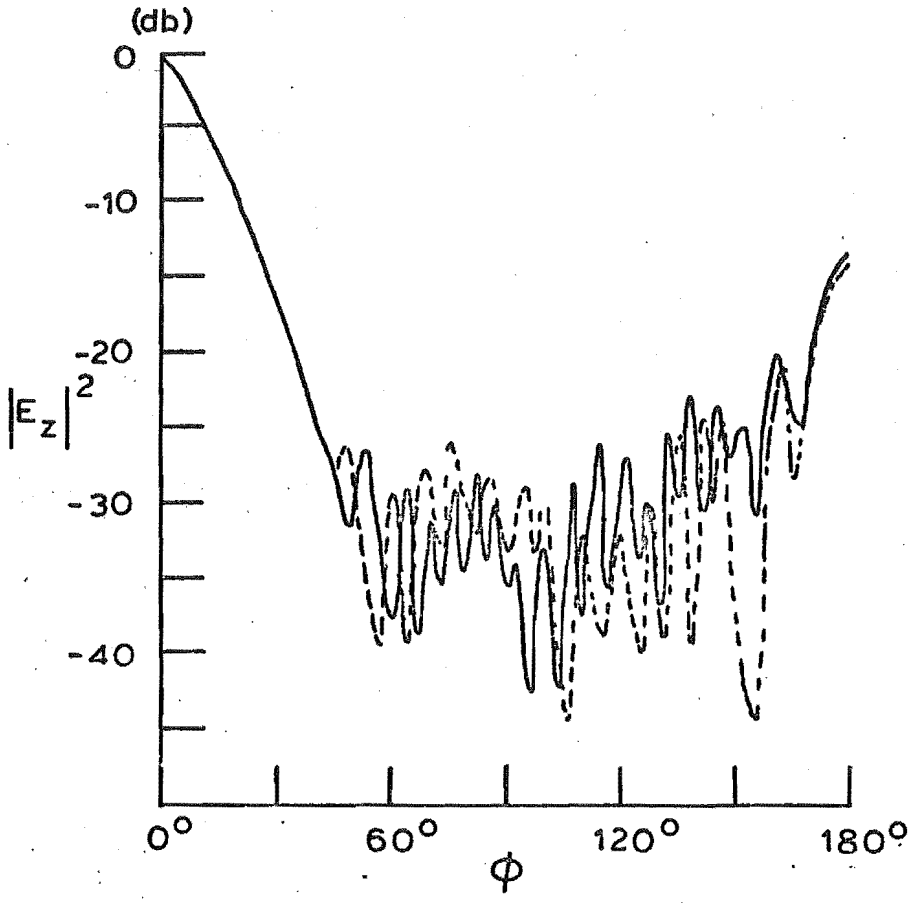

Fig. 3.19 H-plane of H-plane sectoral horn

——————— σ = 0

Measured

- - - - - - - - σ = 0.95λ

We have shown that, theoretically, the stepped edge for grazing incidence to the screen does not increase the amount of diffracted rays since the field is at grazing incidence to the edge. The only effect is that of the displacement of the edge resulting from the step. We can argue qualitatively that this will have little effect on the H-plane radiation pattern.

Fig. 3.2 illustrates the diffraction from the E-plane edges. If the step to these edges is applied as in Fig. 3.17 it will change the phasing between rays from the displaced sections as in the E-plane. However, from the diffraction mechanism shown in Fig. 3.2, we can see that there will be no rays common to each section for planes other than the E-plane because of the conical diffraction. Therefore we would not expect any significant change in the radiation pattern of these planes for a stepped E-plane edge. The H-plane is easily measured to test this argument, but other planes cannot be so readily measured.

The on-axis gain of the H-plane sectoral horn for values of σ up to 3λ remained within ½ db of the unperturbed horn gain. Thus the effect on gain is insignificant for practical values of σ.

3.413 Application to E-plane sectoral horn

Consider the E-plane sectoral horn with the stepped edge at the midpoint of the H-plane edges as in Fig. 3.20(a). The parallel-plate waveguide model is given in Fig. 3.20(b) for the H-plane radiation pattern. This problem is similar to the modified half-plane of Fig. 3.15. The solution, in the (s,φ,y') coordinate system of Fig. 3.20(b), for the radiation field, ${}^{\tau}E_{y'}$, at $x = \tau$ for $|\varphi| < \frac{\pi}{2}$ using the GTD without coupling terms, is given (by similar arguments for the modified half-plane solution in 3.411) by one-half of (3.26), i.e.,

$$ {}^{\tau}E_{y'} = f(\varphi)\ 4E_0\ \frac{e^{-jks}}{\sqrt{8j\pi ks}}\ , \qquad (3.37) $$

where

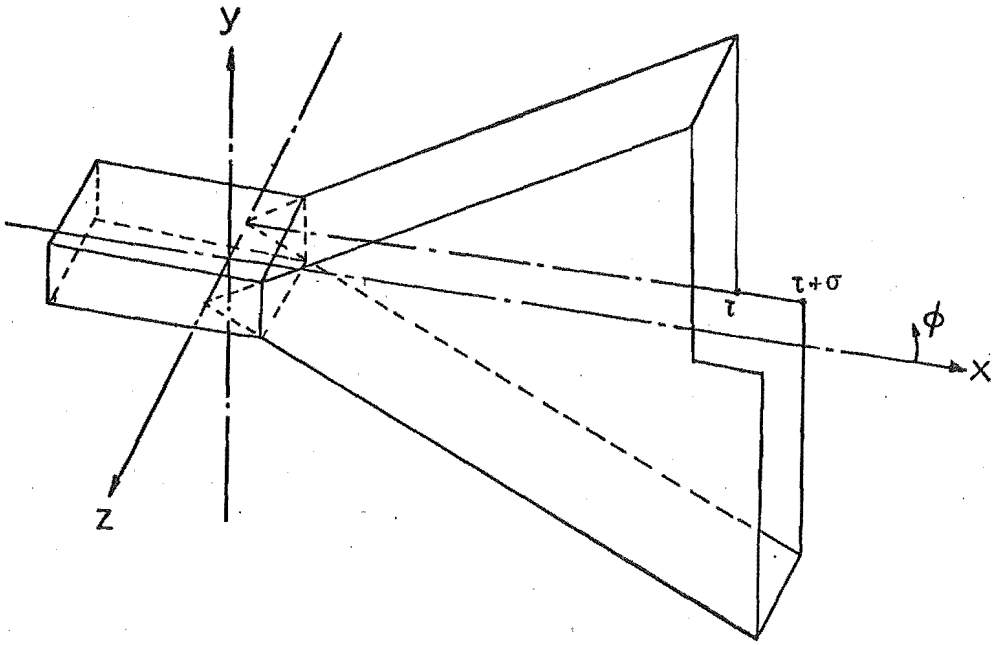

(a)

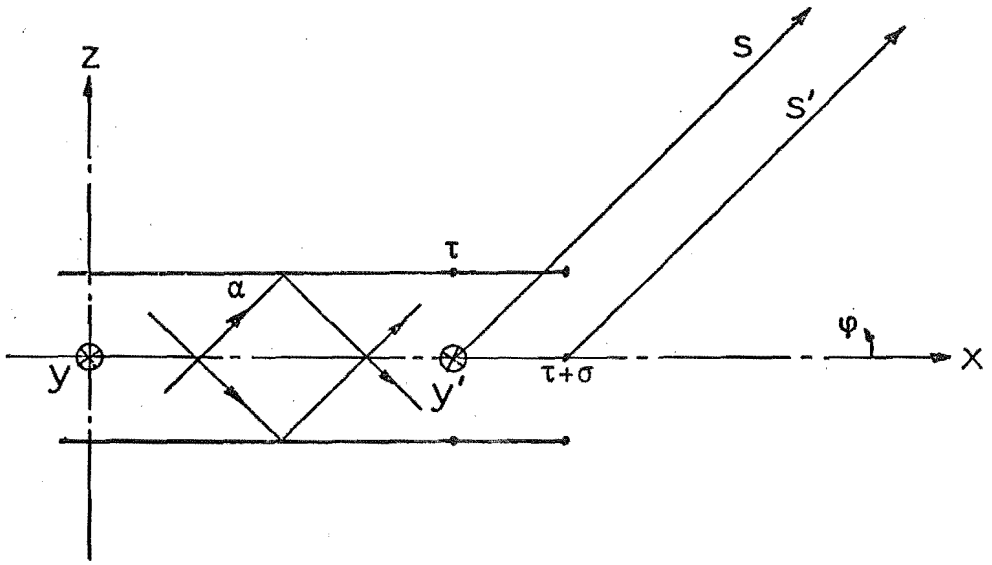

(b)

Fig. 3.20 (a) Stepped H-plane edge E-plane sectoral horn
(b) Parallel-plate waveguide model for H-plane

$$f(\varphi)\Big|_{|\varphi| < \frac{\pi}{2}} = \frac{\text{Cos } u \text{ Cos } \frac{\varphi}{2} \text{ Sin } \frac{\alpha}{2}}{\text{Cos } \alpha - \text{Cos } \varphi} .$$

The progression of energy along the guide for the TE_{10} mode is at the group velocity, v_g, given by c Cos α, where c is the velocity of light. Referring the incident mode phase to the point x = τ in Fig. 3.20(b), we have for the radiation field, ${}^{\tau+\sigma}E_{y'}$ at x = $\tau+\sigma$ for $|\varphi| < \frac{\pi}{2}$ from (3.37)

$${}^{\tau+\sigma}E_{y'} = f(\varphi)4E_0 \frac{e^{-j\beta ks'}}{\sqrt{8j\pi ks'}} e^{-j\beta k\sigma \text{ Cos } \alpha} \qquad (3.38)$$

The resultant far-field, $E_{y'}$, from (3.37), (3.38) is

$$E_{y'} = f(\varphi)4E_0[1 + e^{-j\beta k\sigma(\text{Cos } \alpha - \text{Cos } \varphi)}] \frac{e^{-j\beta ks}}{\sqrt{8j\pi ks}} , \qquad (3.39)$$

from which null positions are given by

$$\varphi = \text{Cos}^{-1} [\text{Cos } \alpha - \frac{n\lambda}{2\sigma}] ; \quad n \text{ odd.} \qquad (3.40)$$

This is the same result given by (3.36) for a plane-wave incident at an angle α to the modified half-plane of Fig. 3.15. For $|\varphi| > \frac{\pi}{2}$ the only change in (3.39) is in the term $f(\varphi)$ which can be derived from (3.24).

Null placement for the plane under consideration will be mainly confined to forward directions since the unperturbed pattern given in Fig. 3.10 decays rapidly with increasing angle. An example is given in Fig. 3.21(a) with the appropriate null placement curves in Fig. 3.21(b) deduced from (3.40). The theoretical result accurately predicted the position of the null.

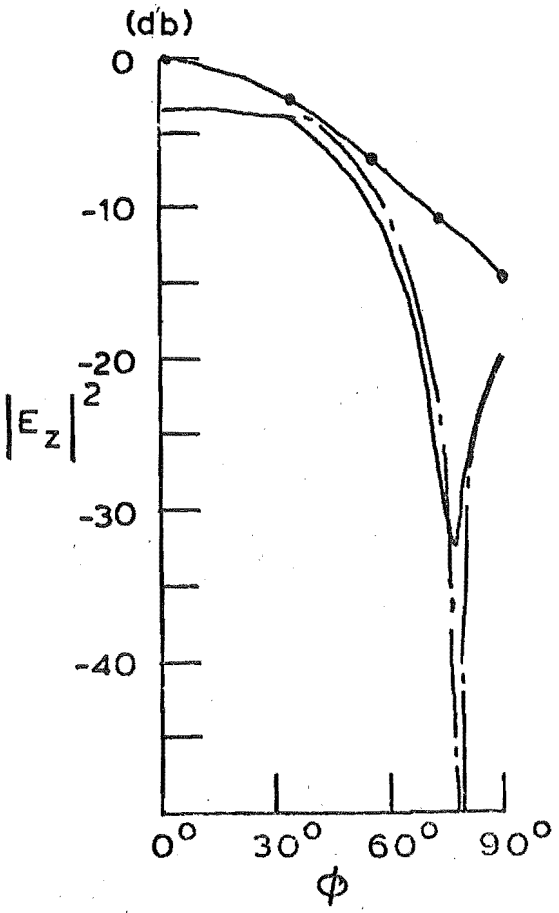

(a) H-plane radiation pattern of E-plane sectoral horn. $a = 0.8\lambda$

—●— $\sigma = 0$] Measured

——— $\sigma = 0.95\lambda$]

—·— $\sigma = 0.95\lambda$ GTD

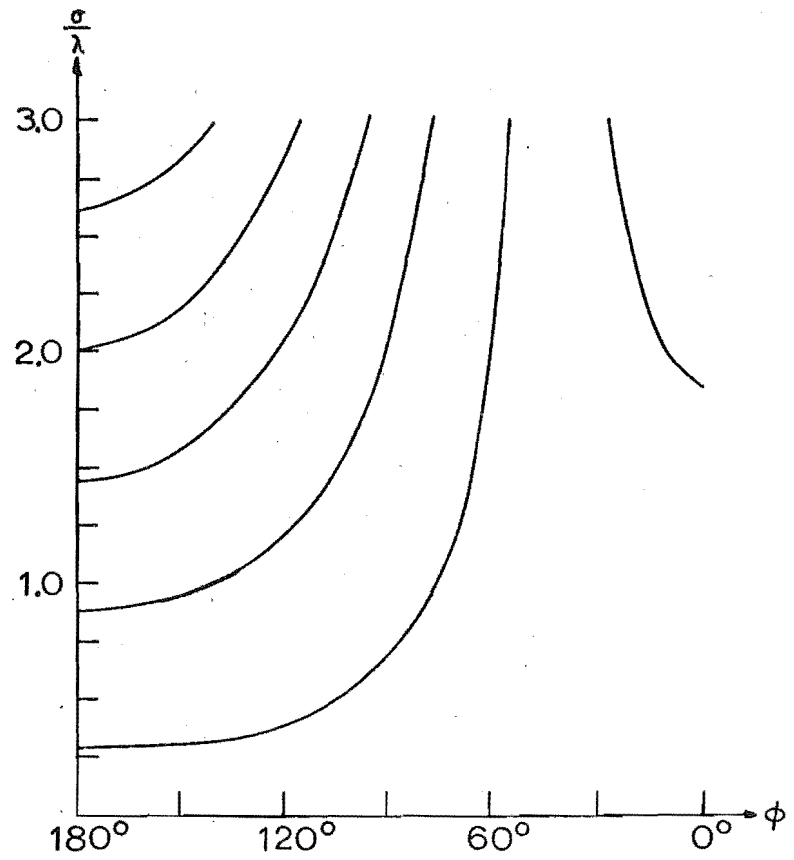

(b) Null-placement for $\alpha = 43^\circ$

Fig. 3.21

It will be seen from Fig. 3.21(b) that it is possible to place a null on the forward axis. This is a disadvantage of the method for this plane as it causes a loss of on-axis gain as seen with the example of Fig. 3.21(a). On-axis gain variation with σ is shown in Fig. 3.22.

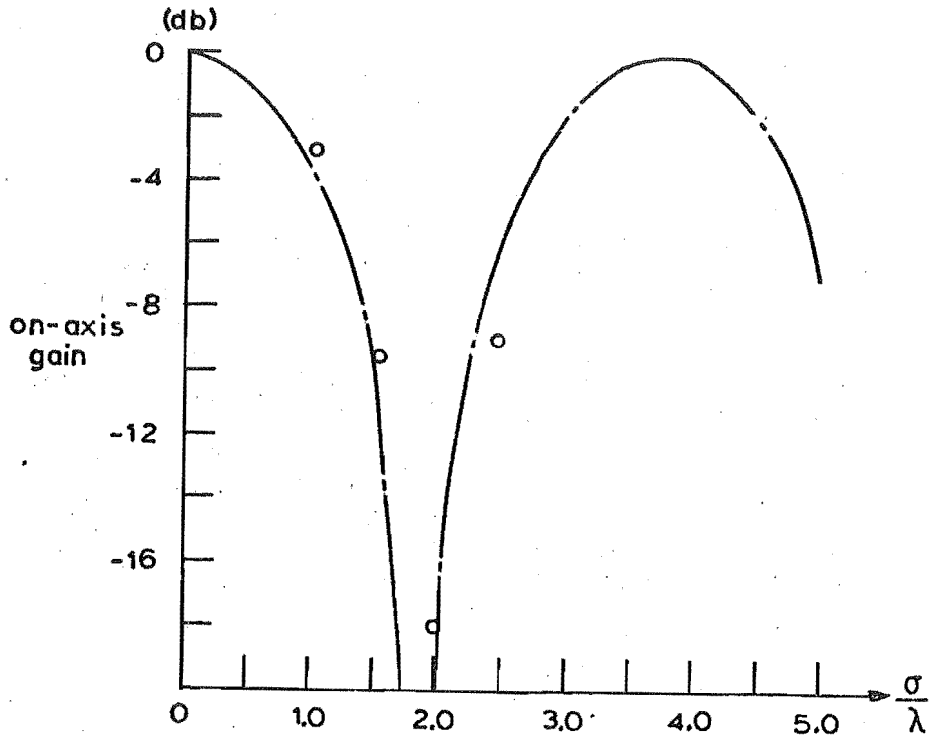

Fig. 3.22 On-axis gain of stepped edge E-plane sectoral horn

o measured values

——·—— GTD

Another disadvantage is that the incident field is not at grazing incidence to the edge along the x-axis (Fig. 3.20(b)) and this element of edge will scatter energy into other planes as discussed in 3.411. Only the E-plane can be readily measured to determine this effect. Fig. 3.23 gives the

corresponding E-plane radiation pattern for the stepped edge horn measured in Fig. 3.21(a).

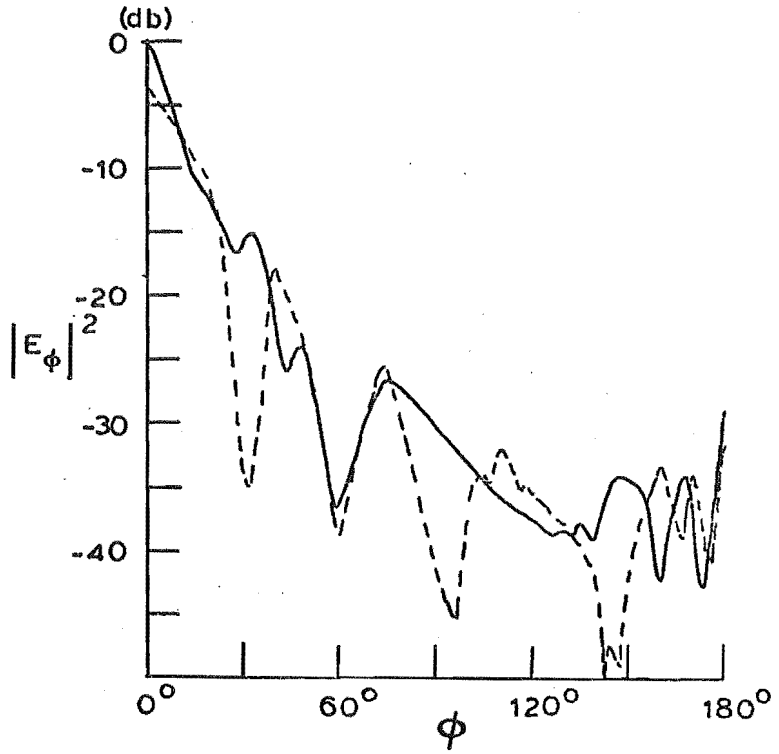

Fig. 3.23 E-plane radiation pattern of E-plane sectoral horn

——— $\sigma = 0$]
- - - - - - - $\sigma = 0.95\lambda$] Measured

The unperturbed pattern is also given. Although the stepped E-plane edges are seen to have affected the E-plane pattern, there has been no significant increase in radiation for this particular example.

3.414 Application to pyramidal horn

It was shown in 3.3 that the E-plane of a pyramidal horn can be given, to a good approximation, by edge sources situated at the midpoint of the E-plane edges together with the direct radiation from inside the horn. From the E-plane model of Fig. 3.12 we see that in the sector of the radiation

pattern $\frac{\pi}{2} \leq |\phi| \leq (\pi-\phi_0)$ only one of the edge sources is radiating into the far-field. The other source is shielded by a horn wall. In this sector we can place a null by shaping the midpoint of the E-plane edges as in Fig. 3.24(a). Fig. 3.24(b) gives the corresponding E-plane model. Since the illuminating field is at grazing incidence to the aperture edges, the position of the nulls can be obtained from Fig. 3.16 with the addition of ϕ_0 to account for the tilt of the E-plane walls to the x-axis. A typical result is given in Fig. 3.25(a).

For the remainder of the radiation pattern, the sources on both the E-plane edges contribute to the pattern. Since the phase centre is not in the plane of the sources for the E-plane pyramidal horn pattern as we had for the sectoral horns considered in 3.412 and 3.413, null placement ceases to be a simple function of ϕ_0 and σ. In addition, because of the phase error across the aperture, we will not get theoretical nulls where the actual field cancels completely. We computed radiation patterns of optimum horns for various values of σ but no consistent null placement characteristics could be discerned for $|\phi| < \frac{\pi}{2}$. It is necessary for each horn to be considered separately. Fig. 3.25(b) gives an example of null placement in the forward direction of a pyramidal horn.

When $|\phi| > (\pi-\phi_0)$ radiation is reduced with small values of σ. An example is given in Fig. 3.25(c). This region, however, is susceptible to scattering from the waveguide and associated feeding arrangement to the horn which will influence the final value of the front-to-back ratio.

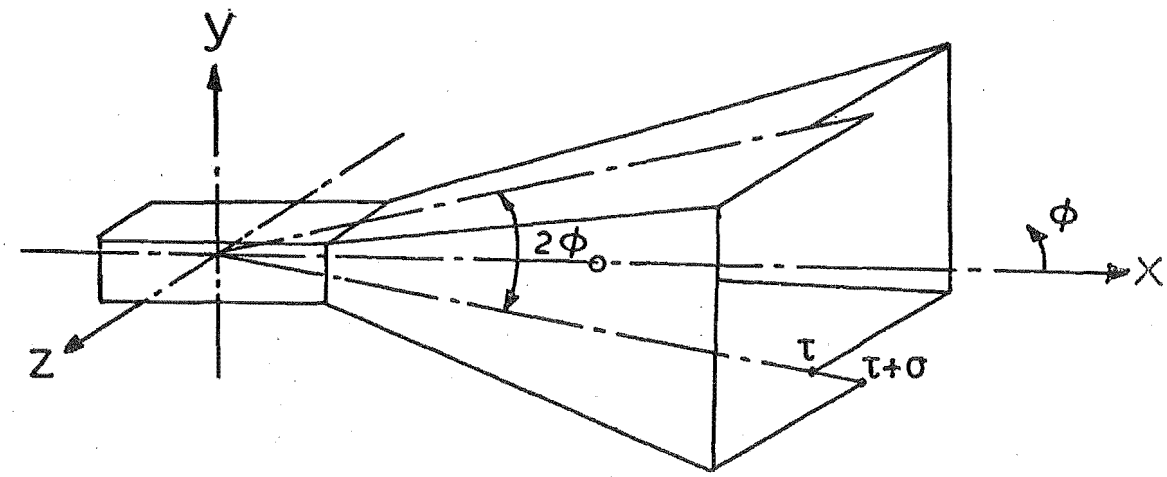

(a)

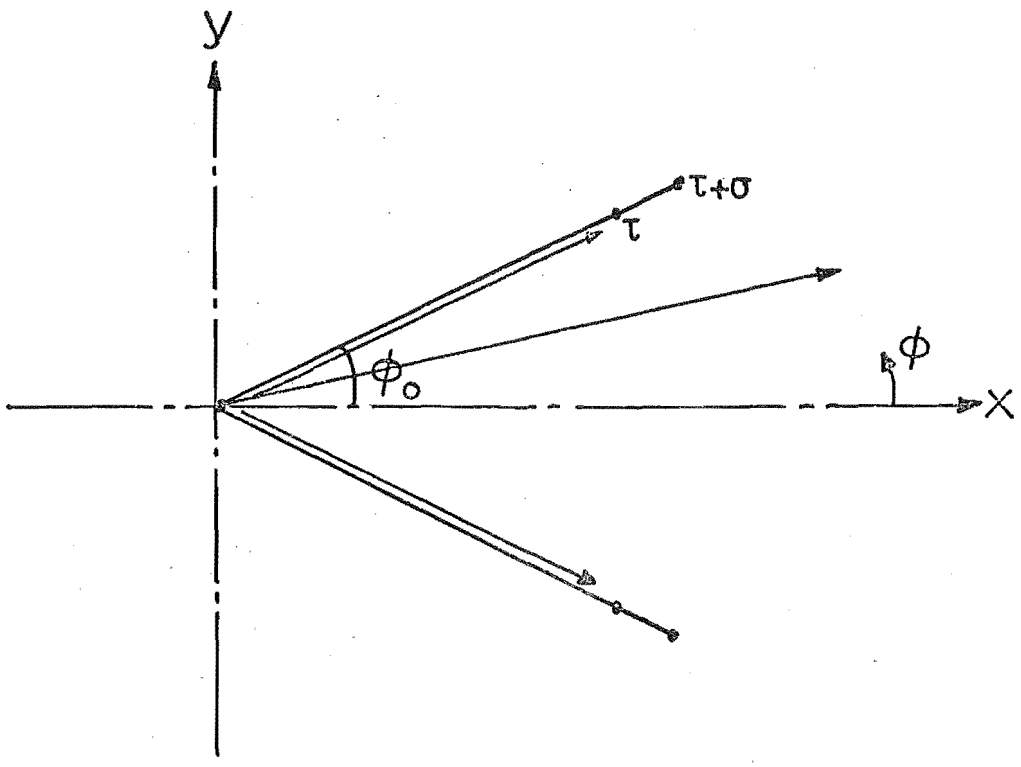

(b)

Fig. 3.24 (a) Stepped E-plane edge pyramidal horn

(b) E-plane model

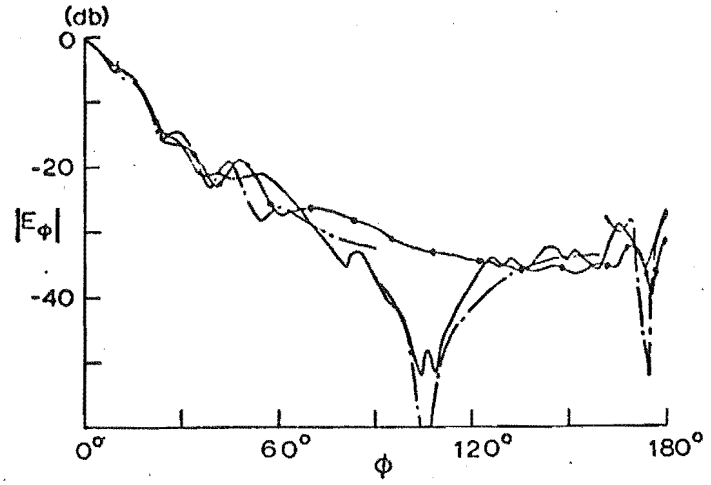

(a) $\sigma = 0.5\lambda$

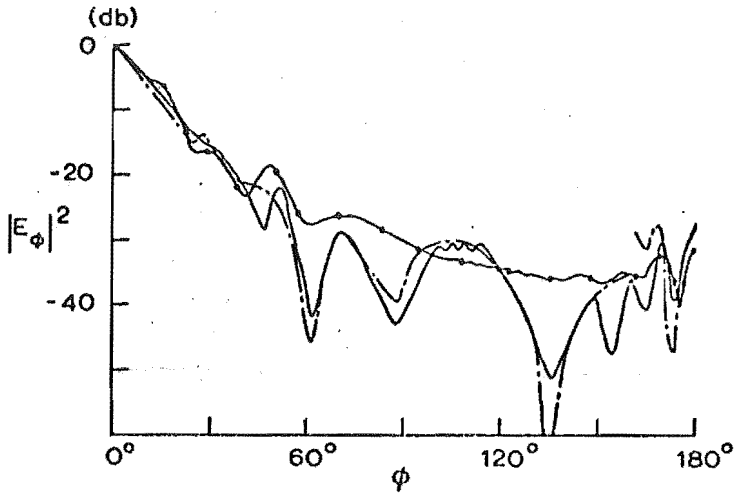

(b) $\sigma = 0.95\lambda$

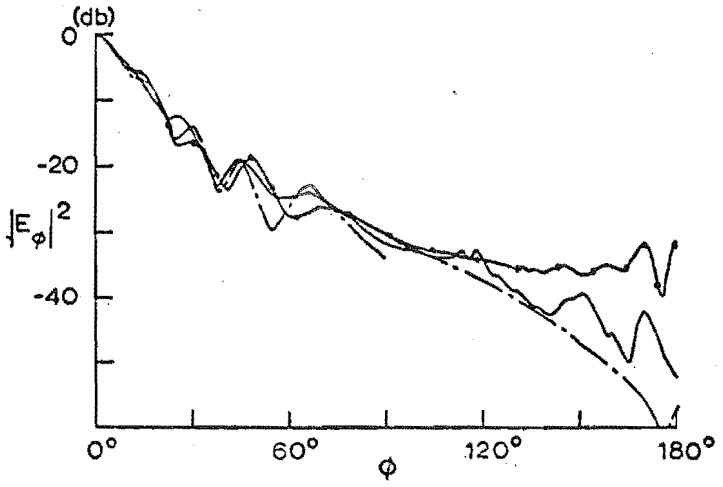

(c) $\sigma = 0.25\lambda$

Fig. 3.25 E-plane radiation pattern of pyramidal horn; $\tau = 8.56\lambda$, $\phi_0 = 15°$

—●—●— unperturbed pattern] Measured

——— perturbed pattern]

—— · —— GTD

The comments made in 3.412 regarding the effect in the H-plane of shaping the E-plane edges applies here. Measurements confirmed these comments. As with the H-plane sectoral horn, the on-axis gain of a stepped edge pyramidal horn is little affected for practical values of σ.

3.42 Flanged aperture horns

The effect on the radiation pattern of metal flanges attached to the aperture edges of horn antennas was originally investigated by Owen and Reynolds (1946) for the E-plane of a small H-plane sectoral horn. Experimental results were obtained with flanges attached to the long sides of the horn. They suggested that the effect of the flanges on the radiation pattern is similar to having a line-source at the edge of each flange. A limited study was made of this in a later paper by Butson and Thompson (1959) who also considered a flanged aperture waveguide and E-plane sectoral horn. Recently further work has been carried out on both E and H-plane sectoral horns, where the main contribution has been to investigate the effect of asymmetrical flanges, the position of the flanges from the open end of the horn, and the effect of flanges on the on-axial gain, (Nair and Srivastava, 1967; Koshy *et al.*, 1968).

All of the above work has been confined mainly to an experimental approach to shaping the forward sector of the radiation pattern. We will briefly discuss a theoretical approach to this problem using the GTD.

In a similar problem to the flanged horns we are about to consider, Thomas (1971) successfully used the GTD to design blinders attached to the aperture edges of horn-reflector type antennas.

3.421 H-plane sectoral horn

Consider the parallel-plate waveguide E-plane model with symmetrical flanges at the aperture shown in Fig. 3.26.

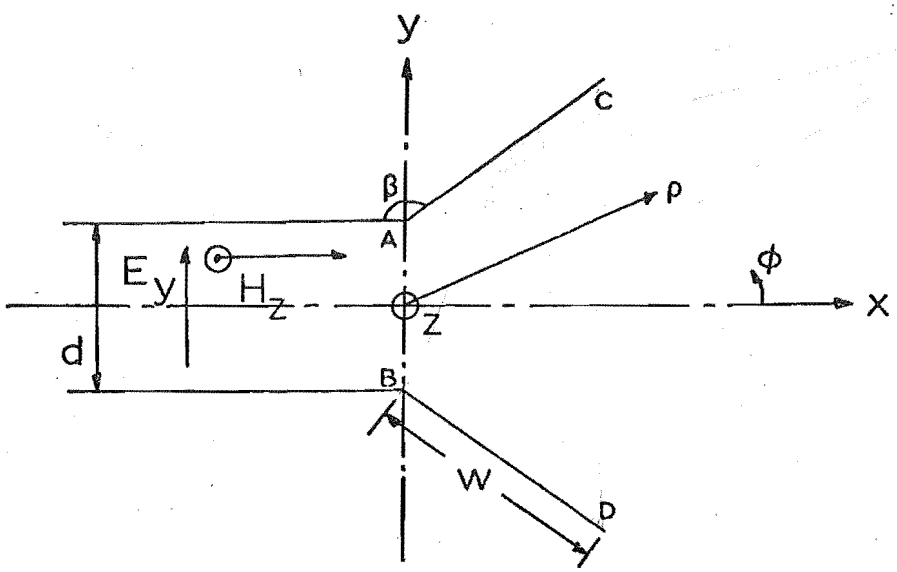

Fig. 3.26 Flanged aperture parallel-plate waveguide

As before, we begin by considering the upper half-plane in isolation. The incident plane-wave creates a line source at A which in turn gives cylindrical-wave diffraction at C. An infinite number of diffractions occur between A and C as we had for the coupling between two parallel plates. For the flanged half-plane, however, the slope-wave diffraction term from A-C and C-A is zero as we can see in (2.75) for magnetic polarization at grazing incidence. This allows all of the diffracted rays between A and C to be summed into a form of an infinite geometrical progression series. Thus we can readily show that the total diffracted far-field from A, ${}^{A}E_{\phi}^{d}$, for plane-wave incidence and with the complete set of coupled rays

between A and C, is given by

$$A_{E_\phi}^{d} = \left[D_N(\pi+\phi) + \frac{D_N(N\pi)\, V_{d2}(w,0)\, V_{dN}(w,\pi-\beta-\phi)}{1 - V_{d2}(w,0)\, V_{dN}(w,0)} \right] e^{\frac{jkd}{2}\mathrm{Sin}\ \phi} \cdot \frac{e^{-jk\rho}}{\sqrt{8j\pi k\rho}} \quad , \tag{3.41}$$

where

$$D_N(\Phi) = \frac{2\ \mathrm{Sin}\ \frac{\pi}{N}\ E_y}{N(\mathrm{Cos}\ \frac{\pi}{N} - \mathrm{Cos}\ \frac{\Phi}{N})} \ ,$$

$$\beta = (2 - N)\pi ,$$

the phase has been referred to the origin of the (ρ,ϕ,z) coordinate system, and the second postscript for the diffraction term refers to the wedge angle.

Similarly for the diffracted far-field from C, $C_{E_\phi}^{d}$, we have .

$$C_{E_\phi}^{d} = \frac{D_N(N\pi)\, V_{d2}(w,\beta+\phi)}{1 - V_{d2}(w,0)\, V_{dN}(w,0)}\ e^{jk(\frac{d}{2}\ \mathrm{Sin}\ \phi\ -\ w\mathrm{Cos}(\beta-\phi))}\ \frac{e^{-jk\rho}}{\sqrt{8j\pi k\rho}} \tag{3.42}$$

This formulation for the truncated wedge was given by Rudduck (1965), where V_{d2} is replaced by the more general V_{dM}; M being associated with the wedge angle.

The validity of taking all the higher order diffraction terms into account was shown by Yu and Rudduck (1967) for the strip under plane-wave illumination. Results comparable to the exact solution were achieved for strip widths as narrow as 0.25λ by using the exact half-plane solution for V_{d2} given by (2.36). (We would expect similar results for the truncated wedge problem by using the exact eigenfunction solution of (2.70) for V_{dN}.)

Another attempt to obtain the diffraction from close edges on perfectly conducting bodies was the iterative surface current density replacement technique of Hunter and Bates (1972). This approach does not give as accurate results as the above GTD method, as Hunter and Bates demonstrated for the strip. In addition, the amount of computer time is excessive compared to the GTD formulation, especially for widths greater than 0.5λ.

Returning to the flanged aperture parallel-plate waveguide illustrated in Fig. 3.26, we have sources at A and C given by (3.41) and (3.42). Ignoring coupling between the plates we have similar sources at B and D. Adding these four sources in the far-field gives us an approximation to the radiation pattern. Fig. 3.27 gives three examples to illustrate the comparison between theoretical and measured results. (For the theoretical results we have taken account of the finite length of the sectoral horn in the determination of where the edge sources operate in the far-field. Hence the nodes and anti-nodes near the back axis.) It is seen that good agreement is achieved, except for the example when $\beta > \frac{\pi}{2}$ where considerable error exists in some forward directions. This may be attributed to the neglected coupling between the flanges - especially the reflection of the edge sources at the opposite flange - not present when $\beta \geq \frac{\pi}{2}$. Coupling can be accounted for by the system of images between the flanges and higher order diffractions between the edges. This considerably complicates the analysis.

The effect of flange length w, and angle β has been thoroughly investigated by previous authors for forward directions of the radiation pattern. For backward directions

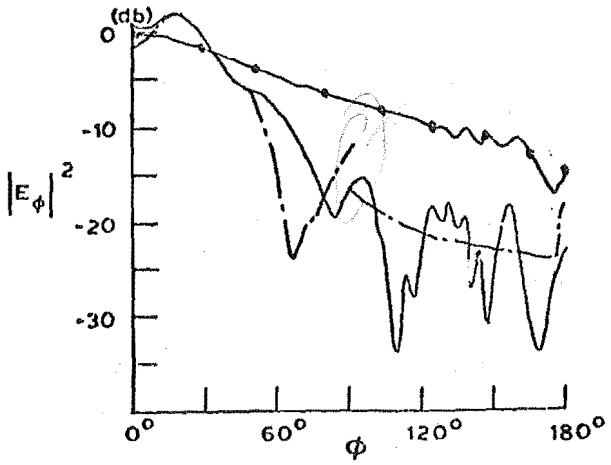

(a) $\beta = 135^\circ$

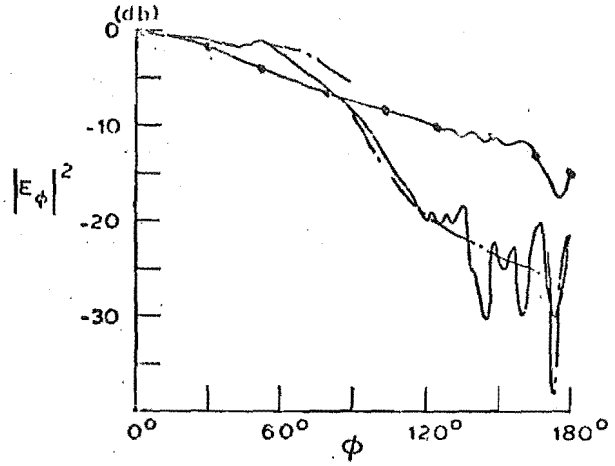

(b) $\beta = 90^\circ$

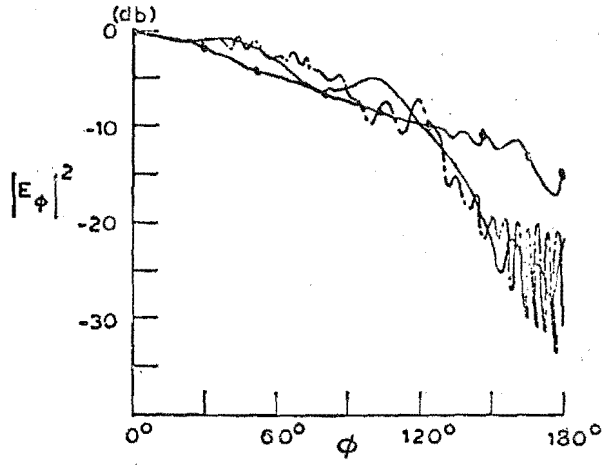

(c) $\beta = 45^\circ$

Fig. 3.27 E-plane of flanged aperture H-plane sectoral horn
$w = 2\lambda$, $d = 0.3\lambda$

unperturbed pattern
perturbed pattern
} Measured

GTD

a reduction in radiation level is achieved. The angle β determines the point where reduction begins, as we see in Fig. 3.27, and the flange length w the amount of reduction. For $w > \lambda$ a reduction of approximately 3 db is achieved in the side-lobe level affected by the flange every time w is doubled.

3.422 E-plane sectoral horn

Koshy *et al.* (1968) have found that flanges attached to the long sides of an E-plane sectoral horn are effective in beam shaping the H-plane radiation pattern provided the angle of the flanges is greater than 135^{o}. The diffraction mechanism for the flanged aperture H-plane is the same as in the H-plane of an H-plane sectoral horn illustrated in Fig. 3.6. Along the flange only the slope-wave term can exist since the field is electrically polarized. Thus for $\beta \geq \frac{\pi}{2}$, the flange edge source will be given entirely by slope-wave (second order) diffraction. Consequently this source will be weak and not capable of significantly affecting the forward radiation pattern. As the flange angle increases the coupling between the plates will give the major diffraction effect at the edges of the flanges, since the incident field from the opposite wall gives first order diffraction. This will increase with increasing values of incidence to the flange edge, i.e., it will increase with β. Thus we can appreciate that beam shaping in forward directions will only occur for large values of flange angle β.

Reduction of sidelobe levels in rearward directions will not be as important as for the H-plane sectoral horn, since the natural sidelobe level is low as we found in 3.2.

3.423 Pyramidal horn

For the pyramidal horn we can place flanges along the E-plane edges to reduce sidelobe radiation in the E-plane (Fig. 3.28).

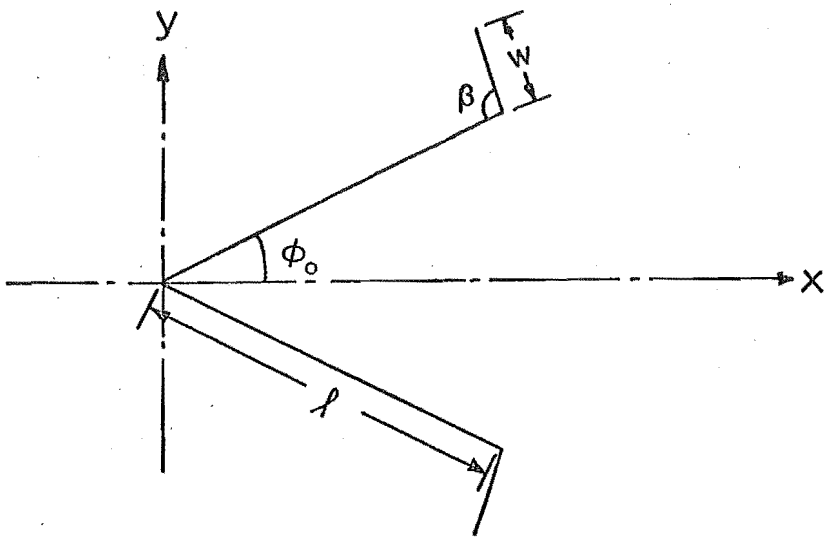

Fig. 3.28 Flanged E-plane of pyramidal horn

(The flanges have little effect on the main beam since the E-plane flare angle and length are the dominant factors, provided the horn length is considerably larger than the flange length.) Reduction of up to 6-8 db is achieved for a flange length of 2λ, as was the case for the H-plane sectoral horn results in Fig. 3.27. An example is given in Fig. 3.29 for a pyramidal horn. The theoretical result is obtained from (3.41), (3.42) with $D_N(\Phi)$ replaced by $V_{dN}(\ell,\Phi)$ for cylindrical-wave incidence at the aperture.

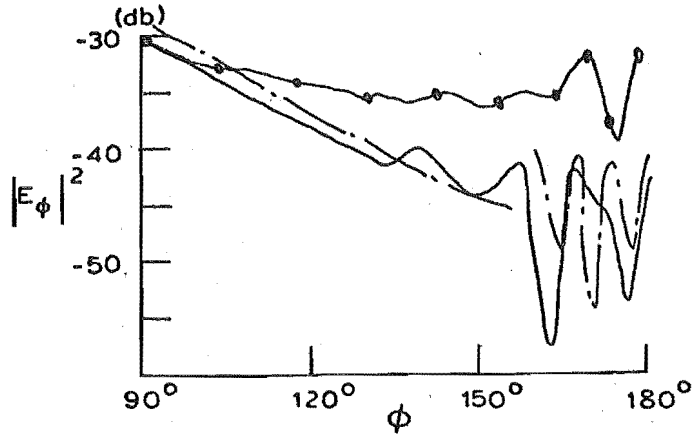

Fig. 3.29 E-plane of flanged pyramidal horn

$w = 2\lambda$, $\beta = 90^\circ$

unperturbed pattern] Measured

perturbed pattern]

GTD

Although greater sidelobe reduction is usually achieved with a stepped edge, the flanged aperture can give reduction over a wider sector of the radiation pattern as in Fig. 3.27(a). It also has the advantage of being relatively insensitive to frequency. We can readily combine both methods by having stepped edge flanges if further sidelobe reduction is required at particular angles. An example is given in Fig. 3.30 for a pyramidal horn. The position of the nulls is readily obtained from Fig. 3.16 with the addition of $\phi_0 + (\pi-\beta)$ from Fig. 3.28.

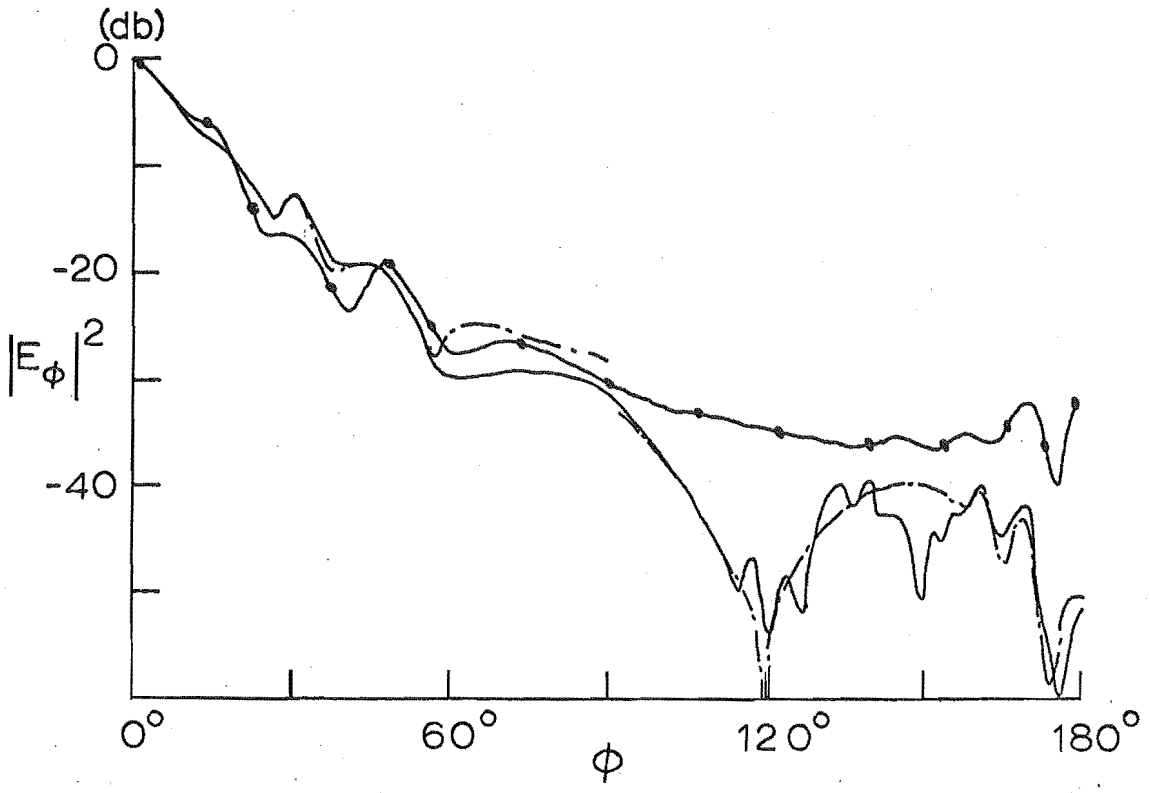

Fig. 3.30 E-plane of pyramidal horn with stepped edge flange
w = 2λ/1λ, i.e. σ = 1λ for stepped edge
β = 135°
(Figure Key as for Fig. 3.29)

3.43 Other methods of radiation pattern control in horns

We attempted radiation pattern control of the E-plane of a pyramidal horn with one or two narrow metal strips placed inside the horn and perpendicular to the E-field. Our intention was to obtain control in the forward direction of the pyramidal horn as the flanged aperture and stepped edge techniques had little effect in this region for this horn. A theoretical and experimental investigation did not give encouraging results and we have nothing of any significance to report. Some success has been reported using sectoral horns. Narrowing of the E-plane pattern of an E-plane sectoral horn has been achieved with a strip placed inside the horn parallel to the E-field (Silver, 1946c). The strip was of considerable

width and gave a troublesome mismatch. More recently (Nair *et al.*, 1969) a successful method has been found by placing two metal strips of half-wavelength in width at the aperture of the E-plane sectoral horn and perpendicular to the E-field. This gave improvement in both gain and beam-width, and slightly improved the matching. We suggest that these strips are behaving as Fresnel zone plates.

Reduction of the sidelobe levels in the E-plane of a pyramidal horn has been obtained by choke slots or a corrugated surface cut into the E-plane walls to reduce the illumination of the E-plane edges (Lawrie and Peters, 1966). This principle has also been applied to conical horns by several authors. A further reduction of the sidelobe level in the E-plane of a pyramidal horn is achieved if higher order modes are allowed to exist in the aperture (Bahret and Peters, 1968). A similar technique was used earlier by Potter (1963) for conical horns.

Dielectrics are often inserted in electromagnetic horns to alter the phase distribution at the aperture of the horn and hence control the radiation pattern (e.g. Quddus and German, 1961; Hamid *et al.*, 1970; Oh *et al.*, 1970). There are several disadvantages in the use of dielectrics. One which can directly interfere with the radiation pattern is the excitation of unwanted modes at the interface between the dielectric and the air in the horn. A phase-correcting method without resorting to dielectrics has been obtained for E-plane sectoral horns by varying the guide wavelength within the horn (Craddock, 1964). The technique gives a slight taper in the H-plane.

CHAPTER FOUR: SCATTERING FROM PARABOLOIDAL REFLECTORS

A clever man is wise and conceals everything,
but the stupid parade their folly.

Proverbs XII.16

Methods of evaluating the field scattered from a reflector antenna fall into three main categories:

induced current methods

aperture field methods

edge diffraction methods.

In the induced current method a rigorous solution to the electromagnetic scattering problem can be achieved if the integral equation for the currents on the reflector is solved numerically, (Rusch and Potter, 1970a). This approach is limited by the capacity of present-day computers. The problem becomes tractable if an estimate of the current distribution on the reflector is made. The best known approximation is that of physical optics (Silver, 1949a), where the current distribution is obtained from the tangential component of the incident magnetic field. The physical optics approximation is capable of providing fields which are in close agreement with experimental results in directions in front of the reflector. It is unreliable, however, in the shadow region because the currents flowing on the back of the reflector are neglected. A correction term to the physical optics current distribution to account for the effect of the Fresnel zone of the illuminating source and the curvature of the reflector has been derived by Kinber (1960) for an infinite reflector. Correction currents to account for the effect of the edges on

a finite reflector, i.e. the application of Ufimtsev's theory discussed in chapter 1, has also been proposed (Pogorzelski, 1967; Kinber and Tseytlin, 1971). We will briefly consider this edge correction current in 4.12 and physical optics in 4.11.

The aperture field method was discussed in chapter 3. This method yields identical results to the physical optics approximation on and near the reflector axis. It is accurate up to a few beamwidths from the axis.

Analysis by edge diffraction methods has found increasing application to reflector antennas (Plonsey, 1958; Kinber, 1961; 1962; Narbut and Khmel'nitskaya, 1970; Lewin, 1972). In all these cases, however, the reflector is treated as a two-dimensional problem (except for the field on the axis) and analysed by the ray tracing methods of the GTD. In 4.13 we consider scattering from a circularly symmetrical paraboloidal reflector as a three-dimensional problem in edge diffraction theory and show the conditions under which it may be reduced to a two-dimensional problem.

Radiation in the shadow region can be attributed to the field diffracted by the reflector rim (as will be shown in 4.13). Thus attempts at reducing radiation in this region have centred on modifications to the reflector geometry in the neighbourhood of the edge, such as castellating the edge (Cornbleet, 1967; Lewin, 1972), fitting chokes and shrouds to the edge (Koch, 1966), and placing a diffracting screen behind the reflector (Corona *et al.*, 1971). Cutting small holes near the edge to allow enough energy to leak through in anti-phase to cancel the rim diffraction has also been suggested (Sletten and Blacksmith, 1965). In 4.2 we investigate radiation pattern

control in the shadow region by changing the reflector edge geometry.

Control of the radiation pattern in the illuminated region is complicated by the presence of the feed. In practice, therefore, the type of feed and its effect is an integral part of the design. We will not consider radiation pattern control in the illuminated region, and a review on the extensive literature on the subject will not be attempted here.

4.1 THE PARABOLOIDAL REFLECTOR

4.11 The Aperture Field and Physical Optics Approximations

To evaluate the radiation field from the paraboloidal reflector by the aperture field or physical optics methods, we begin with the expression for the radiation zone from three-dimensional source distributions given by (2.13), i.e.

$$\underline{E}(\underline{r}) = -j\omega\mu \frac{e^{-jkr}}{4\pi r} \iint_{S'} \left[\sqrt{\frac{\epsilon}{\mu}}\, \underline{M}_{s'} \wedge \hat{r} + \underline{J}_{s'} - (\underline{J}_{s'}\cdot\hat{r})\hat{r}\right] e^{jkr'\cos\xi} dS' . \tag{4.1}$$

The approximate source distributions in (4.1) for both methods is obtained from the illuminating field based on geometrical optics and plane-wave boundary conditions at the reflector surface. If the illuminating field is from a vanishingly small source situated at the focus of the reflector, then, assuming that the reflector is in the far-field of the source and that its presence does not interfere with the source pattern, we can write the incident field, $\underline{E}_i$, $\underline{H}_i$, at the reflector surface as

$$\begin{aligned} \underline{E}_i &= [f_1(\xi,\psi)\hat{u}_\psi + f_2(\xi,\psi)\hat{u}_\xi] \frac{e^{-jk\tau_i}}{\tau_i} , \\ \underline{H}_i &= \sqrt{\frac{\epsilon}{\mu}}\, \hat{u}_\tau \wedge \underline{E}_i , \end{aligned} \tag{4.2}$$

where the (τ,ξ,ψ) coordinate system is defined in Fig. 4.1, $\tau_i = f \sec^2(\frac{\psi}{2})$, and f is the focal length of the reflector.

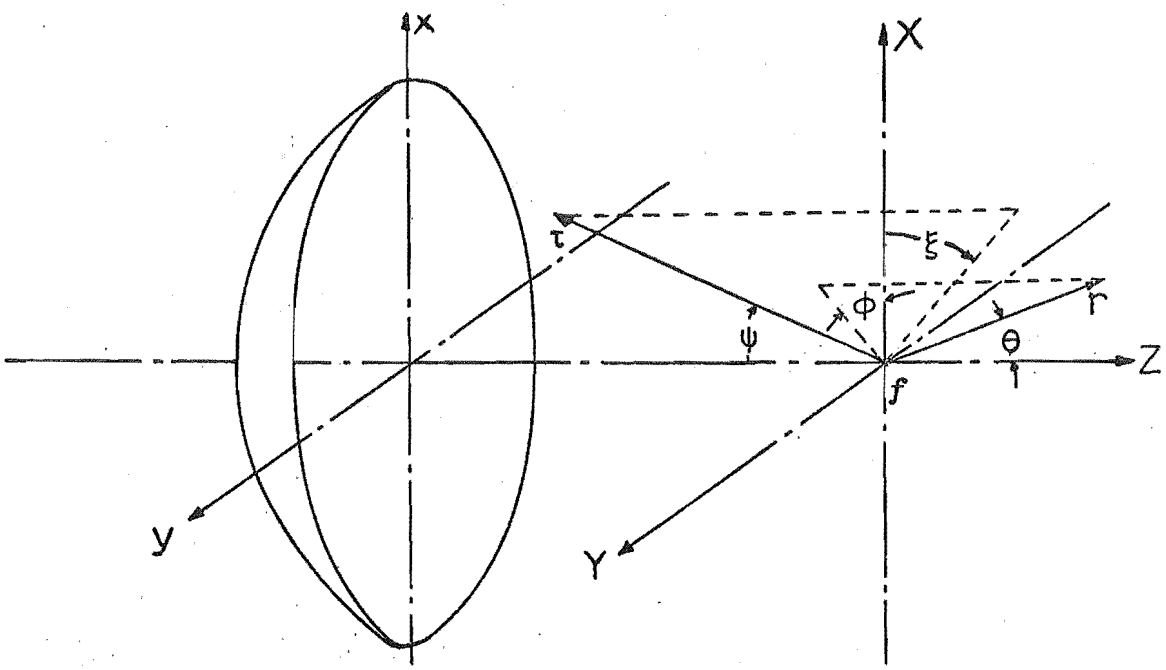

Fig. 4.1 Coordinates for the paraboloid

For the physical optics method, the current distribution over the reflector is approximated from the tangential component of the incident field. Thus, for a perfectly conducting reflector we have at each point

$$\underline{J}_{s'} = 2\hat{n} \wedge \underline{H}_i \ , \quad \underline{m}_{s'} = 0, \tag{4.3}$$

where $\hat{n}$ is the outward normal from the reflector. From (4.3) we can see that the physical optics approximation will give a zero current distribution over the shadow area behind the reflector. Over the illuminated region we can derive $\underline{J}_{s'}$ from (4.2) and (4.3) as

$$\underline{J}_{s'} = 2\sqrt{\frac{\varepsilon}{\mu}} \frac{e^{-jk\tau_i}}{\tau_i} \left[\cos(\tfrac{\psi}{2}) [f_1(\xi,\psi)\cos\xi - f_2(\xi,\psi)\sin\xi]\hat{u}_x \right.$$

$$\left. - \cos(\tfrac{\psi}{2}) [f_1(\xi,\psi)\sin\xi + f_2(\xi,\psi)\cos\xi]\hat{u}_y + f_1(\xi,\psi)\sin(\tfrac{\psi}{2})\hat{u}_z \right]. \tag{4.4}$$

Substitution of $\underline{J}_s$, into (4.1) involves, in general, a double numerical integration. If the source is linearly polarized then we can evaluate one of the integrals analytically. For the incident electric field we now have

$$\underline{E}_i = [f_1(\psi)\,\mathrm{Sin}\,\xi\,\hat{u}_\psi + f_2(\psi)\,\mathrm{Cos}\,\xi\,\hat{u}_\xi]\,\frac{e^{-jk\tau_i}}{\tau_i} \tag{4.5}$$

The resulting expressions for the radiation field in the principal planes for a linearly polarized source are given as follows:

(i) E-plane $(\phi = \frac{\pi}{2})$

$$E_\phi = 0,$$

$$E_\theta = \frac{jkfe^{-jkr}}{r}\int_0^{\psi_e}\Big[(J_0(\gamma_p)f_1(\psi) + \frac{J_1(\gamma_p)}{\gamma_p}[f_2(\psi) - f_1(\psi)])\cdot \cos(\tfrac{\psi}{2})\mathrm{Cos}\,\theta - jf_1(\psi)J_1(\gamma_p)\mathrm{Sin}(\tfrac{\psi}{2})\mathrm{Sin}\theta\Big]e^{-jkf\mathrm{Sec}^2(\frac{\psi}{2})(1+\mathrm{Cos}\psi\mathrm{Cos}\theta)}\cdot \sin\psi\,\mathrm{sec}^3(\tfrac{\psi}{2})\,d\psi, \tag{4.6}$$

(ii) H-plane $(\phi = 0)$

$$E_\phi = \frac{jkfe^{-jkr}}{r}\int_0^{\psi_e}\Big[f_2(\psi)J_0(\gamma_p) + \frac{J_1(\gamma_p)}{\gamma_p}[f_1(\psi) - f_2(\psi)]\Big]\cdot e^{-jkf\mathrm{Sec}^2(\frac{\psi}{2})(1+\mathrm{Cos}\,\psi\,\mathrm{Cos}\theta)}\,\mathrm{Sin}\,\psi\,\mathrm{Sec}^2(\tfrac{\psi}{2})\,d\psi, \tag{4.7}$$

$$E_\theta = 0,$$

where $\gamma_p = kf\,\mathrm{Sec}^2(\frac{\psi}{2})\mathrm{Sin}\,\psi\,\mathrm{Sin}\theta$, and $\psi_e = 2\,\mathrm{Tan}^{-1}(\frac{D}{4f})$.

The inevitable numerical integration involved in the physical optics approach limited its application until the general availability of electronic computers in the 1960's. Prior to this, the aperture field method as discussed in 3.111 was generally used because of the simpler formulation obtained.

The circular aperture at z = 0 in Fig. 4.1 is chosen where the fields in the aperture are approximated by the reflected geometrical optics field from the source. The radiation field is given by (4.1) with the equivalent sources obtained from the aperture fields. For a linearly polarized source, the remaining single integration can be solved analytically for many practical distributions (Silver, 1949b; Rusch and Potter, 1970b).

The two methods give concordant results on and near the forward axis. At wide angles the neglected axial component of current in the aperture field formulation becomes significant (Silver, 1949a). Also the path length discrepancy between the different surfaces of integration for the two methods increases with angle (Rusch and Potter, 1970c). Both of these effects limit the validity of the aperture field method at wide angles. In the shadow region the physical optics method is unreliable because the currents on the back of the reflector are neglected.

If the induced current on an infinite reflector is expressed as a power series in λ, the first term is the physical optics approximation, and the second term in the expansion depends on the local curvature of the body and on the proximity of the source (Kinber, 1960). Provided the radius of curvature at each point is much larger than the incident wavelength, the curvature has a negligible effect on this correction current. For practical reflectors ($f/D \geq 0.2$) the proximity of the source is then the predominant effect in the second term. This proximity effect rapidly diminishes with increase of the uniformity of illumination and becomes zero when the illumination is uniform.

For a finite reflector, the edge correction current as originally proposed by Ufimtsev is significant particularly in the shadow region. We now derive this term and apply it to a paraboloidal reflector so as to give a comparison with the equivalent edge current method to be discussed in 4.13.

4.12 Edge Correction Current to Physical Optics

We derive the edge correction current to physical optics for the half-plane in Fig. 4.2 from the exact solution to the diffracted magnetic field, $\underline{H}^d$, for a normally incident electromagnetic plane-wave.

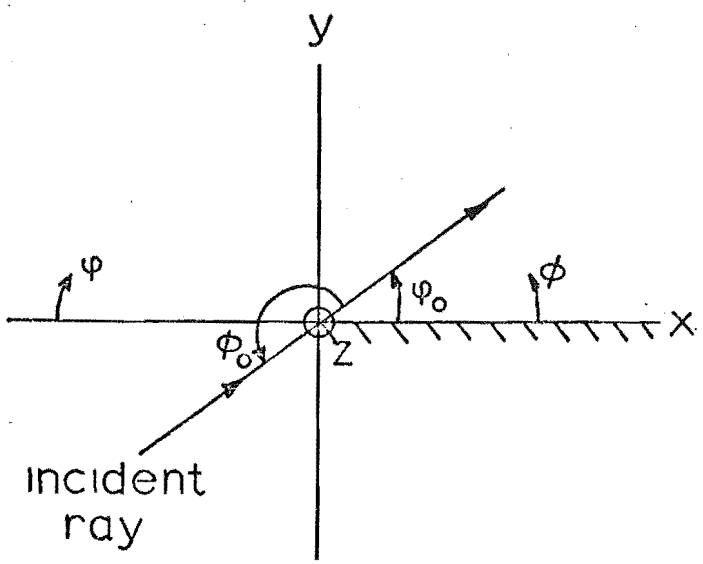

Fig. 4.2 Semi-infinite half-plane

From (2.47) with $\theta_0 = \frac{\pi}{2}$, i.e. normal incidence, we get

$$\underline{H}^d = \frac{a_z}{j\omega\mu}\,\hat{u}_z \wedge \nabla U_a - \frac{a_\phi k}{\omega\mu}\,\hat{u}_z U_f, \tag{4.8}$$

where U_a is given by (2.50). Evaluating (4.8) at the surface of the half-plane when $\phi = 0, 2\pi$; $\phi_0 < \pi$, $x \geq 0$, yields

$$\underline{H}^d = -\sqrt{\frac{\varepsilon}{\mu}}\, a_\phi U_f^0 \hat{u}_z - \frac{a_z}{j\omega\mu}\,\frac{1}{x}\, U_a^{0,} \hat{u}_x, \tag{4.9}$$

where $U_f^0 = U_f\Big|_{\phi=0,2\pi} = \frac{2}{\sqrt{j\pi}}\, e^{jkx\mathrm{Cos}\,\phi_0}\, F(s_0)$,

$$U_a^{0,} = \frac{\partial U_a}{\partial \phi}\Big|_{\phi=0,2\pi} = \frac{2}{\sqrt{j\pi}}\, jkx e^{jkx\,\mathrm{Cos}\,\phi_0}\, G(s_0),$$

$$G(s_0) = [F(s_0) - \frac{e^{-js_0^2}}{2js_0}]\,\mathrm{Sin}\,\phi_0,$$

and $s_0 = \sqrt{kx(1 + \mathrm{Cos}\,\phi_0)}$.

The edge correction current, $\underline{J}_{s'}^c$, for the half-plane is given from (4.9) by

$$\underline{J}_{s'}^c = 2\hat{n} \wedge \underline{H}^d, \tag{4.10}$$

where $\hat{n}$ is the outward normal from the reflector. For $\phi_0 > \pi$ the sign of $\underline{J}_{s'}^c$ is reversed.

Although we have restricted $\underline{J}_{s'}^c$ to the half-plane solution (since it is applicable to the reflector), a correction current can be obtained for the wedge. The expressions for U_f^0, $U_a^{0,}$ for the wedge are not as tractable as for the half-plane because they involve an infinite series solution. The approximation to the wedge currents given by Schretter and Bolle (1969) however, would considerably simplify U_f^0, $U_a^{0,}$ for the wedge.

We will now apply the edge correction current to a paraboloidal reflector illuminated by a source at the focus. From (4.2) the incident electric field, $\underline{E}_e$, at the reflector edge is given by

$$\underline{E}_e = [f_1(\xi,\psi_e)\hat{u}_\psi + f_2(\xi,\psi_e)\hat{u}_\xi]\,\frac{e^{-jk\tau_e}}{\tau_e}\,, \tag{4.11}$$

where $\tau_e = f\,\mathrm{Sec}^2(\frac{\psi_e}{2})$. The current distribution near the edge of the reflector is now approximated by the physical optics current of (4.4) plus the edge correction current of (4.10) for a locally oriented half-plane at each point on the reflector edge. From (4.9), (4.10), (4.11) we derive $\underline{J}_{s'}^{c}$ for the reflector as

$$\underline{J}_{s'}^{c} = \frac{4}{\sqrt{j\pi}}\sqrt{\frac{\varepsilon}{\mu}}\,e^{jk\ell\,\mathrm{Cos}\,\phi_0}\,\frac{e^{-jk\tau_e}}{\tau_e}\Bigg[\mathrm{Cos}\,\frac{\psi}{2}\,[F(s_0)f_1(\xi,\psi_e)\mathrm{Cos}\,\xi$$

$$- G(s_0)f_2(\xi,\psi_e)\mathrm{Sin}\,\xi]\hat{u}_x - \mathrm{Cos}(\tfrac{\psi}{2})[F(s_0)f_1(\xi,\psi_e)\mathrm{Sin}\,\xi$$

$$+ G(s_0)f_2(\xi,\psi_e)\mathrm{Cos}\,\xi]\hat{u}_y + F(s_0)f_1(\xi,\psi_e)\mathrm{Sin}(\tfrac{\psi}{2})\hat{u}_z\Bigg], \tag{4.12}$$

where $s_0 = \sqrt{k\ell(1 + \mathrm{Cos}\,\phi_0)}$, and ℓ is the distance along the reflector measured perpendicular from the edge. It will be noted that $\underline{J}_{s'}^{c}$ in (4.12) is similar to $\underline{J}_{s'}$ in (4.4) if we replace $f_1(\xi,\psi)$, $f_2(\xi,\psi)$ in (4.4) by $F(s_0)f_1(\xi,\psi_e)$, $G(s_0)f_2(\xi,\psi_e)$ and multiply by

$$\frac{2}{\sqrt{j\pi}}\,\tau_i\,e^{jk\tau_i}\,e^{jk\ell\,\mathrm{Cos}\,\phi_0}\,\frac{e^{-jk\tau_e}}{\tau_e}.$$

Thus from (4.6), (4.7) we can write down the edge correction fields E_θ^{c}, E_ϕ^{c} in the principal planes for a linearly polarized source as follows:

(i) E-plane

$$E_\phi^{c} = 0,$$

$$E_\theta^c = A \int_0^{\psi_e} \Big[\Big[f_1(\psi_e)F(s_0)J_0(\gamma_p) + \frac{J_1(\gamma_p)}{\gamma p}[f_2(\psi_e)G(s_0) - f_1(\psi_e)F(s_0)]\Big] \operatorname{Cos}(\tfrac{\psi}{2})\operatorname{Cos}\,\theta - jf_1(\psi_e)F(s_0)J_1(\gamma_p)\operatorname{Sin}(\tfrac{\psi}{2})\,\operatorname{Sin}\,\theta\Big]\operatorname{Sin}\,\psi\,\operatorname{Sec}^5(\tfrac{\psi}{2})\cdot e^{jk\ell\,\operatorname{Cos}\,\phi_0}\, e^{-jkf\,\operatorname{Sec}^2(\frac{\psi}{2})\operatorname{Cos}\psi\operatorname{Cos}\,\theta}\, d\psi, \qquad (4.13)$$

where $A = \dfrac{2jkfe^{-jkr}}{\sqrt{j\pi}\,r}\, e^{-jkf\,\operatorname{Sec}^2(\frac{\psi_e}{2})}\,\operatorname{Cos}^2(\tfrac{\psi_e}{2})$.

(ii) H-plane

$$E_\phi^c = A \int_0^{\psi_e} \Big[\Big[f_2(\psi_e)G(s_0)J_0(\gamma_p) + \frac{J_1(\gamma_p)}{\gamma_p}[f_1(\psi_e)F(s_0) - f_2(\psi_e)G(s_0)]\Big]\cdot \operatorname{Sin}\psi\,\operatorname{Sec}^4(\tfrac{\psi}{2})\, e^{jk\ell\,\operatorname{Cos}\,\phi_0}\, e^{-jkf\operatorname{Sec}^2(\frac{\psi}{2})\operatorname{Cos}\psi\operatorname{Cos}\,\theta}\, d\psi, \qquad (4.14)$$

$$E_\theta^c = 0.$$

Equations (4.13), (4.14) are not suitable for numerical integration in their present form because of the singularity in the term $G(s_0)$ at the edge. Rewriting E_θ^c in (4.13) we get

$$E_\theta^c = A\Bigg[\int_0^{\psi_e} \Big[[f_1(\psi_e)J_0(\gamma_p) + \frac{J_1(\gamma_p)}{\gamma_p}[f_2(\psi_e)\operatorname{Sin}\,\phi_0 - f_1(\psi_e)]]\cdot \operatorname{Cos}(\tfrac{\psi}{2})\operatorname{Cos}\,\theta - jf_1(\psi_e)J_1(\gamma_p)\operatorname{Sin}(\tfrac{\psi}{2})\operatorname{Sin}\,\theta\Big]F(s_0)\operatorname{Sin}\psi\,\operatorname{Sec}^5(\tfrac{\psi}{2})\cdot e^{jk\ell\operatorname{Cos}\phi_0} e^{-jkf\operatorname{Sec}^2(\frac{\psi}{2})\operatorname{Cos}\psi\operatorname{Cos}\theta}\, d\psi - \frac{f_2(\psi_e)\operatorname{Sin}\phi_0\operatorname{Cos}\theta}{2j\sqrt{1+\operatorname{Cos}\,\phi_0}}\int_0^{\psi_e} \frac{e^{-jk\ell}}{\sqrt{k\ell}}\,\frac{J_1(\gamma_p)}{\gamma_p}\cdot \operatorname{Sin}\psi\,\operatorname{Sec}^4(\tfrac{\psi}{2})\, e^{-jkf\operatorname{Sec}^2(\frac{\psi}{2})\operatorname{Cos}\psi\operatorname{Cos}\phi}\, d\psi\Bigg]. \qquad (4.15)$$

The singularity is now confined to the second integral in (4.15) which can be removed by integrating this integral by parts after making some assumptions about ℓ.

The distance ℓ is measured from the edge along the parabolic curve of the reflector and is readily shown to be given by

$$\ell(\psi) = \int_{q}^{f} (1 + \frac{f}{t})^{\frac{1}{2}} dt; \quad q = f(1 - \mathrm{Sec}^2(\frac{\psi}{2}) \cos \psi) \qquad (4.16)$$

In this form, however, $\ell(\psi)$ is not suitable in evaluating the second integral in (4.15) by parts. We now make a further assumption in that the edge correction currents are negligible away from the vicinity of the edge. This is true for electric polarization to which the singularity applies since the function $G(s_0)$ decays rapidly with increasing ℓ. It applies to a lesser extent for magnetic polarization. Thus, if the edge correction currents can be ignored for ℓ greater than about $1-2\lambda$, then we can approximate $\ell(\psi)$ in the vicinity of the edge by

$$\ell(\psi) \approx fh \left[\mathrm{Tan}(\frac{\psi_e}{2}) - \mathrm{Tan}(\frac{\psi}{2})\right], \qquad (4.17)$$

where h is a constant found empirically for the reflector under consideration. (For a focal-plane parabolic reflector, h = 2.8.) With the expression for $\ell(\psi)$ given by (4.17) we can now evaluate the singularity in (4.15). The final solution for E_θ^c in the E-plane becomes

$$E_\theta^c = A\Bigg[\int_{\psi_L}^{\psi_e}\Bigg[\Big[f_1(\psi_e)J_0(\gamma_p) + \frac{J_1(\gamma_p)}{\gamma_p}[f_2(\psi_e)\mathrm{Sin}\phi_0 - f_1(\psi_e)]\Big]\cdot$$

$$\mathrm{Cos}\left(\frac{\psi}{2}\right)\mathrm{Cos}\theta - jf_1(\psi_e)J_1(\gamma_p)\mathrm{Sin}\left(\frac{\psi}{2}\right)\mathrm{Sin}\theta\Bigg]F(s_0)\mathrm{Sin}\psi\mathrm{Sec}^5\left(\frac{\psi}{2}\right)\cdot$$

$$e^{jk\ell(\psi)\mathrm{Cos}\phi_0} - B\mathrm{Cos}\theta\left(\mathrm{Tan}\left(\frac{\psi_e}{2}\right) - \mathrm{Tan}\left(\frac{\psi}{2}\right)\right)^{\frac{1}{2}}\Bigg[\frac{J_1(\gamma_p)}{\gamma_p}C(\psi)$$

$$- J_2(\gamma_p)\Big]e^{-jk\ell(\psi)}\mathrm{Sec}^2\left(\frac{\psi}{2}\right)\Bigg]\ e^{-jkf\mathrm{Sec}^2\left(\frac{\psi}{2}\right)\mathrm{Cos}\psi\mathrm{Cos}\theta}\ d\psi$$

$$- B\mathrm{Cos}\theta\left(\mathrm{Tan}\left(\frac{\psi_e}{2}\right) - \mathrm{Tan}\left(\frac{\psi_L}{2}\right)\right)^{\frac{1}{2}}\frac{J_1(\gamma_p)}{\gamma_p}\mathrm{Sin}\psi_L\mathrm{Sec}^2\left(\frac{\psi_L}{2}\right)e^{-jkfD(\psi_L)}\Bigg], \tag{4.18}$$

where

$$B = -\frac{f_2(\psi_e)\mathrm{Sin}\phi_0}{j\sqrt{fhk(1+\mathrm{Cos}\ \phi_0)}},$$

$$C(\psi) = [1 + \tfrac{1}{2}(jkf\mathrm{Sin}\,\psi\,\mathrm{Sec}^2\left(\tfrac{\psi}{2}\right)(\mathrm{Sin}\,\psi\,\mathrm{Sec}^2\left(\tfrac{\psi}{2}\right)\mathrm{Cos}\ \theta+h))],$$

$$D(\psi_L) = \mathrm{Sec}^2\left(\frac{\psi_L}{2}\right)\mathrm{Cos}\ \psi_L\mathrm{Cos}\ \theta + h\left(\mathrm{Tan}\left(\frac{\psi_e}{2}\right) - \mathrm{Tan}\left(\frac{\psi_L}{2}\right)\right).$$

Similarly we can evaluate E_ϕ^c in the H-plane, giving

$$E_\phi^c = A\Bigg[\int_{\psi_L}^{\psi_e}\Bigg[[f_2(\psi_e)J_0(\gamma_p)\mathrm{Sin}\phi_0 + \frac{J_1(\gamma_p)}{\gamma_p}[f_1(\psi_e) - f_2(\psi_e)\mathrm{Sin}\phi_0]]\cdot$$

$$F(s_0)\mathrm{Sin}\psi\mathrm{Sec}^4\left(\frac{\psi}{2}\right)e^{jk\ell(\psi)\mathrm{Cos}\phi_0} - B\left(\mathrm{Tan}\left(\frac{\psi_e}{2}\right) - \mathrm{Tan}\left(\frac{\psi}{2}\right)\right)^{\frac{1}{2}}$$

$$\Big[\Big(J_0(\gamma_p) - \frac{J_1(\gamma_p)}{\gamma_p}\Big)C(\psi) - J_1(\gamma_p)\gamma_p + J_2(\gamma_p)\Big]e^{-jk\ell(\psi)}\mathrm{Sec}^2\left(\frac{\psi}{2}\right)\Bigg]\cdot$$

$$e^{-jkf\mathrm{Sec}^2\left(\frac{\psi}{2}\right)\mathrm{Cos}\psi\mathrm{Cos}\theta}\ d\psi - B\left(\mathrm{Tan}\left(\frac{\psi_e}{2}\right) - \mathrm{Tan}\left(\frac{\psi_L}{2}\right)\right)^{\frac{1}{2}}\Big(J_0(\gamma_p) - \frac{J_1(\gamma_p)}{\gamma_p}\Big)$$

$$\mathrm{Sin}\psi_L\mathrm{Sec}^2\left(\frac{\psi_L}{2}\right)e^{-jkfD(\psi_L)}\Bigg]. \tag{4.19}$$

The lower limit ψ_L in (4.18), (4.19) is a result of the approximation used for $\ell(\psi)$. For a maximum value of ℓ, denoted by ℓ_{max}, we get from (4.17)

$$\psi_L = 2\ \mathrm{Tan}^{-1}\left(\mathrm{Tan}\left(\frac{\psi_e}{2}\right) - \frac{\ell_{max}}{fh}\right) .$$

On the illuminated region of the reflector the physical optics current will dominate the edge correction currents up to about one wavelength from the edge. In the shadow region only the edge correction currents will exist which, for electric polarization will be small for $\ell > 1\text{-}2\lambda$. For ℓ beyond this value the approximation of (4.17), using the same value of h will tend to be too large thus increasing the rate of decay of the magnetic current from the edge. This increased rate of decay along the convex surface of the reflector in the shadow region is in keeping with the creeping wave concept around a curved body. However, if the exact half-plane magnetic currents are required, then it will be necessary to solve for the $f_1(\psi_e)$ components in (4.18), (4.19) with $\psi_L = 0$ and use the exact value for $\ell(\psi)$ as given by (4.16).

4.13 Edge Diffraction Method

There are two main limitations to the straightforward application of the GTD, as used in the previous chapter, to radiation pattern analysis of reflector antennas. They are the infinities in the radiation fields obtained in certain directions (along shadow boundaries, and at caustics of the diffracted rays as discussed in 2.4 for a curved edge), and the cases where the incident field tapers to zero at the reflector edge. If the source is at a known finite distance from the edge, then cylindrical-wave diffraction coefficients discussed in 2.33 can be used to yield finite solutions in the

shadow boundary regions. To overcome the remaining limitations we will use the equivalent edge current method discussed in 2.4. By including the slope-wave term in the equivalent current formulation we account for the general case of non-uniform incidence at the edge, e.g., the case when the illumination is tapered.

We begin our analysis by considering uniform incidence only, and then later extend it to incorporate the slope-wave term. As before we have the illuminating field from a source at the focus of the reflector. Thus from (4.2) the electric field incident at the edge, $\underline{E}_e$, is given by

$$\underline{E}_e = [f_1(\xi,\psi_e)\hat{u}_\psi + f_2(\xi,\psi_e)\hat{u}_\xi] \frac{e^{-jk\tau_e}}{\tau_e}, \tag{4.20}$$

where the symbols are defined in Fig. 4.3(a).

The cross-section of the reflector through (a,ϕ') in Fig. 4.3(a) is shown in Fig. 4.3(b), where α is the angle between the tangent to the reflector edge at (a,ϕ') and the ρ'-axis, and β_0' is the angle of incidence of $\underline{E}_e$ to this tangent. For a symmetrical reflector, the quantities α,β_0', ψ_e,τ_e, given for a paraboloidal reflector by

$$\begin{aligned} \alpha &= \frac{\pi}{2} - \mathrm{Tan}^{-1}\left(\frac{4f}{D}\right), \\ \beta_o' &= \alpha + \left(\frac{\pi}{2} - \psi_e\right), \\ \psi_e &= 2\ \mathrm{Tan}^{-1}\left(\frac{D}{4f}\right), \\ \tau_e &= \frac{D^2}{16f} + f, \end{aligned} \tag{4.21}$$

are independent of ϕ', and the incident field is everywhere normal to the edge. Initially assume that Fig. 4.3(b) represents a two-dimensional problem with a line-source at the focus, f. Then, from (4.20), the amplitude of the source in

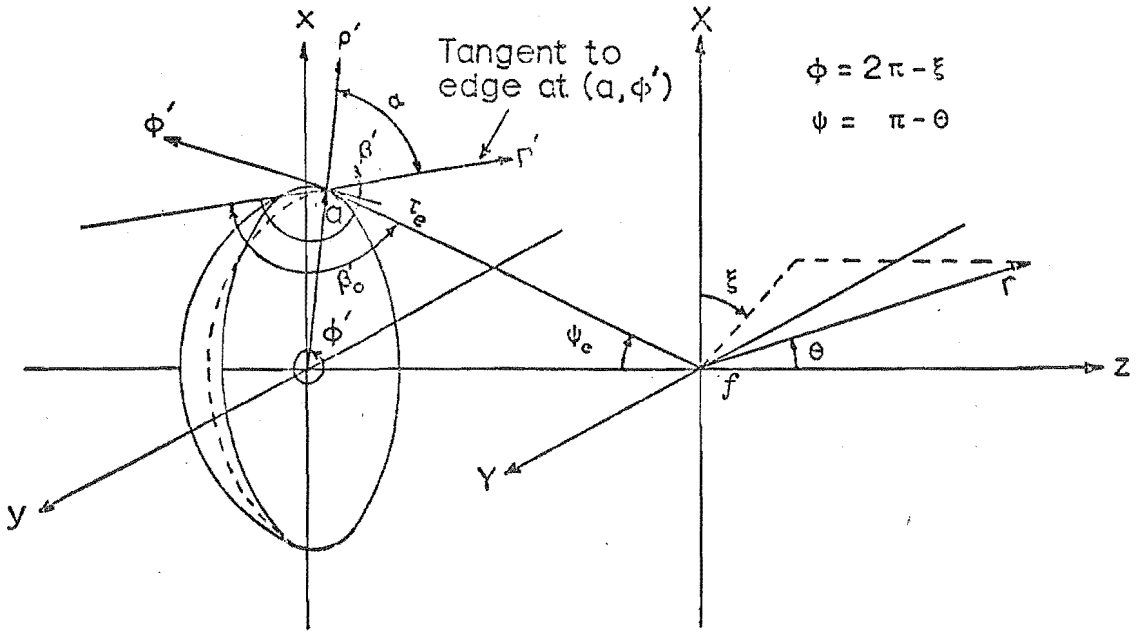

(a)

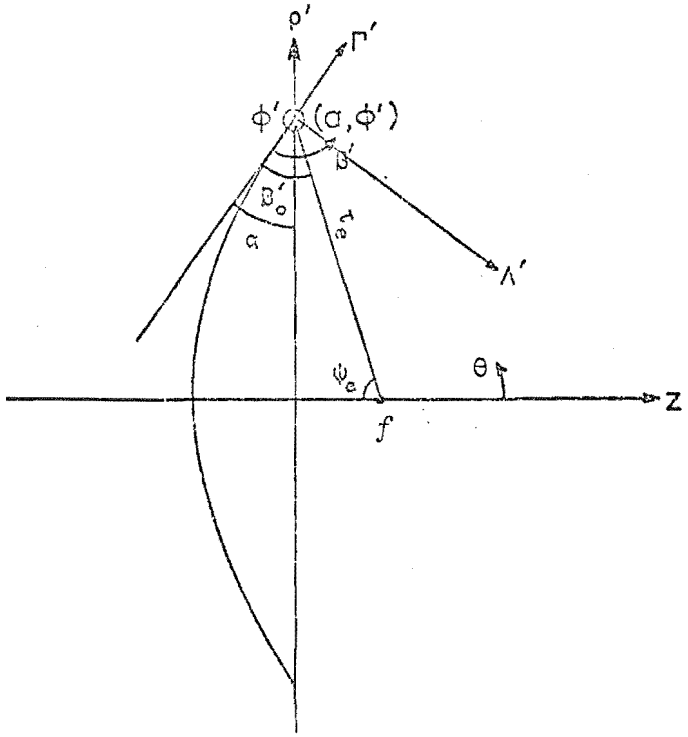

(b)

Fig. 4.3 Coordinates for paraboloid

the direction of the edge is given by

$$\underline{E}_e = [f_1(2\pi-\phi',\psi_e)\hat{u}_\psi + f_2(2\pi-\phi',\psi_e)\hat{u}_\xi]\sqrt{\frac{8j\pi k}{\tau_e}}\ , \qquad (4.22)$$

where we have substituted $2\pi-\phi$ for ξ. From the uniform incidence source current formulation of (2.91) in conjunction with (4.22) we obtain the elemental equivalent electric (magnetic) source current $d\underline{J}'$ ($d\underline{M}'$) in the element of edge dC' at (a,ϕ') for the diffracted field. Since the field from the source is at normal incidence to the edge, then $\Theta_0 = \frac{\pi}{2}$ and the direction of the source currents is along the edge. Writing dC' as $ad\phi'$ we get

$$\begin{aligned} d\underline{J}' &= \hat{u}_\phi,\varepsilon_1' \frac{A}{j\omega\mu} f_2(2\pi-\phi',\psi_e) I_e^{c'} d\phi', \\ d\underline{M}' &= \hat{u}_\phi,\varepsilon_1' \frac{A}{jk} f_1(2\pi-\phi',\psi_e) I_m^{c'} d\phi', \end{aligned} \qquad (4.23)$$

where $A = a\sqrt{\frac{8j\pi k}{\tau_e}}$ and I_e^c (I_m^c) is given by (2.84). The term ε_1' accounts for the blocking effect of the reflector on the far-field radiation from the equivalent currents. From the geometry of the paraboloidal reflector we can express ε_1' as

$$\varepsilon_1' = \begin{bmatrix} 0 & \text{for } \beta' \leqslant \alpha' \\ 1 & \text{for } \beta' > \alpha' \end{bmatrix}\ , \qquad (4.24)$$

where β' is the angle measured from the tangent to the edge at (a,ϕ') in the ρ'-z plane of Fig. 4.3(b), and α' is defined as

$$\alpha' = \frac{\pi}{2} - \mathrm{Tan}^{-1}\left[\frac{4f}{D|\mathrm{Cos}(\phi-\phi')|}\right]\ . \qquad (4.25)$$

Integration of the current elements around the reflector edge yields the diffracted fields, E_θ^d, E_ϕ^d, by the substitution of the potential integral solution of (2.8) into (2.12), i.e.

$$\begin{matrix} E_\theta^d \\ E_\phi^d \end{matrix} = -A \frac{e^{-jkr}}{4\pi r} \int_0^{2\pi} \left[f_2(2\pi-\phi',\psi_e) I_e^{c'} \begin{matrix} \text{Cos}\,\theta\,\text{Sin}(\phi-\phi') \\ \text{Cos}\ (\phi-\phi') \end{matrix} \right.$$

$$\left. \pm\, f_1(2\pi-\phi',\psi_e) I_m^{c'} \begin{matrix} \cos(\phi-\phi') \\ \cos\theta\,\sin(\phi-\phi') \end{matrix} \right] \varepsilon_1' \, e^{j\gamma_e \text{Cos}(\phi-\phi')} \, d\phi', \quad (4.26)$$

where $\gamma_e = ka\ \text{Sin}\ \theta$.

For a symmetrical reflector, quantities $I_e^{c'}$, $I_m^{c'}$ are functions only of the angle β' in Fig. 4.3. From the relationship $\text{Tan}\ \beta' = \frac{A_\Lambda'}{-A_\Gamma'}$, we get

$$\text{Tan}\ \beta' = \frac{\text{Sin}\,\theta\,\text{Cos}(\phi-\phi')\text{Sin}\ \alpha - \text{Cos}\,\alpha\,\text{Cos}\ \theta}{\text{Sin}\,\theta\,\text{Cos}(\phi-\phi')\text{Cos}\ \alpha + \text{Sin}\,\alpha\,\text{Cos}\ \theta} . \quad (4.27)$$

If the phase variations in f_1, f_2 with respect to ϕ' are small, then for γ_e large, direct application of the method of stationary phase (Erdelyi, 1956) to (4.26) yields

$$E_\theta^d \sim \frac{Ae^{-jkr}}{4\pi r} \left[\frac{2\pi}{\gamma_e}\right]^{\frac{1}{2}} \left[\varepsilon_1^{+}\ I_m^{c+}\ f_1(2\pi-\phi,\psi_e)\ e^{j(\gamma_e-\frac{\pi}{4})}\right.$$

$$\left. - \varepsilon_1^{-}\ I_m^{c-}\ f_1(3\pi-\phi,\psi_e)\ e^{-j(\gamma_e-\frac{\pi}{4})} \right] , \quad (4.28)$$

$$E_\phi^d \sim \frac{Ae^{-jkr}}{4\pi r} \left[\frac{2\pi}{\gamma_e}\right]^{\frac{1}{2}} \left[\varepsilon_1^{+}\ I_e^{c+}\ f_2(2\pi-\phi,\psi_e)\ e^{j(\gamma_e-\frac{\pi}{4})}\right.$$

$$\left. - \varepsilon_1^{-}\ I_e^{c-}\ f_2(3\pi-\phi,\psi_e)\ e^{-j(\gamma_e-\frac{\pi}{4})} \right] , \quad (4.29)$$

where $\varepsilon_1^{\pm} = \begin{bmatrix} 0 & \text{for } \beta^{\pm} < \alpha \\ 1 & \text{otherwise} \end{bmatrix}$, $\beta^{\pm} = \frac{\pi}{2} + \alpha \pm \theta$,

and $I_{e\ m}^{c+}$ ($I_{e\ m}^{c-}$) is a function of β^+ (β^-).

Asymptotic expressions similar to (4.28), (4.29) have frequently been used in the analysis of reflector antennas by edge diffraction methods (e.g. Kinber (1961)). By (4.28) and

(4.29) the diffracted field in any plane through a paraboloidal reflector is reduced to the two-dimensional problem of a parabolic cylinder (as in Fig. 4.3(b)) with a line-source along each edge. The two opposite positions on the edge where the plane cut is taken through the paraboloidal reflector are the stationary phase points on the edge for that plane. The two-dimensional problem mentioned above, with a source at each stationary phase point, can be analysed by the ray tracing methods of the GTD. This has been the starting point for all previous attempts at radiation pattern analysis of paraboloidal reflectors. The limitations of this approach, however, have not always been made clear. We can readily see that the method fails if the incident field goes to zero at the stationary phase points on the reflector edge for the plane under consideration. Also the stationary phase method, which led to the two-dimensional model, is not applicable in the axial regions of the reflector where $\gamma_e \to 0$ or when the phase variation with respect to ϕ' in the source functions f_1, f_2, is comparable to the phase variation of the exponential term in (4.14). For these cases it is necessary to evaluate the integral in (4.26). This will, in general, involve numerical integration. For the back-axial region, however, we can derive an approximate analytical solution. Assuming that the equivalent currents do not vary greatly with θ in the back-axial region, then we can write (4.26) for this region as

$$\begin{matrix} E_\theta^d \\ E_\phi^d \end{matrix} = A \frac{e^{-jkr}}{4\pi r} \left[I_e^c (\alpha + \frac{3\pi}{2}) \int_0^{2\pi} f_2(2\pi+\upsilon-\phi, \psi_e) \begin{matrix} -\sin\upsilon \\ \cos\upsilon \end{matrix} e^{j\gamma_e \cos\upsilon} \, d\upsilon \right.$$

$$\left. \pm I_m^c (\alpha + \frac{3\pi}{2}) \int_0^{2\pi} f_1(2\pi+\upsilon-\phi, \psi_e) \begin{matrix} \cos\upsilon \\ -\sin\upsilon \end{matrix} e^{j\gamma_e \cos\upsilon} \, d\upsilon \right], \quad (4.30)$$

where $\upsilon = \phi - \phi'$.

The integrals in (4.30) are of the form

$$\Xi(\gamma_e) = \int_0^{2\pi} g(\upsilon)\, e^{j\gamma_e \mathrm{Cos}\ \upsilon}\, d\upsilon. \tag{4.31}$$

Expressing $g(\upsilon)$ in a Fourier series we have

$$g(\upsilon) = \sum_{n=-\infty}^{\infty} G_n\, e^{jn\upsilon}, \tag{4.32}$$

where

$$G_n = \frac{1}{2\pi} \int_0^{2\pi} g(\upsilon)\, e^{-jn\upsilon}\, d\upsilon. \tag{4.33}$$

Substituting (4.32), (4.33) into (4.31) gives

$$\Xi(\gamma_e) = \sum_{n=-\infty}^{\infty} G_n K_n, \tag{4.34}$$

where

$$K_n = \int_0^{2\pi} e^{jn\upsilon}\, e^{j\gamma_e \mathrm{Cos}\ \upsilon}\, d\upsilon$$

$$= 2\pi j^n J_n(\gamma_e). \tag{4.35}$$

Substituting (4.34), (4.35) into (4.30) we get

$$\begin{matrix} E_\theta^d \\ E_\phi^d \end{matrix} = A\, \frac{e^{-jkr}}{4\pi r} \sum_{n=-\infty}^{\infty} \left[I_e{}^c(\alpha + \tfrac{3\pi}{2}) \begin{matrix} a_n \\ c_n \end{matrix} \pm I_m{}^c(\alpha + \tfrac{3\pi}{2}) \begin{matrix} b_n \\ d_n \end{matrix} \right] j^n J_n(\gamma_e), \tag{4.36}$$

where

$$\begin{matrix} a_n \\ c_n \end{matrix} = \int_0^{2\pi} f_2(2\pi+\upsilon-\phi, \psi_e) \begin{matrix} -\mathrm{Sin}\ \upsilon \\ \mathrm{Cos}\ \upsilon \end{matrix} e^{-jn\upsilon}\, d\upsilon,$$

$$\begin{matrix} b_n \\ d_n \end{matrix} = \int_0^{2\pi} f_1(2\pi+\upsilon-\phi, \psi_e) \begin{matrix} \mathrm{Cos}\ \upsilon \\ -\mathrm{Sin}\ \upsilon \end{matrix} e^{-jn\upsilon}\, d\upsilon.$$

We now have in (4.36) an analytical solution for the diffracted fields in the back-axial region of the reflector.

A similar solution can be derived for the forward-axial region. This solution, however, is more complicated since the equivalent currents change rapidly with θ in the forward-axial solution. Also, from the numerical solutions, we will show that the equivalent current method does not adequately describe the diffracted fields in the forward-axial region and thus there is little point in deriving analytical solutions for this region.

The scattered field from the reflector is given by the sum of the diffracted field and the geometrical optics field. For a paraboloidal reflector the geometrical optics field exists only along the forward axis. Thus the scattered field from the equivalent edge current approach is given everywhere, except on the forward axis, by (4.26).

In many practical applications the source is linearly polarised, so that (4.20) becomes

$$\underline{E}_e = [f_1(\psi_e)\ \mathrm{Sin}\ \xi\, \hat{u}_\psi + f_2(\psi_e)\ \mathrm{Cos}\ \xi\, \hat{u}_\xi]\ \frac{e^{-jk\tau_e}}{\tau_e}\ , \qquad (4.37)$$

and (4.36) reduces to

$$\begin{matrix} E^d_\theta \\ E^d_\phi \end{matrix} = A\ \frac{e^{-jkr}}{4r} \begin{matrix} -\mathrm{Sin}\ \phi \\ \mathrm{Cos}\ \phi \end{matrix} \left[I_e^c(\alpha + \tfrac{3\pi}{2}) f_2(\psi_e) \begin{matrix} G_A \\ G_B \end{matrix} + I_m^c(\alpha + \tfrac{3\pi}{2}) f_1(\psi_e) \begin{matrix} G_B \\ G_A \end{matrix} \right], \qquad (4.38)$$

where

$$G_{\substack{A \\ B}} = J_0(\gamma_e) \pm J_2(\gamma_e).$$

For non-uniform wave incidence at the reflector edge, we can readily include the slope-wave term in the above expressions to yield a more accurate solution. The equivalent source currents including the slope-wave term are given by (2.96),

where we see that this term is added to the uniform incident term. From our general equation for the diffracted far-field given by (4.26), we can readily see that to account for the slope-wave term for cylindrical-wave diffraction it becomes

$$\begin{matrix} E_\theta^d \\ E_\phi^d \end{matrix} = -A \frac{e^{-jkr}}{4\pi r} \int_0^{2\pi} \left[\left[f_2(2\pi-\phi',\psi_e) I_e^{c'} + f_2'(2\pi-\phi',\psi_e) I_{se}^{c'} \right] \begin{matrix} \text{Cos } \theta \text{ Sin}(\phi-\phi') \\ \text{Cos } (\phi-\phi') \end{matrix} \right.$$

$$\pm \left. \left[f_1(2\pi-\phi',\psi_e) I_m^{c'} + f_1'(2\pi-\phi',\psi_e) I_{sm}^{c'} \right] \begin{matrix} \text{Cos } (\phi-\phi') \\ \text{Cos } \theta \text{ Sin}(\phi-\phi') \end{matrix} \right] \cdot$$

$$\varepsilon_1' \, e^{j\gamma_e \text{Cos}(\phi-\phi')} \, d\phi. \qquad (4.39)$$

For cylindrical-wave diffraction we have from (2.73)

$$f_{\begin{matrix}1\\2\end{matrix}}'(2\pi-\phi',\psi_e) = \frac{1}{\tau_e} \frac{\partial}{\partial\psi} f_{\begin{matrix}1\\2\end{matrix}}(2\pi-\phi',\psi) \Big|_{\psi=\psi_e}.$$

The asymptotic solution of (4.39) can be obtained from (4.28), (4.29) to give

$$\begin{matrix} E_\theta^d \\ \phi \end{matrix} \sim \frac{Ae^{-jkr}}{4\pi r} \left[\frac{2\pi}{\gamma_e} \right]^{\frac{1}{2}} \left[\varepsilon_1^+ (I_{\underset{e}{m}}^{c+} f_{\begin{matrix}1\\2\end{matrix}}(2\pi-\phi,\psi_e) + I_{\underset{se}{sm}}^{c+} f_{\begin{matrix}1\\2\end{matrix}}'(2\pi-\phi,\psi_e)) \right.$$

$$\cdot e^{j(\gamma_e - \frac{\pi}{4})} - \varepsilon_1^- (I_{\underset{e}{m}}^{c-} f_{\begin{matrix}1\\2\end{matrix}}(3\pi-\phi,\psi_e)$$

$$\left. + I_{\underset{se}{sm}}^{c-} f_{\begin{matrix}1\\2\end{matrix}}'(3\pi-\phi,\psi_e)) e^{-j(\psi_e - \frac{\pi}{4})} \right], \qquad (4.40)$$

where $I_{\underset{sm}{se}}^{c+}$ ($I_{\underset{sm}{se}}^{c-}$) is a function of β^+ (β^-); $\beta^\pm = \frac{\pi}{2} + \alpha \pm \theta$.

Similarly we can modify (4.38) to account for slope-wave diffraction, although the back-axis field region is usually well removed from a shadow boundary and the slope-wave term will be insignificant in this region.

It was mentioned earlier that the physical optics approach can be extended to include the Fresnel region of the illuminating source. A similar refinement based on the Fresnel region of the source can be employed using edge diffraction theory when the edge of the reflector is weakly illuminated. An example is given by Kinber (1962) for a two-element array at the focus of a parabolic cylinder. The field incident to the edge is regarded as the sum of two waves formed by the elements in the array. Since the elements are separated in space, then if the edge is in the Fresnel zone of the feed, the angle of incidence to the edge differs for each element, giving different diffraction patterns for each element. Thus, even if the total incident field is zero at the edge, the total diffraction pattern will be non-zero.

A further refinement is possible with the GTD approach by considering the reflection of the diffracted rays from the surface of the reflector and higher order diffraction between edges. This latter effect will be negligible for reflectors of practical dimensions (i.e., $D \geq 5\lambda$), but the reflected diffracted rays will be significant in a sector of space in the forward direction. An example is given by Narbut and Khmel'nitskaya (1970) for a parabolic reflector of dimensions $f/D = 0.625$, $D = 10\lambda$. The reflected rays contributed to the radiation pattern in the region $42^{\circ} \leq \theta \leq 78^{\circ}$.

4.14 Comparison of methods and experimental results

To compare the application of the physical optics and equivalent current methods to radiation pattern analysis of reflector antennas we begin by considering a focal-plane reflector ($f/D = 0.25$) illuminated by a short electric dipole at the focus. The theoretical radiation pattern of a short dipole, normalised to unity at its maximum value, gives $f_1(\psi) = \text{Cos } \psi$, $f_2(\psi) = 1$ in (4.5). For a focal plane reflector we have $\psi_e = \frac{\pi}{2}$, giving $f_2'(\psi_e) = f_1(\psi_e) = 0$, and $f_1'(\psi_e) = -\frac{1}{\tau_e}$, $f_2(\psi_e) = 1$ in (4.37), including the slope-wave term for cylindrical-wave diffraction. Fig. 4.4 gives the theoretical radiation pattern scattered from the reflector in the H-plane from the above two methods. It is seen that the agreement between the two methods is poor in the forward-axial and shadow regions. It is interesting to compare this forward on-axial result with that obtained for the parallel-plate waveguide supporting the *TEM* mode using edge diffraction methods as derived in 3.12. In both cases the forward axis is along one of the shadow boundaries of the incident field to the edge. The incident field to the edges at the open-end of the waveguide is a plane-wave. Although plane-wave diffraction coefficients are invalid in the shadow boundary region (as discussed in 2.33), we showed in 3.12 that by taking the limit of the total edge diffracted fields a result was obtained, despite the invalidity of the coefficients, that agreed with the aperture field method. If in the waveguide problem the plane-wave incidence is approximated by the field from a magnetic line-source situated in the waveguide at a large distance from the open end, then using cylindrical-wave coefficients, which are valid in the shadow boundary regions,

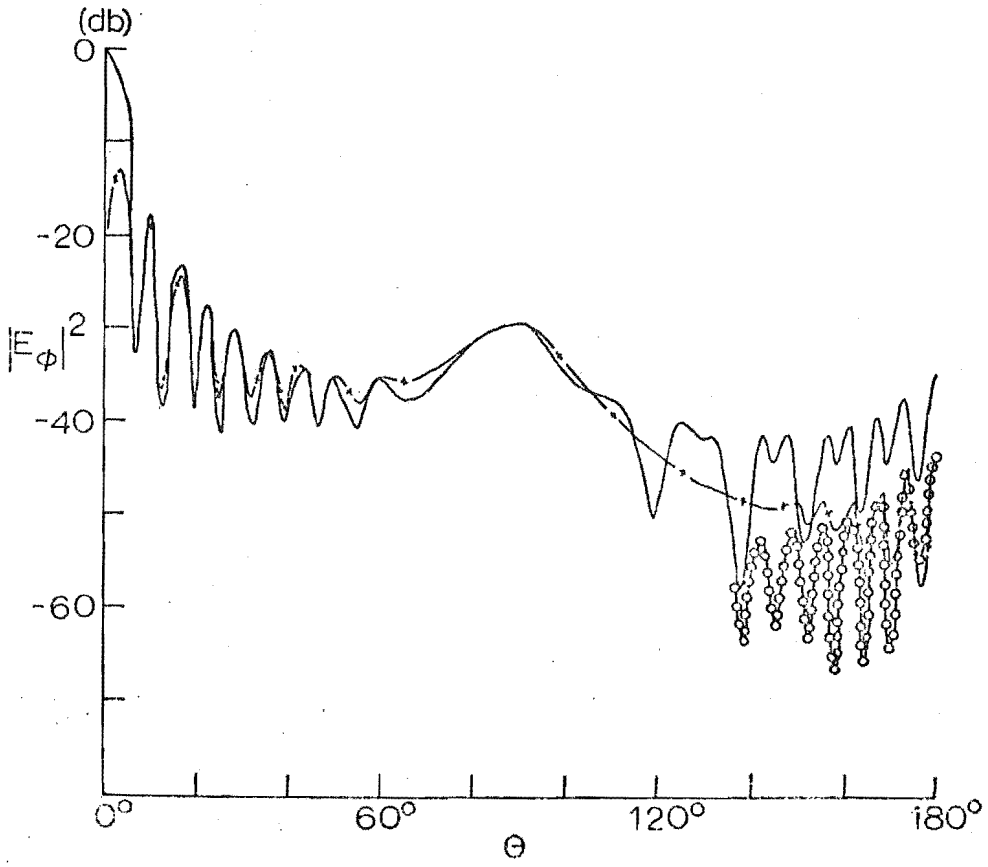

Fig. 4.4 H-plane field scattered from paraboloid illuminated by a short dipole; $f/D = 0.25$, $D = 10\lambda$.

———— Physical optics

——+—— Equivalent current (from James and Kerdemelidis, 1973)

—o—o— Edge correction current

we get a result in the forward axial region similar to that obtained for the reflector as given in Fig. 4.4. Using plane-wave coefficients in the equivalent current formulation of (4.26) for the paraboloidal reflector does not give any improvement in the forward axial region representation as obtained in the waveguide problem. This is because the limit is approached in a different manner in the three-dimensional

reflector problem from that in the two-dimensional waveguide problem. Also, on the axis itself we must include the geometrical optics field.

Away from the axial regions, the stationary phase formulation of (4.29) yields the edge diffraction result. Thus the field is then given, by the ray tracing methods of the GTD, from currents on the reflector surface lying in the H-plane. This is also a well-known characteristic of the physical optics formulation for the field away from the axis. In the forward direction the edge correction current field to physical optics given by (4.19) has a negligible effect. Therefore, the very good agreement between the two methods in the forward direction demonstrates that the GTD includes physical optics effects. This is to be expected since physical optics is formulated with currents taken over a finite body and will include edge diffraction effects. Near the forward-axis, Fig. 4.4 shows that edge diffraction has a negligible effect on the radiation pattern.

In the shadow region of the reflector, the currents are ignored in the physical optics approach but are accounted for implicitly in the equivalent current formulation. Hence the latter method will be expected to be more accurate in this region. Fig. 4.4 shows that there is a significant difference between the two methods in the shadow region.

In directions behind the reflector it would be reasonable to speculate that contributions from the exact induced currents on the illuminated surface of the reflector to be completely cancelled by the primary source of illumination. The field would then be given entirely by the currents on the shadow side of the reflector. Since physical optics is an

approximation, the cancellation with the primary source is not complete in directions behind the reflector as seen from Fig. 4.4. The addition of the edge correction current to physical optics, discussed in 4.12, does not give a significant reduction in the resultant field. An alternative approach is to assume that the shadow region field is given only by the edge correction currents on the back of the reflector. We then have the field given directly by (4.19) for the H-plane. This has been plotted in Fig. 4.4 for the back axial region. A comparison with GTD can only realistically be made in this region where there is no blocking effect of the reflector. The two approaches do not give identical results since one method uses a direct far-field approximation from the half-plane solution and the other approximates the currents on the curved surface of the reflector from the currents in the shadow region of the half-plane.

The various theoretical predictions for the scattered field from the reflector in the E-plane are given in Fig. 4.5.† For the edge diffraction approach, this is an example where, without the slope-wave term, the commonly used stationary phase formulation of (4.28) fails since the incident field is zero at the stationary phase points. With the slope-wave term included by using (4.40) we see from Fig. 4.5(b) that, except for the lateral region, the sidelobe level is considerably lower than that predicted by physical optics. The GTD formulation of (4.40) is only a local edge effect, whereas physical optics accounts for currents over the entire surface of the reflector. Thus, when the currents are weak towards the edge, edge diffraction is no longer the predominant diffraction effect of the current distribution on the reflector.

† Further discussion regarding Fig. 4.5 to that given here will be found

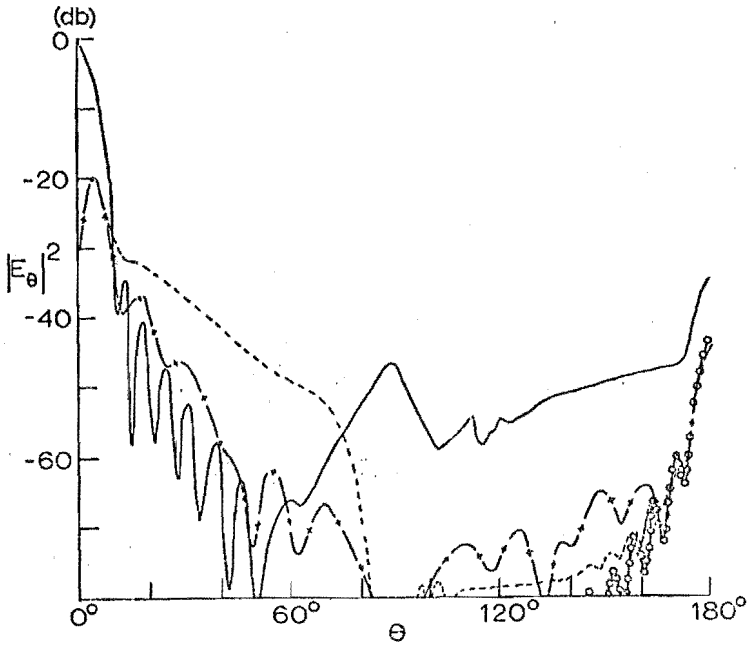

(a) without slope-wave term

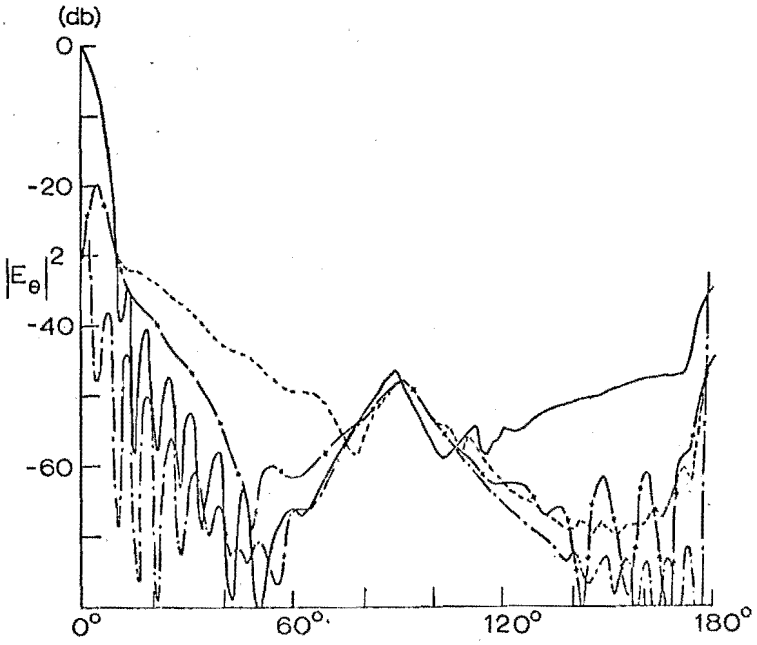

(b) with slope-wave term

Fig. 4.5 E-plane field scattered from paraboloid illuminated by a short dipole $f/D = 0.25$; $D = 10\lambda$.

——————— Physical optics

——+—— Equivalent current (from James and Kerdemelidis,1973)

- - - - - - - Equivalent current as in text

——·—— Stationary phase result from equivalent current

—o—o— Edge correction current

When we evaluate the equivalent current formulation of (4.39) we obtain results in the forward direction that differ widely from physical optics. A similar result can be had even where the edge is strongly illuminated. Fig. 4.6 gives the H-plane for a uniformly illuminated focal-plane reflector.

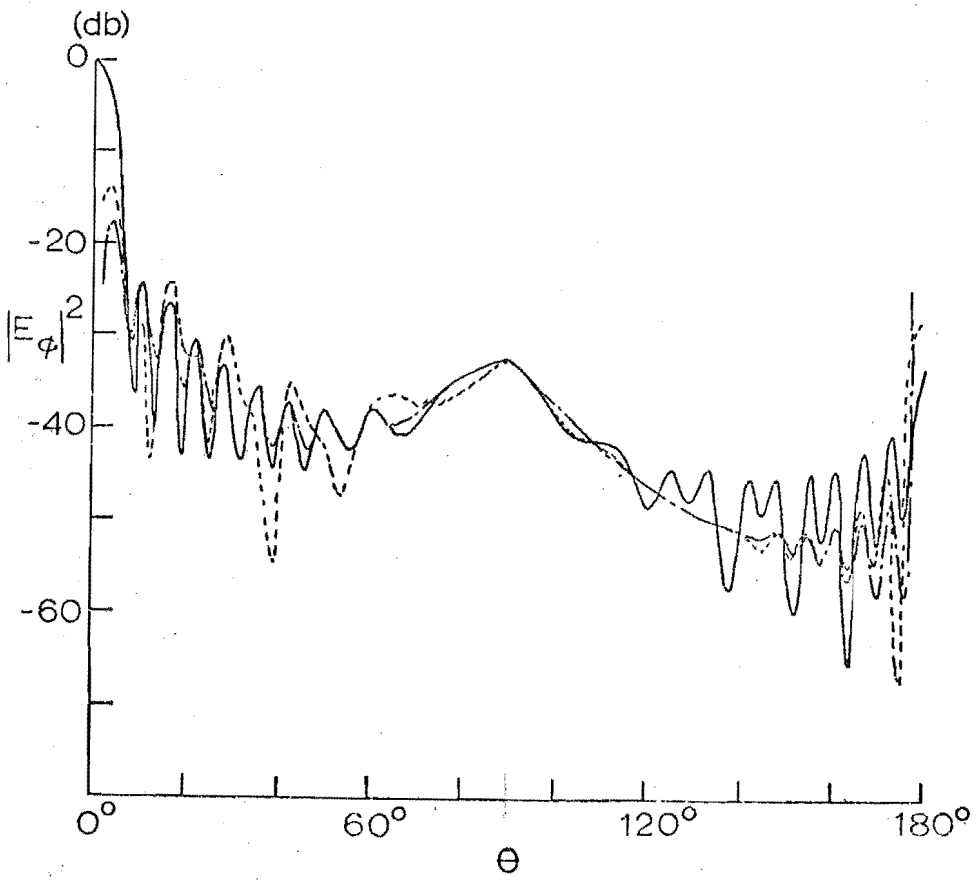

Fig. 4.6 H-plane field scattered from paraboloid for uniform illumination $f/D = 0.25$; $D = 10\lambda$

———— physical optics

- - - - - - - equivalent current as in text

—— · —— stationary phase result from equivalent current.

Excellent agreement is obtained in the forward direction away from the axis between the physical optics approach and the GTD result given by (4.40). The inclusion of the magnetic currents

(whose stationary phase points are in the E-plane) from the equivalent current approach given by (4.39) gives rise to considerable differences in the forward direction.

Away from the forward-axis the physical optics field is largely dependent on currents on the reflector surface lying in the E-plane, the currents on the remainder of the reflector tending to cancel each other out. The equivalent edge current formulation of (4.39) is, however, only the edge effect and does not completely describe the scattered field in the forward direction (as discussed earlier). We may conclude from this incomplete representation of the field that the cancelling of the currents is not as complete as in the physical optics method. Alternatively, since we can readily show that the equivalent current concept does not obey the reciprocity theorem for oblique incidence to the edge (i.e. for points on the edge away from the stationary phase points with the incoming field incident from a non-axial direction), we may conclude that the equivalent current method is invalid except when the field is at normal incidence to the edge. In other words, we cannot meaningfully extend the GTD to three-dimensions in this way. It must be noted, however, that physical optics obeys the reciprocity theorem in one direction only, the direction of specular scattering (Kouyoumjian, 1965).

In a recent paper (James and Kerdemelidis, 1973) we replaced the value of β' defined in (4.27) with that value appropriate for the stationary phase points and the axial regions, i.e.,

$$\beta' = \frac{\pi}{2} + \alpha + \theta \quad \text{for} \quad -\frac{\pi}{2} \leqslant (\phi-\phi') < \frac{\pi}{2},$$
$$\beta' = \frac{\pi}{2} + \alpha - \theta \quad \text{for} \quad \frac{\pi}{2} \leqslant (\phi-\phi') < \frac{3\pi}{2}, \tag{4.41}$$

where $0 \leqslant \beta' \leqslant 2\pi$.

With this value of β' an analytical solution was derived for the diffracted fields which gives (4.26) using (4.27) in the axial and lateral regions of the radiation pattern. Elsewhere the difference between the two solutions is considerable as shown in Fig. 4.5. The closer agreement to physical optics using the value of β' in (4.41) is achieved by the equivalent currents being modified for oblique incidence.

As a check on the validity of the equivalent current concept, we have plotted in Fig. 4.5(a) the edge correction current formulation of (4.18) for the back-axial region. This indicates that within the accuracy and validity of the $\hat{n} \wedge \underline{H}_i$ approximation to the current distribution the original equivalent current method of (4.26) using (4.27) is the correct approach for the fields in the shadow region.

We could extend the edge correction current to include the slope-wave term. The equivalent current method is to be preferred, however, because it is a simpler formulation and can readily allow for physical interpretation such as blocking effects of the reflector, higher order diffractions, creeping wave effects, etc.

To test the validity of the above theoretical methods, we carried out measurements on a focal plane reflector (f/D = 0.25) with a dipole feed as illustrated in Fig. 4.7. The measurement procedure is discussed in Appendix C. Fig. 4.8 gives the measured dipole pattern in the E-plane along with the theoretical and an approximated pattern to the measured

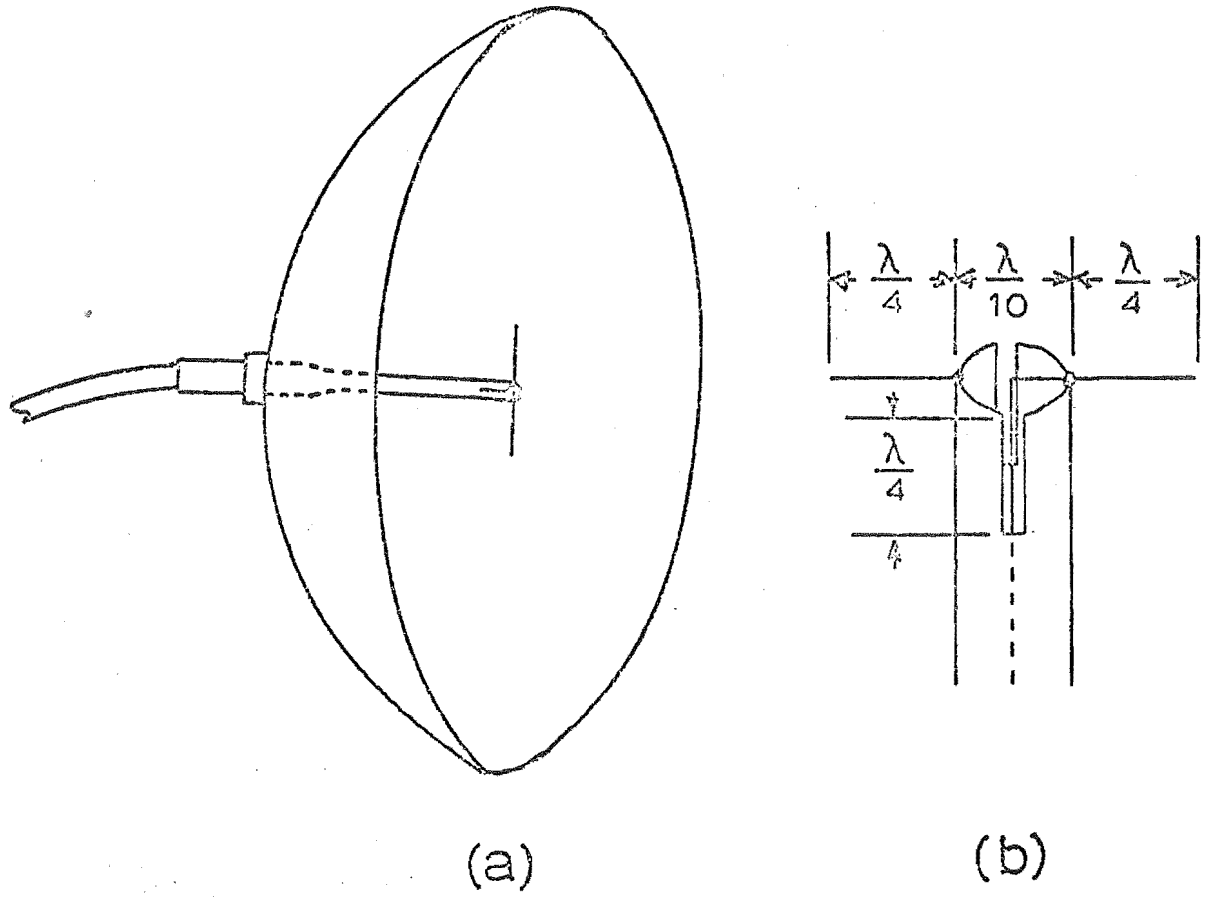

Fig. 4.7 (a) Focal-plane reflector with dipole feed; D = 10λ.
(b) Details of feed.

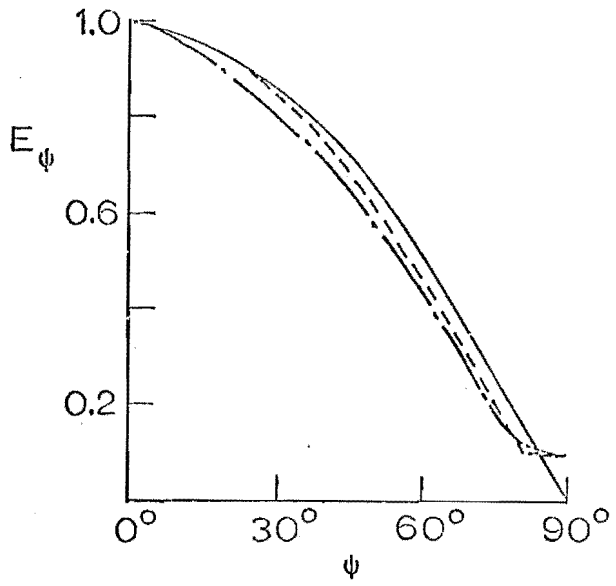

Fig. 4.8 Dipole patterns

———— Theoretical pattern; $E_\psi = \text{Cos}\ \psi$

—— - —— Measured pattern

– – – – – – Approximation to measured pattern given by

$$E_\psi = \begin{cases} \text{Cos}(\psi + 0.05\text{Sin}\psi) & \text{for } \psi \leq 80^\circ \\ 0.1 & \text{otherwise.} \end{cases}$$

result. In a practical dipole feed, the field on the axis of the dipole is finite as we see in Fig. 4.8 and $f_1(\psi_e)$ is not zero as given by the theoretical pattern. The slope-wave term, $f_1'(\psi_e)$, is reduced for the measured pattern. Although the value of $f_1(\psi_e)$ may be small, it is significant in the E-plane since it is the incident field at the stationary phase points on the reflector edge for this plane.

Fig. 4.9 gives the total radiation pattern in the principal planes for the antenna illustrated in Fig. 4.7. It is seen that the direct field from the dipole considerably alters the radiation pattern in the forward direction. The superiority of the equivalent edge current method in the shadow region is evident. The dip in the measured pattern on the back axis was caused by the feeding arrangement at the back of the reflector. With $f_1(\psi_e)$ non-zero, the only effect in the H-plane is to increase the magnitude of the back-axial field in the equivalent current formulation. The effect on the E-plane pattern is much more pronounced, where we observe that the shadow region radiation pattern is significantly different from the ideal result cited in Fig. 4.5(b). With $f_1(\psi_e)$ non-zero the slope-wave term has been relegated to a higher order effect. Combined with the reduction in $f_1'(\psi_e)$, the slope-wave term has lost its significance and has in this particular practical case only a minor effect on the radiation pattern in the lateral region.

As another example we considered a front-horn-fed reflector system where the back of the reflector was clear of obstacles as illustrated in Fig. 4.10. The radiation pattern of the small horn was calculated from the aperture field method with the assumption that the phase error across the aperture

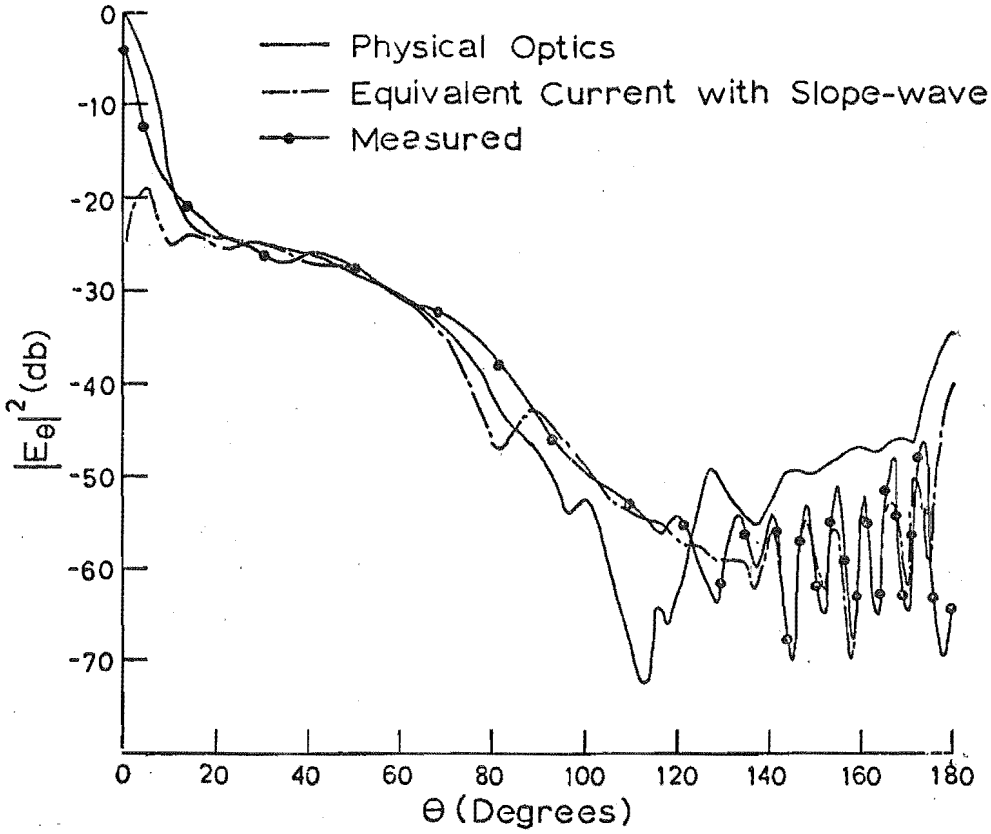

(a) E-plane

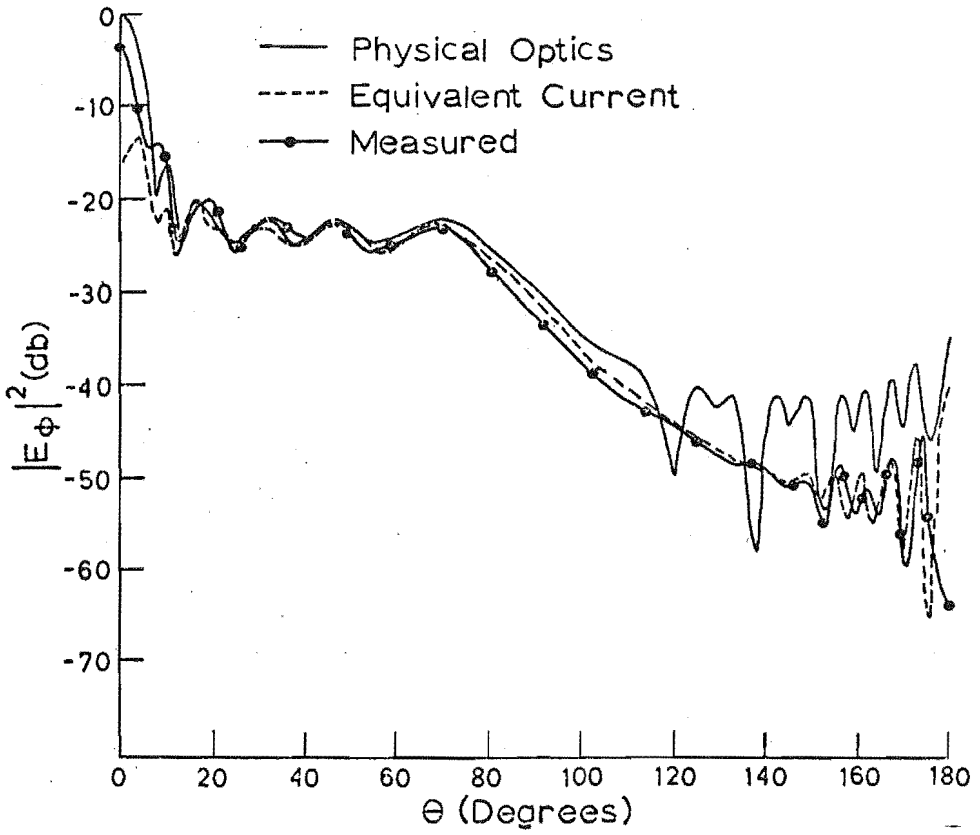

(b) H-plane

Fig. 4.9 Total field for paraboloid illuminated by a short dipole; $f/D = 0.25$, $D = 10\lambda$.

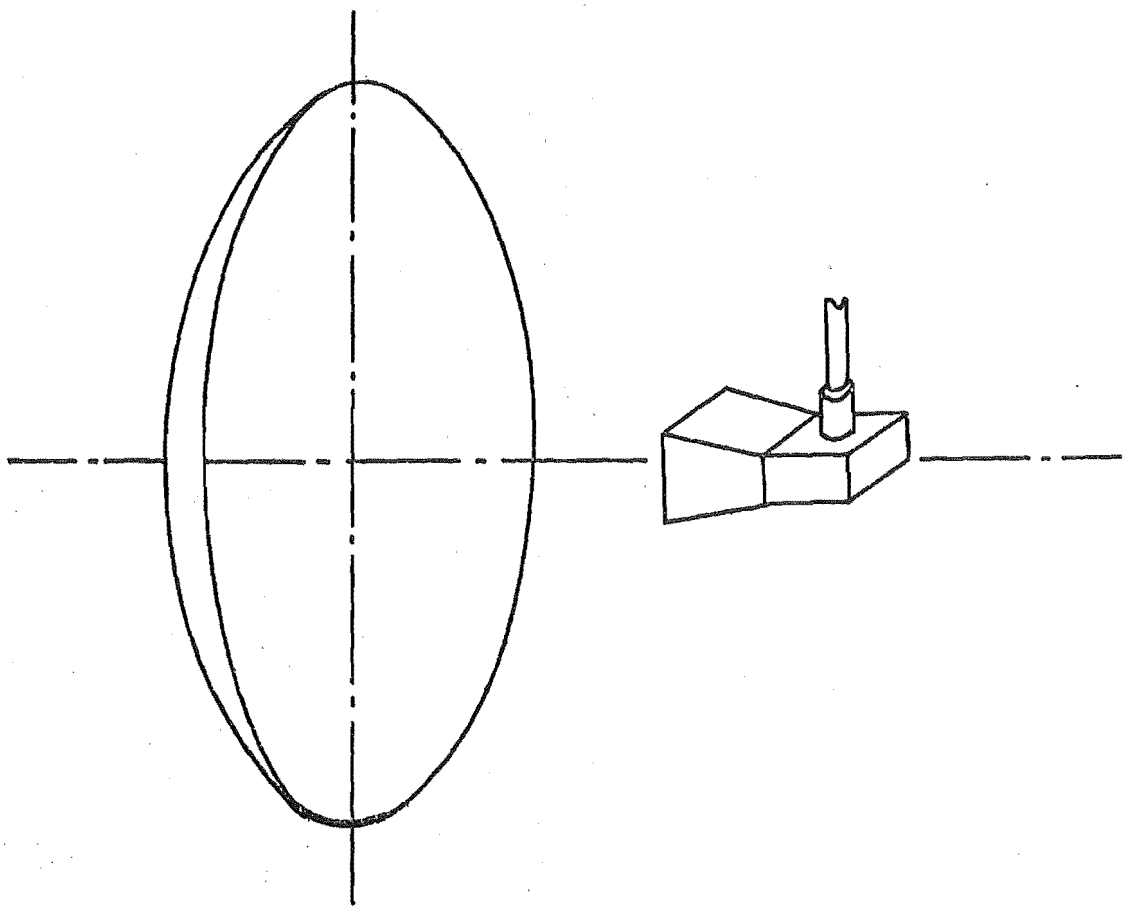

(a)

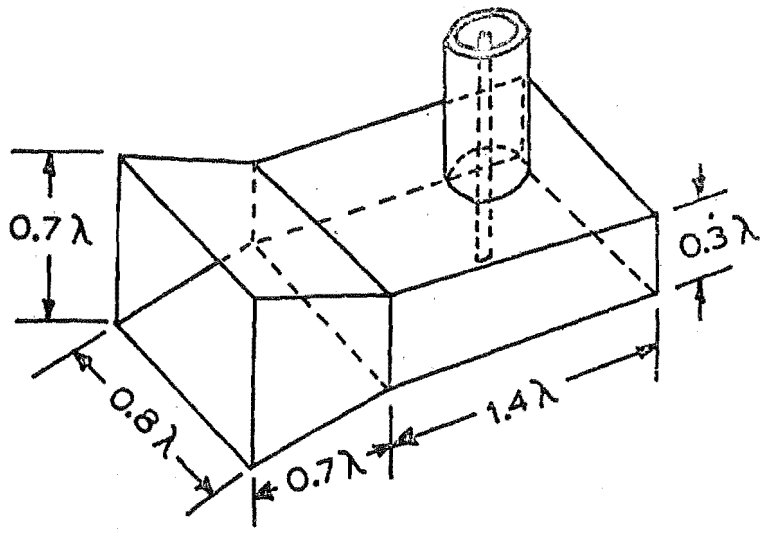

(b)

Fig. 4.10 (a) Shallow reflector with horn feed ($f/D = 0.43$)

(b) Details of feed.

is negligible. The appropriate formulas for the principal planes are given by Silver (1949c) and are shown graphically in Fig. 4.11 together with the measured patterns for the feed horn used.

For the reflector used $f/D = 0.43$, so that $\psi_e = 60^o$. From Fig. 4.11 we can see that the theoretical pattern in the principal planes of the feed horn are in excellent agreement with the measured pattern within this range of ψ. Using the aperture field equations for the functions $f_1(\psi)$, $f_2(\psi)$ we get the shadow region fields in the principal planes of the reflector as shown in Fig. 4.12 together with the measured patterns. Again the superiority of the equivalent current method is evident. The measured back axial field is this time in excellent agreement with the theory. (We do not consider the illuminated region as the theoretical result is complicated by the aperture blocking effect of the horn and support structure. In addition the direct field from the horn is not well represented by the aperture field method for $\psi > 90^o$ as shown in Fig. 4.11.)

From this section we can conclude that the physical optics and edge diffraction methods complement each other.

In the illuminated region the physical optics method is to be preferred since it accounts for the current distribution over the entire surface of the reflector. Physical optics is not readily extended to the shadow region. In this region edge diffraction methods should be used as they have been shown to accurately predict the field in the shadow and lateral regions of the radiation pattern. Both the physical optics and equivalent edge current methods have the limitation of not, in general, satisfying the reciprocity theorem.

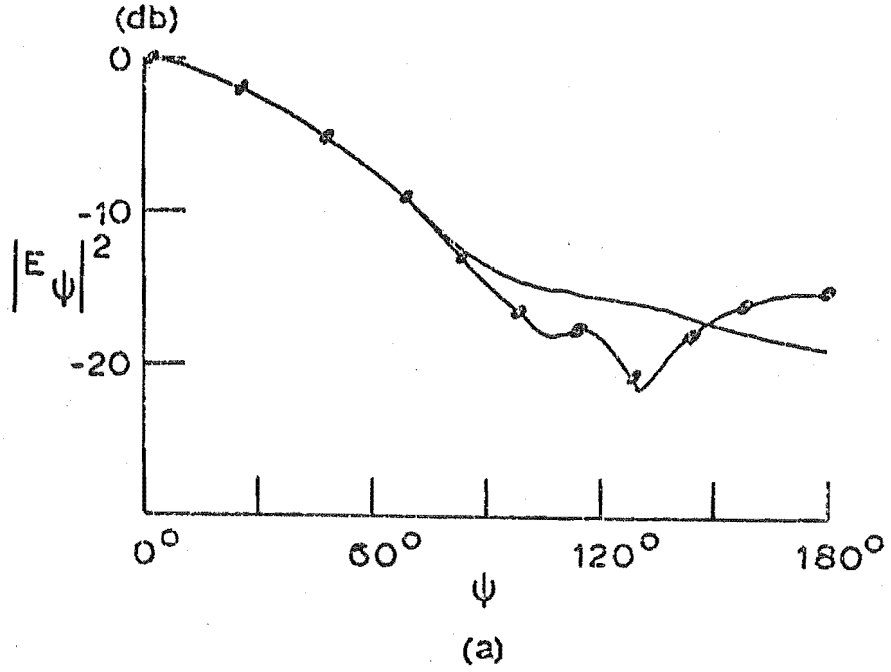

(a)

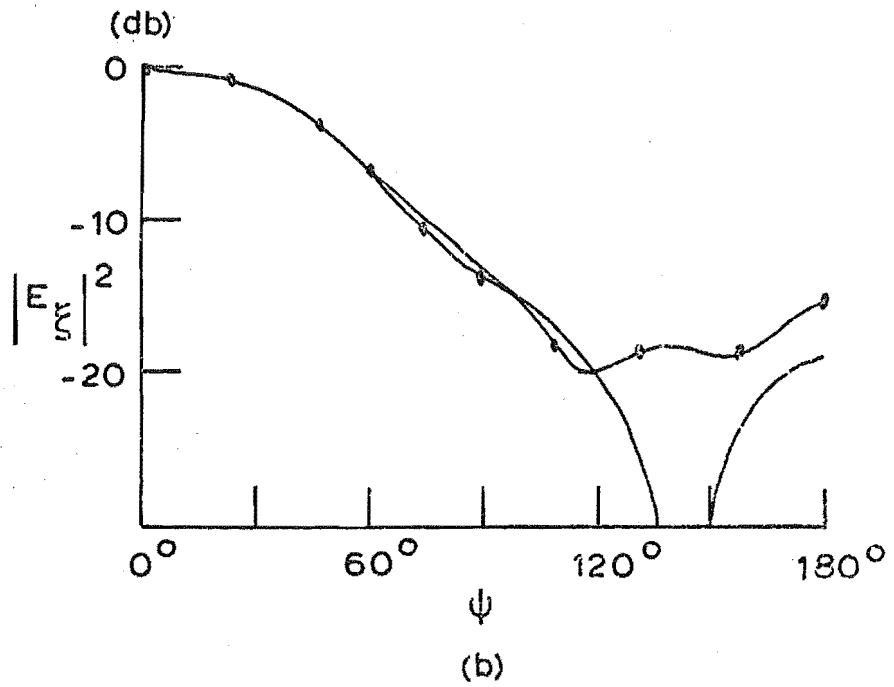

(b)

Fig. 4.11 (a) E-plane

(b) H-plane for a small horn feed

——— Aperture field method

—•—•— Measured.

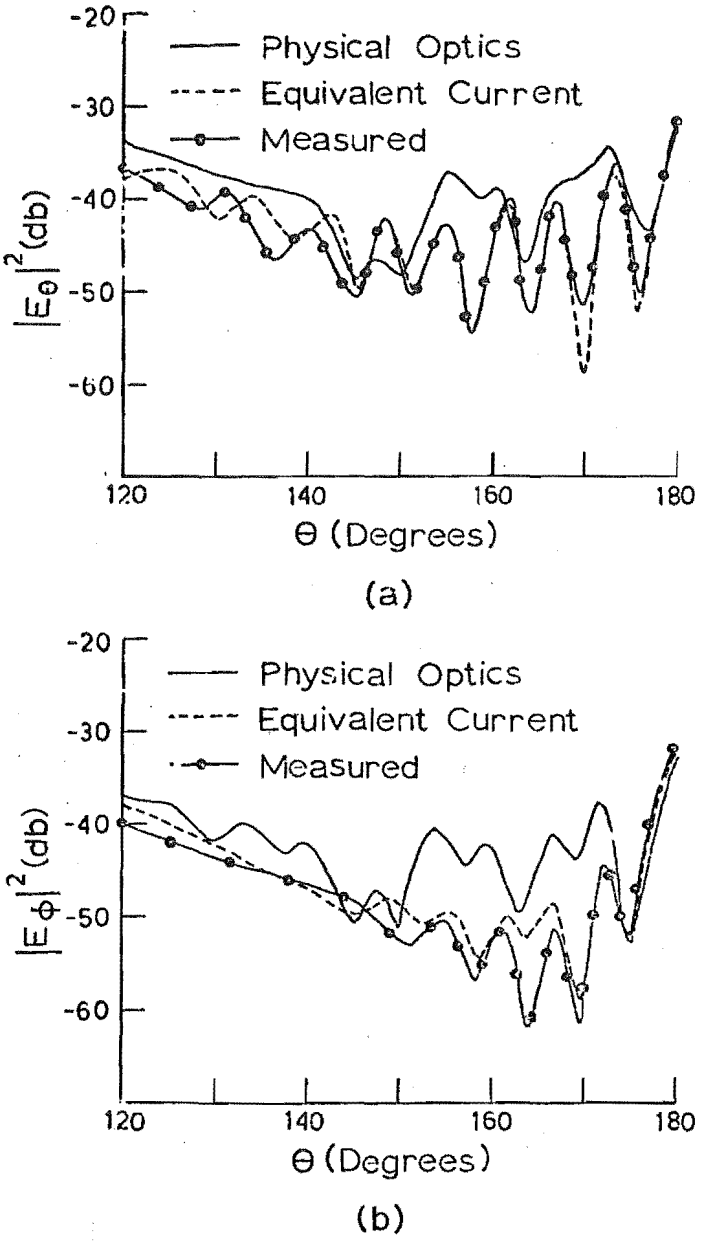

Fig. 4.12 Shadow region fields for paraboloid illuminated by a small horn, $f/D = 0.43$, $D = 10\lambda$.
(a) E-plane (b) H-plane

Table 4.1 On-axis gain

Source characteristic	f/D	D	Gain over maximum value of source function	
			Theoretical	Measured
Uniform illumination	0.25	10λ	26.7 db	
Uniform illumination	0.43	10λ	23.8 db	
Dipole feed	0.25	10λ	24 db	21 db
Horn feed	0.43	10λ	20.34db	17 db

In table 4.1 we give the on-axis gain for the radiation patterns considered in this section. The theoretical results are taken from physical optics.

4.2 EDGE PERTURBATIONS TO PARABOLOIDAL REFLECTORS

In 4.1 we found that edge diffraction methods gave satisfactory results for the radiation pattern in the lateral and shadow regions of the reflector. We now attempt to modify the radiation pattern in these regions by changing the edge geometry.

By the same procedure for the unshaped edge reflector in 4.13, we can derive an expression for the radiation field using equivalent edge currents. The problem is complicated by the edge geometry which gives rise to oblique incident edge diffraction. Consequently, the equivalent edge currents are not always oriented in the direction of the edge. We perform the analysis in Appendix B for an arbitrarily shaped edge. The only limitation is that the edge perturbation is much smaller than the radius of the reflector. Equation (B.18) is

the resultant expression for the radiation fields. For convenience we shall write (B.18) as

$$E^{d}_{\substack{\phi \\ \theta}}(\gamma_e) = \int_0^{2\pi} g_{\substack{\phi \\ \theta}}(\phi')\, e^{j\gamma_e h(\phi')}\, d\phi', \qquad (4.42)$$

where

$$g_{\substack{\phi \\ \theta}}(\phi') = \frac{a\varepsilon_1' e^{-jkr}}{4\pi r}\left[\mathrm{Cosec}^2\,\delta_0' L_e' \begin{matrix}\chi' \\ \Omega'\end{matrix} \pm \mathrm{Cosec}\,\delta_0' L_m' \begin{matrix}\Omega' \\ \chi'\end{matrix}\right] \mathrm{Sec}\gamma',$$

$$h(\phi') = (1 + \frac{f(\phi')}{a}\,\mathrm{Cos}\,\alpha)\,\mathrm{Cos}(\phi-\phi') + \frac{f(\phi')}{a}\,\mathrm{Sin}\,\alpha\,\mathrm{Cot}\,\theta.$$

The terms $\varepsilon_1, \delta_0, \gamma, L_{\substack{e \\ m}}$, $f(\phi'), \chi', \Omega'$, are defined in Appendix B. With $f(\phi') = 0$, (4.42) reduces to (4.26) for the unshaped edge reflector.

4.21 Contributions from the stationary phase points on the reflector edge

If the phase variation in $g(\phi')$ is small with respect to ϕ', then for γ_e large, we can apply the method of stationary phase directly to (4.42) as we did to the equivalent expression in 4.13 for the unshaped reflector. The major contribution to the integral in (4.42) is then taken to come from the stationary phase points on the reflector edge at which $h'(\phi') = 0$, (Erdelyi, 1956). For an unshaped reflector, there are only two such points contributing to the field in a given plane. We will call these the principal stationary phase points. When the edge is perturbed it would appear that we have considerable freedom in controlling the radiation pattern by judiciously choosing $f(\phi')$ to give us a number of stationary phase points around the reflector edge. Provided these points are well separated then the field is given as for a circular array of sources. Unfortunately we have little control over the

relative amplitude and phase of these sources as they are determined by the function $g(\phi')$. For stationary phase points other than the principal values, the amplitude of $g(\phi')$ is reduced because the shaped edge necessary to obtain these addition points gives rise to oblique incidence edge diffraction with a consequent reduction in the effective radiation into the plane under consideration. This effect is enhanced with increasing values of α. In practice, therefore, changing the edge shape in the neighbourhood of the principal stationary phase points in the most effective way of controlling the radiation pattern in those regions where the stationary phase method is applicable. If the incident field goes to zero at the principal points then the other stationary phase points will become important. For this condition, however, the side-lobes will be very low (as in the example of the E-plane for a dipole feed in Fig. 4.5) and there will be little value in attempting to reduce the radiation further.

Where the radiation pattern is given mainly from the principal stationary phase points, then the unshaped edge reflector reduces to a two-dimensional problem as explained in 4.13 and illustrated in Fig. 4.3(b). It is evident from this figure that the stepped-edge null placement technique, developed in chapter 3 for the horns, can be applied directly to the reflector with a step at the principal stationary phase points as shown in Fig. 4.13. The problem is similar to the stepped edge pyramidal horn discussed in 3.44 and illustrated in Fig. 3.24. In the region where all four sources contribute to the pattern, the null placement formula given by (3.36) may not be valid and it is necessary to compute the radiation pattern from the four sources to determine where the nulls, if

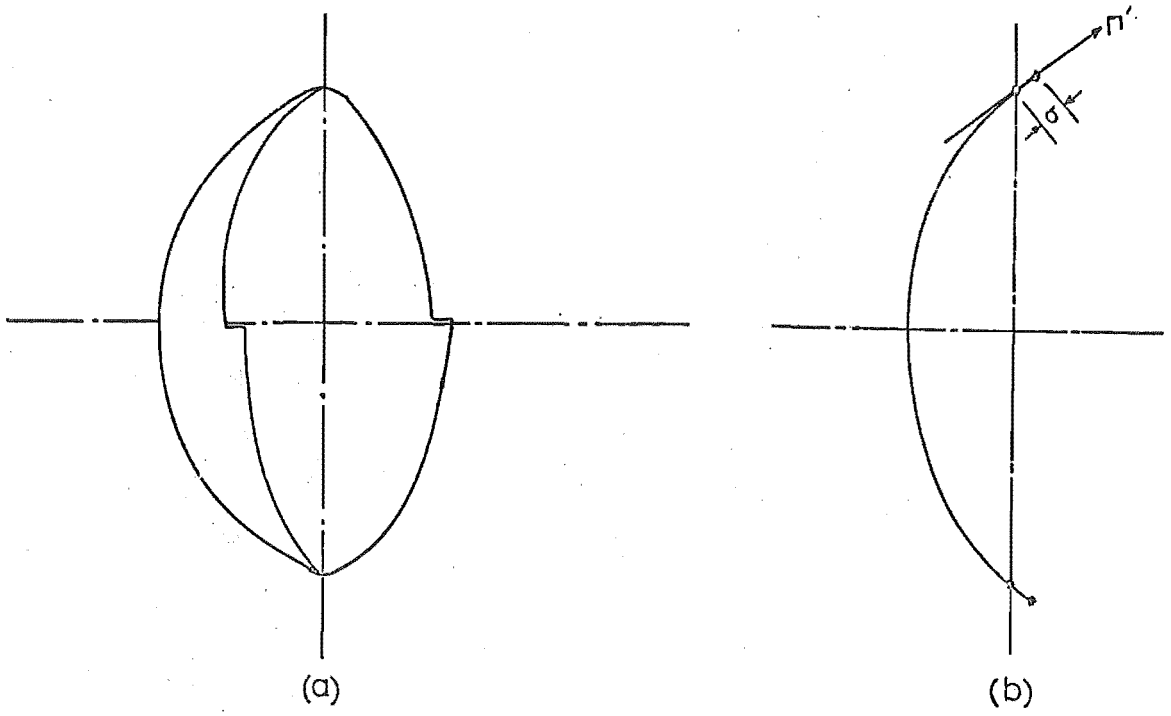

Fig. 4.13 Stepped edge reflector

any, are situated. For a focal-plane reflector (as above) we found that (3.30) was valid for the entire shadow region but did not apply in the illuminated region.

The two-source formulation given in chapter 3 to describe diffraction from a stepped edge cannot be deduced for the reflector illustrated in Fig. 4.13 by the method of stationary phase since $h(\phi')$ in (4.42) is not twice continuously differentiable for the step, and $g(\phi')$ is discontinuous. Solving (4.42) by numerical integration we find that the contribution from the equivalent currents along the $\hat{\Gamma}'$-axis in Fig. 4.13 dominate the radiation pattern in the region of the null given by the simple source formulation mentioned above. Fig. 4.14 gives the theoretical results compared to the measured pattern in the H-plane of the reflector in Fig. 4.7 for a step depth of 0.7λ . It is seen that the total solution (4.42) fails to predict the measured null in the radiation pattern.

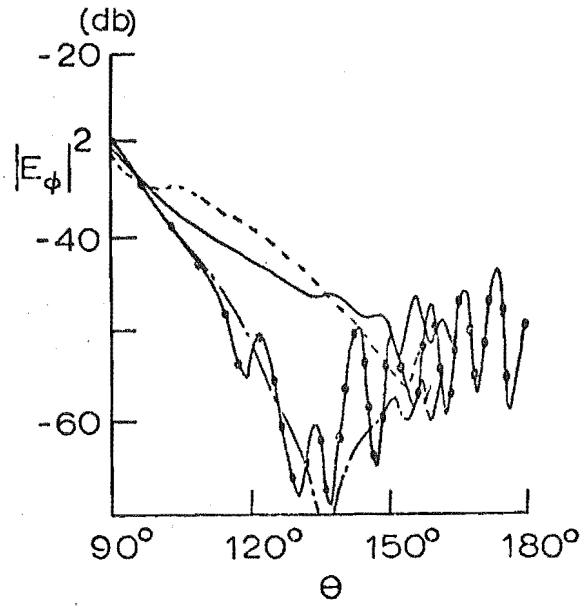

Fig. 4.14 Shadow region for stepped edge paraboloid.
$f/D = 0.25$, $D = 10\lambda$.

——— $\sigma = 0$ ⎫
—●—●— $\sigma = 0.7\lambda$ ⎭ measured

- - - - - - - $\sigma = 0.7\lambda$; equivalent current

——·—— $\sigma = 0.7\lambda$; neglecting equivalent currents along Γ'-axis in Fig. 4.13(b)

If we neglect the equivalent currents along the Γ'-axis in Fig. 4.13, then (4.42) gives the same result as the two source formulation.

The diffraction effect of a quarter-infinite screen in the z-y plane at x = 0 shown in Fig. 4.15 was considered by Horton and Watson (1950) for a normally incident plane wave to the x-axis.

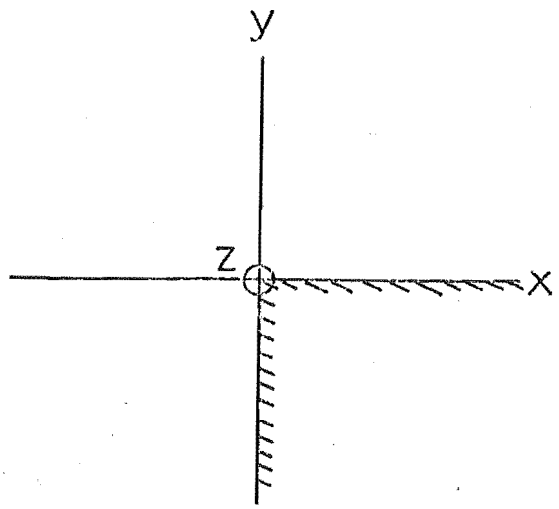

Fig. 4.15 Quarter-infinite screen in x-y plane

They considered the effect of termination of the edges at the point of intersection by assuming a source of spherical waves at the corner. The total solution is then given from the line-sources along the diffracting edges, the incident wave, and the point at the corner. Results were restricted to the shadow region where fair agreement was obtained with experiment. The measured diffraction patterns showed surprising similarity to the semi=infinite plane results. This suggests that in the z-y plane of Fig. 4.15 the diffraction equations for a semi-infinite screen are valid up to the corner; the effect of diffraction from the corner and the other edge being negligible in this plane. Our results confirmed this when we neglected the equivalent currents on the edge along the Γ'-axis in Fig. 4.13. Also, the equivalent currents on this section of the edge do not obey the reciprocity theorem (discussed in 4.14) when radiating into the H-plane, and their validity is therefore suspect.

Thus, to summarise, we may say that the application of (4.42) to an arbitrarily shaped edge reflector may be

invalidated for the following two reasons:

(1) the equivalent currents do not always obey the reciprocity theorem,

(2) corner diffraction effects are not adequately recognized.

In practice, the stepped edge can be easily achieved by placing metal plates onto the reflector rim at the appropriate positions. For the 10λ diameter reflectors used in the experiments, the width of these plates (W in Fig. 4.16) needed to be 2λ or greater; smaller widths gave less reduction in radiation at the null positions as the effect of the other edge began to be felt.

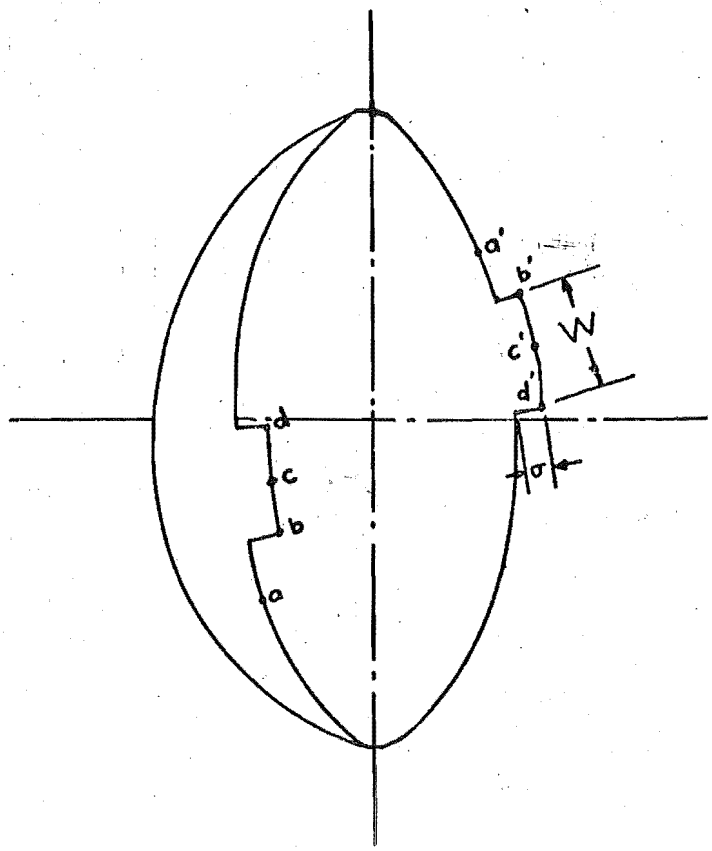

Fig. 4.16 Stepped edge reflector.

A finite width of 2λ for the plates did have the advantage of giving nearly identical patterns for the planes taken through bb', cc' and dd' in Fig. 4.16. At aa', with a separated from b by 1λ, the null was lost and the radiation pattern was close to the unshaped edge result. Measurements on the reflectors illustrated in Figs 4.7 and 4.10 indicated that for values of σ in Fig. 4.16 up to 1.5λ had little effect on the on-axis gain, the cross-polarization component in the principal plane under test, and on the radiation in the other principal plane.

Other shapes for the edge perturbation in the region of the principal stationary phase points for the reflector in Fig. 4.7 were experimentally investigated. Regular and irregular square wave, sawtooth and combinations of both were experimented with. Only one type gave significant and consistant reduction in radiation. This was the double step illustrated in Fig. 4.17(a). By a suitable choice of σ_1, σ_2, W_1 and W_2 we can obtain a reduction in radiation over a considerable section of space. Fig. 4.17(b) and (c) shows the σ_1, σ_2 components of Fig. 4.17(d) as used for a single step. With their combination in Fig. 4.17(d) an 8 db reduction is achieved in the section 100°-155°. Other values for σ_1, σ_2 gave similar results but over a smaller range of angles. In all cases the optimum results were obtained with the larger value of σ at the principal stationary phase point, $W_2 > 2\lambda$, and W_1 remaining at 1λ. (These results all refer to a 10λ diameter reflector.)

4.211 Nulls in the illuminated region

So far we have investigated the effects of the shaped edge reflector in the shadow region only. We will now briefly consider the illuminated region.

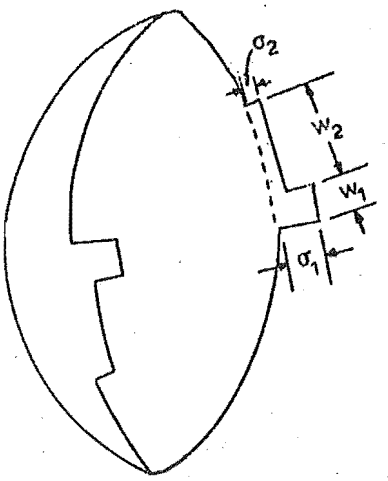

(a)

Double-stepped reflector

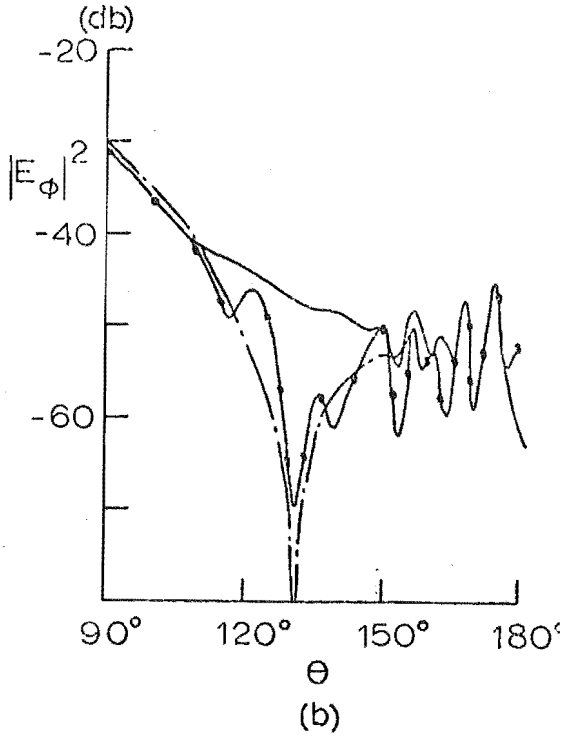

(b)

$\sigma_1 = 0.8\lambda$ $\sigma_2 = 0.\lambda$
$W_1 = 2\lambda$ $W_2 = 0.\lambda$

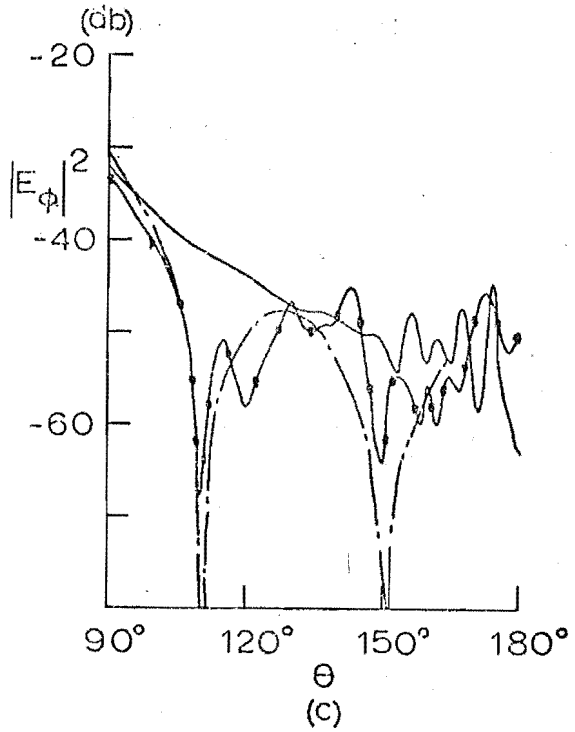

(c)

$\sigma_1 = 1.5\lambda$ $\sigma_2 = 0\lambda$
$W_1 = 2\lambda$ $W_2 = 0\lambda$

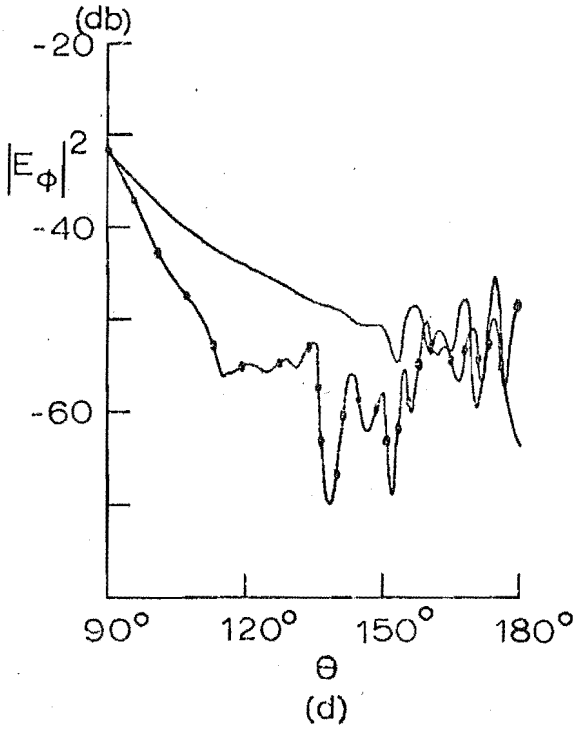

(d)

$\sigma_1 = 1.5\lambda$ $\sigma_2 = 0.8\lambda$
$W_1 = 1\lambda$ $W_2 = 4\lambda$

Fig. 4.17 Shadow region for focal plane reflector with a double-stepped edge in H-plane

——— unperturbed ⎫
———●——— perturbed ⎭ measured

——·—— equivalent current result with currents neglected along Γ'-axis in Fig. 4.13.

For a stepped edge reflector the analysis away from the axial regions for the radiation pattern is the same as for the stepped edge pyramidal horn in 3.414. In the illuminated region all the four sources contribute and any nulls must be determined by computing the field from these sources. It was shown in 4.1, however, that the GTD approach to obtain the reflector radiation pattern in forward directions is only reliable if edge diffraction effects predominate, such as for uniform illumination. Also the direct radiation from the feed is often the significant component for directions removed from the forward axis. Unless this field can be reduced to below the level being scattered from the reflector there is no point in modifying the reflector edge. Even if these difficulties are overcome, we may not be able to obtain a null in the desired direction using a stepped edge as this problem is the same as the forward direction of the pyramidal horn. Thus we can give no general characteristics and each reflector system must be considered separately.

4.22 Contributions from all points on the reflector edge

In the back-axial region the stationary phase method is not applicable and it is necessary to consider the diffraction around the entire rim. Our previous analysis has shown that a stepped edge is effective in reducing radiation in predetermined directions. For the back-axial region we must castellate (square-wave perturbation) the complete edge to obtain a similar reduction. The depth of the castellations are given from (3.36) for a particular f/D ratio. It is necessary now to determine the optimum width of the castellations (or frequency of square wave).

From the previous section it was found that a step width (W in Fig. 4.16) of 2λ gave nearly identical patterns for planes taken through the step without, appreciably, affecting the depth of the null. For values of $W < 2\lambda$ the null effect was reduced. Thus, the optimum value (with respect to front-to-back ratio) for evenly-spaced castellations, W wavelengths apart, will be expected to be around 2λ or less for a 10λ diameter reflector. This corresponds to a square-wave frequency of 8 cycles or more.

Experiments were carried out on the two reflector systems illustrated in Figs 4.7 and 4.10 for square-wave frequencies of 10, 15 and 20 cycles. For $f/D = 0.25$ the step depth from (3.36) is 0.35λ, and for $f/D = 0.43$ is 0.5λ. Of the three frequencies, 15 cycles gave the optimum result with an improvement of 4-6 db in the front-to-back over the 10 and 20 cycle square-wave frequencies. Fig. 4.18 gives the result in the H-plane for the focal-plane reflector.

Reduction of radiation by a stepped edge is a frequency sensitive technique, especially for small σ (step depth) and small α (dependent on the f/D ratio for a paraboloidal reflector) in (3.36). For example we found that for the $f/D = 0.43$ reflector, a 3% change in frequency reduced the front-to-back ratio from 50 db to 46 db, and an 8% change gave 38 db. (The unperturbed value was 30 db.) A less frequency sensitive null could be achieved by increasing σ to the next value where the null occurs in the same position, given by (3.36). The larger step depth, however, will give higher levels of cross-polarization components which may be unacceptable.

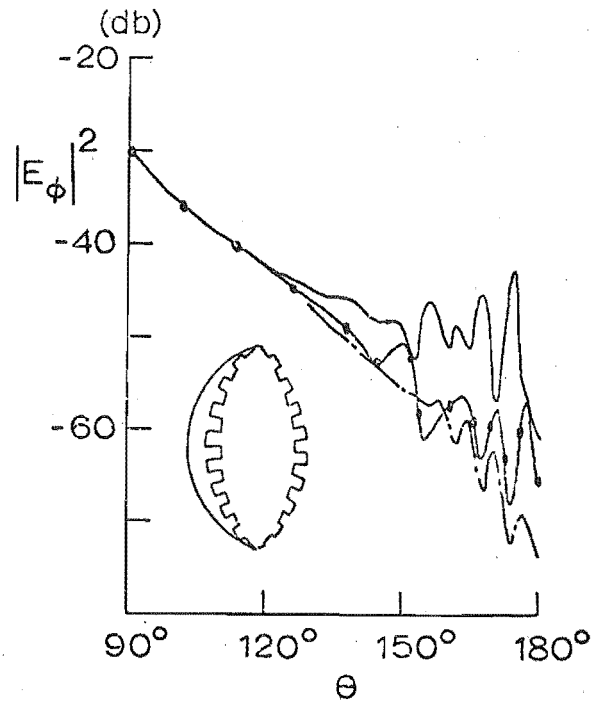

Fig. 4.18 H-plane shadow for castellated edge paraboloidal reflector, $f/D = 0.25$, $D = 10\lambda$.
Castellation freq. = 15 cycles, depth = 0.35λ.

——— unperturbed] measured
—●—●— castellated]

— - — equivalent current result neglecting currents along the steps (Γ'-axis in Fig. 4.13(b)).

Also the bigger the value of σ, the narrower is the null, and consequently the reduction in radiation will be over a narrower sector of space.

Sawtooth shaped edges were also investigated experimentally. This shape was found to behave in an analogous way to the square-wave for a depth 1.43 times greater than the square-wave. For example, a sawtooth of 15 cycles and depth 0.5λ on the edge of the focal plane reflector gave an almost identical radiation pattern in the shadow to that given in

Fig. 4.18 for the square-wave.

In Fig. 4.19 we plot the cross-polarization components in the H-plane of the focal-plane reflector for the unshaped edge, and the square-wave and sawtooth edges discussed above. We cannot read too much into this result since for each shape a different antenna was used. The indications are, however, that in ths shadow region, increases of up to 10 db can be expected in the cross-polarization component for small edge perturbations.

There was no measurable loss in the on-axis gain for the reflectors with fully castellated or sawtooth edges.

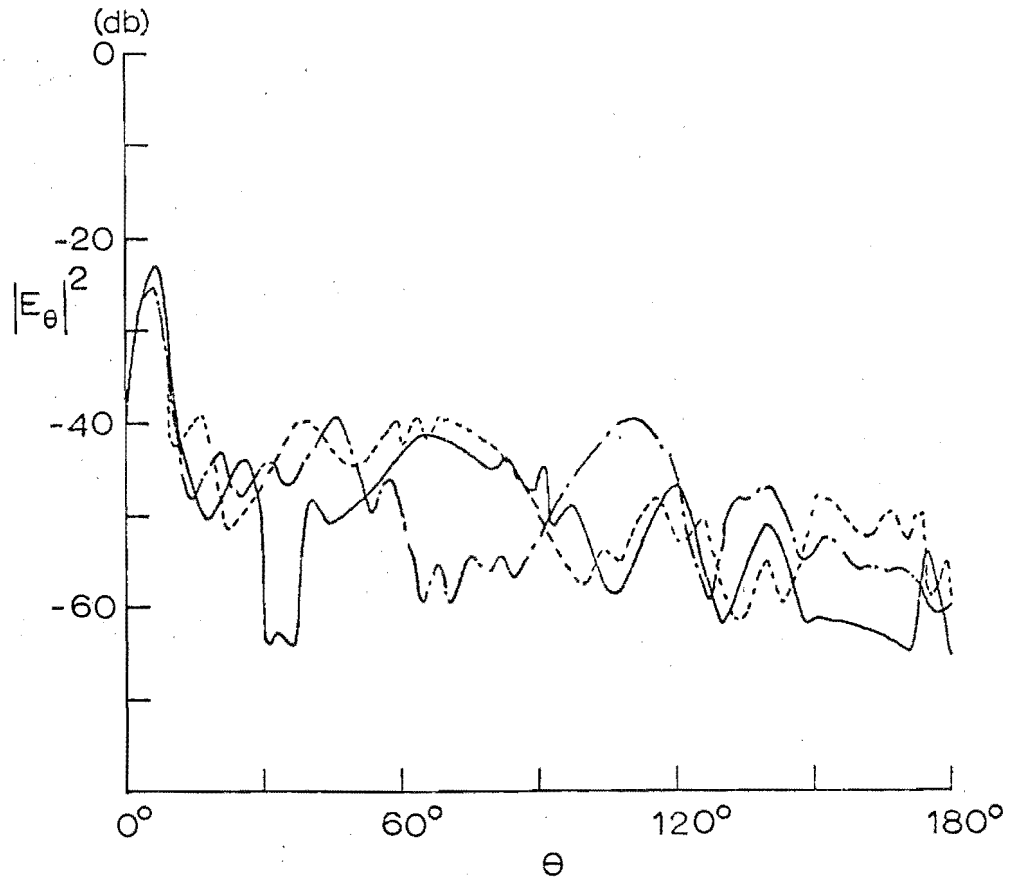

Fig. 4.19 Measured cross-polarization components in H-plane of focal-plane reflector; D = 10λ.

———— unshaped

—— - —— sawtooth, 15 cycles, 0.5λ deep

- - - - - - square-wave, 15 cycles, 0.35λ deep

CHAPTER FIVE: CONCLUSIONS

The advantage of doing one's praising for oneself is that one can lay it on so thick and exactly in the right places.

Samuel Butler (1835-1902)

In the preceding chapters we have assessed the effect of the edges in radiation pattern analysis of horn and reflector type antennas. Edge diffraction methods have been shown to be particularly useful in evaluating the field in the lateral and far sidelobes where the classical methods of physical optics and aperture field integration fail. In forward directions, however, the edge diffraction approach does not always give an adequate representation of the field. In these cases the classical methods must be used.

For three-dimensional problems, the GTD is replaced by the equivalent edge current concept. In common with physical optics, this method, in general, fails to obey the reciprocity theorem, and results must be treated with caution.

A simple, but frequency sensitive, null-placing technique has been developed by shaping the antenna edge in the form of a step at the critical point of radiation. The diffraction effect of the step was adequately represented in two-dimensions by the GTD, but our attempt to include the third dimension by using the equivalent edge current method failed. If an adequate description of the surface field in the neighbourhood of the step could be obtained (or, as an initial problem, the corner of a quarter-infinite screen), then it may be possible to derive diffraction coefficients applicable to three-

dimensions after the manner of Senior (1972). Alternatively, if the surface currents in the region of the step are measured, then it would be possible to obtain from the experimental data the three-dimensional diffraction effect.

A similar problem is the field in the vicinity of the corners of open-ended waveguides and horns. This will limit the application of the equivalent edge current method (as suggested in chapter 3) to this type of antenna.

The techniques and analytical methods presented in this thesis should be readily applicable to other antenna systems involving edges.

APPENDIX A: SLOPE-WAVE DIFFRACTION

The derivation of slope-wave diffraction for a half-plane begins with the results of Ahluwalia *et al.* (1968). They considered a field of the form

$$\Psi_0 \sim e^{-jks(\underline{\xi})} \sum_{m=0}^{\infty} (jk)^{-m} z_m(\underline{\xi}) \tag{A.1}$$

incident upon a screen which lies in the y = 0 plane (see Fig. A1) and has a regular edge curve $\underline{\gamma} = \gamma_0(e)$, where e denotes arc length along the edge.

The asymptotic solution for the diffracted field of the problem is given by

$$\Psi^d = \frac{e^{-jks'(\underline{\xi})}}{\sqrt{k}} \sum_{m=0}^{\infty} (jk)^{-m} z'_m(\underline{\xi}). \tag{A.2}$$

Previously, only the first term of this asymptotic series was given by the GTD. Ahluwalia *et al.* give the functions z'_m recursively along the diffracted rays as

$$z'_m(\rho) = \frac{\delta_m(e,\phi)}{\chi(\rho)} - \tfrac{1}{2} \int_0^{\rho} \frac{\chi(\rho')}{\chi(\rho)} \Delta z'_{m-1}(\rho')d\rho', \tag{A.3}$$

$$m = 0,1,2,\ldots$$

where $\chi = |\rho(1 + \frac{\rho}{\sigma})|^{\frac{1}{2}}$, σ denotes the radii of curvature of the edge, and the finite part integral $\int\!\!\!\!\!\!-$ is defined as follows. For $\tau \geq 0$, let $f(\tau)$ have an asymptotic expansion in powers of τ as $\tau \to 0$. Let $f_\infty(\tau)$ denote the negative powers of τ. Then the finite part of $f(\tau)$ as $\tau \to 0$ is defined by

$$\underset{\tau \to 0}{\text{fin}}\, f(\tau) = \lim_{\tau \to 0} [f(\tau) - f_\infty(\tau)]. \tag{A.4}$$

If $\int_0^a g(u)\,du$ is divergent or convergent at $u = 0$, then the finite part of the integral is defined as

$$\oint_0^a g(u)\,du = \underset{\tau \to 0}{\text{fin}} \int_\tau^a g(u)\,du. \tag{A.5}$$

For the non-uniform expansion given by Ahluwalia *et al.*, which is valid away from the shadow boundaries and the edge, δ_m is given by

$$\delta_m = \sum_{n=0}^{m} D_n z_{m-n}, \tag{A.6}$$

where the diffraction coefficients D_n are given by

$$D_{n\,\substack{a\\f}} = D_n(\varphi) \mp D_n(2\pi-\varphi) \quad \text{for } -\pi \leqslant \varphi \leqslant \pi, \tag{A.7}$$

with φ as given in Fig. A1. D_n are linear operators defined by

$$D_n z = -\frac{1}{2\sqrt{j\pi}} (\tfrac{1}{2})_n \underset{\rho \to 0}{\text{fin}} [(\sqrt{s'-s})^{-2n-1} \chi z], \tag{A.8}$$

where $(\frac{1}{2})_n$ has been defined in (2.37).

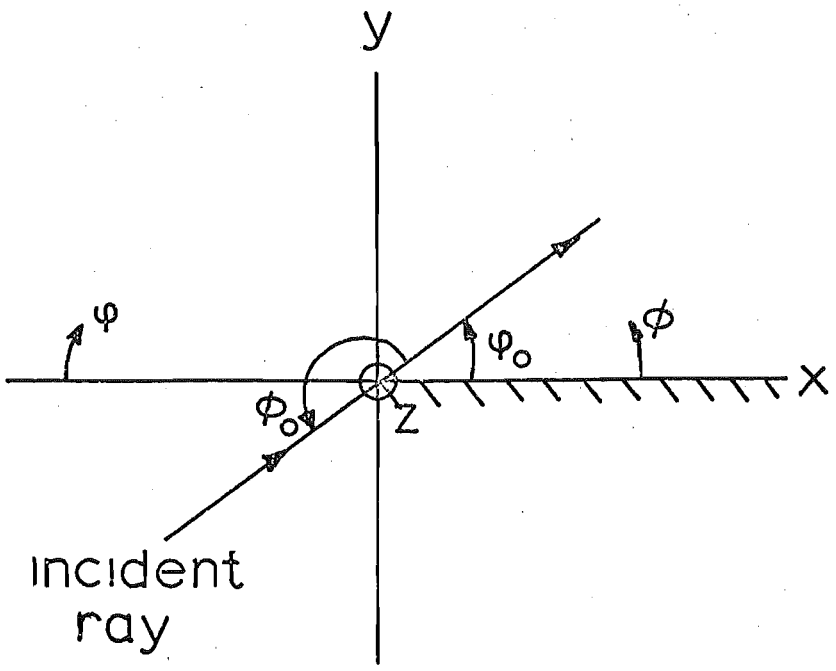

Fig. A1 Semi-infinite screen

For the correction term z_1', Ahluwalia *et al.* evaluate $D_1 z$ as

$$D_1 z = -\frac{1}{\sqrt{2^7 j\pi}}(\text{Sin}\ \theta_0 \text{Sin}\ \tfrac{\alpha}{2})^{-3}\left[\left(\frac{1}{2\sigma} + \frac{3b}{4\ \text{Sin}^2\theta_0 \text{Sin}^2\ \frac{\alpha}{2}}\right) z(\underline{\xi}_0) + \underline{u}.\nabla z(\underline{\xi}_0)\right], \tag{A.9}$$

where

$$\underline{u} = \text{Cos}\ \theta_0 \hat{u}_z + \text{Sin}\ \theta_0\ \text{Sin}\ \varphi \hat{u}_y - \text{Sin}\ \theta_0 \text{Cos}\ \varphi \hat{u}_x, \tag{A.10}$$

$$b = \tfrac{1}{2} \sum_{i,j=1}^{3} \frac{\partial^2 s(\underline{\xi}_0)}{\partial \xi_i \partial \xi_j} u_i u_j,$$

$$\alpha = \pi - \varphi - \varphi_0.$$

Consider the special case of a normally incident non-uniform plane-wave on a half-plane. We have

$$\begin{aligned} &\sigma \to \infty, \\ &z_m = 0 \quad \text{for} \quad m > 0, \\ &\theta_0 = \frac{\pi}{2}, \\ &s = -x \text{Cos}\ \varphi_0 - y \text{Sin}\ \varphi_0, \\ &\chi = \rho^{\frac{1}{2}}. \end{aligned} \tag{A.11}$$

Hence

$$b = 0 \quad \text{since} \quad \frac{\partial^2 s}{\partial \xi_i \partial \xi_j} = 0,$$

from (A.9)

$$D_1 z = -\frac{1}{\sqrt{2^7 j\pi}} (\text{Sin}\ \tfrac{\alpha}{2})^{-3}\ \underline{u}.\nabla z(\underline{\xi}_0), \tag{A.12}$$

and from (A.3)

$$z_1' = \frac{D_1 z_0}{\sqrt{\rho}} - \frac{1}{2\sqrt{\rho}} \int_0^{\rho} \sqrt{\rho'}\ \Delta z_0'(\rho') d\rho'. \tag{A.13}$$

From 2.2 and (A.2) for scalar plane-wave diffraction we get

$$\Psi^{d}_{\substack{a\\f}} = e^{-jks'(\underline{\xi})} z'_{0\,\substack{a\\f}},$$

where

$$z'_{0\,\substack{a\\f}} = \frac{-1}{\sqrt{8j\pi k\rho}} D^{0}_{\substack{a\\f}}(\phi)\; z_0(0), \tag{A.14}$$

$$D^{0}_{\substack{a\\f}}(\phi) = \left[\operatorname{Sec}\frac{\phi-\phi_0}{2} \mp \operatorname{Sec}\frac{\phi+\phi_0}{2}\right],$$

and

$$\phi = \pi - \psi$$

$$\phi_0 = \pi + \psi_0.$$

Now

$$\Delta z'_{0\,\substack{a\\f}} = \frac{1}{\rho}\frac{\partial}{\partial\rho}\left(\rho\frac{\partial}{\partial\rho} z'_{0\,\substack{a\\f}}\right) + \frac{1}{\rho^2}\frac{\partial^2}{\partial\phi^2} z'_{0\,\substack{a\\f}} + \frac{\partial^2}{\partial z^2} z'_{0\,\substack{a\\f}}$$

$$= \frac{-1}{\sqrt{8j\pi k\rho^5}}\left[\tfrac{1}{4} D^{0}_{\substack{a\\f}} z_0(0) + G''(\phi)\right], \tag{A.15}$$

where

$$G''(\phi) = \frac{\partial^2}{\partial\phi^2}\left[D^{0}_{\substack{a\\f}} z_0(0)\right].$$

Substituting (A.15) into the second term of (A.13) we get

$$\frac{1}{2\sqrt{\rho}}\int_0^{\rho}\sqrt{\rho'}\Delta z'_{0\,\substack{a\\f}}(\rho')d\rho' = \frac{-1}{2\sqrt{8j\pi k\rho}}\left(\tfrac{1}{4} D^{0}_{\substack{a\\f}} z_0(0) + G''(\phi)\right)\int_0^{\rho}(\rho')^{-2}d\rho'$$

$$= \frac{-1}{2\sqrt{8j\pi k\rho}}\left(\tfrac{1}{4} D^{0}_{\substack{a\\f}} z_0(0) + G''(\phi)\right)\rho^{-1}.$$

Thus, in the far-field, this term becomes negligible, and

$$z_1' \sim \frac{D_1 z_0}{\sqrt{\rho}} , \tag{A.16}$$

$$D_1 z_0 = - \frac{1}{\sqrt{2^7 j\pi}} \left(\operatorname{Sin} \frac{\alpha}{2}\right)^{-3} \left[- \frac{\partial z_0}{\partial x} \operatorname{Cos} \psi + \frac{\partial z_0}{\partial y} \operatorname{Sin} \psi \right]. \tag{A.17}$$

Along the incident ray $\frac{\partial z_0}{\partial \rho} = 0$, $\frac{\partial z_0}{\partial x} = \frac{\partial z_0}{\partial \phi_0} \operatorname{Sin} \psi_0$, $\frac{\partial z_0}{\partial y} = - \frac{\partial z_0}{\partial \phi_0} \operatorname{Cos} \psi_0$, where $\frac{\partial z_0}{\partial \phi_0} = \left.\frac{\partial z_0}{\partial \phi}\right|_{\phi=\phi_0}$. Now (A.17) becomes

$$D_1 z_0 = \frac{1}{\sqrt{2^5 j\pi}} \frac{\operatorname{Sin} \frac{\psi+\psi_0}{2}}{\operatorname{Cos}^2 \frac{\psi+\psi_0}{2}} \frac{\partial z_0}{\partial \phi_0} . \tag{A.18}$$

From (A.16), (A.18) and (A.7) we get

$$z_{1\,a,f}' = - \frac{1}{2\sqrt{8j\pi k\rho}} \left[\frac{\operatorname{Sin} \frac{\phi-\phi_0}{2}}{\operatorname{Cos}^2 \frac{\phi-\phi_0}{2}} \pm \frac{\operatorname{Sin} \frac{\phi+\phi_0}{2}}{\operatorname{Cos}^2 \frac{\phi+\phi_0}{2}} \right] \frac{\partial z_0}{\partial \phi_0} . \tag{A.19}$$

If $D_{a,f}^0(\phi)$ is differentiated with respect to ϕ_0, then

$$\frac{\partial}{\partial \phi_0} D_{a,f}^0(\phi) = - \tfrac{1}{2} \left[\frac{\operatorname{Sin} \frac{\phi-\phi_0}{2}}{\operatorname{Cos}^2 \frac{\phi-\phi_0}{2}} \mp \frac{\operatorname{Sin} \frac{\phi+\phi_0}{2}}{\operatorname{Cos}^2 \frac{\phi+\phi_0}{2}} \right] \tag{A.20}$$

Thus, $z_{1\,a,f}' = \frac{1}{\sqrt{8j\pi k}} \frac{\partial}{\partial \phi_0} D_{a,f}^0 \left.\frac{\partial z_0}{\partial \phi}\right|_{\phi=\phi_0}$.

From (A.2) we get

$$\psi_{a,f}^d = - \frac{e^{-jks'(\xi)}}{\sqrt{8j\pi k\rho}} \left[D_{a,f}^0(\phi) z_0(0) - \frac{1}{jk} \frac{\partial}{\partial \phi_0} D_{a,f}^0(\phi) \left.\frac{\partial z_0(0)}{\partial \phi}\right|_{\phi=\phi_0} \right] . \tag{A.21}$$

The second term in (A.21) verifies the slope-wave diffraction analysis of Rudduck and Wu (1969), and agrees with the approach taken by Keller (1962) for the special case when $\phi_0 = 0, \pi$.

Although the above derivation was for a half-plane, (A.21) can be used for wedge when $N \neq 2$. This procedure, however, has not formally been proved for the general wedge.

APPENDIX B: RADIATION PATTERN ANALYSIS FOR REFLECTOR ANTENNAS WITH EDGE PERTURBATIONS USING EQUIVALENT EDGE CURRENTS

In this appendix we derive the far field expressions for a shaped edge reflector using the method of equivalent edge currents. We begin the analysis by considering a disc illuminated from a point source (Fig. B.1) with deviations in the shape of the edge about a basic unperturbed circular disc of radius a.

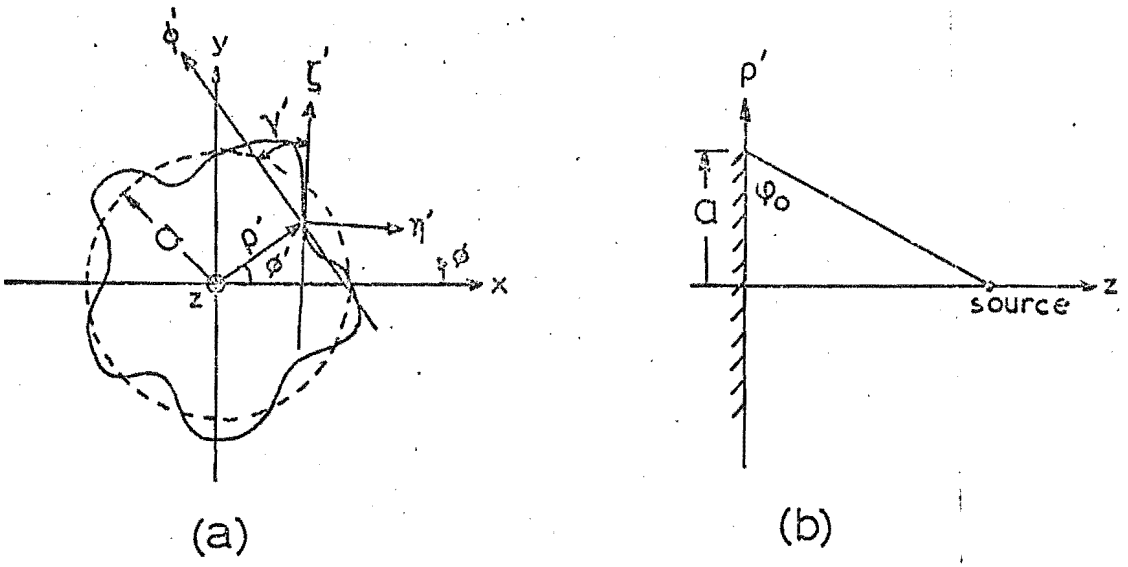

Fig. B.1 Shaped-edge disc

For an arbitrarily shaped edge the following equation can be written

$$\rho' = a + f(\phi'), \tag{B.1}$$

where a is the radius of the unperturbed disc, and $f(\phi')$ describes the perturbation of the edge at ϕ'. Differentiating (B.1) with respect to ϕ we can obtain the angle, γ, between the $\hat{\phi}$-axis and the tangent to the edge at each point, i.e.,

$$\frac{\partial \rho'}{\partial \phi} = f'(\phi') \approx a \text{ Tan } \gamma', \tag{B.2}$$

provided $a >> f(\phi)_{max}$. Also for this condition, the angle, ψ_0, of the incident field to the ρ-axis in Fig. B.1(b) can be assumed to have the same value as for the unperturbed disc. The value of this angle is independent of ϕ for the source on the axis of the circular disc as shown in Fig. B.1(b). For the equivalent edge currents we need to know the angle of incidence to the edge and to the illuminated surface of the wedge (Θ_0, ϕ_0, respectively, as in (2.89)). At each point on the edge of the shaped edge disc we can readily show that the corresponding angles, δ_0', β_0', of the local coordinate system (given by Fig. B.2(b) with Λ' replaced by z) are related to ψ_0, γ' as follows:

$$\begin{aligned} \text{Cos } \delta_0' &= \text{Cos } \psi_0 \text{ Sin } \gamma', \\ \text{Cos } \beta_0' &= \text{Cos } \psi_0 \text{ Cos } \gamma' \end{aligned} \tag{B.3}$$

At the point (ρ', ϕ') in Fig. B.1 the local rectangular coordinates, (η', ζ', z), are related to the general cylindrical coordinate system (ρ, ϕ, z) by

$$\begin{aligned} \hat{\eta}' &= -\hat{\phi}' \text{ Sin } \gamma' + \hat{\rho}' \text{ Cos } \gamma', \\ \hat{\zeta}' &= \hat{\phi}' \text{ Cos } \gamma' + \hat{\rho}' \text{ Sin } \gamma'. \end{aligned} \tag{B.4}$$

For a reflector, (B.1) - (B.4) are valid if the edge perturbation is considered to lie in the tangent plane to the back of the reflector at (ρ', ϕ') ($\hat{\Gamma}'$-$\hat{\phi}'$ plane in Fig. B.3).

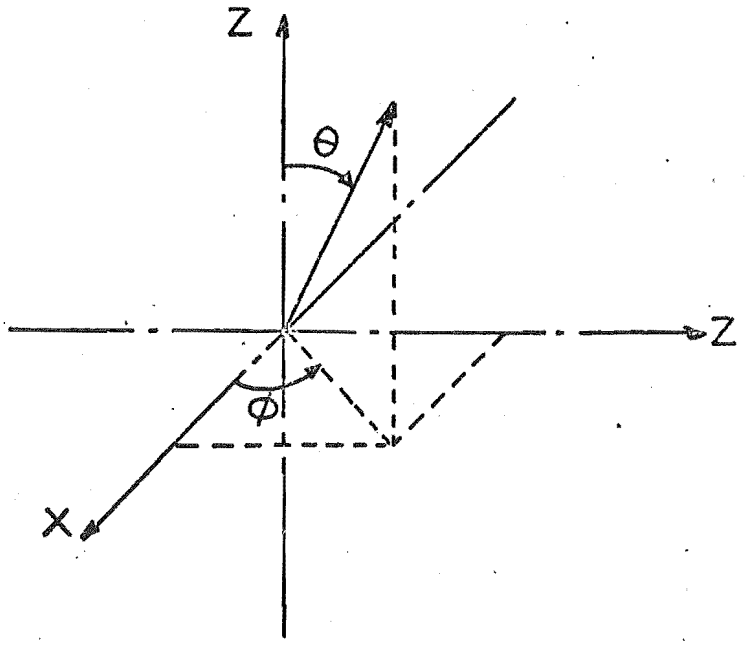

(a)

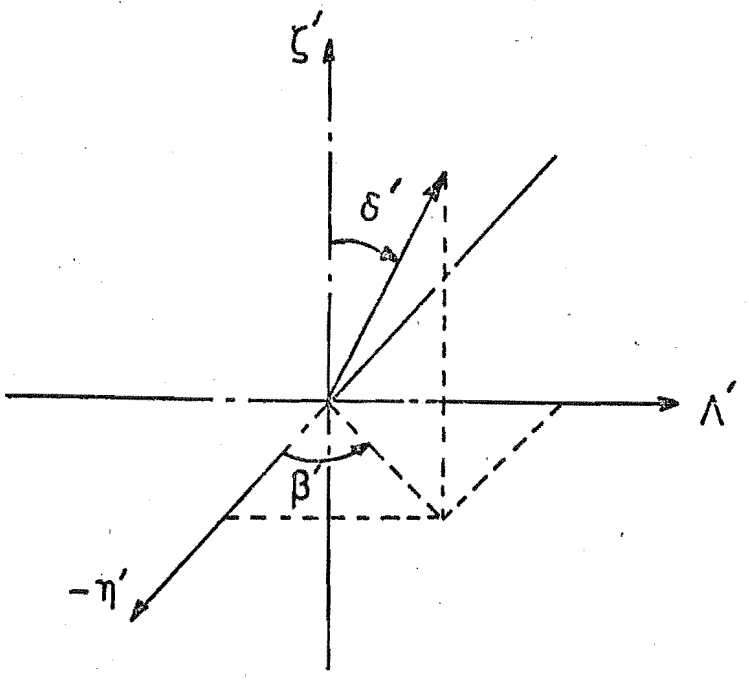

(b)

Fig. B.2 Relationships between coordinates

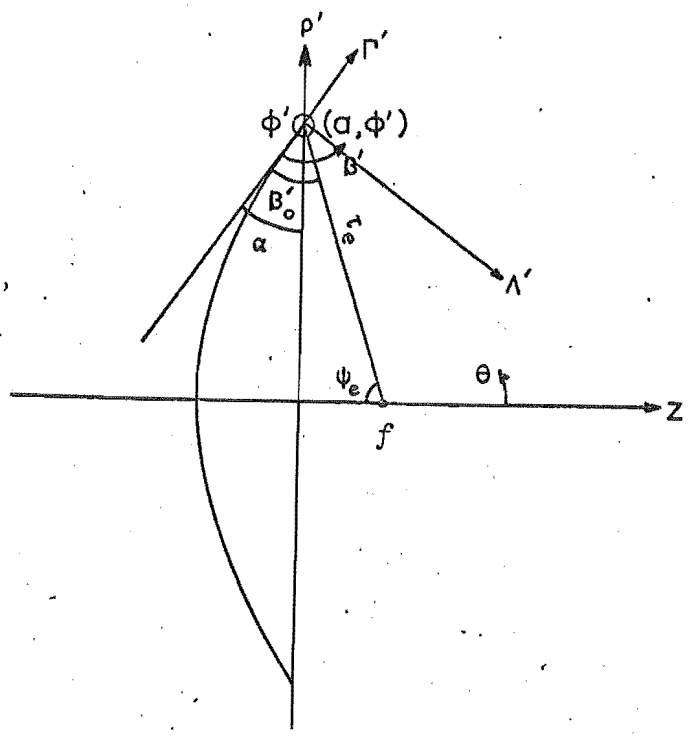

Fig. B.3 Cross-section of paraboloid through (a,ϕ')

The unit vectors $\hat{\Gamma}'$, $\hat{\Lambda}'$ (as in Fig. B.3) are related to $\hat{\rho}'$, $\hat{z}$ by

$$\hat{\Gamma}' = \hat{\rho}' \text{ Cos } \alpha + \hat{z} \text{ Sin } \alpha,$$
$$\hat{\Lambda}' = -\hat{\rho}' \text{ Sin } \alpha + \hat{z} \text{ Cos } \alpha, \qquad \text{(B.5)}$$

and (B.4) is modified to become

$$\hat{\eta}' = -\hat{\phi}' \text{ Sin } \gamma' + \hat{\Gamma}' \text{ Cos } \gamma',$$
$$\hat{\xi}' = \hat{\phi}' \text{ Cos } \gamma' + \hat{\Gamma}' \text{ Sin } \gamma' \text{ .} \qquad \text{(B.6)}$$

Equations (B.2), (B.3) remain true where ψ_0 is measured from the tangent to the reflector in the $\hat{\Gamma}'$-$\hat{\phi}'$ plane and thus given by β_0' in (4.31) for the unshaped reflector, and ρ' is

replaced with Γ'. If a is the radius of the unperturbed reflector and s is the distance from the centre of the general cylindrical coordinate system (ρ, ϕ, z) to the edge of the perturbed reflector, then

$$s \approx a + f(\phi) \text{ Cos } \alpha, \tag{B.7}$$

provided $a >> f(\phi)_{max}$.

In the general solution for the equivalent edge currents, (2.96), their orientation, $\hat{\iota}$, is given by $-\hat{\rho} \text{ Cos } \Theta_0 + \hat{z} \text{ Sin } \Theta_0$. For the local coordinates at a point (s', ϕ'), given by Fig. B.2(b), on the shaped edge of the reflector, we get

$$\hat{\iota}' = -\text{Cos } \delta_0' (\hat{\Lambda}' \text{ Sin } \beta' - \hat{\eta}' \text{ Cos } \beta') + \hat{\zeta}' \text{ Sin } \delta_0'. \tag{B.8}$$

From the general equivalent source current formulation of (2.96) we can write down the elemental equivalent source currents *at* the element of edge dC' at (s', ϕ') to yield

$$\begin{aligned} d\underline{J}' &= -\hat{\iota}' \frac{\varepsilon_1'}{j\omega\mu} \text{Cosec}^2 \delta_0' L_e' dC', \\ d\underline{M}' &= \hat{\iota}' \frac{\varepsilon_1'}{jk} \text{Cosec } \delta_0' \; L_m' \; dC', \end{aligned} \tag{B.9}$$

where

$$\begin{aligned} L_e' &= a_\zeta', I_e' + g_\zeta', I_{se}', \\ L_m' &= a_\beta', I_m' + g_\beta', I_{sm}', \end{aligned} \tag{B.10}$$

$$\varepsilon_1' = \begin{bmatrix} 0 & \text{for } \beta' < \alpha' \\ 1 & \text{for } \beta' > \alpha' \end{bmatrix}, \text{ and we have substituted}$$

$d\zeta' = \text{Cosec } \delta_0' dC'$. The blocking effect of the reflector for a shaped edge reflector is dependent on γ', θ, ϕ and ϕ'. We will not determine the expression for the general case since, as discussed in 4.2, shaping the entire edge is effective

mainly in the back axial region where no blocking occurs. For edge perturbations around the stationary phase points, the blocking effect can be given approximately as

$$\alpha' = \frac{\pi}{2} - \mathrm{Tan}^{-1} \frac{4f}{D \cos \gamma'} . \tag{B.11}$$

The equivalent currents are functions of the angles β', β_0', δ_0' at each point, where the latter two angles are given by (B.3). For the angle β' we have from Fig. B.2 the relationship

$$\mathrm{Tan}\ \beta' = \frac{-A_{\Lambda'}}{A_{\eta'}} . \tag{B.12}$$

Using the relationships

$$\mathrm{Tan}\ (\phi-\phi') = \frac{A_{\phi'}}{A_{\rho'}} ,$$

$$\mathrm{Tan}\ \theta\ \mathrm{Cos}(\phi-\phi') = \frac{A_{\rho'}}{A_z} , \tag{B.13}$$

$$\mathrm{Tan}\ \theta\ \mathrm{Sin}\ (\phi-\phi') = \frac{A_{\phi'}}{A_z} ,$$

we can express (B.12) as

$$\mathrm{Tan}\ \beta' =$$

$$\frac{\mathrm{Cos}\ \theta\ \mathrm{Cos}\ \alpha - \mathrm{Sin}\ \theta\ \mathrm{Sin}\ \alpha\ \mathrm{Cos}(\phi-\phi')}{\mathrm{Sin}\theta\,[\mathrm{Sin}(\phi-\phi')\mathrm{Sin}\gamma'-\mathrm{Cos}(\phi-\phi')\mathrm{Cos}\alpha\mathrm{Cos}\gamma'] - \mathrm{Cos}\theta\mathrm{Cos}\gamma'\mathrm{Sin}\alpha} . \tag{B.14}$$

To express the total diffracted field from the shaped edge reflector expressed in terms of the elemental source currents in (B.9) we need to express dJ_{ℓ}', , dM_{ℓ}', in terms of ϕ,θ in the general coordinate system. A straightforward manipulation of vector relationships yields

$$\begin{matrix} dJ_\phi(dM_\phi) \\ dJ_\theta(dM_\theta) \end{matrix} = dJ'_{\ell'}(dM'_{\ell'}) \begin{matrix} \chi' \\ \Omega' \end{matrix} , \qquad \text{(B.15)}$$

where

$$\chi' = \text{Cos}(\phi-\phi')[\text{Sin}\ \delta_0'\text{Cos}\ \gamma' - \text{Cos}\ \delta_0'\text{Sin}\ \gamma'\ \text{Cos}\ \beta']$$

$$- \text{Sin}(\phi-\phi')[\text{Sin}\ \delta_0'\ \text{Sin}\gamma'\ \text{Cos}\ \alpha$$

$$+ \text{Cos}\ \delta_0'[\text{Cos}\ \gamma'\ \text{Cos}\ \beta'\ \text{Cos}\ \alpha + \text{Sin}\ \beta'\ \text{Sin}\ \alpha]], \qquad \text{(B.16)}$$

$$\Omega' = \text{Cos}\ \theta[\text{Cos}(\phi-\phi')[\text{Sin}\ \delta_0'\ \text{Sin}\ \gamma'\ \text{Cos}\ \alpha$$

$$+ \text{Cos}\ \delta_0'[\text{Cos}\ \gamma'\ \text{Cos}\ \beta'\ \text{Cos}\ \alpha + \text{Sin}\ \beta'\ \text{Sin}\ \alpha]]$$

$$+ \text{Sin}(\phi-\phi')[\text{Sin}\ \delta_0'\ \text{Cos}\ \gamma' - \text{Cos}\ \delta_0'\ \text{Sin}\ \gamma'\ \text{Cos}\ \beta']]$$

$$- \text{Sin}\ \theta[\text{Sin}\ \delta_0'\ \text{Sin}\ \gamma'\ \text{Sin}\ \alpha + \text{Cos}\ \delta_0'[\text{Cos}\ \gamma'\ \text{Cos}\ \beta'\ \text{Sin}\ \alpha$$

$$- \text{Sin}\ \beta'\ \text{Cos}\ \alpha]] \ . \qquad \text{(B.17)}$$

We can now write down the diffracted far fields E_ϕ^d, E_θ^d for the shaped edge reflector from the potential integral solution of (2.8) in conjunction with (2.12), (B.9), (B.15) to give

$$\begin{matrix} E_\phi^d \\ E_\theta^d \end{matrix} = \frac{e^{-jkr}}{4\pi r} \oint_C \varepsilon_1' \left[\text{Cosec}^2\delta_o' L_e' \begin{matrix} \chi' \\ \Omega' \end{matrix} \pm \text{Cosec}\ \delta_0' L_m' \begin{matrix} \Omega' \\ \chi' \end{matrix} \right] e^{jkr'\text{Cos}\xi_{dC'}} \qquad \text{(B.18)}$$

where C is the contour of the edge, and r' Cos ξ is given from (2.10), which, for the shaped edge, becomes

$$r'\text{Cos}\ \xi = (a + f(\phi')\text{Cos}\ \alpha)\text{Sin}\ \theta\ \text{Cos}(\phi-\phi') + f(\phi')\text{Sin}\ \alpha\ \text{Cos}\ \theta . \qquad \text{(B.19)}$$

If we choose cylindrical-wave equivalents in (B.10), then the amplitude of the source in the direction of the edge is given by (4.22). Relating the directions $\hat{\psi},\hat{\xi}$ of the functions f_1, f_2 in (4.22) to the local coordinate directions ζ', β' (B.10) becomes

$$L_e' = \sqrt{\frac{8j\pi k}{\tau_e'}}\left[[f_1(2\pi-\phi',\psi_e)\sin\psi_0\sin\gamma' - f_2(2\pi-\phi',\psi_e)\cos\gamma']I_e^{c'}\right.$$
$$\left.+[f_1'(2\pi-\phi',\psi_e)\sin\psi_0\sin\gamma' - f_2'(2\pi-\phi',\psi_e)\cos\gamma']I_{se}^{c'}\right],$$

$$L_m' = \sqrt{\frac{8j\pi k}{\tau_e'}}\left[[f_1(2\pi-\phi',\psi_e)(\sin\psi_0\cos\gamma'\sin\beta_0' + \cos\psi_0\cos\beta_0')\right.$$
$$+ f_2(2\pi-\phi',\psi_e)\sin\gamma'\sin\beta_0']I_m^{c'}$$
$$+ [f_1'(2\pi-\phi',\psi_e)(\sin\psi_0\cos\gamma'\sin\beta_0' + \cos\psi_0\cos\beta_0')$$
$$\left.+ f_2'(2\pi-\phi',\psi_e)\sin\gamma'\sin\beta_0']I_{sm}^{c'}\right]. \qquad \text{(B.20)}$$

The distance from the source to the edge, τ_e', is given by

$$\tau_e' = \tau_e + f(\phi)\cos\psi_0, \qquad \text{(B.21)}$$

provided $a >> f(\phi)_{max}$.

APPENDIX C: RADIATION PATTERN MEASUREMENTS

For accurate far-field pattern measurements of an antenna, the following criteria must be satisfied:

(1) the measurements be made at a sufficiently large distance from the test antenna,

(2) the measurements carried out in an open area free of reflecting objects.

The minimum distance, a, between two antennas in a pattern measuring arrangement to ensure that the far-field pattern only is being measured, can be given as

$$a = \frac{B(d_1+d_2)^2}{\lambda} , \qquad (C.1)$$

where d_1, d_2 are the electrical aperture sizes of the antennas in the plane under test, and B is a constant. It is commonly recommended that B = 2. For experimental work where it may be difficult to realize this distance, values for B down to B = 1 are acceptable (Montgomery, 1947).

For the second criteria we found that an effective antenna range was obtained by situating it parallel to the side of a building, as illustrated in Fig. C.1, with the antenna under test suspended out of a window.

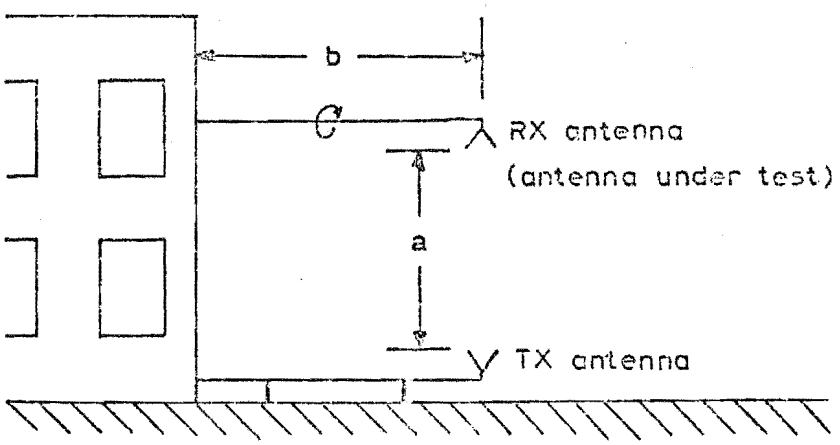

Fig. C.1

A small pyramidal horn of aperture dimensions 2.5λ by 2.5λ at 10 GHz was used as the transmitting antenna so that most of the energy was directed skyward into an object free environment. The only object of reflection to consider was the side of the building parallel to the test range (other buildings were 50-60 metres away). To minimize this reflection it was necessary to have the antennas at a sufficiently large distance out from the wall. To determine the minimum distance we could use, we carried out measurements on an antenna using the following criteria:

(1) symmetry in the radiation pattern;

(2) negligible changes in the radiation pattern with changes in distance from the wall;

(3) negligible changes in the radiation pattern with small changes in frequency;

(4) repeatability of experiments.

For paraboloidal reflector antennas 10λ in diameter with a = 5 metres, b > 2.7 metres in Fig. C.1, the above criteria were satisfied over a 50 db range within ±1 db deviation in the maxima of the radiation pattern. The value of 5 metres for a was the maximum value we could obtain and gives, at 10 GHz, a value for B in (C.1) of 1.1. Fig. C.2 shows two views of the antenna range for testing the paraboloidal reflectors 10λ in diameter.

A similar setup was used for the horn antennas except that b was shortened because of the mechanical difficulty in supporting the weight of the horns. Since the horns tested had smaller apertures than the reflectors, we were able to compensate by reducing the distance a. This was achieved by mounting the transmitting horn on a tripod stand. Site tests

Fig. C.2 View of antenna range

for the horn gave similar results as for the paraboloidal reflector.

The heterodyne detection system used in the experiments is shown in schematic form in Fig. C.3. This is a standard procedure and requires no further comment. A potentiometer coupled to the rotating shaft provided the input for the X-coordinate of the plotter. Calibration of the Y-coordinate was obtained by the variable attenuator. The system was automated by a motor driving the shaft. All experiments were carried out within the range 9 GHz-10 GHz.

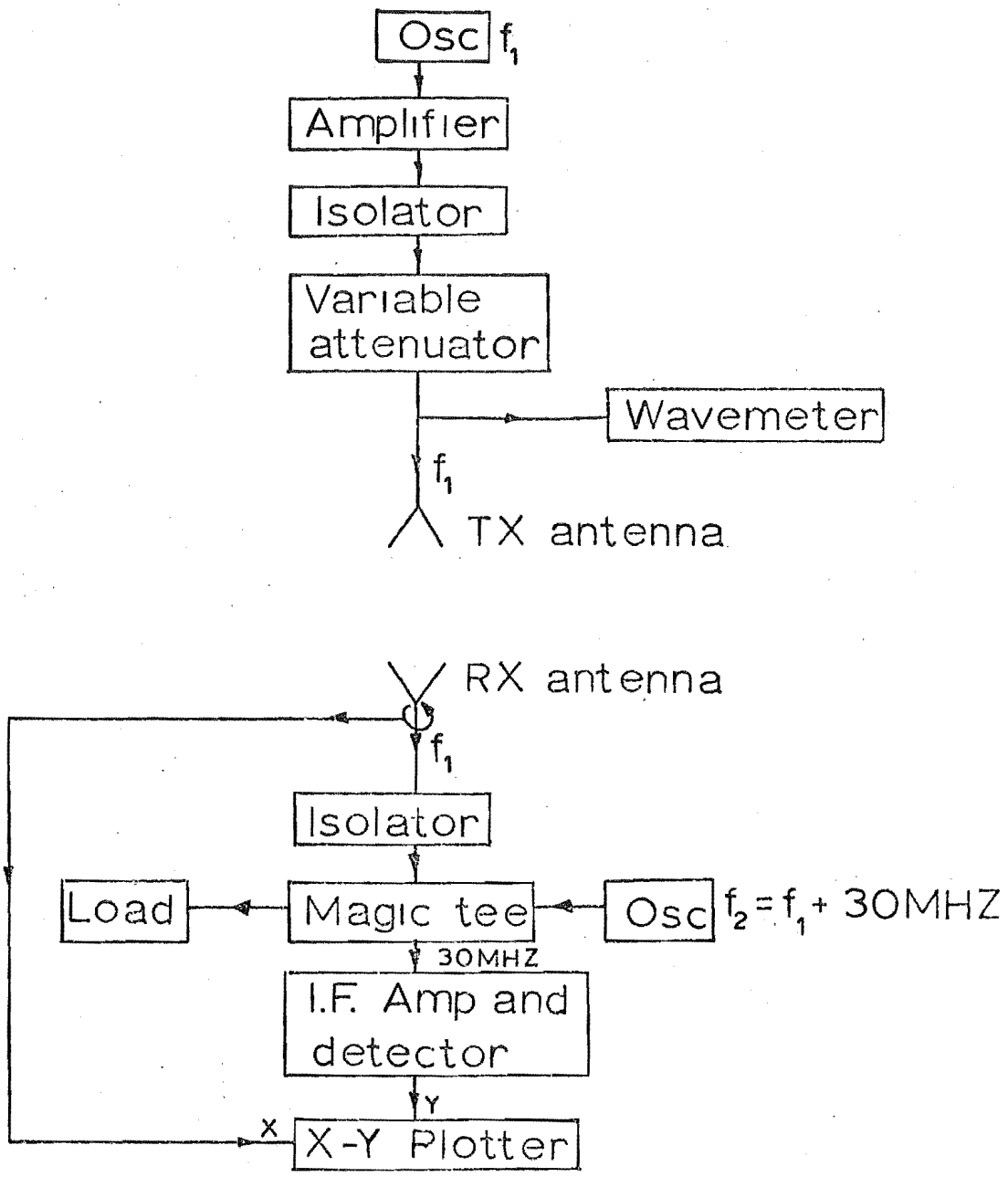

Fig. C.3 Heterodyne detection system for radiation pattern measurements.

APPENDIX D: NUMERICAL CONSIDERATIONS

The numerical evaluation of the mathematical equations in this thesis were carried out on the University of Canterbury IBM 360/44 machine. Except for using standard IBM subroutines for the generation of Bessel functions and Fresnel integrals, the computer programs were written by the author.

The mathematical formulations in chapters 2 and 3 were readily evaluated and no further comment is required. For the numerical integration of the physical optics and edge correction current formulations in 4.11, 4.12, we used the well-known Simpson's rule with Richardson's extrapolation term (Hildebrand, 1956). Convergence tests were carried out by continually halving the integration step and comparing the result with the previous answer. Integration was terminated when the difference between the modulus of two successive answers was within a specified accuracy, which we fixed at 5% for all computations. The number of integration steps was printed out with each answer. This was to check for spurious results, indicated if large differences in the number of steps to compute adjacent field points occurred, or if too few steps were taken.

The integrals of the equivalent edge current formulation in 4.13 and Appendix B are around a closed loop and are therefore periodic in nature. Numerical integration of periodic functions can be accurately computed using the simple ordinate rule (Davis and Rabinowitz, 1967). Indeed, it appears that there is no advantage in using higher order approximations. This is true for the widely used Simpson's rule since for an odd number of points, N, the mean value of

the two possible solutions for integrating a periodic function using Simpson's rule, equals the solution given by ordinate rule integration of the function for the same number of points*. Thus we used the ordinate rule for the equivalent edge current method and applied the same convergence test as given earlier for Simpson's rule.

The CPU time taken to compute a field point from the equations in chapter 3 and the stationary phase approximations in chapter 4 (i.e., all the two-dimensional formulations) was usually well within 1 sec. For the integrations in chapter 4, CPU time could take up to 40 secs to evaluate one field point, depending on the steps required for convergence, and, in the case of the edge correction current method, the limit ψ_L. The number of steps required was a function of the field angle θ, more steps being required the further θ was from the axis of the reflector. This did not hold for a shaped edge reflector where a consistently large number of steps was required for the equivalent edge current formulation to converge. This considerably increased the overall computer time to evaluate a field pattern, compared to the unshaped reflector. For an unshaped edge, the physical optics and equivalent edge current methods took approximately the same order of computer time.

---

*We are indebted to Mr R. Dunlop, Assistant Lecturer in the Electrical Engineering Department, University of Canterbury, for this observation.

APPENDIX E: SYMBOLS, NOTATIONS AND ABBREVIATIONS

The symbols and notations listed here are only those that have widespread use and a common meaning throughout the text. Other symbols are defined in each chapter or section where they are used.

Coordinate systems:

(x,y,z)	rectangular coordinates
(ρ,ϕ,z)	cylindrical coordinates
(s,φ,y)	
(r,ϕ,θ)	spherical coordinates
(τ,ξ,ψ)	

Subscripts:

a	relates to magnetic vector potential
d	diffracted field
e	electric currents
f	electric vector potential
ir	geometrical optics field
m	magnetic currents
se	slope-wave electric currents
sm	slope-wave magnetic currents

Other subscripts usually refer to the component of the field or to a particular diffracting edge.

Superscripts:

c	relates to cylindrical-wave diffraction
c	correction current to physical optics
d	diffracted field
p	plane-wave diffraction
s	slope-wave field

Prescripts:

Always refer to a particular diffracting edge.

Symbols:

a_ξ electric field component in ξ direction

a radius of paraboloid

$\underline{A}$ magnetic vector potential

c $s\sqrt{\text{Sin } \theta_0}$

D diameter of paraboloid

$\underline{E}$ electric field intensity vector

$F(\xi)$ Fresnel integral defined as $\int_\xi^\infty e^{-jt^2} dt$

f focal length of paraboloid

$\underline{F}$ electric vector potential

g_ξ electric field component in ξ direction for slope-wave term

$\underline{H}$ magnetic field intensity vector

$H_\nu^{(2)}$ ν^{th} order Hankel function of the second kind

I equivalent edge current

j $\sqrt{-1}$

$\underline{J}$ electric source current

J_ν ν^{th} order Bessel function of the first kind

k $\omega\sqrt{\mu\varepsilon}$

$\underline{M}$ magnetic source current

N $\frac{2\pi-\beta}{\pi}$ where β is the wedge angle

s $\sqrt{k\rho(1+\text{Cos } \Phi)}$

U diffraction coefficient, i.e., see (2.50)

V a component of the scalar potential Ψ, i.e., see (2.24) and (2.67)

γ_e ka Sin Θ

γ_p kF $\text{Sec}^2 \frac{\psi}{2}$ Sin ψ Sin Θ

ε permittivity of free space

λ free space wavelength

μ permeability of free space

π 3.14592

Θ_0 angle of incidence to the edge of the infinite wedge

σ depth of step (in wavelengths) in modified half-plane

T scalar potential for oblique incidence to edge

ϕ_0 angle of incidence to the infinite wedge face

Φ $\phi \pm \phi_0$

Ψ scalar potential

ω angular frequency

∇ vector operator

$\hat{\xi}, \hat{u}_\xi$ unit vector in ξ direction

Abbreviations:

GTD Geometrical Theory of Diffraction

REFERENCES

AHLUWALIA, D.S., LEWIS, R.M., and BOERSMA, J. (1968)
'Uniform asymptotic theory of diffraction by a plane screen', SIAM J. Appl. Math., Vol. 16, p.783.

BACON, J.M., and MEDHURST, R.G. (1969)
'Superdirective aerial array containing only one fed element', Proc. IEE, Vol. 116, p.365.

BAHRET, W.F., and PETERS, L. (1968)
'Small-aperture small-flare-angle corrugated horns', IEEE Trans. Antennas and Propagation, Vol. AP-16, p.494.

BARROW, W.L., and CHU, L.J. (1939)
'Theory of the electromagnetic horn', Proc. IRE, Vol. 27, p.51.

BLOCH, A., MEDHURST, R.G., and POOL, S.D. (1953)
'A New Approach to the Design of Super-Directive Aerial Arrays', Proc. IEE, Vol. 100, Pt 3, p.303.

BUCHAL, R.N., and KELLER, J.B. (1960)
'Boundary layer problems in diffraction theory', Comm. Pure and Appl. Math., Vol. 13, p.85.

BUDIN, J. (1968)
'Diffraction field of stepped fences', Elektrotehniski Vestnik, Vol. 35, p.a-21.

BUTSON,P.C., and THOMPSON, G.T. (1959)
'The effect of flanges on the radiation patterns of waveguide and sectoral horns', Proc. IEE, Vol. 106, p.422.

CORNBLEET, S. (1967)
'Progress in microwave communication antennas in the U.K.', Microwave J., Vol. 10, No. 12, p.84.

COLLIN, R.E., and ZUCKER, F.J. (1969)
Antenna Theory, McGraw-Hill, New York. Ch. 15.

CORONA, P., D'AMBROSIO, G., and FRANCESCHETTI, G. (1971)
'Reflector antennas with very high front-to-back ratio theory and experiment on models', Proc. European microwave conference, Stockholm, Sweden, 23-28 August 1971.

CRADDOCK, I.D. (1964)
'Phase-corrected E-plane horns', Proc. IEE, Vol. III, p.1379.

DAVIS, P.J., and RABINOWITZ, P. (1967)
Numerical Integration, Blaisdell Publishing Company, Waltham, Massachusetts. pp53-59.

DRANE, C., and McILVENNA, J. (1970)
'Gain maximization and controlled null placement simultaneously achieved in aerial array patterns', Rad. El. Eng. (GB), Vol. 39, p.49.

ERDELYI, A. (1956)
Asymptotic Expansions, Dover, p.51.

HAMID, M.A.K. (1968)
'Diffraction by a conical horn', IEEE Trans. Antennas and Propagation, Vol. AP-16, p.520.

HAMID, M.A.K., BOULANGER, R.J., MOSTOWY, N.J., and MOHSEN, A. (1970)
'Radiation characteristics of dielectric-loaded horn antennas', Electronic Letters, Vol. 6, p.20.

HARRINGTON, R.F. (1961a)
Time-Harmonic Electromagnetic Fields, McGraw-Hill, New York, pp 228-229.

HARRINGTON, R.F. (1961b)
ibid, p.224-225.

HILDEBRAND, F.B. (1956)

Introduction to Numerical Analysis, McGraw-Hill, New York, p.78.

HORTON, C.W., and WATSON, R.B. (1950)

'On the diffraction of radar waves by a semi-infinite conducting screen', J. App. Phys., Vol. 21, p.16.

HUNTER, J.D., and BATES, R.H.T. (1972)

'Secondary diffraction from close edges on perfectly conducting bodies', Int. J. Electronics, Vol. 32, p.321.

JAMES, G.L. and KERDEMELIDIS, V. (1972)

'Null placing in radiation patterns by shaping antenna edges', Electronic Letters, Vol. 8, p.439.

JAMES, G.L. and KERDEMELIDIS, V. (1973)

'Reflector antenna radiation pattern analysis by equivalent edge currents', to appear in Jan. (1973) issue of IEEE Trans. Antennas and Propagation.

JONES, D.S. (1953)

'Diffraction by a thick semi-infinite plate', Proc. Roy. Soc., Vol. A21, p.153.

JONES, D.S. (1964a)

The Theory of Electromagnetism, Pergamon, London, pp 608-615.

JONES, D.S. (1964b)

ibid, pp 481-3, pp 590-4.

JONES, D.S. (1964c)

ibid, p.336-346.

KAY, I., and KELLER, J.B. (1954)

'Asymptotic evaluation of the field at a caustic', J. Appl. Phys., Vol. 25, p.876.

KELLER, J.B. (1957)

'Diffraction by an aperture', J. Appl. Phys. Vol. 28, p.426.

KELLER, J.B. (1962)

'Geometrical theory of diffraction', J. Opt. Soc. Am., Vol. 52, p.116.

KINBER, B.E. (1960)

'The condition of shadowing and diffraction correction to current distribution', Rad. Eng. El. Phys., Vol. 5, p.1407.

KINBER, B.E. (1961)

'Sidelobe radiation of reflector antennae', Rad. Eng. El. Phys., Vol. 6, p.545.

KINBER, B.E. (1962a)

'Diffraction at the open end of a sectoral horn', Rad. Eng. El. Phys., Vol. 7, p.1620.

KINBER, B.E. (1962b)

'The role of diffraction at the edges of a paraboloid in fringe radiation', Rad. Eng. El. Phys., Vol. 7, p.79.

KINBER, B.E. and TSEYTLIN, V.B. (1971)

'Phase centres of parabolic antennas', Rad. El. Eng. Phys., Vol. 16, p.218.

KLINE, M., and KAY, I. (1965)

Electromagnetic Theory and Geometrical Optics, Interscience, New York.

KOCH, G.F. (1966)

'Paraboloid antennas with a low noise temperature', Nachrichtentech. Z.-CJ, Vol. 19, p.125.

KONTOROWICH, M.J., and LEBEDEV, N.N. (1939)

'On a method of solution of some problems of the diffraction theory', J. Phys. USSR, Vol. 1, p.229.

KOSHY, V.K., NAIR, K.G., and SRIVASTAVA, G.P. (1968)

'An experimental investigation of the effect of conducting flanges on the H-plane radiation patterns of E-plane sectoral horns', J. Telecom. Engrs (India), Vol. 14, p.519.

KOUYOUMJIAN, R.G. (1965)

'Asymptotic high-frequency methods', Proc. IEEE, Vol. 53, p.864.

LAWRIE, R.E., and PETERS, L. (1966)

'Modifications of horn antennas for low sidelobe levels', IEEE Trans. Antennas and Propagation, Vol. AP-14, p.605.

LEE, S.W. (1969)

'On edge diffracted rays of an open-ended waveguide', Proc. IEEE, Vol. 57, p.1445.

LEWIN, L. (1972)

'Main-reflector-rim diffraction in back direction', Proc. IEE, Vol. 119, p.1100.

MacDONALD, H.M. (1902)

Electric Waves, Cambridge University Press.

MacDONALD, H.M. (1915)

'A class of diffraction problems', Proc. London Math. Soc., Vol. 14, p.410.

MILLAR, R.F. (1955)

'An approximate theory of the diffraction of an electromagnetic wave by an aperture in a plane screen', Proc. IEE, Vol. 103C, p.177.

MILLAR, R.F. (1956a)

'The diffraction of an electromagnetic wave by a circular aperture', Proc. IEE, Vol. 104c, p.87.

MILLAR, R.F. (1956b)

'The diffraction of an electromagnetic wave by a large aperture', Proc. IEE, Vol. 104c, p.240.

MONTGOMERY, C.G. (1947)

Technique of Microwave Measurements, McGraw-Hill, New York, pp 900-907.

NAIR, K.G., and SRIVASTAVA, G.P. (1967)

'Beam shaping of H-plane sectoral horns by metal flanges', J. Telecom. Engrs (India), Vol. 13, p.76.

NAIR, K.G., SRIVASTAVA, G.P., and HARIHARAN, S. (1969)

'Sharpening of E-plane radiation patterns of E-plane sectoral horns by metallic grills', IEEE Trans. Antennas and Propagation, Vol. AP-17, p.91.

NARBUT, V.P., and KHMEL'NITSKAYA, N.S. (1970)

'Polarization structure of radiation from axisymmetric reflector antennas', Rad. Eng. El. Phys., Vol. 15, p.1786.

OH, L.L., PENG, S.Y., and LUNDEN, C.D. (1970)

'Effects of dielectrics on the radiation patterns of an electromagnetic horn', IEEE Trans. Antennas and Propagation, Vol. AP-18, p.553.

OSEEN, C.W. (1922)

'Die Einsteinsche Nadelstichstrahlung und die Maxwellschen Gleichungen', Annalen der Physik, Vol. 69, p.202.

OWEN, A.R.G., and REYNOLDS, L.G. (1940)

'The effect of flanges on the radiation patterns of small horns', J. Inst. Elect. Engrs, Vol. 93, IIIA, p.1528.

PAULI, W. (1938)

'On asymptotic series for functions in the theory of diffraction of light', Phys. Review, Vol. 54, p.924.

PLONSEY, R. (1958)

'Diffraction by cylindrical reflectors', Proc. IEE, Vol. 105C, p.312.

POGORZELSKI, S. (1967)

'Diffraction by the edge of an antenna reflector', Rozprawy Elect., Vol. 13, p.451.

POTTER, P.D. (1963)

'A new horn with suppressed sidelobes and equal beam-widths', Microwave J., Vol. 6, No. 6, p.71.

QUDDUS, M.A., and GERMAN, J.P. (1961)

'Phase correction by dielectric slabs in sectoral horn antennas', IRE Trans. Antennas and Propagation, Vol. AP-9, p.413.

RIBLET, H.J. (1947)

'A current distribution for Broadside arrays which optimizes the relationship between beam width and side-lobe level', Proc. IRE, Vol. 35, p.489.

RUDDUCK, R.C. (1965)

'Application of wedge diffraction to antenna theory', NASA Grant NSG-448, Dept 1691-13, June 30, 1965.

RUDDUCK, R.C., and WU, D.C.F. (1969)

'Slope diffraction analysis of TEM parallel-plate guide radiation patterns', IEEE Trans. Antennas and Propagation Vol. AP-17, p.797.

RUSCH, W.V.T., and POTTER, P.D. (1970a)

Analysis of reflector antennas, Academic Press, New York, p.52, p.111-2.

RUSCH, W.V.T., and POTTER, P.D. (1970b)

ibid, p.94.

RUSCH, W.V.T., and POTTER, P.D. (1970c)

ibid, p.91.

RUSSO, P.M., RUDDUCK, R.C., and PETERS, L. (1965)

'A method for computing E-plane patterns of horn antennas', IEEE Trans. Antennas and Propagation, Vol. AP-13, p.219.

RYAN, C.E., and RUDDUCK, R.C. (1968)

'Radiation patterns of rectangular waveguides', IEEE Trans. on Antennas and Propagation, Vol. AP-16, p.488.

RYAN, C.E., and PETERS, L. (1969)

'Evaluation of edge-diffracted fields including equivalent currents for the caustic regions', IEEE Trans. Antennas and Propagation, Vol. AP-17, p.292.

SCHELKUNOFF, S.A. (1943)

'A mathematical theory of linear arrays', Bell System Tech. J., Vol. 22, p.80.

SCHRETTER, S.J., and BOLLE, D.M. (1969)

'Surface currents induced on a wedge under plane wave illumination: an approximation', IEEE Trans. Antennas and Propagation, Vol. AP-17, p.246.

SENIOR, T.B.A. (1972)

'The diffraction matrix for a discontinuity in curvature', IEEE Trans. Antennas and Propagation, Vol. AP-20, p.326.

SILVER, S. (1949a)

Microwave antenna theory and design, McGraw-Hill, New York, pp 144-149, pp 417-420.

SILVER, S. (1949b)

ibid, p.192.

SILVER, S. (1949c)

ibid, p.383. p. 344

SLETTEN, C.J., and BLACKSMITH, P. (1965)

'The paraboloid mirror', Appl. Optics, Vol. 4, p.1239.

SOMMERFELD , A. (1954)

Optics, Academic Press, New York. pp 245-265.

STRAIT, B.J. (1967)

'Antenna arrays with partially tapered amplitudes', IEEE Trans. Antennas and Propagation, AP-15, p.611.

THOMAS, D.T. (1971)

'Analysis and design of elementary blinders for large horn reflector antennas', Bell System Tech. J., Vol. 50, p.2979.

UFIMTSEV, P.Ya. (1962)

The method of fringe waves in the physical theory of diffraction. Sovyetskoye radio, Moscow, 1962.

WOLFF, E.A. (1966)

Antenna Analysis. Wiley, New York. p.128.

WU, D.C.F., RUDDUCK, R.C., and PELTON, E.L. (1969)

'Application of a surface integration technique to parallel-plate waveguide radiation pattern analysis', IEEE, Trans. Antennas and Propagation, Vol. AP-17, p.280

YARU, N. (1951)

'A note on supergain antenna arrays', Proc. IRE, Vol. 39, p.1081.

YU, J.S., RUDDUCK, R.C., and PETERS, L. (1966)

'Comprehensive analysis for E-plane of horn antennas by edge diffraction theory', IEEE Trans. Antennas and Propagation, Vol. AP-14, p.138.

YU, J.S., and RUDDUCK, R.C. (1967)
'On higher-order diffraction concepts applied to a conducting strip', IEEE Trans. Antennas and Propagation Vol. AP-15, p.662.

YU, J.S., and RUDDUCK, R.C. (1969)
'H-plane pattern of a pyramidal horn', IEEE Trans. Antennas and Propagation, Vol. AP-17, p.651.